STUDIES ON HIGH-PERFORMANCE THERMOSETS AND THEIR INTERFACE AND INTERPHASE WITH CARBON-NANOTUBES

A Dissertation
Presented to
The Academic Faculty

by

Mohammad Hamza Kirmani

In Partial Fulfillment
of the Requirements for the Degree
Doctor in Philosophy in the
School of Materials Science and Engineering

Georgia Institute of Technology
December 2020

STUDIES ON HIGH-PERFORMANCE THERMOSETS AND THEIR INTERFACE AND INTERPHASE WITH CARBON-NANOTUBES

Approved by:

Dr. Satish Kumar, Advisor
School of Materials Science and Engineering
Georgia Institute of Technology

Dr. Naresh Thadhani
School of Materials Science and Engineering
Georgia Institute of Technology

Dr. Karl Jacob
School of Materials Science and Engineering
Georgia Institute of Technology

Dr. Seung Soon Jang
School of Materials Science and Engineering
Georgia Institute of Technology

Dr. Kyriaki Kalaitzidou
School of Mechanical Engineering
Georgia Institute of Technology

Date Approved: October 16, 2020

This dissertation is dedicated to my Nana,
Syed Zubair Ahmed

ACKNOWLEDGEMENTS

गुरू बिन ज्ञान न उपजै, गुरू बिन मिलै न मोष।
गुरू बिन लखै न सत्य को, गुरू बिन मिटै न दोष।।

Guru bin gyan na upajai, Guru bin mile na mosh,
Guru bin lakhai na satya ko, Guru bin mite na dosh

This famous Hindi duplet by Kabir, translates to, "Without the 'Guru' (teacher), one can neither obtain knowledge, nor salvation. Without the 'Guru', one can neither see the truth nor have their doubts removed".

I feel lucky to have Dr. Satish Kumar as my 'Guru', my advisor. This journey of my dissertation has been a beautiful one and this would have not been possible without the immense support and guidance that Dr. Kumar has provided throughout this process. I am grateful to Dr. Kumar for the rigorous training, the innumerous insightful discussions, to all the tough questions, his thorough feedbacks, the support and guidance related to my career development, all of which have prepared me well for my future ventures. Thank you, Dr. Kumar!

I would also like to thank my committee members – Dr. Karl Jacob, Dr. Kyriaki Kalaitzidou, Dr. Naresh Thadhani, and Dr. Seung Soon Jang for their time and very valuable advice.

This journey would not have been possible without the amazing professional and social support system I had by my side. I am grateful to Shruti Venkatram and Jonathan Leung for helping with vital resources that I needed moving to Atlanta. I am grateful to Dr. Prabhakar Gulgunje, Dr. Kishor Gupta, Dr. Po-Hsiang Wang, Dr. Sourangsu Sarkar, Dr.

Huibin Chang, Dr. Clive Luo, Dr. Jeffrey Luo and Shruti Venkatram for training on various equipment. I am grateful to Dr. Prabhakar Gulgunje, Dr. Po-Hsiang Wang and Dr. Sourangsu Sarkar for training and their guidance with experiments and analysis. The grad study groups helped immensely with the core classes and the qualifier exam. I am grateful to have had Winston (Hongfang) Lu (referred as Professor by members of the study group), Pedro Arias- Monje, Francisco Quintero, Andrew Boddorff, Fatima Hafsa, Abigail Advincula, Aditi Khirbat, Narayan Shirolkar, Jyotsna Ramachandran, Edward DiLoreto and many more to have worked through with.

Pedro, Jyotsna, Narayan and Mingxuan Lu have always been there to discuss, exchange or bounce ideas off each other, be it during our regular coffee sessions in the office, or during our lunch sessions. From work, politics, cooking, travel and what not, we had it all covered. From working together in the labs, doings experiments, characterization or fixing the tools, we were always there to help each other and this was a great support system to have. I am grateful to have worked with Dr. Kishor Gupta. I enjoyed exchanging and discussing ideas with him. Dr. Kishor Gupta always had a very calming presence and I enjoyed his company. I acknowledge the Institute of Electronics and Nanotechnology (IEN) at Georgia Tech for offering the state-of-the-art equipments without which this dissertation would not have been possible. I would specially like to thank Mr. Eric Woods, Mr. David Tavakoli and Miss Rebhadevi Monikandan for their support with SEM, XPS, Raman and SAXS tools. I am also grateful to Dr. Neha Kondekar for her help in conducting XPS.

I am glad to have been a part of the US-COMP, which is a multi-university NASA funded institute. The bi-annual review meetings meant coming together of ~70 people from

at least 11 different universities, 2 industries and 2 federal agencies. The meetings provided many opportunities for exchange of ideas, brainstorming and collaboration. I would specially like to acknowledge Dr. Emilie J. Siochi, Dr. Gregory Odegard, Dr. Richard Liang, Dr. Michael Czabaj, Dr. Susanta Ghosh, Dr. Jin Gyu Park and Dr. Chad Zeng.

I am also grateful to Dr. Prabhakar Gulgunje, Dr. An-Ting Chien, Dr. Amir Bakhtiari, Dr. Godfrey Sauti, Dr. Neha Kondekar, Dr. Bradley Newcomb, Dr. Jing Liu, Dr. Po-Hsiang Wang, Dr. Sudhakar Jagannathan, Dr. Kishor Gupta and Dr. Kristopher E. Wise for their support related to my career development.

It goes without saying that this journey would not have been possible without the continuous support, motivation, patience, sacrifices and love of my family. While my father, Dr. Wasif Kirmani and my mother, Mrs. Nuzra Zubair were ~7500 miles away in Saudi Arabia, they were often the first ones to inform me about some activity taking place on the Georgia Tech campus, an upcoming hurricane that i need to be cautious about or a new restaurant in Atlanta that I should go check-out. My elder sister, Mrs. Abeer Kirmani has been in Malaysia while my younger sister, Miss Rehab Kirmani has been in India, which meant that our family was in 4 different time zones, but we managed getting our group calls through. I am grateful to my brother-in law, Mr. Faiz Alam Kirmani for his guidance. It would not have been possible for me to be where I am today, without the support of my mamu, Mr. Syed Zuhair Ahmed.

This journey would also not have been possible without the friends who became family: Neha, Piyush, Atishay, Prakshi, Anirudh, Siddhant, Anagha, Rakshith, Supriya, Shreya and Siddhartha. I have been lucky to have some of the best roommates, Apaar, Deepak, Sangy, Bhuvesh and Nirbhay.

I am fortunate to have experienced so much and to have made fantastic memories during my stay here. I will always cherish these memories.

TABLE OF CONTENTS

LIST OF TABLES

LIST OF FIGURES

SUMMARY

Materials with higher strength to weight ratio than the current state of the art (SOA) carbon fiber reinforced plastics (CFRP) are desired by NASA to support affordable space exploration, including human travel to mars and beyond [1]–[3]. The carbon nanotube-polymer (CNT-polymer) composites are expected to have significantly better mechanical properties than the current SOA CFRP [1], [4] and qualify as a potential system for achieving the target mechanical properties in materials required to support human travel to mars. CNT containing polymer composites, however, have some limitations, one of which is the load transfer at the CNT- polymer interface [4]–[7]. The interface plays a critical role in determining the overall macroscale properties of the composite [8]–[12]. While, significant attention has been directed to this end [5], [7], [10], [13]–[19] the CNTs in the composites have not yet reached their full potential.

There are several aspects of the CNT-polymer composites which can help create the next generation of high strength and lightweight materials, to help support human travel to mars and beyond. These include, (a) improving the fracture toughness of the polymer resin, (b) understanding and optimizing the CNT-polymer interactions, (c) understanding the effects of CNTs on the polymer cure reactions, which consequently can alter the mechanical properties of the composite, (d) modifying the CNT-polymer interface-interphase through surface treatment and sizing, (e) understanding the effects of amorphous carbon on the CNT-polymer interface-interphase. Herein, the first part of the dissertation focuses on the effect of processing on the molecular structure and the properties of a multi-component aerospace grade bismaleimide (BMI) resin, containing no CNTs, and is

discussed in Chapter 2. Materials in nature such as nacre that are made of mechanically inferior building blocks exhibit extreme toughness at the macro scale because of the geometry and arrangement of their constituents. Taking a cue from these systems, we have investigated whether the molecular rearrangement in a heterogeneous BMI system can alter toughness at the macro scale. To this end, a multicomponent BMI system is processed by using (a) a melt and cast (termed Melt) approach and (b) a dual asymmetric centrifuge based high-speed shear mixing (termed HSSM) approach to enforce molecular rearrangement. FTIR, Raman, and NMR spectroscopies have been used to study the molecular rearrangement upon HSSM processing. Small-angle X-ray scattering has been used to study the effect of processing on the molecular arrangement of the BMI.

The second part of this dissertation focuses on the structure, process and properties of CNT modified BMI, with tailored interface-interphase and is discussed in Chapter 3. With the recent large-scale production and availability of the CNT macro-assemblies in the yarn, tape and sheet forms, CNT-polymer composites could now be prepared through conventional CFRP manufacturing techniques such as filament winding. It is however expected that the resin dominated properties, such as the inter and intra laminar fracture toughness in these CNT- polymer composites would still remain relatively weak, as they have been for the CFRPs. Modifying the resin with CNTs is an attractive route for further improving the resin properties. Herein, CNT- BMI nanocomposites using three different CNTs and via two different processing routes, have been prepared and studied.

The third part of this dissertation focuses on the effects that the CNT have on the cure of the BMI, as well as the effects that the cure of BMI has on the CNTs, in the nanocomposites containing up to 40 wt% CNTs, and is discussed in Chapter 4. CNTs can

interact with the BMI system through the NH$-\pi$ [20], [21], $\pi-\pi$ [22], CH$-\pi$ [16], [22], and OH$-\pi$ [23], non-covalent interactions. The individual components of the BMI however can have exclusive non-covalent interactions with the CNTs. For example, in a BMI system containing 4,4'- bismaleimidodiphenylmethane (BDM) and diallylbisphenol A (DABA) components [24], only the BDM component contains the maleimide functional group which can potentially interact with the CNTs through the NH$-\pi$ bonding, while only the DABA component, containing the OH functional group can potentially interact with the CNTs through the OH$-\pi$ interactions. The potential for the preferential stacking of the different BMI components around the CNTs, can have important implications on the cure behavior of the BMI in the nanocomposite and consequently on the overall mechanical properties of the nanocomposite. Herein, two different types of CNTs in the sheet form: unbaked and baked (termed as UB and B CNT), have been employed. The effects of the varying CNT content on the inter-CNT spacing, cure reactions of the BMI, compression of CNTs and the thermomechanical properties of the nanocomposites have been investigated. The thermomechanical results and the theoretical calculations have then been used to estimate the interphase thickness of the CNT- BMI nanocomposites.

The fourth part of this dissertation focuses on sizing and tailoring the CNT- BMI interface - interphase using a carbon fiber sizing, and is discussed in Chapter 5. Sizing of carbon and glass fibers is a critical step in the manufacturing of their respective composites with polymers and has led to improved interfacial shear strength (IFSS), inter-laminar shear strength (ILSS) and fracture toughness of the composites. As the CNT-polymer composites could now be prepared through conventional CFRP manufacturing techniques such as

filament winding, the question is, could we integrate another critical step of the conventional CFRP manufacturing, i.e., 'sizing', to the CNT-polymer composite preparation to tailor the CNT-polymer interface-interphase? To be able to answer that question, we first need to understand the sizing-CNT interactions and reactions. To this end, herein, the effects that (a) CNTs, (b) the degree of functionalization and defects (DOFD) in the CNTs and (c) the sizing content, have on the sizing cure reaction and cure kinetics have been evaluated. CNTs with three different DOFD have been employed. The sizing coated CNTs have then been used to prepare nanocomposite films with a high-performance aerospace grade bismaleimide (BMI) resin. Overall three different types of CNT- BMI interface-interphase have been prepared and studied in nanocomposites containing 60 wt% CNTs: (a) pristine CNT- BMI, (b) functionalized CNT- BMI, and (c) sizing coated functionalized CNT- BMI. The effect of CNT, CNT functionalization and sizing coated CNTs on the BMI cure reactions, thermomechanical properties and the molecular heterogeneity and hierarchy of the nanocomposites have been studied and discussed.

Finally, CNTs may contain amorphous carbon,[25] among other impurities which consequently could interfere with the interfacial interactions of the CNT and the polymer. While such impurities are expected to have a negative effect on the polymer-CNT interface,[5] quantitative evidence of the extent of such negative effects is lacking. Herein, the effect that the amorphous carbon and the baking of CNTs to remove the amorphous carbon have, on the interfacial stress transfer with the polyurea matrix has been studied and discussed in Chapter 6. During CNT synthesis, by products such as amorphous carbon [25] may be formed which consequently could interfere with the interfacial interactions of the

CNT and the polymer. While such impurities are expected to have a negative effect on the polymer-CNT interface [5], quantitative evidence of the extent of such negative effects is lacking. Herein, the difference in interfacial straining has been studied in composites of polyurea with two types of CNT sheets: (a) sheets containing amorphous carbon (termed as unbaked CNT sheet) and (b) sheets that are thermally treated to remove amorphous carbon (termed as baked CNT sheet). The understanding of the effects of the amorphous carbon and the baking treatment, based on the CNT- polyurea system should be translatable to other CNT-polymer system, including the CNT-BMI system.

It is expected that these studies will provide guidance for the manufacturing of CNT, or CNT and carbon fiber hybrid based laminates that will ultimately meet NASA mechanical property goals.

CHAPTER 1. INTRODUCTION

1.1 Overview

Bismaleimides (BMI) are attractive candidates for advanced high-performance aerospace applications[26]–[28]. They have high temperature resistance, great dimensional stability, excellent physical property retention at elevated temperatures, both in dry and humid conditions [29], [30] and exhibit non-flammability properties [31], [32]. BMI are extensively employed in aerospace applications including the US Air Force's F-22 [33] and F-35 [27] fighter jets. About 50% of the total number of parts in the F-22 that contain thermoset resins, use BMI as the resin [33].

Multi-walled carbon nanotubes (MWCNTs) have garnered great attention since the historic publication in 1991 by Iijima [34], owing to their outstanding mechanical [35]–[37], thermal [38], [39] and electrical [40] properties. Theoretical tensile strength and Young's modulus of an individual CNT is predicted to be > 100 GPa and 1 TPa, respectively. Experimentally, tensile strength of up to 100 GPa and Young's modulus of up to 950 GPa have been reported [36].

CNT-BMI nanocomposites can have significantly better mechanical properties than those of the current SOA CFRP [1], [4]. However, to realize these properties, it is critical to (a) understand the interaction and the effects that the CNTs and BMI can have on each other, within the nanocomposite and (b) optimize these interactions by tailoring their interface and interphase.

1.2 Bismaleimide

BMI resins are a family of thermosetting resins which are generally low molecular weight oligomers, at least di functional - maleimide terminated monomers that undergo polymerization to form highly cross linked network without evolution of by-products [30], [41] (based on most favorable reactions). They are relatively young materials with first patent on homopolymerization of BMI granted in 1968 to Friedrich Grundschober from France [42]. These materials have evolved tremendously since then. Robert J. Iredale and coworkers [43] have classified BMI into "conventional 'first generation' and second generation 'toughened' BMI systems". The first-generation BMIs had high temperature performance because of high crosslinking density. The high cross-linking density however rendered brittleness and low fracture toughness to the material, making way for a modified two-component copolymerization of bisphenol A (BA) based monomer, diallylbisphenol A (DABA/ DABPA) and a BMI monomer-based system that showed better toughness [44]. 4,4'- bismaleimidodiphenylmethane (BDM), one of the many BMI monomers[41] along with DABA, make as a standard BMI system currently. The maximum impact strength achieved for a BMI system however still remained at 19 kJ/m^2 and further improvement in the fracture toughness of the BMI system is highly desirable.

BMI undergoes a complex cure reaction. Reactions proposed and widely accepted include, "ene" reaction of the allyl group in DABA with BMI monomer, "diels-alder", "homopolymerization", "aromatization" and "etherification" [43], [45]–[49] as illustrated in Figure 1.1. The ene reaction is suggested to occur between 80- 160 °C [49]. The unsaturated ene product is suggested to undergo a Diels-Alder reaction between 160- 220 °C to form a di-adduct [49]. The di-adduct is further suggested to undergo a Diels-Alder

reaction between 225-275 °C [49]. The tri-adduct is also suggested to undergo a thermal rearrangement between 250- 300 °C [49].

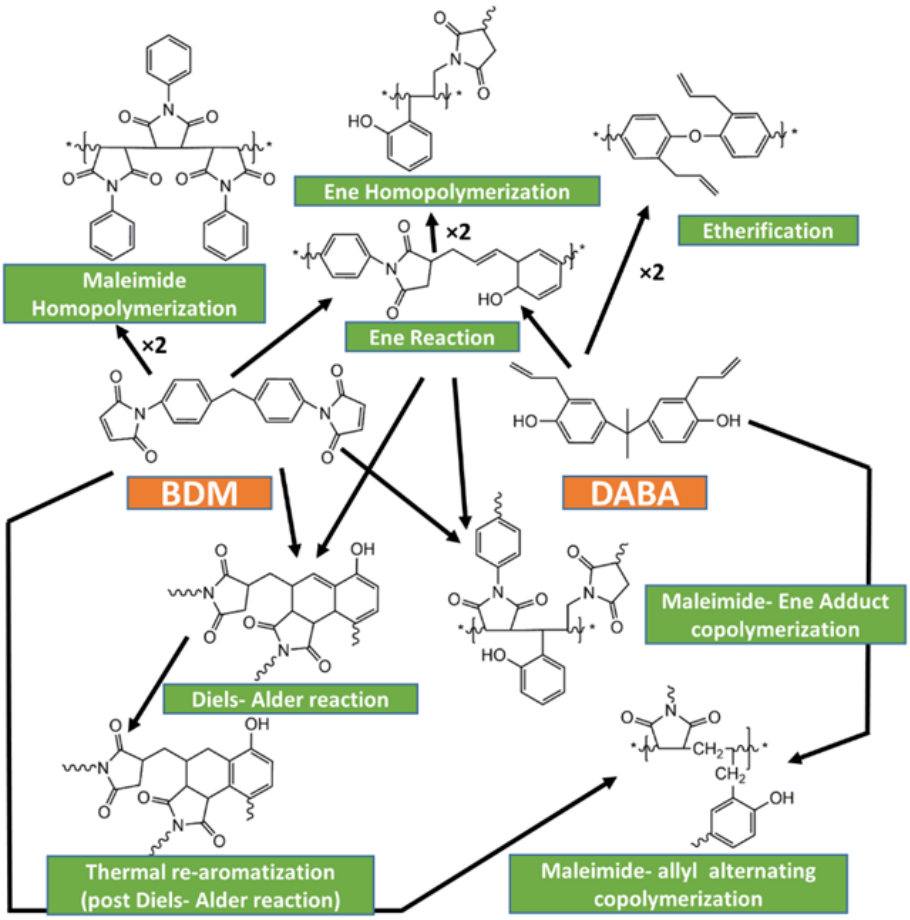

Figure 1.1. Bismaleimide (BMI) system containing 4,4'- bismaleimidodiphenylmethane and diallylbisphenol A (DABA) as the two starting components. BMI system undergoes a complex cure reaction involving simultaneous, multiple cure reaction pathways that lead to the formation of multiple products. The major reactions and products proposed for the system are illustrated here. Voids can be formed as a result of dehydration reaction that could take place through the etherification of DABA-DABA adducts or homo/co-polymerization of any adducts with OH groups available [43], [45]–[48].

1.3 Carbon Nanotubes

A SWNT is analogous to a rolled and zipped graphene in a hollow cylindrical tube form, where, graphene is a single layer of carbon atoms in a sp^2 hybridized state. Depending

on the number of concentric shells/tubes around the hollow core, CNTs could be classified as either SWNT (one shell), double wall CNT (DWCNT) (two concentric shells) or multi-wall CNT (more than two concentric shells). The angle between the edge of the graphene layer and the rolling axis is defined as the chiral angle (θ) (Figure 1.2). A CNT (SWNT or an individual tube of a DWCNT or MWCNT) can be represented through indices (n, m), where (n, m) corresponds to the graphene unit cell vector. The rolling of graphene into CNT could be done in a number of ways, where, (a) θ = 0° (termed as zigzag) (m=0), (b) θ = 30° (termed as armchair) (m = n), (c) any θ ≠ 0°or 30° (termed as chiral) [50].

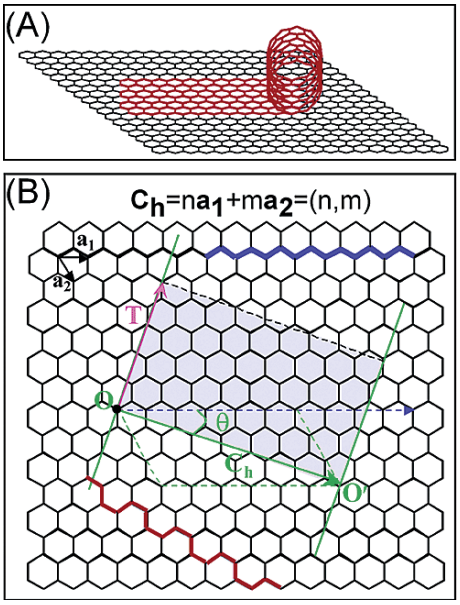

Figure 1.2 : (a) Schematic of rolling graphene into CNT. (b) θ represents the chiral angle, C_h represents the chiral vector. The blue pattern represents a zig-zag (n,0) rolling direction whereas the red pattern represents an arm-chair (n=m) rolling direction [50].

1.3.1 CNT Macroscopic Assemblies

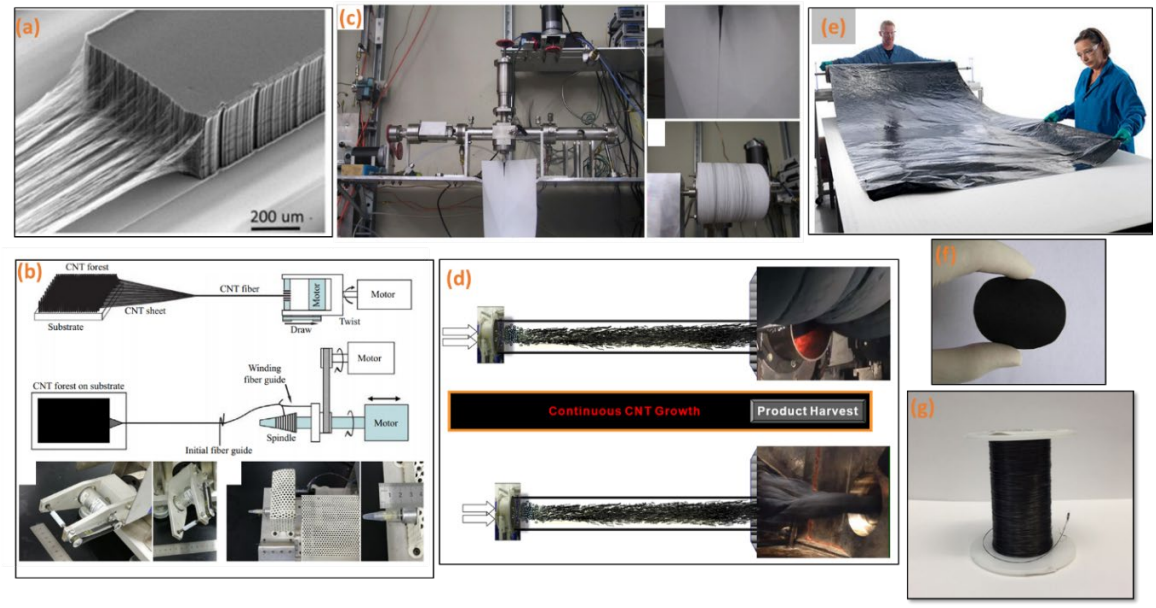

Figure 1.3 (a) CNT forest.[51]. The CNT forests could be drawn to make CNT yarns. (b) Schematic of CNT yarn manufacturing from a CNT forest.[51] (c) CNT yarn processed through wet spinning in a 102% sulphuric acid solution.[52] (d) Schematic of floating catalyst chemical vapor deposition process [53]. (e) CNT sheet [54], (f) CNT buckypapers [55], (g) CNT yarn (yarn diameter ~0.2 mm)

The macroscopic form that the CNTs are assembled in is critical to their overall mechanical strength. CNT macro-assembly with a poor microstructure (from a mechanical strength standpoint), can lead to insignificant strength, e.g., CNTs in a powder form. However, tensile strength and Young's modulus of up to 10 GPa/g/cm^3 and 400 GPa/g/cm^3, respectively have been reported [56] for CNT yarns. CNTs in this work [56] were stretched and aligned and the 10 GPa/g/cm^3 and 400 GPa/g/cm^3 tensile strength and modulus, respectively were obtained for specimens with a 1 mm gauge length. For a 20 mm gauge length the strength reported was 1 GPa/g/cm^3 [56]. The macroscopic form of CNT also dictates the scope of further processing with a resin/matrix, as well as its potential applications. The various macroscopic assemblies of CNTs (Figure 1.3) are discussed below.

CNT forests involves growing CNTs on a substrate that has catalyst deposited on its surface following a chemical vapor deposition (CVD) of carbon atoms obtained through the decomposition of a hydrocarbon [57], [58]. The CNT forests grown on a substrate can be directly used for certain applications while the CNTs are on the substrate [59], [60]. However there is also a need that the CNTs be detached from the substrate in order for them to be employed any further. CNTs can be grown and used without the substrate in the powder form. The CNT powder essentially has no significant strength of its own and is thus mixed in a matrix for achieving enhanced properties in the composite, compared to the neat matrix.

Buckypapers refer to aggregates of CNTs (typically, randomly oriented CNTs), which are generally obtained through filtering of CNTs from a dispersed/suspended state in a solvent, followed by drying of the filtered CNTs. Davijani *et. al.* [17] reported a tensile strength and modulus of 16 MPa and 1.1 GPa, respectively for buckypaper made using HiPCO SWNT through dispersion in dimethylformamide (DMF). Sreekumar *et. al.* [61] reported a tensile strength and modulus of 30 MPa and 8 GPa, respectively for buckypaper made using HiPCO SWNT through dispersion in oleum. Nanocomp Inc. use a floating catalyst chemical vapor deposition process for producing continuous non-woven CNT sheets [54]. Their brochure quotes the specific strength at 0.07 GPa/g/cc [54]. Jensen *et. al* .[62] used acetone condensed CNT sheets from Nanocomp Inc. with an axial specific strength and modulus of 0.3 and 8 GPa/g/cc, respectively. The sheet were then stretched by 43% to align the CNTs which resulted in an improvement of the axial specific strength and modulus to 0.56 and 22 GPa/g/cc, respectively. A pulsed electrical current, temperature, and pressure treatment was introduced for creating inter-CNT bonds. Post

treatment of the 43% stretched sheets at 1000 °C and 40 MPa pressure, specific strength and modulus of 1 and 100 GPa/g/cc, respectively has been reported [62].

1.4 CNT- Polymer Interactions

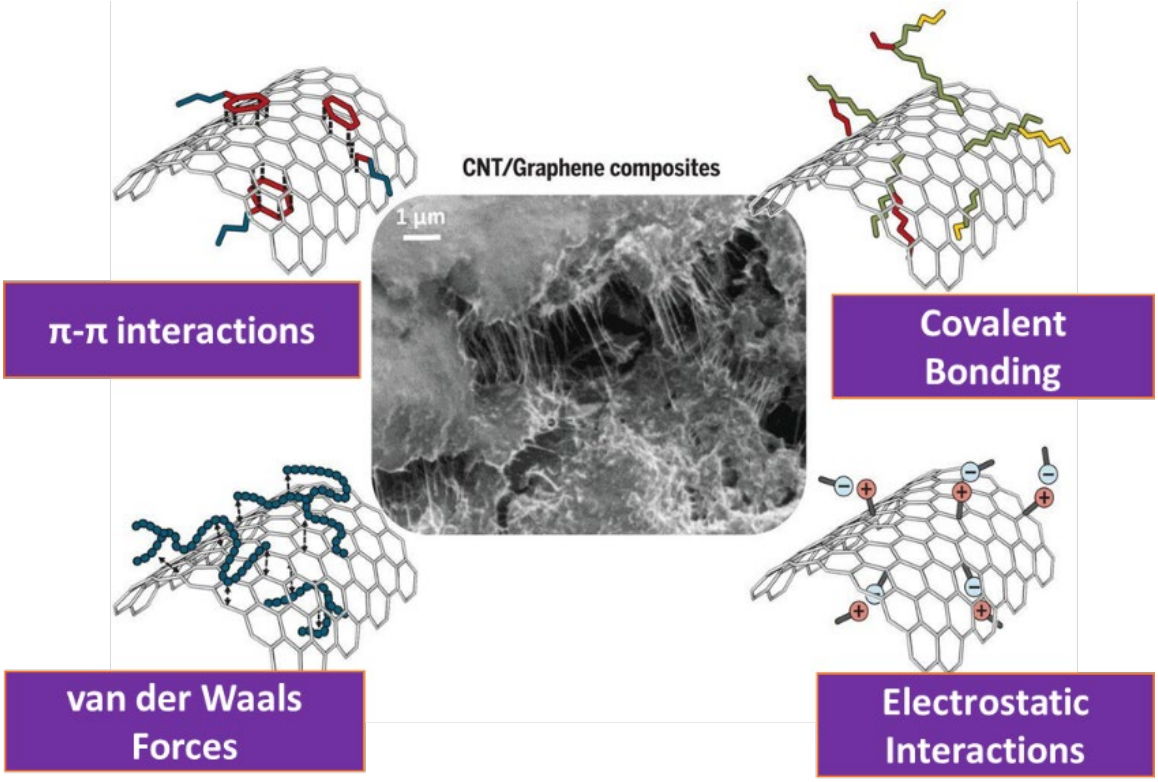

Figure 1.4. The polymer and CNTs can interact through covalent or non-covalent interactions [4]. While covalent bonding of CNTs with the matrix offers stronger interaction, it comes at the cost of reducing the inherent strength of CNTs [63].

Several factors contribute to the load transfer efficacy of the CNT- polymer interface and interphase. Some of these are closely inter-related and inter-dependent. First, the CNT related variables include its helicity [64], number of walls [15], length [65], functionalization [66], and defects [63], [67]. Second, the polymer related variables include, functional groups [23], [68]–[70], conjugation and aromaticity [22], [23], [69], crystalline/amorphous [71] content, and the polymer molecular weight [72]. Third category

of factors include combination of polymer and CNT related variables [73], [74]. The polymer-CNT interaction can be covalent [68], or non-covalent [20], [22], [23], [69]. Examples of non-covalent interactions include $\pi - \pi$ [22], CH$-\pi$ [16], [22], NH$-\pi$[20], [21] and OH$-\pi$[23] interactions. Fourth, composite processing related variables include, solution processing [71]. melt processing [16], in-situ polymerization [75] and molecular layer deposition [76]. The processing route is closely tied to the macroscopic form of CNTs used for composite preparation. CNTs can be in various forms including : powder/fluff [5], [16], [77], forest [78], buckypaper/sheet/tape [17], [79]–[81], or yarn [82]. Finally, CNTs may contain amorphous carbon [25], among other impurities which consequently could interfere with the interfacial interactions of the CNT and the polymer. While such impurities are expected to have a negative effect on the polymer-CNT interface [5] quantitative evidence of the extent of such negative effects is lacking.

Typically, a solution or melt processing based dispersion technique is used to make a polymer-CNT composite when CNTs are in the powder/fluff form [5]. The challenge however is to disperse the CNTs in the matrix, as CNTs agglomerate resulting from van der Waals interactions between them. CNT agglomerates tend to be the limiting factor from a mechanical strength standpoint as the shear modulus for SWNT bundles can be as low as 1 GPa [83]. When CNTs are in a sheet form, the infiltration of CNT network with polymer in the solution [84]–[86] or melt form [79] has proven to be a successful technique for composite manufacturing. The solution infiltration, however is preferred over melt infiltration to facilitate better polymer diffusion into the CNT network. The challenge however, is to completely infiltrate the CNT network.

Studies on the interfacial characterization of polymer-CNT composites have been conducted using Raman spectroscopy [19], wetting measurements [87], Fourier transform infrared spectroscopy (FTIR) [16], [87], X-ray scattering [71], electron energy loss spectroscopy (EELS) [88], [89] and CNT pullout tests using atomic force microscopy (AFM) [90]–[93]. Theoretical [94], [95] and computational models [10], [96], [97] have been developed and utilized towards this end as well. Raman spectroscopy has proven to be a powerful tool for characterizing the interfacial load transfer [19], [98]. The tensile strain in CNTs results in Raman band frequency downshift of the following bands: D ~ 1300 cm^{-1}, G ~ 1580^{-1}, G' ~ 2600^{-1}. This, in turn is associated with the weakening of $C-C$ bonds [99].

1.5 CNT- BMI Nanocomposites

BMI containing CNT nanocomposites have achieved uniaxial tensile strength and modulus of up to 6.5 [100] and 350 GPa [84], and an impact strength of up to 30 kJ/m^2 [101].

1.5.1 CNT- BMI Nanocomposites with Low CNT Content

Impact strength of the nanocomposites of BMI with both, pristine-CNTs (p-CNT) and CNTs with different functionalization (f-CNTs) has been evaluated in prior works [101]–[107] and is summarized in Table 1.1. Two major processing techniques have been employed in these studies [101]–[107], first, where the CNTs are sonicated in a solvent and/or DABA. The BMI monomer is then added, melt and mixed through mechanical stirring to the sonicated CNT dispersion. While a good dispersion of CNTs in the DABA might be achieved through sonication, since the BDM is melted and mixed only through mechanical stirring, this strategy could be detrimental to the final dispersion level of the

CNTs in the BMI system. Second, the dry CNTs are directly added to the BMI- DABA melt and is then mechanically stirred. These studies [101]–[107] reported in the literature have used a two component BMI system with a BMI monomer and DABA modifier.

Jun Qiu and co-workers [102] functionalized CNTs with hyperbranched polyethyleneimine (PEI) to make nanocomposites with 0.5- 4 wt% loading of CNTs and obtained an impact strength of up to 9.1 kJ/m^2 in the nanocomposite containing PEI functionalized CNTs. The pristine BMI had an impact strength of 6.9 kJ/m^2 [102]. CNTs were ultrasonicated in ethanol for 30 mins. Ethanol soluble DABA was then added dropwise to the suspension, while the suspension was still ultrasonicated. Post evaporation of ethanol at 80°C and under stirring for 24 h, BMI monomer were added to CNT-DABA and melted at 140°C for 30 mins after which the prepolymer was poured in a mold and cured.

Aijuan Gu and coworkers [103] used a two component BMI- DABA system to make nanocomposites with aminated f-CNTs containing up to 1.4 wt% f-CNTs. BDM was melted at 110°C-130°C and the pristine and functionalized CNTs were then added and mixed through mechanical stirring. Impact strength increased from 11.1 kJ/m^2 for the p-BMI to 15.3 kJ/m^2 for the nanocomposite containing 0.28% f-CNT. Others [104], [106] used similar processing method as Aijuan Gu and coworkers [103] where CNTs were simply added to the melt BMI monomer- DABA melt and stirred without having them dispersed in a solvent initially. Wang Chong and coworkers [104] functionalized CNTs with N-phenyl maleimide which were dispersed in the two component BMI- Bisphenol A slurry by stirring and then cured to make BMI/CNT composites up to 2 wt.% CNT loading. Impact strength showed a maximum value at 1.5 wt.% f-CNT loading, being 16 kJ/m^2, an

increase from 4.7 kJ/m^2 for p-BMI. Shuang Li and coworkers [106] used p-CNTs to make nanocomposites with two component BMI-DABA having CNT loadings of up to 1.25 wt.%. Maximum impact strength was observed at 0.75wt% CNT loading being 16.6 kJ/m^2 [106].

Yue Han and coworkers [101] used CNTs functionalized with nitric acid (A-CNT), ethylene di amine (E-CNT) and diaminodiphenylmethane (M-CNT) to prepare nanocomposites with a two component BMI system (BDM-DABA). Samples were prepared with up to 1 wt. % loading of CNTs. CNTs were added to the DABA component of the resin and mechanically stirred for 15 mins followed by probe-sonication for 120 minutes. The BDM component was then added to the suspension and stirred. Composites containing 0.50 wt.% diaminodiphenylmethane-functionalized CNTs showed an improvement of 60% in the impact strength (from 18 to 30 kJ/m^2). Shuang Li and co-workers[106] dispersed vacuum dried CNTs in DABA through stirring at 140°C, for an hour. BDM was then added and mixed for 20 minutes. The impact strength increased from 12.2 to 16.6 kJ/m^2 for the 0.75 wt.% CNT- BMI nanocomposite compared to the p-BMI.

Table 1.1. Impact strength of p-BMI and BMI nanocomposites from literature.

Filler type	Filler loading (wt.%)	Impact Strength (kJ/m^2)	Mixing Method for BDM-DABA	Notes
p-CNT	0, 1	6.8, 7.8	Melt and add	Hyperbranched PEI f-CNTs, 2 component BMI, Izod impact test- ASTM D256.[102]
f-CNT	2.5	9.1		
p-CNT	0, 0.28	11.1, 7.8	Stirring	Amine f-CNTs, 2 component BMI, Unnotched izod impact test - ASTM 4812.[103]
f-CNT	0.28	15.3		
p-CNT	0, 1.5	4.7, -	Stirring	N-phenyl maleimide f-CNTs, 2 component BMI, Unnotched izod impact test - ASTM 4812. [104]
f-CNT	1.5	16		
p-CNT	0, 0.5	18, 24	Stirring	Diaminodiphenylmethane-f-CNTs, 2 component BMI, Charpy impact test post polishing with sand paper – ISO 179-2 [101]
f-CNT	0.5	30		
p-CNT	0, 0.75	9.8, 12.7	Stirring	Hyperbranched aliphatic polyimide f-CNTs, 2 component BMI, Izod impact test – ASTM D256. [105]
f-CNT	0.75	21.5		
p-CNT	0, 0.75	12.2, 16.6	Melt and add	p-CNTs, 2 component BMI [106]
DOPO; p-CNT	0; 0 4; 1	10.5 8.4	Stirring	DOPO used as flame retardant agent, Silane f-CNT, 2 component BMI, unnotched impact test-GB/T2571-1995.[107]
DOPO; f-CNT	4; 1	13		
GO	0, 0.3	12.5, 8	Melt and add	Silane f-GO by grafting MPTS on GO sheets, 2 component BMI, Unnotched impact test - ASTM 4812 using charpy impact testing machine.[108]
f-GO	0.3	20.8		
f-GO	0, 0.1	12.5, 23	Melt and add	APTES f-GO, 2 component BMI, Unnotched Impact Test - ASTM 4812 using charpy impact testing machine.[109]
f-GO	0, 0.1	12.5, 22	Melt and add	MAH f-GO, 2 component BMI, Unnotched Impact Test - ASTM 4812 using charpy impact testing machine. [110]
RGO	0, 0.6	10.7, 9.8	Stirring	HBPT f-RGO, 2 component BMI, GB/T2567-2008 standard for impact testing. [111]
f-RGO	0.6	16.7		
RGO	0, 0.3	18.8, 18	Stirring	Diazonium f-RGO, 2 component BMI, Unnotched Impact Test - ASTM 4812 using charpy impact testing machine.[112]
f-RGO	0.3	26.2		

1.5.2 CNT-BMI Nanocomposite with High CNT Content

Solution assisted infiltration of BMI into the macro-assembly of CNTs, such as a yarn or sheet, is an attractive route for making CNT-BMI nanocomposites containing more than 10 wt% CNT loadings [79], [80], [119], [84], [100], [113]–[118]. Prior studies on the CNT-BMI nanocomposites prepared through the solution assisted infiltration approach have demonstrated significant improvement in the tensile strength and modulus (summarized in Table 1.2) compared to either the neat BMI or the neat CNT sheet/yarn. Li et. al.[122] reported that the strength of the CNT-BMI and CNT-polyimide nanocomposites depend on the temperature that the nanocomposites were cured at. The CNT-BMI nanocomposites cured at 150, 240 and 280 °C had a tensile strength of ~1.6, 2.3 and 1.7 GPa, respectively [122]

Table 1.2. The tensile strength and modulus reported in the literature on CNT-BMI nanocomposites prepared by solvent assisted infiltration of BMI.

CNT Content (wt%)	Tensile Strength (MPa)	Tensile Modulus (GPa)	CNT Alignment Degree	Remarks
90	1855	174	N/A	CNT sheets: epoxide functionalized, 15% stretching post infiltration with BMI/DMF at 0.05 mm/min strain rate.[114]
90	2518	176	N/A	CNT sheets: epoxide functionalized, 15% stretching post infiltration with BMI/DMF, 40 mm/min strain rate.[114]
60	2088	169	0.8	Nanocomp CNT sheets, Cytec 5240 BMI, 40% stretching-dry.[115]
60	3081	350	N/A	Nanocomp CNT sheets, Cytec 5240 BMI, 40% stretching-dry, epoxidation functionalization.[84]
60	700	92	0.93	Nanocomp CNT sheets, Cytec 5240 BMI, resin infused 80% stretching.[80]

Table 1.2 continued

60	**1580**	**252**	**0.92**	**Nanocomp CNT sheets, Cytec 5240 BMI, 70% resin infused heating assisted stretching at 70°C.[116]**
70	6500	300	0.82	CNT sheets synthesized using CVD, densification with ethanol followed by BMI/Acetone, 34% stretching.[100]
61	609	71	0.79	Nanocomp CNT sheets/tape, RM-3010 BMI Renegade in toluene/MEK infiltrated, 34% stretching, RHAIC cure.[79]
50-55	3500	266	N/A	Aligned CNTs drawn, stretched using a winder, Designer Molecules BMI/toluene infiltrated post 12% dry stretching.[117]
54-66	4500	275	N/A	Aligned CNTs drawn, 1.5% stretching post infiltration with BMI/DMF.[118]
100: 0	900	-		The cross-linked structure and consequently the nanocomposite strength depended on the curing temperature.[119]
-	2380	110		

1.6 Sizing

Sizing of the carbon fibers is a critical step in the manufacturing of carbon fiber reinforced plastics (CFRPs). Sizing serves two major purposes: (a) facilitates easier handling of the fibers by preventing fiber breakage and misalignment during processing [120] and (b) alters the interfacial strength of the fiber and the matrix [120]–[128]. Sizing refers to a thin coating applied on the fiber surface. Sizing could comprise of several components including coupling, cross-linking, anti-static agents and film formers [129]–[131]. Sizing has demonstrated significant improvements in the IFSS [121]–[124] and the ILSS [125]–[128] of the fiber reinforced polymer composites. Downey *et. al.* [121] for example, reported an increase of up to 84% and 100% in the mode-I fracture toughness

and the IFSS, respectively, of the carbon fiber- epoxy composites made using the sized carbon fiber compared to carbon fibers with no sizing. Results from some other studies in the literature that have reported an improved IFSS [121]–[124] and ILSS [125]–[128] through the use of sizing have been summarized in Table 1.3.

Pristine carbon fibers tend to misalign and/or break during the prepreg process from the frictional forces that the fibers experience while winding and/or unwinding. The need for an easier handling of the carbon fibers during the CFRP manufacturing lead to the inception of sizing. As the sizing remains in the CFRPs post processing, it was soon realized post its inception that the sizing shouldn't have any detrimental effects on the carbon fiber adhesion with the matrix. Moreover, an enhancement in the adhesion was desirable [132]. This required that the sizing components be compatible with the specific resin being used. Today, a range of sizing agents, tailored for specific resins are commercially available.

Sumida *et. al.*[133] pointed several considerations that went in their reported invention on the epoxy based sizing. Their considerations provides us with some perspective on the selection criterion of the different components that make the sizing. First, from a compatibility stand point as the epoxy resin was the most commonly used matrix for the CFRP, they developed an epoxy based sizing. Second, epoxy based sizing that existed before their invention, used methyl ethyl ketone as a solvent which posed serious safety and health hazard and the industry called for safer alternatives. Third, while water, being a safer solvent was considered as a replacement to methyl ethyl ketone, the epoxy did not form a stable and homogenous suspension in water. To this end, Sumida *et.*

al. [133] used a polyurethane compound, alongside the epoxy, where the polyurethane assisted in forming a stable dispersion of epoxy in water.

Suguiri *et. al.*[134] reported using an amphoteric surfactant in the sizing made from a thermoplastic resin. The rationale being that the amphoteric surfactant behaves as anionic in the basic medium, as cationic in the acidic medium. Thus, it provides for a sizing solubility in water over a wide pH range.

Mader *et. al.*[135] used a silane coupling agent, γ-aminopropyltriethoxy silane (APS), with a polyurethane (PU) or epoxy resin (EP) film formers as the components of sizing. Glass fibers as the reinforcement and an epoxy resin as matrix, were used. A 75% increase in the ultimate adhesion strength was reported when only APS was used as the sizing agent, while a 30% and 62% increase in the ultimate adhesion strength was reported when APS with PU and EP were used, respectively

Table 1.3 Selected studies from the literature that have reported improved IFSS and ILSS in the composites prepared using sized carbon fibers.

System	Sizing	Improvements Reported	Reference
CF-epoxy	Epoxy based aromatic and aliphatic	Up to 32% improvement in the interfacial shear strength (IFSS) (54 and 41 MPa for ultra-violet ozone treated carbon fibers with and without sizing treatment, respectively).	Downey and Drzal.[121]
CF-epoxy	Commercial sizing with added luminescent nanoparticles (LN)	71% in IFSS (113.2 and 66.3 MPa for CF-epoxy composites with and without sizing, respectively). 102% in transverse fiber bundle tensile test (23.8 and 11.8 MPa for CF-epoxy composites with and without sizing, respectively). The interfacial layer tagged with LN showed the interphase to be 1.2 μm thick.	Liu *et. al*. [122]

Table 1.3 continued

CF-epoxy	Carbon nanotube (CNT) and poly (phthalazinone ether ketone) containing sizing	Up to 70% in the IFSS (81 and 48 MPa for CF-epoxy composites with and without sizing, respectively).	Liu *et. al.*[124]
CF- poly (phthalazinone ether ketone)	CNT modified sizing agent	Up to 75% in IFSS (70 and 40 MPa for composites with and without sizing, respectively).	Zhang *et. al.*[136]
CF-Bismaleimide (BMI)	LaRC PETI-5	Up to 40% improvement in storage modulus at 250 °C (38 and 27 MPa for composites with and without sizing, respectively). Up to 70% in ILSS (30.8 and 18.2 MPa for composites with and without sizing, respectively). Up to 34% in IFSS (31.4 and 23.5 for composites with and without sizing, respectively).	Cho *et. al.*[128]

1.7 Polyurea

Polyurea are a family of thermosetting polymers that are formed through reaction between diiso-cyanate and polyamines.

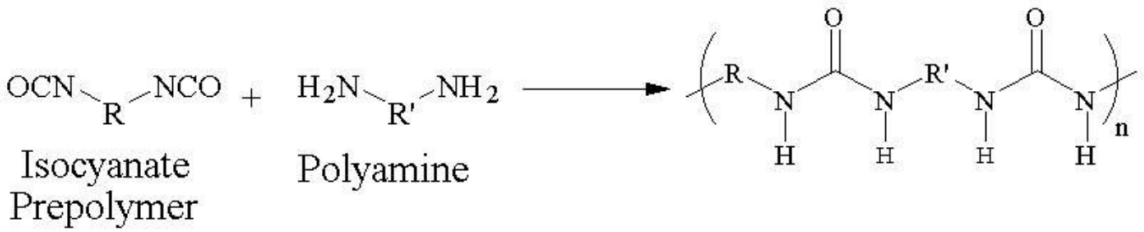

Figure 1.5: Diiso- cyanate and polyamines react to form polyurea [137].

In prior studies, polyurea has been grafted on amine functionalized multi wall carbon nanotubes (MWCNTs) [138]. Polyurethane/hyper branched Poly(urea-urethane)-grafted multi-walled carbon nanotube composites were synthesized in another study [139] which demonstrated a 9-12 nm thick shell of hyper branched poly(urea-urethane) around the carbon nanotubes as observed through TEM imaging. The CNT content was limited to 1

wt. %. Another set of study reports the use of poly (urea-urethane) based CNT composite for electromagnetic interference shielding applications [140], [141]. While Polyurea promises for a good molecular interaction with CNTs through $\pi - \pi$ [22], CH$-\pi$ [16], [22], and NH$-\pi$ [20], [21] interactions, the experimental validation for such interfacial interactions is lacking.

1.8 Thesis Objectives and Layout

As discussed in the previous sections, a multi-component bismaleimide system undergoes complex cure reactions. An understanding of the potential effects of the processing, on the molecular arrangement of the different components and consequently the structure and properties of the BMI however is lacking. While the addition of CNTs under selected conditions have resulted in an improvement of the impact strength in the CNT- BMI nanocomposite containing low loadings of CNTs, these studies have been limited to a two-component BMI system. The studies reported in the literature on the CNT-BMI nanocomposites containing more than 10 wt% CNTs, have one major limitation: their focus has remained on the CNT related factors within the nanocomposite, including CNT densification and alignment. BMI related factors, for example, the effect of CNTs on the cure of the BMI, or the effect of the cure of BMI on the CNTs have not been studied. While sizing have been used to achieve significant improvements in the IFSS of the carbon and glass fiber based composites, it remains to be seen if sizing could be used to tailor the interface-interphase of a CNT- polymer system. Additionally, carbonaceous impurities such as amorphous carbon are expected to have a negative effect on the polymer-CNT interface, the quantitative evidence of the extent of such negative effects however is lacking.

To address these limitations, the following objectives have been set out for this thesis:

First, the effect of processing on the molecular structure and the properties of the pristine BMI system (containing no CNTs) has been studied and discussed in Chapter 2.

Second, CNT modified nanocomposites of BMI containing less than 1 wt.% CNT have been studied and discussed in Chapter 3. CNT- BMI nanocomposites have been prepared using three different types of CNTs and via two different processing routes to elucidate the effects of processing, CNT type and the CNT-BMI interface, on the structure and properties of the CNT modified BMI nanocomposites.

Third, the effects that the CNTs have on the cure of the BMI, as well as the effects that the cure of BMI has on the CNTs, in the nanocomposites containing up to 40 wt% CNTs have been studied and discussed in Chapter 4.

Fourth, the effects that (a) CNTs, (b) the degree of functionalization and defects (DOFD) in the CNTs and (c) the sizing content, have on the sizing cure reaction and cure kinetics have been studied and discussed in Chapter 5. CNTs with three different DOFD have been employed. The sizing coated CNTs have then been used to prepare nanocomposite films with BMI. Three different types of CNT- BMI interface-interphase have been prepared and studied in nanocomposites containing 60 wt% CNTs: (a) pristine CNT- BMI, (b) functionalized CNT- BMI and (c) sizing coated functionalized CNT- BMI.

Finally, the effects that the amorphous carbon and the baking of CNTs to remove the amorphous carbon have, on the interfacial stress transfer with the polyurea matrix have been studied and discussed in Chapter 6. The difference in the interfacial straining has been

studied in composites of polyurea containing up to ~50 wt% polyurea and containing two types of CNT sheets: (a) sheets containing amorphous carbon (termed as unbaked CNT sheet) and (b) sheets that are thermally treated to remove amorphous carbon (termed as baked CNT sheet).

The conclusion of this dissertation as well as some recommendations for future work are presented in Chapter 7.

CHAPTER 2. PRISTINE BMI SYSTEM: THE EFFECTS OF PROCESSING ON THE MOLECULAR ARRANGEMENT OF A HETEROGENEOUS BISMALEIMIDE SYSTEM

2.1 Introduction

Geometry and arrangement of constituent building blocks in a material is extremely critical to its overall toughness [142]–[147]. Materials made with mechanically inferior, brittle building blocks such as silica [142], calcium carbonate [144], [145] or with relatively weak molecular interactions such as hydrogen bonding [148] in silk, exhibit extreme toughness at the macro scale, owing to the arrangement of its constituents. E.g., nacre has a work of fracture ~3000 times higher than its building block (monolithic calcium carbonate). Structural hierarchies in bone [146], nanofibrils in fibroin in spiders [149] or cellulose in wood [147], 'brick and mortar architecture' in nacre [150] provide an explanation for the enhanced fracture energy dissipation.

Taking a cue from these systems, we ask, if the molecular arrangement in polymeric materials composed of multiple building blocks, can be altered to enhance toughness? A bismaleimide (BMI) system, with a brittle bismaleimide based monomeric component and a bisphenol A based modifier undergoes complex cure reactions with simultaneous, multiple cure pathways and consequently multiple products are formed (Figure 1.1) [48], [151]–[154]. Molecular modeling of BMI system has revealed formation of heterogeneous structure with domains of varying density and void content [155]. The void-size and void distribution is also reported to be critical for the overall toughness of the material [156]–

[161]. Given the possibility of presence of multiple components, structural heterogeneity, as well as voids, bismaleimide system qualifies as a system of interest for seeking answers to the question raised above.

Bismaleimide (BMI) resins are a family of thermoset resins that are extensively employed in high-performance aerospace applications [27], [28], [154] owing to their extraordinary thermal stability under both, dry and humid conditions [29], [30]. However, BMIs are inherently brittle and improvement in their fracture toughness is desirable.[13] Here, a multi-component BMI system, CYCOM 5250-4 RTM, is employed.[162], [163] In the current study, this BMI system is processed under two conditions (Figure 2.1) (a) as received resin is melted and degassed at 110 °C. This specimen is referred to as 'Melt BMI'. (b) In the second case, a dual asymmetric centrifugal based high speed shear mixer (HSSM) is used in order to promote rearrangement of constituent components. This specimen is referred to as 'HSSM BMI'. These two BMI systems were then cured under identical conditions. The impact strength of these specimens and factors leading to the differences in impact strength have been studied in this work.

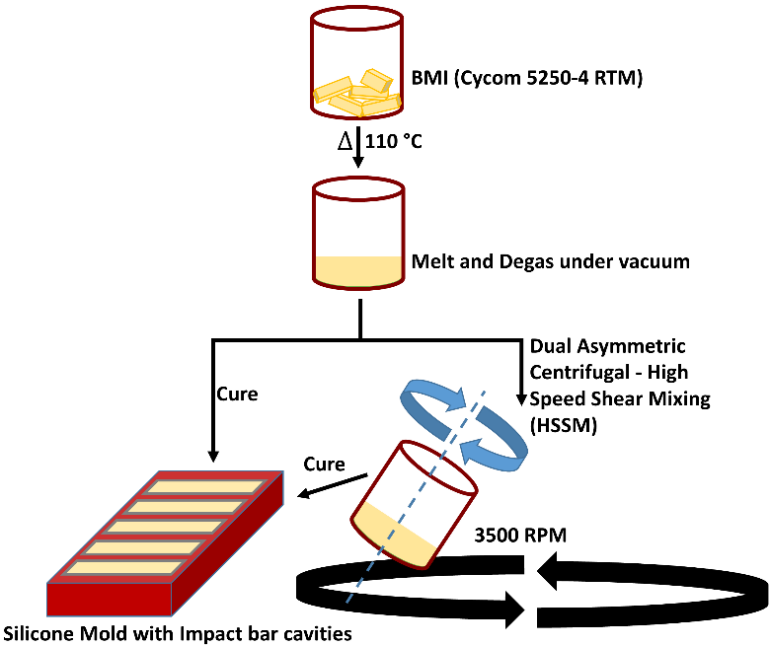

Figure 2.1. Schematic of the BMI processing, in this work. Two processes are pursued: (1) The as-received BMI system is melted and degasssed at 110 °C, and is referred to as 'Melt BMI'. (2) The melted and degased BMI system at 110 °C is subjected to dual asymmetric centrifugal high speed shear mixing for 10 minutes, and is referred to as 'HSSM BMI'.

2.2 Results and Discussion

2.2.1 High Impact Strength BMI

Impact strength of HSSM BMI is 4.9 times the impact strength of Melt BMI (Figure 2.2) Melt and HSSM BMI exhibited an impact strength of 14 ± 6 and 69 ± 13 kJ/m^2, respectively. Maximum impact strength reported in the literature for any BMI system is 19 kJ/m^2. Even for the nanocomposites of BMI with various fillers or blends and interpenetrating networks with other resins, where attempts to enhance the impact strength have been made (with BMI being the major component), the maximum impact strength reported is only 30 kJ/m^2 (Table 1.1 and Table 2.1) None of these studies investigated the effect of processing factors such as the one reported in the current study, i.e., the high shear

mixing. The impact strength of HSSM BMI is also ~4 times the value (17 kJ/m^2) reported by the resin manufacturer [164]. HSSM specimens of BMI cast under a different cure

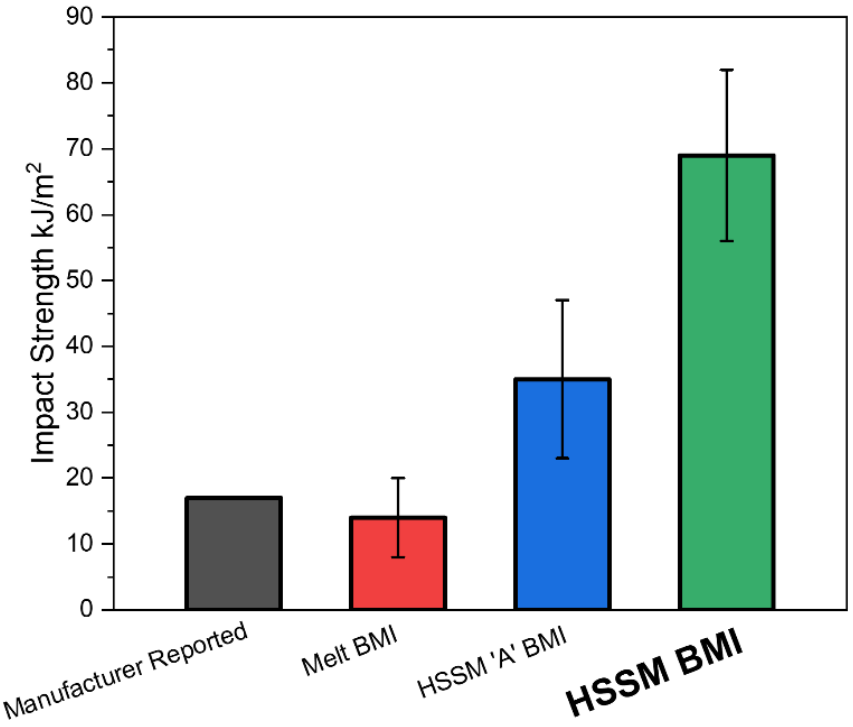

Figure 2.2. Plot comparing the impact strength value exhibited by cured, Melt, HSSM 'A' and HSSM BMI specimens in this study with resin manufacturer reported value.[164] The impact strength of HSSM BMI is ~5 times the impact strength of Melt BMI. HSSM BMI 'A' are specimen cast under a different cure condition compared to HSSM BMI. HSSM BMI 'A' exhibited an impact strength of 37 ± 12 kJ/m^2 (details in table S3).

Table 2.1. Impact Strength of p-BMI and blends of BMI and their IPNs with thermosets and thermoplastics and their ternary nanocomposites from literature.

BMI blends/IPNs with thermosets and their ternary nanocomposites					
Resin/s; Filler	**BMI; Resin/s; (wt. %)**	**Filler (wt.%)**	**Impact Strength (kJ/m^2)**	**Mixing Method for BMI-Resin/s**	**Notes**
Bz-Allyl	100; 0	-	6.1	Stirring	BMI monomer, BDM blended with Bz-allyl, GB/T2567-2008 standard for impact testing.[165]
	70; 30	-	11.8		
BADCy; Bz-Allyl	43; 57; 0	-	12	Stirring	BMI monomer, BDM blended with BADCy in 3:4 ratio which further is blended with Bz-Allyl. GB/T2567-2008 standard for impact testing.[166]
	39; 52; 9	-	18		
BADCy; TDE-85	33; 67; 0	-	9.8	Stirring	BMI monomer, BDM blended with BADCy in 1:2 ratio which further is blended with TDE-85 epoxy, Unnotched impact test- GB/T2571-1995 standard.[167]
	27; 53; 20	-	13.5		
CE	-	-	10.1	-	Pre-polymerized BMI/CE was acquired and used. GB/T3960-1983 standard for impact testing.[168]
CE; p-CNT	-	0.6	10.6		
CE; f-CNT	-	0.6	13.7		
CE; OMMt	-	0	8.2	Stirring	BMI monomer, BDM blended with CE the ratio of which isn't specified, GB/T2567-2008 Standard for impact testing.[169]
	-	4	17.2		
BMI blends/IPNs with thermoplastics					
Resin/s; Filler	**BMI; Resin/s; Filler (weight %)**	**Filler**	**Impact Strength (KJ/m^2)**	**Mixing Method for BMI-Resin/s**	**Notes**
MEMBI; AE; PEK-C	80; 20; 0; 0	-	6.3	-	Two component BMI system modified with MEMBI, AE and PEK-C, GB1043-79 standard for impact testing. [170]
	64; 16; 0; 20	-	17		
	48; 12; 20; 20	-	18.9		

condition than HSSM BMI, referred to as HSSM BMI 'A' exhibited an impact strength of 37 ± 12 kJ/m^2 (details in Appendix A).

Factors that could affect the impact strength of BMI system, include the following: (a) structural hierarchy, geometry and arrangement of molecular building blocks [142]–[147]. (b) rate of reaction. A higher rate of reaction could lead to increased internal stresses which in turn could lead to lower energy absorption capacity [171]. (c) Inter and intra molecular interactions. Ordered carbonyl stacking in BMIs, for example, is related with lower impact strength [154]. (d) Porosity. Presence of nanopores is reported in the literature to be linked with enhanced impact strength in various systems. Porosity can result in crack arrest, triaxial stress relief ahead of the crack tip, and crack deflection [156]–[161]. Geng and co-workers [156] reported an increase in impact strength of poly(lactic acid) from 3.8 kJ/m^2 to 20.5 kJ/m^2 by introducing nano-pores (< 50 nm) using a supercritical carbon dioxide low temperature foaming technique. (e) Heterogeneity. Interfacial energy between domains of different constituent structures. Higher interfacial energy between domains could lead to low energy absorption [172]. (f) Cure condition. Molecular modeling of bismaleimide system has revealed variation in the degree of heterogeneity and void formation, with change of major reaction mechanism and with change in extent of cure [155]. Increased void content was also reported with increasing degree of cure. Varying the cure conditions in the current study also led to differences in impact strength (Table A 1)

2.2.2 Molecular Rearrangement in BMI: FTIR, Raman and NMR Analysis

To investigate the effect of HSSM on the molecular arrangement in the BMI system, fourier-transform infrared (FT-IR), Raman and nuclear magnetic resonance (NMR) spectroscopies have been used (Figure 2.3). A peak shift or a change in the peak intensity in the FTIR, Raman or NMR spectra signifies a difference in the molecular

environment. FTIR was employed on uncured (Figure 2.3 a), as well as on the cured specimens (Figure 2.3 e, f, g) of both Melt and HSSM BMI. Major groups and the peak

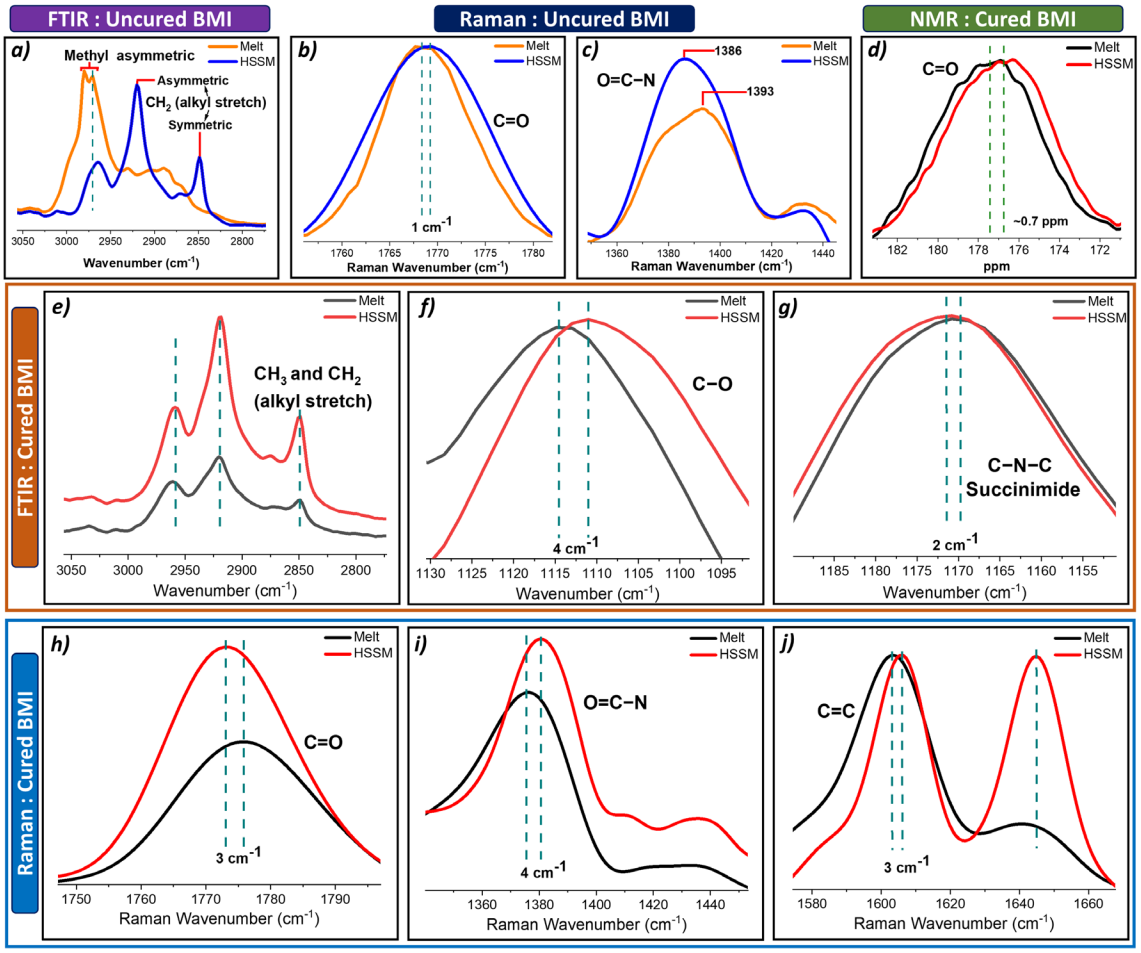

Figure 2.3. Molecular rearrangement in HSSM BMI compared to Melt BMI observed through significant differences in the position and/or FWHM of peaks in both uncured and cured forms of Melt and HSSM BMI, analyzed through FTIR, Raman and NMR spectroscopies. (a) FTIR spectra of uncured BMI, (b and c) Raman spectra of uncured BMI, (d) ^{13}C CP MAS solid state NMR spectra of cured BMI, (e-g) FTIR spectra of cured BMI, (h-j) Raman spectra of cured BMI. The y-axis for all plots represents normalized intensity.

positions associated with their respective infra-red vibration modes [151], [163], [173]–[175] are listed in Table S5. All curves were normalized to the intensity of C = C peak at 1509 cm^{-1}. The uncured, Melt and HSSM BMI specimens demonstrated differences in the

peak positions associated with symmetric and asymmetric vibration modes of CH_2 and CH_3 groups (Figure 2.3a). While the uncured Melt BMI exhibited a doublet peak associated with the methyl asymmetric vibration at about 2971 cm^{-1} and 2980 cm^{-1}, the uncured HSSM BMI, showed a single peak at 2960 cm^{-1}. Distinct peaks associated with symmetric and asymmetric alkyl stretch are observed in uncured HSSM BMI at 2848 cm^{-1} and 2920 cm^{-1} while these peaks are not observed in uncured Melt BMI. Cured, Melt and HSSM BMI specimens exhibited identical peak positions associated with the symmetric and asymmetric vibration modes of CH_2, however, a shift of about 3 cm^{-1} towards a higher wavenumber in HSSM BMI was observed for the CH_3 asymmetric vibration peak (Figure 2.3e). The peak observed at 1115 cm^{-1} in cured Melt BMI, associated with $(C-O)$ stretch of either phenol or ether groups, shifts to 1111 cm^{-1} in cured HSSM BMI (Figure 2.3f). The cured Melt BMI exhibited succinimide peak at 1169 cm^{-1}, which shifts to 1171 cm^{-1} for the cured HSSM BMI (Figure 2.3g).

FTIR or Raman activity in a molecule depends on the point group of the molecule, for instance, N-Phenylmaleimide has 54 normal modes of vibration which are divided into A_1, B_2, B_1, B_2 modes based on the group theory of vibration where the A_1, B_1, B_2 modes are IR active while all modes are Raman active [173]. Hence, Raman spectroscopy was undertaken to further investigate the chemical structure in both uncured (Figure 2.3 b and c) and cured (Figure 2.3 h, i and j) forms of Melt and HSSM BMI. The major Raman peaks observed and their assignments [151], [173]–[175] are listed in Table A 3. All curves are normalized to the intensity of $C=C$ peak (1603 cm^{-1} to 1607 cm^{-1}). The uncured Melt BMI exhibited $C=O$ peak at 1768 cm^{-1} which shifts to 1769 cm^{-1} for HSSM BMI with an increase of 16% in the full width at half maxima (FWHM) (Figure 2.3b). Upon curing,

the $C=O$ peak shifts to 1776 cm^{-1} for the Melt BMI and to 1773 cm^{-1} for HSSM BMI (Figure 2.3h). The peak intensity and FWHM associated with $C=O$ stretch of cured HSSM is about 71% and 8% higher, respectively, than for the cured Melt BMI. Uncured, Melt and HSSM BMI exhibited $O=C-N$ peaks at 1395 and 1386 cm^{-1}, respectively (Figure 2.3c). For the cured, Melt and HSSM BMI, this peak shifts to 1377 cm^{-1} and 1381 cm^{-1}, respectively (Figure 2.3i). Furthermore, a doublet peak of equal intensities is observed in the cured HSSM BMI (Figure 2.3j). One of the peak is observed at 1606 cm^{-1} and is associated with the aromatic $C=C$ stretch. The observance of the peak at 1645 cm^{-1} is not reported in the literature for the BMI system. This peak is observed at 1641 cm^{-1} in cured Melt BMI, with only 38% intensity than in HSSM BMI. There is a downshift shift of 3 cm^{-1} in the aromatic $C=C$ stretch peak in the cured Melt BMI compared to the cured HSSM BMI, and the peak position is 1603 cm^{-1}. The FWHM of this peak for cured HSSM BMI is smaller by 33% as compared to cured Melt BMI.

To further understand the molecular rearrangement in cured HSSM BMI, ^{13}C cross polar magic angle spin (CP MAS) solid state NMR spectroscopy has also been carried out on the cured, Melt and HSSM BMI. A down shift by 0.7 ppm in the $C=O$ peak is observed in the cured HSSM BMI as compared to the Melt BMI (Figure 2.3d) where the peak position of $C=O$ group for cured melt BMI is at 177.4 ppm. ^{13}C NMR shifts, for the major structures expected to be formed upon curing of BMI (Figure 1.1) were predicted using ChemDraw Professional software (Figure A 1). While an absolute one-to-one comparison of the predicted and the experimental values is not possible, the predictions would still assist in understanding the contribution of individual components to the ^{13}C NMR shifts. The carbonyl groups in the product formed as a result of the 'ene' reaction (Figure A 1a),

maleimide homopolymerization (Figure A 1b) and 'etherification and ene' (Figure A 1f) reactions have a ^{13}C NMR shift prediction of 177.8 to 176.2 ppm, while the products formed as a result of 'Diels-Alder', thermal re-aromatization (post Diels-Alder), re-aromatization through 'ene' have a ^{13}C NMR shift prediction of 177.2 to 173 ppm (Figure A 1 c, d, e). The shift in the peak position of the $C = O$ group could be attributed to factors including, (a) variations in intramolecular interactions [176], (b) differences in the local composition of constituent products, where a higher ratio of Diels Alder reaction based products is predicted in HSSM BMI. Through FTIR, Raman and NMR spectroscopies, molecular rearrangement in HSSM BMI as compared to Melt BMI is thus established.

2.2.3 Cure Kinetics

The cure activation energy and cure kinetics were investigated using DSC. Kissinger [177] and Ozawa [178] methods have been used for analyzing the non-isothermal curing (Figure 2.4 a, b, c and d). The activation energy is calculated using equation 1 for the Kissinger method and equation 2 for the Ozawa method, where Ea, Φ, T_p, R are the activation energy, heating rate (°C/min), peak temperature (Kelvin) and universal gas constant, respectively. The pre-exponential factor (A) of the Arrhenius equation, which represents the collision frequency of the reactants, was calculated using equation 3. The cure reaction rate constant (k), which represents the cure reaction rate was calculated using equation 4.

$$\frac{-E_a}{R} = \frac{d(ln\frac{\Phi}{T_{p^2}})}{d(ln\frac{1}{T_p})} \quad (1)$$

$$\frac{-E_a}{R} = \frac{1}{0.4567} \times \frac{d(\ln \Phi)}{d(\ln \frac{1}{T_p})} \quad (2)$$

$$A = \frac{\Phi E_a}{R T_{p^2}} e^{E_a/RT_p} \quad (3)$$

$$k = A \times e^{-E_a/RT} \quad (4)$$

The activation energy and the cure kinetics parameters are summarized in Table A 4. Following the Kissinger method, the activation energy of the Melt BMI is 73 kJ/mol, which increases to 83 kJ/mol for the HSSM BMI, an increase of 14%. The cure reaction rate constant k is calculated for temperatures between 150 °C to 250 °C. k at 150 °C for the Melt BMI is 54% higher than that for the HSSM BMI. This difference in reaction rate constant decreases with increasing temperatures up to 250 °C. At 200 °C, the reaction rate constant for the Melt BMI is 20% higher than that for the HSSM BMI, while at 250 °C the reaction rate constant for the Melt and HSSM BMI are comparable. The Ozawa method results in kinetics parameters that are comparable to the ones obtained using the Kissinger method and these values are listed in Table A 4. The DSC curve of the as received BMI that undergoes neither Melt nor HSSM processes exhibits two endothermic spikes at 150 °C and 167 °C (e). The melting temperature of the BDM monomer is reported to be 155 °C [41]. These two spikes, thus, correspond to melting of the two bismaleimide monomers in the system which signifies the presence of clusters of individual components and a deviation of the system away from a homogenous mixture in the as received BMI system (illustrated in Figure 2.4). While neither Melt nor HSSM BMI demonstrated these

endothermic spikes in their DSC curves, a strong small angle X-ray scattering (SAXS) peak was observed at 0.38 2θ (Figure A 2), in the uncured Melt BMI, signifying heterogeneity on the scale of ~23 nm (assuming Bragg's diffraction). Uncured HSSM BMI, on the contrary only exhibited a weak SAXS peak at 0.81 2θ Figure A 2).

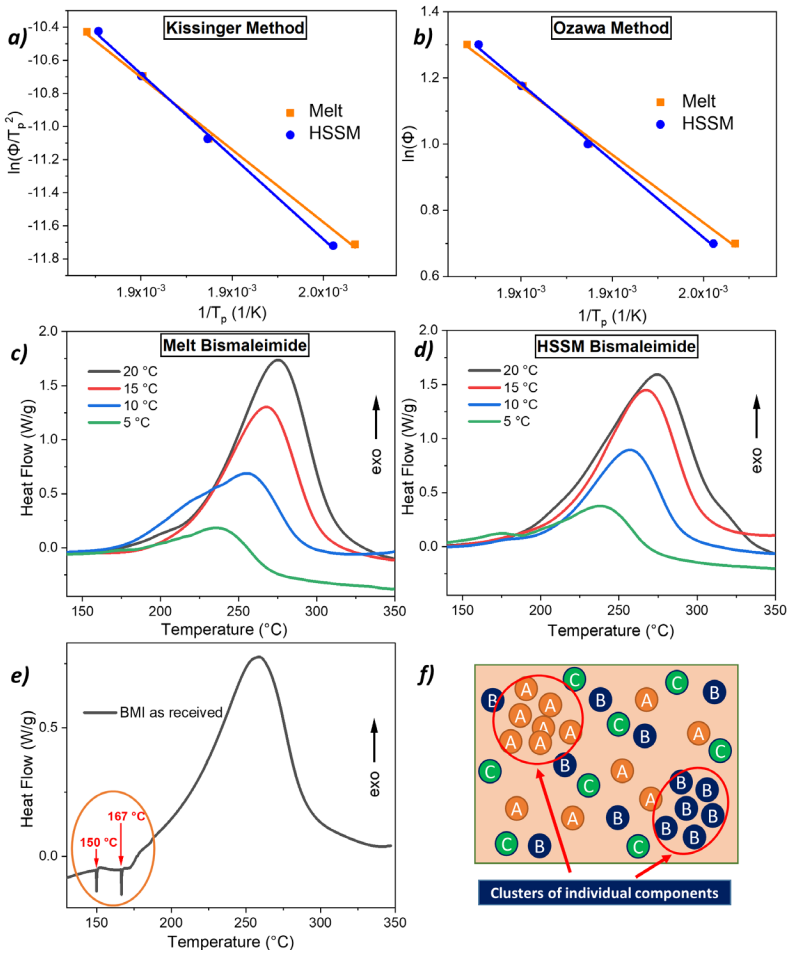

Figure 2.4. (a and b) Plots for determining activation energy using (a) Kissinger method, (b) Ozawa method. The slope of the linear plots is used for calculating activation energy. (c and d) DSC curves at various heating rates in air atmosphere of (c) melt Bismaleimide and (d) HSSM Bismaleimide. (e) DSC curve in air at 10 °C/min ramp rate of as received BMI system that undergoes neither melt nor HSSM processes. Two endothermic spikes at 150 °C and 167 °C are observed. These temperatures are in the range of individual melting temperatures of the two bismaleimide monomers in the system suggesting a deviation of the system away from homogeneity. (f) Schematic showing clusters of individual constituents in uncured Melt BMI which upon HSSM get redistributed. Note: This illustration is not representative of the weight/volume fraction of individual components in the BMI system.

2.2.4 Comparing BMI Molecular Architectures using SAXS

SAXS has been used to study the structure of Melt and HSSM BMI specimens. SAXS peak can arise from structural hierarchy or order [179], and can be determined from Bragg's diffraction equation. SAXS peak can also arise from electron density differences due to heterogeneity [180], [181], of constituents, or due to presence of voids. If the SAXS intensity arises due to heterogeneity, then scattered intensity $I \propto \Delta\rho\, \varphi_\alpha\, \varphi_\beta$, where $\Delta\rho$ is the difference in density of the two phases and $\varphi_\alpha, \varphi_\beta$ the volume fractions of the two phases (assuming a two phase heterogeneous system). Given the complex cure of BMI systems, there is potential for existence of more than two solid BMI phases in Melt and HSSM BMI, which could be with or without voids. Here, a strong SAXS peak is observed in cured HSSM BMI with the peak position at ~ 0.57 2θ (Figure 2.5a). A relatively low intensity peak is observed in cured Melt BMI at ~ 0.83 2θ. Assuming these to be Bragg's diffraction peaks, results in d spacing of ~15.5 nm for the cured HSSM BMI and ~10.6 nm for cured Melt BMI. SAXS was also conducted on HSSM BMI 'A' that exhibited an impact strength of 37 ± 12 kJ/m^2. The observed peak intensity for HSSM BMI 'A' is weaker than that for the cured HSSM BMI, but stronger than cured Melt BMI, and the peak is observed at ~ 0.67 2θ, and the corresponding d spacing is ~ 13.2 nm. A direct relationship between the domain size calculated from the SAXS peak position, its intensity and the impact strength is thus established, where an increasing atomic distance from 10.6 nm to 15.5 nm and an increase in the peak intensity relates directly to an increase in the impact strength. All SAXS curves were normalized to the intensity at 0.35 2θ.

The measured density of cured HSSM BMI is lower than that for the cured Melt BMI, being 1.17 ± 0.03 g/cc and 1.24 ± 0.02 g/cc, respectively. This shows that the cured HSSM BMI either has a lower overall packing density or has higher volume of voids than cured melt BMI. No significant differences in the wide angle X-ray diffraction (WAXD) of Melt and HSSM BMI, both in cured or uncured state is observed (Figure A 3). The uncured and cured specimens demonstrated amorphous halo peak at ~18.7 and ~17.3 2θ, respectively. A peak at ~ 6.25 2θ is observed only in cured specimen (Figure A 3 a). This peak has not been reported previously for the BMI systems in the literature. This diffraction peak could originate from the aliphatic groups between two phenyl rings as has been reported in a prior study for an epoxy system, where a diffraction peak associated with isopropylidene group between the two phenyl rings was observed at ~5.5 2θ [182].

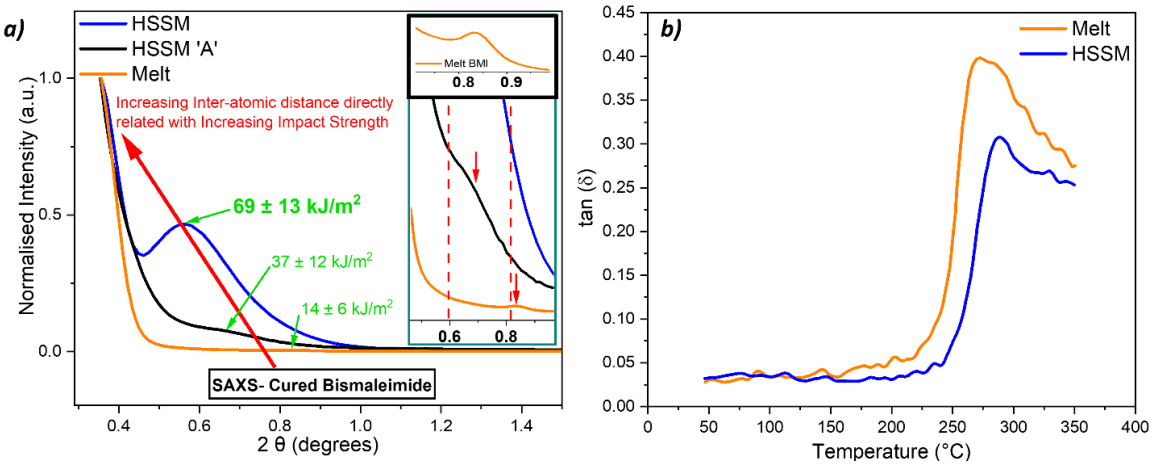

Figure 2.5. (a) Direct correlation between the interatomic distance (calculated from SAXS peak position, assuming Bragg's diffraction), peak intensity and impact strength. (b) The glass transition temperature (temperature associated with tan δ peak position) of cured HSSM BMI increased by 16° C to 288° C compared to 272° C for cured Melt BMI.

2.2.5 Thermomechanical properties

The cured HSSM BMI exhibits an enhanced glass transition temperature (T_g) as compared to cured Melt BMI (Figure 2.5b). The temperature corresponding to the tan δ peak position (from dynamic mechanical analysis) is taken as the T_g. Melt BMI and HSSM BMI demonstrated a T_g of 272 °C and 288 °C, respectively. Similar T_g values were also observed from DSC (Figure A 4a). This increased Tg result for high impact strength specimen is important, as normally an increase in impact strength is achieved at the expense of glass transition temperature. Thermogravimetric analysis (TGA) was used to evaluate the thermal degradation temperature of cured Melt and HSSM BMI. Cured HSSM BMI degraded at 445 °C, while cured Melt BMI degraded at 441 °C (Figure A 4b). No statistical difference in the values of tensile strength, tensile modulus and elongation at break is observed for cured, Melt and HSSM BMI (Table A 5). Details of tensile properties under varying cure conditions and their statistical significance are listed in, Table A 6, Table A 7, Table A 8, Table A 9, Table A 10, Table A 11. Storage modulus plots of cured Melt and HSSM BMI are shown in Figure A 4c.

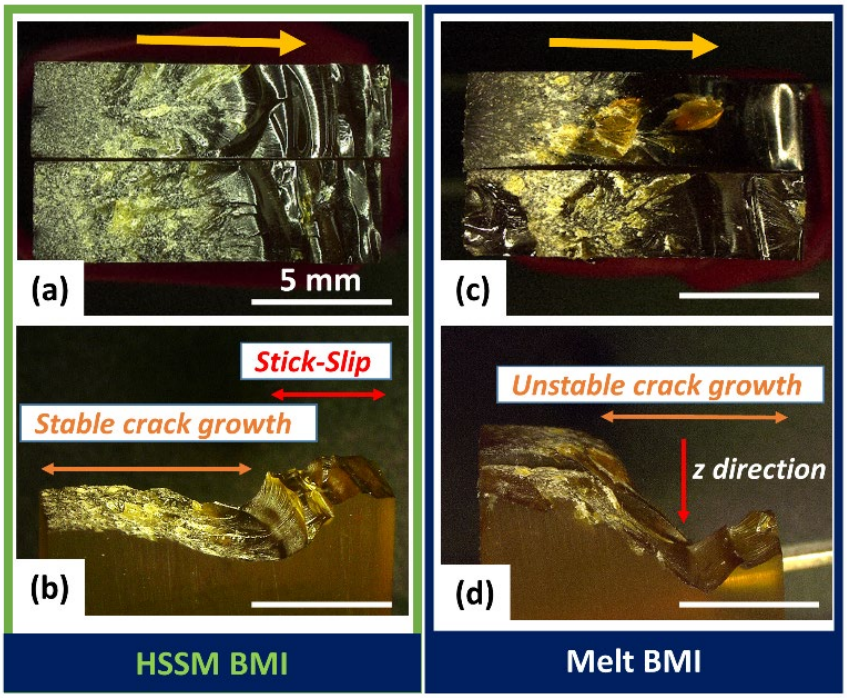

Figure 2.6. (a-d) Representative optical micrograph of impact fractured surfaces of cured (a,b) HSSM BMI and (d,e) Melt BMI. (a) Extremely rough fracture surface associated with high fracture energy absorption, (b) Majority area exhibiting stable crack growth followed by stick slip mode of failure. (c) Relative smaller area associated with rough fracture surface exhibited in Melt BMI accompanied with (d) catastrophic failure/ unstable crack growth, post crack initiation and propagation. The yellow arrow refers to the direction of crack propagation.

2.2.6 Fractography

The impact fracture surfaces of cured Melt and HSSM BMI were examined using optical microscopy (OM) and SEM (Figure 2.6, Figure 2.7 and Figure 2.8). Overall, the HSSM BMI exhibits stable crack growth coupled with extremely rough surface signifying intense plastic deformation which is associated with high energy absorption (Figure 2.6 a and b, Figure A 5) as against the Melt BMI, which exhibits relatively smoother fracture surface and undergoes catastrophic failure (unstable crack growth in z direction) [183] (Figure 2.6 c and d, Figure A 6, Figure A 7, Figure A 8). The area of plastic deformation is directly related with the fracture energy [184]. 3D optical imaging has been used to

evaluate differences in the surface roughness of the crack initiation region in Melt and HSSM BMI, where the latter demonstrates about 2 times higher roughness (Figure A 9). Three zones on the fracture surface are defined, zone 1 as crack initiation and slow propagation, zone 2 as fast propagation, and zone 3 as stick-slip (Figure 2.7 a). The crack initiation and propagation zone in HSSM BMI exhibits plastic deformation, and no signs of crack propagation path can be traced signifying extreme levels of crack arrests and crack deflection throughout this region (Figure 2.7 b and Figure A 5). Near spherical nodular features that have a diameter in the range of ~10 - 20 μm (Figure 2.8) were observed in HSSM BMI. These features weren't observed in Melt BMI (Figure A 6, Figure A 7). The fast propagation zone (2) in HSSM BMI exhibits deep ridges/ furrows (Figure 2.7 b) with crack deflections that extend in directions up to 90 degrees to the direction of crack propagation (Figure 2.7 d, e). The stick and slip region (zone 3) in HSSM BMI is marked by a step style geometry where the crack stops (crack arrest), i.e., stick and once the stress builds up, the crack advances again (slip) [185] (Figure 2.6b and Figure A 8). The Melt BMI on the other hand exhibits a shorter crack initiation and propagation zone compared to HSSM BMI (Figure 2.6). The fast propagation zone is marked by a catastrophic failure with smooth brittle-like failure that continues up to the end of zone 3 (Figure 2.6d).

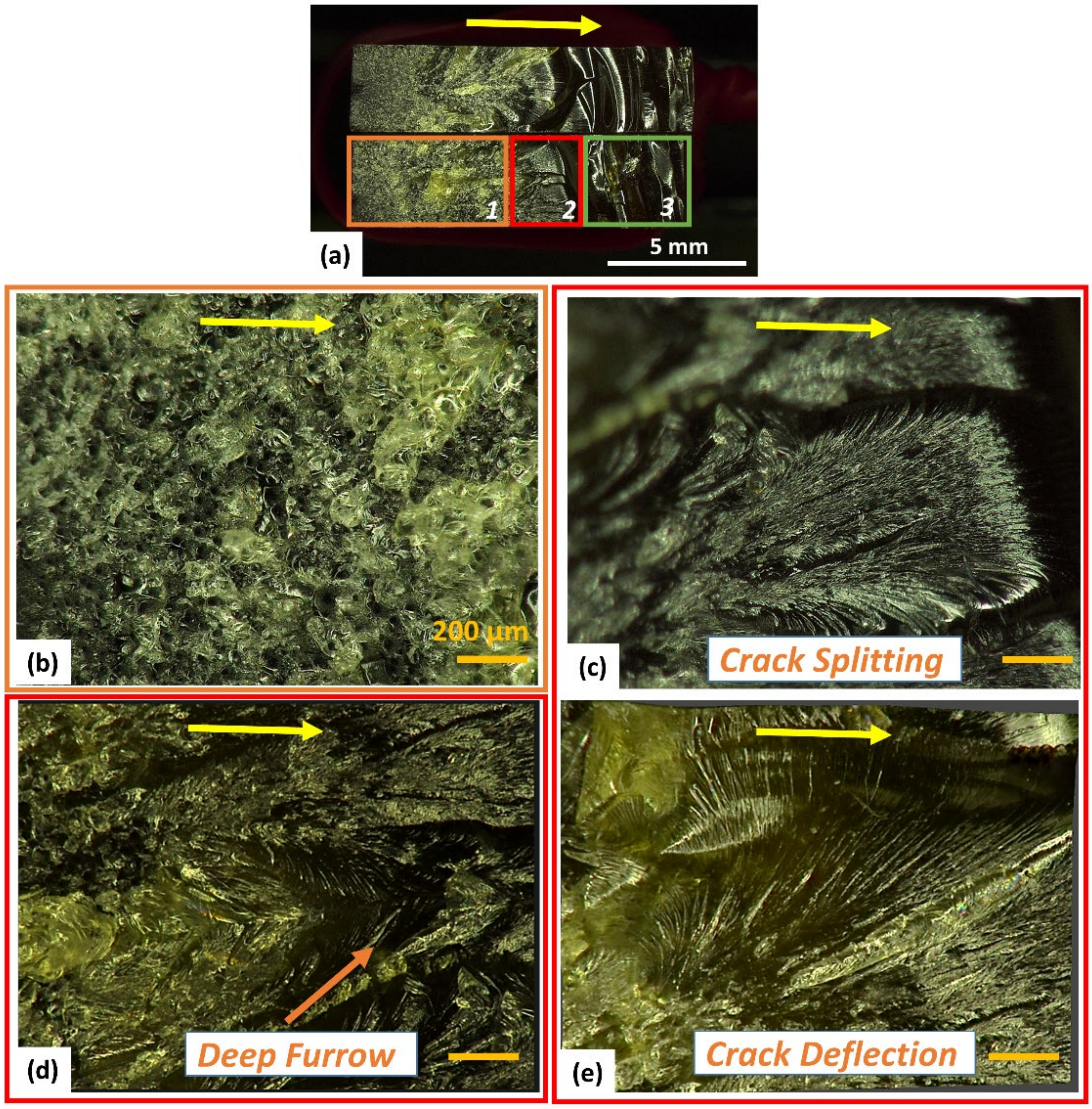

Figure 2.7. Optical micrograph of the fracture surface of cured HSSM BMI exhibiting features associated with enhanced fracture energy absorption. (a) Surface defined on the basis of three zones where zone 1 is associated with crack initiation and slow propagation, zone 2 is associated with fast propagation and zone 3 is associated with stick-slip mode of failure. (b-e) Magnified image of (b) zone 1 exhibiting extreme roughness. (c-e) zone 2 exhibiting (c) deep ridges and furrows, (d) crack split, (e) crack deflection. The yellow arrow represents the direction of crack propagation.

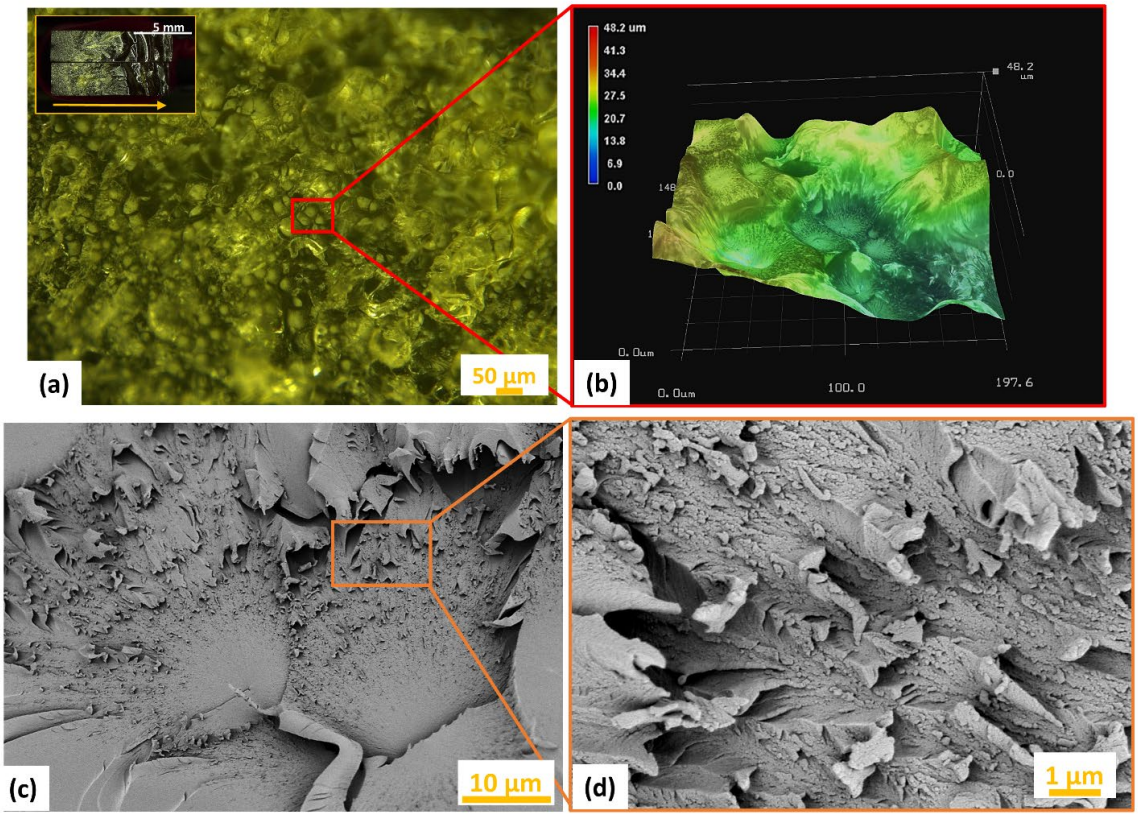

Figure 2.8. (a and b) Optical micrographs, (c and d) scanning electron micrographs of cured HSSM BMI fracture surface in the crack initiation zone demonstrating 'nodular' morphology. Near spherical nodules with diameter in the range of ~ 10-20 µm could be seen. Such morphology isn't observed in the fracture surface of Melt BMI. (b) 3D optical micrograph of micro nodules. Yellow arrow points to the crack propagation direction. The dimensions of the imaged section are ~ 198 µm × 148 µm × 48 µm. (c) Nodular features surrounded by areas undergoing intense plastic deformation. (d) Higher magnification image demonstrating intense plastic deformation.

2.3 Experimental

A multi- component Bismaleimide system, Cycom 5250-4 RTM from Solvay is used in this study. Two processing routes were undertaken : (1) The as-received BMI system was melted and degased at 110 °C. This sample is referred to as 'Melt BMI'. (2) The melted and degased BMI system at 110 °C was further subjected to dual asymmetric centrifugal high speed shear mixing using a DAC 150.1 from Flacktec Inc. for 10 minutes.

This sample is referred to as ‘HSSM BMI’. A silicone mold with impact bar and tensile ‘dog-bone’ specimen cavities was used for casting specimens. A mold release agent, Ease release 205 from Mann formulated products was applied to the mold and left to dry for 30 minutes at room temperature. The mold was then preheated to 191 °C and held under vacuum for 10 minutes along with the resin in a separate beaker. The resin was then poured into the cavities of the mold and undergoes curing at 191 °C for 4 hours with no external pressure applied. The oven was then cooled down to room temperature and the specimens drawn out of the mold and then postcured at 227 °C for 2 hours in a free standing form with no external pressure applied. The samples were then polished on a Buehler MetaServ polisher using a silicon carbide paper, first with abrasive grade P280, followed by P600, and then by P1200.

3 variations in specimen casting conditions were explored:

a) Condition ‘A’- Specimens are in the mold (cure + post cure) for complete duration.

b) Condition ‘B1’- Specimens are in the mold while curing but free standing for post cure, that is, specimens are demolded while in the oven at curing temperature upon completion of cure cycle of 4 hours for further free-standing post-cure.

c) Condition ‘B2’- Specimens are in the mold while curing but free standing for post cure, oven is cooled down to room temperature after completion of cure cycle, specimens are demolded, and oven is heated to post cure temperatures for free-standing post-cure.

FTIR spectra were recorded on Shimadzu Prestige 21 FT-IR spectrometer in attenuated total reflectance (ATR) mode with a spectral resolution of 0.5 cm^{-1}. Raman

spectra were collected using a HORIBA XploRA ONE (λ=785 nm) spectrometer with a spectral resolution of 0.4 cm^{-1} and spatial resolution of 520 nm. ^{13}C solid state CP/MAS NMR spectra was collected at room temperature on a Bruker AV3-400 spectrometer operating at 400 MHz with a 10 kHz spinning frequency. 1024 scans were performed with 5 μsec pulse duration and 4 sec repetition time. Predictions of ^{13}C NMR shift for the various possible structures expected to be formed upon curing were made using ChemDraw Professional 16.0 software provided by PerkinElmer.

Cure kinetics was studied using DSC on a TA Q100 Instrument under air atmosphere at various heating rates (5, 10, 15, 20 °C/ min) for a temperature range of 25 °C to 380 °C.

TGA study was carried out at a heating rate of 10 °C/min under nitrogen atmosphere using TA Instrument Q500. The peak of the derivative curve of weight % with temperature was taken as degradation temperature. Dynamic mechanical analysis was conducted using a 3 point bending mode on a TA Instruments DMA Q800 at a frequency of 1Hz with 2 N load and 0.01% strain over 35 °C - 350 °C temperature range at a heating rate of 3 °C/min. The sample dimensions used for the DMA were 30 × 12 × 3.2 (length × width × thickness) (mm). Impact tests were conducted following ASTM D4812 standard. which is an unnotched cantilever beam impact resistance test. The sample dimensions are 63.5 × 12 × 3.2 (length × width × thickness) (mm). Tensile tests were conducted on dog-bone shaped specimens following ASTM D638 standard. The sample dimensions were 63.5 × 3.2 × 3.2 (length × width (gauge section) × thickness) (mm). Tests were conducted at 10 mm gauge length and strain rate of 25.4 mm/min. Engineering strain was measured using Instron extensometer 2630-101. At least 5 samples were tested for the impact test,

and at least 5 samples were tested for the tensile test. The statistical significance of mechanical properties was evaluated using the p-values from comparison of individual pairs using student's T test using JMP Pro 13 software. Density was calculated by dividing the weight to volume using impact specimens. Keyence VHX-600 Digital Microscope with a 54 megapixel 3CCD camera was used for capturing optical micrographs of the impact fractured surfaces. SEM images were collected on a Hitachi SU8230 SEM with an accelerating voltage of 0.5 kV on samples that were sputter coated with Au using a Hummer 6 sputterer.

SAXS was conducted on Panalytical Empyrean (Cu Kα λ= 0.1542 nm, operating voltage and current 40 kV and 0.40 mA, respectively). WAXD was conducted on Rigaku MicroMax-002 beam generator (Cu Kα λ= 0.1542 nm, operating voltage and current 50 kV and 0.60 mA, respectively) equipped with R-axis IV++ detector.

2.4 Conclusion

This work highlights the importance of molecular arrangement on the impact strength in a heterogeneous polymeric system. Learning from various material systems in nature that are made of mechanically inferior, 'brittle' molecular building blocks, but that exhibit extreme toughness at the macro scale, in this study, highest impact strength for any BMI system reported to-date has been achieved. The cured HSSM BMI exhibited an impact strength of 69 ± 13 kJ/m^2, whereas to-date, studies in the literature have reported a maximum impact strength of only 19 kJ/m^2 for any BMI system. The differences in impact strength have been analyzed in terms of fractography, chemical rearrangement of building blocks, and by SAXS, WAXD, and DSC. The cured HSSM BMI also exhibited an increase in the glass transition temperature by 16° C compared to cured Melt BMI.

CHAPTER 3. CNT-BMI NANOCOMPOSITES WITH LOW CNT CONTENT: THE EFFECTS OF PROCESSING AND CARBON NANOTUBE TYPE ON THE IMPACT STRENGTH OF CNT-BISMALEIMIDE NANOCOMPOSITES

3.1 Introduction

CFRPs are widely used in high-performance structural applications, including those in the aerospace [186] and the automotive sector [187] owing to their high in-plane specific strength and stiffness, compared to metals like aluminum and steel. The inter and intra-laminar, regions of the CFRP however remain relatively weak, limiting the overall fracture toughness of the composite. Various strategies have been employed to improve the toughness of the CFRPs including, (a) 'interlayer toughening', where, thermoplastic resin [188], [189], thermoplastic nanofibers[190]–[192], carbon nanofibers [193], CNT forest [81], [194], and CNT sheet [195] have been employed as/or in the toughening layer between the plies. (b) Z-pining [196], [197], z-stiching [198], [199]. (c) Using 'thin-ply'[200]–[202] that is, plies with less than one-third the thickness of the conventional plies. (d) Interlocking the 'thin' plies [203], [204]. (e) coating the carbon fiber with graphene nanoflakes [205], CNTs [206]. (f) Improving the matrix toughness [162], [207]–[209]. Nano-fillers including CNTs [114], [210]–[215], graphene [211], [215] and nanoclay [207] have been used to reinforce the matrix aswell.

The 'nano-filler reinforced matrix' toughening strategy involves dispersing the nano-fillers throughout the matrix and not just limiting to the interlayer, as is the case in

interlayer toughening. In interlayer toughened composites, once the crack starts to propagate, it can bifurcate into the next weakest region, the interface of the interlayer and the base resin [188] and/or the intra-laminar region [194]. Interlayer toughening, thus only solves part of the problem in toughening the overall composite. Simultaneous toughening of both the inter-laminar and intra-laminar regions is desirable and using the 'nano-filler reinforced matrix' strategy for making the CFRP composites, provides that opportunity. Fenner and Daniel [210] used 0.5 wt.% CNTs to reinforce the epoxy matrix. The uncured CNT-reinforced epoxy was then employed in two different ways, (a) cured to make CNT-epoxy nanocomposites and (b) wet lay-up of CNT-reinforced epoxy into the carbon fiber fabric, followed by curing, to obtain CNT-reinforced-CFRP hybrid. The CNT-epoxy nanocomposite demonstrated 30 and 70% improvements in the Mode I toughness (from 693 to 910 kPa/m^2) and strain energy release rates (from 106 to 182 J/m^2), respectively, compared to the cured epoxy without CNTs. The CNT-reinforced-CFRP hybrid showed a 180% improvement in the Mode I interlaminar fracture toughness (from 176 to 498 J/m^2). The study [210] demonstrated that not only the energy absorption characteristics of the CNTs in the CNT-epoxy nanocomposites translated to the CNT-reinforced-CFRP hybrid, the nano-reinforcement effects were infact further enhanced. The CNT-reinforced nanocomposites can hence serve as a predictor for the CNT-reinforced-CFRP hybrids fracture properties. The improvements and limitations reported in the literature for CFRPs, toughened through 'nano-filler reinforced matrix', 'interlayer toughening' and other strategies (stitching, z-pins, 'thin ply', interlocking) are summarized in Table B 1, Table B 2 and Table B 3, respectively. There are two major limitations in the literature involving the toughening of CFRPs: (a) prior studies have focused on epoxy as the matrix. (b) for the

studies employing the 'CNT reinforced matrix' toughening strategy, the effects that the factors including: CNT type, CNT-matrix interactions and the processing method, have on the toughness of the CNT-CFRP hybrid has not garnered attention.

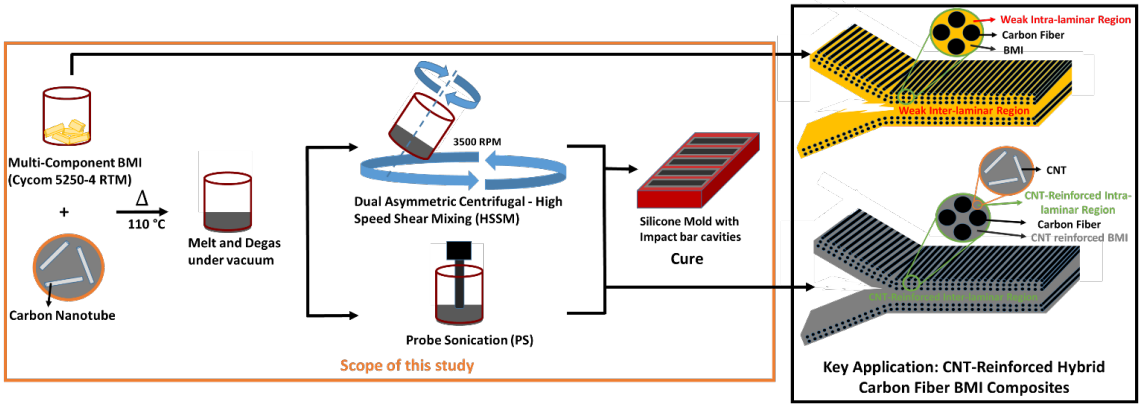

Figure 3.1. Schematic of the CNT-BMI processing in this work. p-CNT_A and f-CNT_A are processed with BMI through HSSM while CNT_B are processed with BMI through PS. The uncured HSSM and PS processed CNT-BMI can be used to manufacture CNT reinforced-carbon fiber-BMI hybrid as well as the analogous CNT reinforced- CNT yarn- BMI hybrid composites with improved inter and intra laminar toughness.

With the recent large-scale production and availability of the CNT macro-assemblies in the yarn, tape and sheet forms, CNT-polymer composites could now be prepared through conventional CFRP manufacturing techniques such as filament winding. It is however expected that the resin dominated properties, such as the inter and intra laminar fracture toughness in these CNT- polymer composites would still remain relatively weak, as they have been for the CFRPs. Modifying the resin with CNTs could be an attractive route for further improving the resin properties.. In this study, a multi-component [162] aerospace grade BMI has been employed. BMIs are a family of resins which are extensively employed in aerospace applications. The US Air Force's F-22 fighter for example, uses BMI in 50% of its total parts that use a thermoset resin [33]. All the exterior skins of the F-22 are made using BMI aswell [33]. In our prior work [209], we demonstrated ~4x

improvement in the impact strength (from 14 to 69 kJ/m^2) of the multi-component BMI resin through a molecular rearrangement which was induced through a HSSM and without addition of any reinforcing agents. In this study, we examine the effects that up to 0.3 wt% CNTs in pristine (p-CNT$_A$) and functionalized (f-CNT$_A$) states have on the impact strength of CNT-BMI nanocomposites processed through HSSM (Figure 3.1). We also employ a different CNT (termed CNT$_B$) through a different process, using PS (Figure 3.1) and examined its effect on the impact strength of the nanocomposite. Furthermore, the effect of the BMI cure on the CNTs aswell as the effect of CNTs on the molecular structure of BMI has been investigated. The results and understanding from this study would facilitate rational down-selection of the CNT-BMI system for making CNT reinforced-carbon fiber-BMI hybrid composites (Figure 3.1).

3.2 Results and Discussion

3.2.1 Impact Strength of HSSM BMI and HSSM CNT-BMI nanocomposites

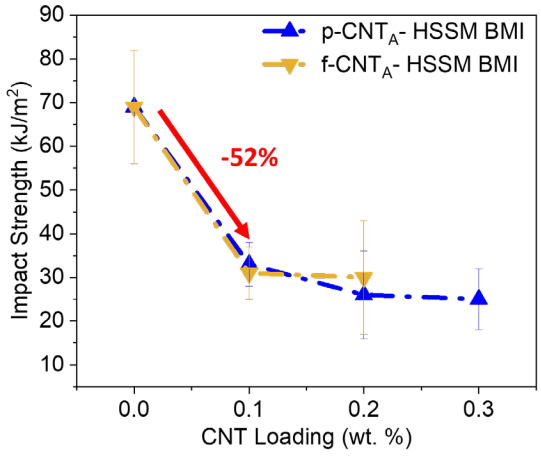

Figure 3.2. Impact strength of HSSM BMI, p-CNT$_A$- HSSM BMI and f-CNT$_A$- HSSM BMI containing up to 0.3 wt% CNT$_A$. Addition of both, the p-CNT$_A$ and f-CNT$_A$ to BMI reduces the impact strength. The 0.1wt% p-CNT$_A$- HSSM BMI and 0.1wt% f-CNT$_A$- HSSM BMI exhibited comparable impact strength and it is ~52% lower than the HSSM BMI with no CNTs.

The impact strength of the HSSM BMI decreased by 52% (from 69 ± 13 to 33 ± 5 kJ/m^2) (Figure 3.2) upon addition of 0.1 wt% p-CNT_A (0.1 wt% p-CNT_A- HSSM BMI). Well dispersed CNTs in the nanocomposite, typically improve its impact strength compared to the neat polymer through several energy absorbing mechanisms involving CNT breakage, elongation and pullouts during the bridging of the propagating crack.[216], [217] p-CNTs in the nanocomposite can have poor dispersion and agglomeration [218]. These agglomerates act as stress concentrated defect sites, leading to lower impact strength in the nanocomposite [217], [218]. Functionalization of CNTs can not only improve the dispersion of CNTs in the nanocomposite [218], but can also enhance the CNT-polymer interactions [217]. The enhanced interaction consequently improves the energy associated with CNT pullouts and elongation during the bridging of cracks [217], and leads to CNT breakage during failure, instead of CNT pullouts [218]. These mechanisms lead to improved impact strength in the nanocomposites. Herein, the impact fracture surface of 0.1 wt% p-CNT_A- HSSM BMI exhibits CNT agglomerates and CNT pullouts (Figure B 1 a and b) while the 0.1 wt% f-CNT_A- HSSM BMI exhibits dispersed CNTs with broken ends (Figure B 1 c and d). While an improvement in the impact strength of the 0.1 wt% f-CNT_A- HSSM BMI nanocomposites was thus expected, the impact strength (31 ± 6 kJ/m^2) remained comparable to the 0.1 wt% p-CNT_A- HSSM BMI. This suggests that the CNT dispersion and agglomeration related factors are not the limiting case for the impact strength of CNT containing HSSM BMI nanocomposites.

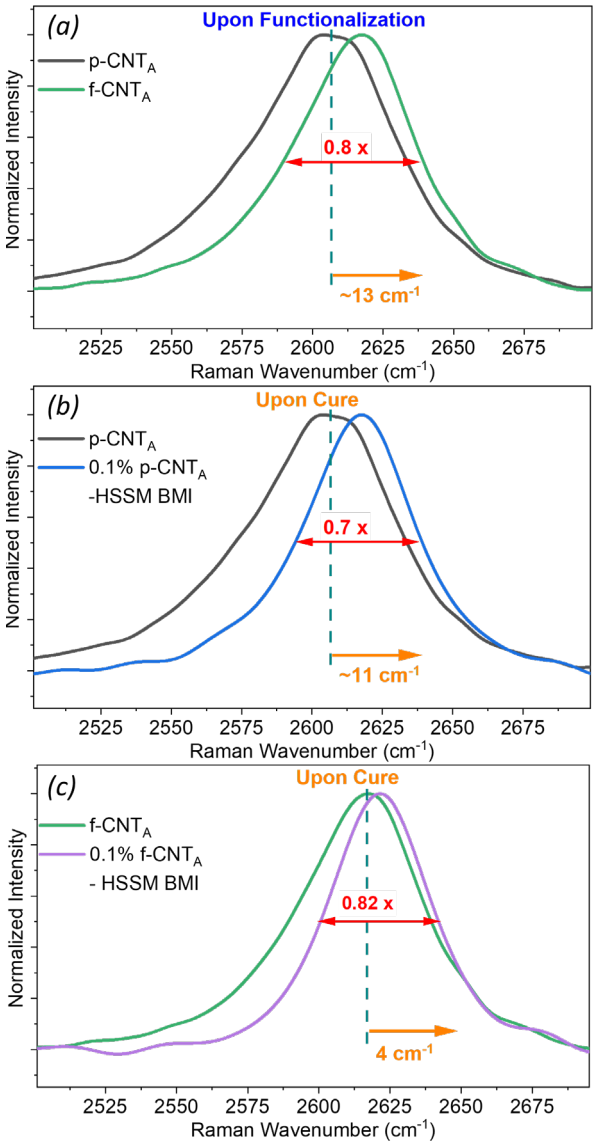

Figure 3.3. Raman G' band of (a) p-CNT$_A$ and f-CNT$_A$, (b) p-CNT$_A$ and 0.1 wt% p-CNT$_A$- HSSM BMI and (c) f-CNT$_A$ and 0.1 wt% f-CNT$_A$- HSSM BMI. (a) Raman G' band upshifts by 13 cm^{-1} upon functionalization of CNTs (f-CNT$_A$) and the FWHM reduces to 0.8x, compared to p-CNT$_A$. (b) Raman G' band also upshifts by 11 cm^{-1} upon cure of BMI in 0.1 wt% p-CNT$_A$- HSSM BMI and the FWHM is 0.7x, compared to p-CNT$_A$. (c) Raman G' band upshifts by 4 cm^{-1} upon cure of BMI in 0.1 wt% f-CNT$_A$- HSSM BMI and the FWHM is 0.82x, compared to f-CNT$_A$. The overall Raman shift in the 0.1 wt% f-CNT$_A$- HSSM BMI compared to the p-CNT$_A$ is 17 cm^{-1} and it corresponds to a compressive stress of 4.5 GPa. The compressive stress in the CNTs can contribute towards a lower impact strength in the CNT$_A$- HSSM BMI nanocomposites. All curves were normalized to the Raman G' peak.

3.2.2 BMI Curing Induced CNT Compression in the Nanocomposites

To investigate the cause of the reduced impact strength in the nanocomposites, we first used Raman spectroscopy to examine any cure induced stresses (tension or compression) in the CNT_A (Figure 3.3). Raman spectroscopy has been employed in prior studies[219], [220] for evaluating the tensile stress at the polymer-CNT interface, where the polymer-nanocomposites were stretched under a Raman spectroscope and their Raman spectra collected. The tensile strain in the CNTs result in a downshift of the Raman band frequencies (D ~ 1300 cm^{-1}, G ~ 1580^{-1}, and G′ ~2600^{-1}), due to the weakening of C=C bonds. Raman spectroscopy has also been used to study compressive stresses in the CNTs, induced upon cooling of the polymer nanocomposites [221]. Cooling the CNT fiber-epoxy nanocomposite from 60 to -150° C, upshifted the Raman G' band by 15 cm^{-1} due the shortening of the C=C bonds from the compressive stresses induced by the polymer matrix [221]. The C=C bond strength of the CNTs can also be altered through doping with electron donor or acceptor groups [21], [222], [223]. Charge acceptor groups withdraw electrons from the anti-bonding orbitals of CNTs, thus strengthening the C=C bond and upshifting the Raman band. Nitric acid functionalization treatment of the CNTs involves oxidation or removal of electrons from the CNTs which upshifts the Raman band [16].

Here we observed the Raman G' band upshift by 13 cm^{-1} in f-CNT_A, compared to p-CNT_A (Figure 3.3a). The Raman G' (full width at half maxima (FWHM)) of f-CNT_A was 20% lower compared to p-CNT_A, signifying reduced CNT crystallinity [224]. The Raman G' band upshifted by 11 cm^{-1} in the 0.1 wt% p-CNT_A- HSSM BMI compared to the p-CNTs (Figure 3.3b) and by 4 cm^{-1} in the 0.1 wt% f-CNT_A- HSSM BMI compared to the f-CNT_A (Figure 3.3c). The total upshift in the Raman G' band of the f-CNT_A-HSSM BMI

compared to p-CNTs however is 17 cm^{-1}. These results signify that, CNT_A in both the pristine and functionalized forms compress upon the cure of BMI. This compression could result from (a) physical compression upon the cure of BMI and/or (b) electron charge transfer between the CNT_A and the BMI, during cure. The Raman G' band upshifts of 17, 11 and 4 cm^{-1} corresponds to compressive stress of 4.5, 2.9 and 0.1 GPa, respectively [99]. It is likely that the compressed CNTs ease the growth of the propagating crack during impact by releasing their compressed energy and thus reducing the overall impact strength of the p and f CNT-HSSM BMI nanocomposites. The Raman G' band of the cured 0.1 wt% p-CNT_A- HSSM BMI also has a 30% reduction in the peak width FWHM, compared to p-CNT_A and by 18% in the 0.1 wt% f-CNT_A- HSSM BMI, compared to f-CNT_A.

3.2.3 Non-covalent CNT-BMI interactions: Effect of CNT functionalization

The molecular interactions between the CNT_A and the BMI in the 0.1 wt% p and f CNT_A- HSSM BMI nanocomposites were investigated using Fourier-transform infrared (FT-IR) spectroscopy (Figure 3.4). FT-IR peak shifts and change in the peaks FWHM signify a difference in the molecular interaction [209]. Here, we observe that the f-CNTs interact non-covalently with the BMI (Figure 3.4 f- h). The 0.1 wt% f-CNT_A- HSSM BMI nanocomposites demonstrated an upshift in the symmetric alkyl stretch, asymmetric alkyl stretch, $O = C - N$ and $C - N - C$ peaks by ~3- 4 cm^{-1} compared to the HSSM BMI. The 0.1 wt% p-CNT_A- HSSM BMI nanocomposites on the other hand demonstrated symmetric alkyl stretch, asymmetric alkyl stretch and $O = C - N$, peak positions and FWHM similar to the HSSM BMI (Figure 3.4 b-d). The $C - N - C$ peaks position in the 0.1 wt% p-CNT_A- HSSM BMI downshifted by 2 cm^{-1} compared to the HSSM BMI (Figure 3.4d), signifying some molecular interaction between the p-CNT_A and the BMI. The HSSM BMI

demonstrated a broad hydrogen bond peak between 3100-3650 cm^{-1}, within which distinct peaks are observable at 3192, 3365 and 3460 cm^{-1} (Figure 3.4 a and d). The distinct peaks are also observed in 0.1 wt% p-CNT-HSSM BMI nanocomposites but the intensity of the overall broad peak (3100-3650 cm^{-1}) is significantly lower (Figure 3.4a). The 0.1 wt% f-CNT-HSSM BMI nanocomposites also demonstrate a broad hydrogen bond peak with similar intensity to HSSM BMI, but a distinct peak at 3192 cm^{-1} is missing (Figure 3.4e). These observations signify that the inter/intra-molecular interactions in the HSSM BMI, 0.1 wt% p and f CNT_A- HSSM BMI systems are different.

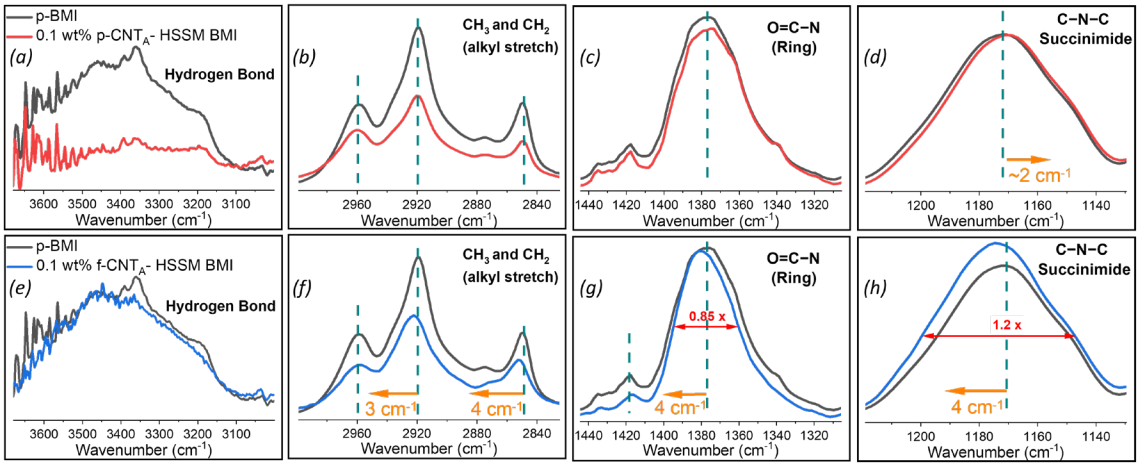

Figure 3.4. FT-IR spectra of (a-d) HSSM BMI and 0.1 wt% p-CNT_A- HSSM BMI and (e-h) HSSM BMI and 0.1 wt% f-CNT_A- HSSM BMI. Peak shifts and the change in the FWHM signify a difference in the inter and intra molecular interactions in the system.[209] These plots thus suggest that the inter/intra-molecular interactions in the HSSM BMI, 0.1 wt% p and f CNT_A- HSSM BMI systems are different from each other. All curves were normalized to the intensity of the C=C peak at 1509 cm^{-1}.

3.2.4 Two thermal relaxations in the Nanocomposites of functionalized CNTs with BMI

The non-covalent interactions between the CNT_A and BMI in the 0.1 wt% f-CNT_A-HSSM BMI observed through FT-IR is further corroborated through the tan δ plots of the dynamic mechanical analysis (Figure 3.5). The tan δ plots demonstrated two thermal

relaxation of the BMI in the 0.1 wt% f-CNT_A- HSSM BMI, with glass transition (T_g) peaks at 288 and 328 °C, a difference of 40 °C. Relaxations in the similar temperature range were also observed through DSC (Figure B 2). The two step relaxation signifies the formation of an interphase due to the non-covalent interactions between the f-CNT_A and the BMI, where the interphase has restricted mobility compared to the bulk and thus relaxes at a higher temperature [225], [226]. The peak of the bulk BMI relaxation in the 0.1 wt% f-CNT_A-HSSM BMI and the HSSM BMI are at a similar temperature (~288 °C). The two step relaxation was also observed in the 0.2 wt% f-CNT_A- HSSM BMI. The tan δ peak increased by 30% and 63% in the 0.1 wt% and the 0.2 wt% f-CNT_A-HSSM BMI nanocomposites, respectively, compared to the HSSM BMI. The p-CNT_A- HSSM BMI nanocomposites with 0.1, 0.2 and 0.3 wt% CNTs demonstrated a single tan δ relaxation peak (Figure 3.5 a), signifying an absence of the interphase. The tan δ peak value in these nanocomposites increased by up to 48%. The increase in the tan δ peak intensity signifies that the presence of both, the p-CNT_A and the f-CNT_A, disrupt the BMI cross-linked network. The storage modulus of the HSSM BMI increased with increasing temperature in the rubbery region and did not plateau, signifying thermal stiffening post T_g (Figure 3.5c). The storage modulus of p-CNT_A- HSSM BMI nanocomposites plateaued in the rubbery region signifying an absence of stiffening post T_g in these nanocomposites (Figure 3.5c). The f-CNT_A-HSSM BMI nanocomposites with 0.1 wt% CNT demonstrated slight stiffening in the rubbery region whereas the nanocomposite with 0.2 wt.% CNT demonstrated a rubbery plateau.

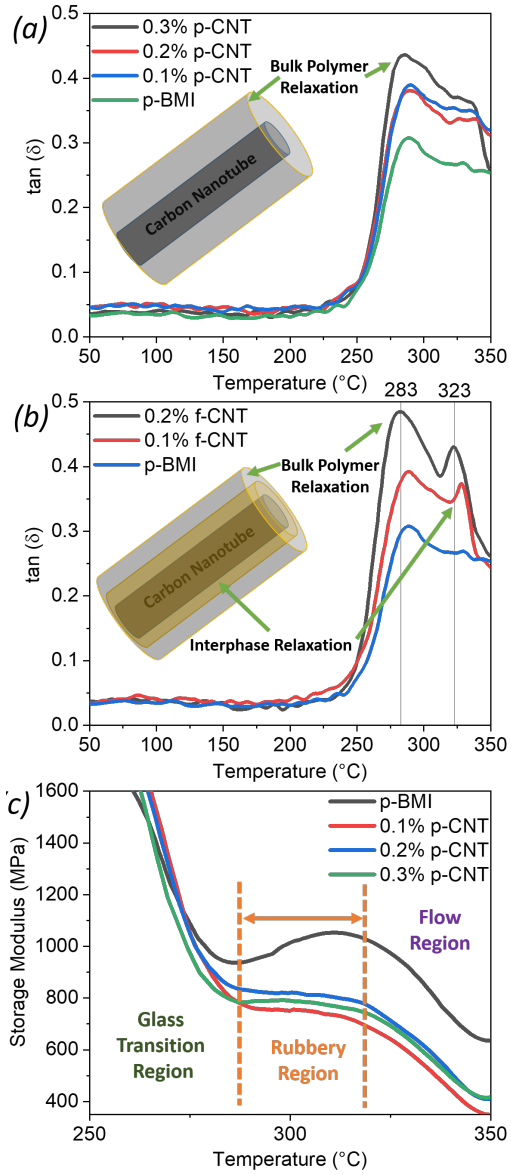

Figure 3.5. (a,b) tan δ plots of (a) HSSM BMI and p-CNT$_A$- HSSM BMI with up to 0.3 wt% p-CNT$_A$. (b) HSSM BMI and f-CNT$_A$- HSSM BMI with up to 0.2 wt% f-CNT$_A$. Both, the p-CNT$_A$ and f-CNT$_A$ containing nanocomposites have a higher tan δ peak compared to the HSSM BMI, suggesting that the addition of CNT$_A$ disrupts the HSSM BMI cross-linked network making it less elastic. This disruption of cross-linked network can also contribute towards lower impact strength in the nanocomposites. The f-CNT$_A$ containing nanocomposites demonstrate a distinct two step relaxation associated with the bulk phase and the interphase. The interphase relaxes at ~43 °C higher temperature than the bulk phase. (c) Storage modulus of HSSM BMI and p-CNT$_A$- HSSM BMI nanocomposites. The HSSM BMI demonstrates thermal stiffening in the rubbery region whereas the p-CNT$_A$- HSSM BMI nanocomposites do not stiffen and show a rubbery plateau.

3.2.5 High Impact in PS processed BMI and CNT- BMI nanocomposites

Next, we evaluated the impact strength of the nanocomposite made through a different process of PS, and using CNT_B. The impact strength of the PS BMI increased by 143% (from 14 ± 6 to 34 ± 6 kJ/m^2) compared to the Melt BMI that was processed without PS treatment (Figure 3.6). The nanocomposites of the PS BMI with 0.1 wt% CNT_B exhibited a further 60% increase in the impact strength compared to the PS BMI (from 34 ± 6 to 54 ± 8 kJ/m^2). The impact strength of the 0.1 wt% CNT_B- PS BMI is also 64% higher compared to the 0.1 wt% p-CNT_A- HSSM BMI (from 33 ± 5 to 54 ± 8 kJ/m^2) (Figure 3.6). The impact strength of the 0.1 wt% CNT_B- PS BMI is also 80% higher than the maximum impact strength reported for a CNT reinforced BMI nanocomposite in the literature, being 30 kJ/m^2 [101]. The impact strength reported in the literature for the BMI and their CNT reinforced nanocomposites are summarized in Table 1.1 and Table 2.1

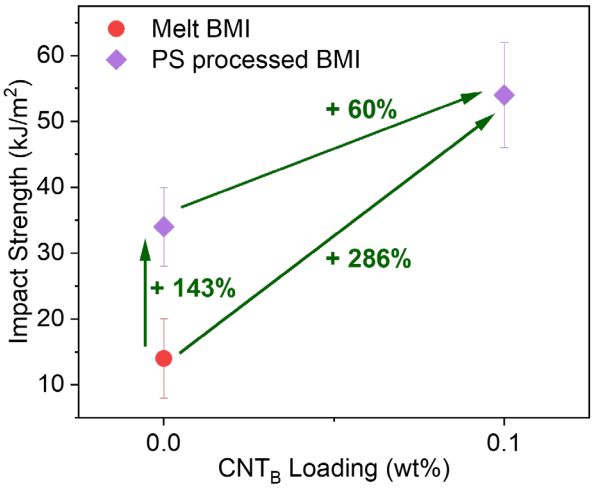

Figure 3.6. Impact strength of the Melt BMI, PS BMI and 0.1 wt% CNT_B- PS BMI. PS BMI demonstrates a 143% improvement in the impact strength compared to Melt BMI. Melt BMI refers to BMI that was neither HSSM nor PS. 0.1 wt% CNT_B- PS BMI demonstrates a 60% and 286% improvement in the impact strength compared to the PS BMI and Melt BMI, respectively.

HSSM processed BMI lead to a 4x increment in the impact strength compared to the Melt BMI (BMI processed without the HSSM step), owing to the molecular rearrangement of the multi components of the BMI system during processing [209]. The PS p-BMI demonstrates significant differences in the molecular environment compared to the Melt BMI aswell. The FT-IR of PS p-BMI shows peak shifts of up to 6 cm^{-1} compared to the Melt BMI (Figure S3 a-d). The addition of 0.1 wt% CNT_B further alters the inter and intramolecular interactions within the 0.1 wt% CNT_B- PS BMI compared to the PS p-BMI. The 0.1 wt% CNT_B- PS BMI nanocomposite demonstrated a downshift of 2 cm^{-1} in the alkyl asymmetric stretch peak, aswell as a 20 and 15% reduction in the FWHM of the $O=C-N$ and $C-N-C$ peaks, respectively, compared to the PS BMI (Figure B 4 e-h). Raman spectra were then collected to explore any cure induced tension or compression of the CNT_B in the 0.1 wt% CNT_B- PS BMI but the Raman bands associated with the CNT_B could not be observed in the nanocomposite (Figure B 4 c-e). We then explored the effect of CNT_B on the cross-linking of BMI, through the DMA, tan δ and storage modulus plots. The PS-BMI and the 0.1 wt% CNT_B- PS BMI demonstrated comparable tan δ peak intensity (Figure B 5b) and rubbery moduli (Figure B 5d), signifying that the addition of 0.1 wt% CNT_B does not disrupt the BMI cross-linked network, as was observed in the case of CNT_A- HSSM BMI nanocomposites. Since the CNT_B are able to reinforce the BMI without disrupting the BMI network, this could be one of the reasons, why an improved impact strength is achieved upon its addition in the nanocomposite while in the case of CNT_A, the impact strength decreases.

3.2.6 Fractography

The impact fracture surface of the BMI with the highest impact strength reported in the literature (HSSM BMI with impact strength of 69 ± 13 kJ/m^2) demonstrated micro nodular features in the crack initiation and propagation regions [209]. Here, we examined the crack initiation and propagation region within the impact fractured surface of the 0.1 wt% p-CNT_A- HSSM BMI (Figure 3.7a), 0.1 wt% f-CNT_A- HSSM BMI (Figure 3.7b) and 0.1 wt% CNT_B- PS BMI (Figure 3.7 c,d), through SEM. While all three nanocomposites exhibited rough fracture surfaces signifying plastic deformation, the 0.1 wt% CNT_B- PS BMI which demonstrated the highest impact strength among all nanocomposites studied in this work (54 ± 8 kJ/m^2) demonstrated micro nodular morphology. These micro-tubules are 10-20 μm in diameter, very similar to what was observed for HSSM BMI with no CNTs (impact strength of 69 ± 13 kJ/m^2) in our prior work [209]. Microtubular features were neither observed in the 0.1 wt% p-CNT_A- HSSM BMI, nor in the 0.1 wt% f-CNT_A- HSSM BMI. These observations signify a direct association between the micro-nodules and high impact strength of the BMI system and its CNT based nanocomposites.

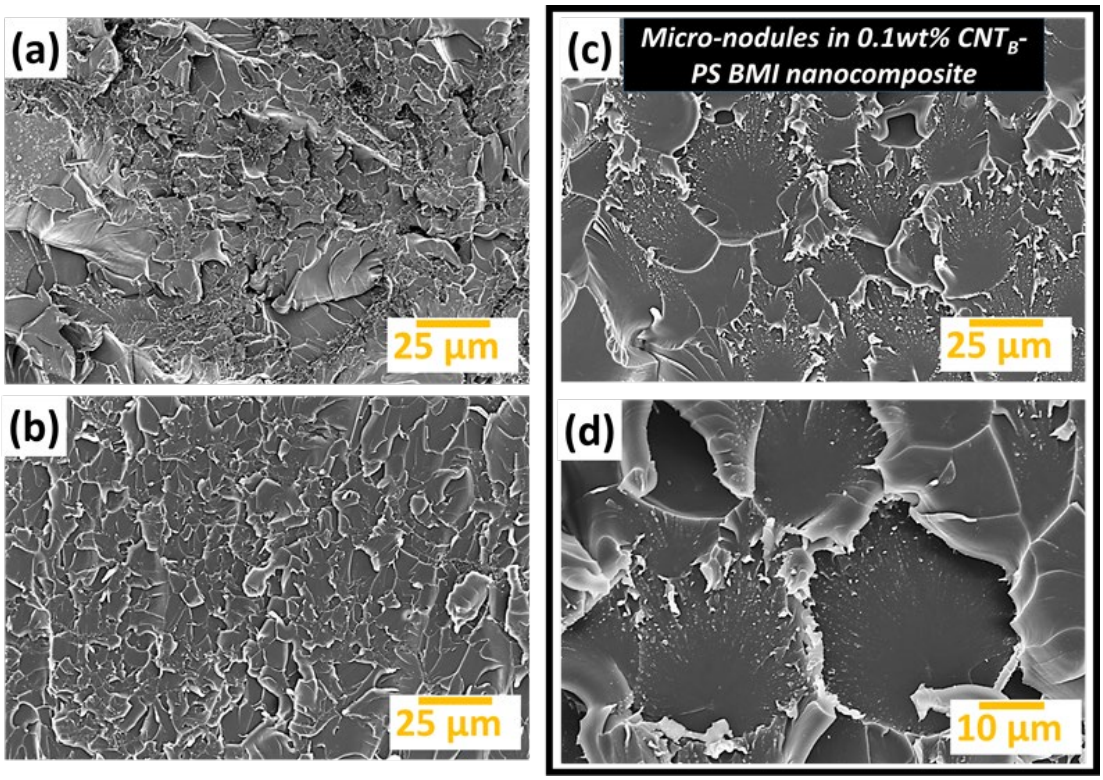

Figure 3.7. SEM micrographs of (a) 0.1 wt% p-CNT_A- HSSM BMI, (b) 0.1 wt% f-CNT_A- HSSM BMI and (c-d) 0.1 wt% CNT_B- PS BMI. (a-d) While all three nanocomposites exhibit rough fracture surfaces signifying plastic deformation, the 0.1 wt% CNT_B- PS BMI demonstrates micro nodules of ~10-20 µm diameter. Similar micro nodules were observed in HSSM BMI in our prior work where the impact strength of HSSM BMI is 69 ± 13 kJ/m^2. Herein, the 0.1 wt% CNT_B- PS BMI have an impact strength of 54 ± 8 kJ/m^2.

3.2.7 Comparing Molecular Architectures using SAXS

SAXS has been used in prior studies to calculate the domain size associated with the molecular heterogeneity of the BMI [209] or CNT-BMI composites [226], [227], inter-CNT distance [228] and CNT bundle size [228]. In our prior work [209], assuming Bragg's diffraction, SAXS peak corresponding to Bragg's d-spacing of 15.5 nm was observed in the HSSM BMI. The BMI that did not undergo a HSSM process (termed Melt BMI) demonstrated three peaks corresponding to Bragg's d-spacing of 10.6, 5.4 and 4 nm [227]. Herein, we have analyzed the SAXS peaks assuming Bragg's diffraction. While the SAXS

peaks could also result from scattering, any differences in the SAXS peak positions would still signify a different molecular architecture, irrespective of how they are analyzed. The PS BMI demonstrates SAXS peaks at q values of 0.026 and 0.155 A^{-1} which correspond to the Bragg's d-spacing of 23.6 and 4 nm (Figure B 6), signifying that the PS BMI has a different molecular architecture compared to both, the HSSM and Melt BMI. The 0.1 wt% CNT_B- PS BMI demonstrates a SAXS peak deflection at a q value of 0.025 (d ~25 nm) and a peak at a q value of 0.146 A^{-1} (d ~ 4.3 nm) (Figure 3.8). The scattering intensity (I (q)) decay in the 0.1 wt% CNT_B- PS BMI onsets at a q value of 0.025 (d ~25 nm). The I (q) decay is faster between the q values of 0.0275 (d ~ 22.8 nm) and 0.038 A^{-1} (d~ 16.2 nm), where the slope of the I (q) decay is -10.6. The I (q) decay slope however is -3.29, between the q values of 0.041 (d ~ 15.1 nm) and 1 A^{-1} (d ~ 6.3 nm). The 0.1 wt% p-CNT_A- HSSM BMI demonstrates SAXS peak deflections at q values of 0.02 (d~ 31.3 nm) and 0.029 A^{-1} (d~ 21.3 nm), and a peak is observed at a q value of 0.15 A^{-1} (d~ 4.2 nm) (Figure 3.8). The slope of the I(q) decay between the q values of 0.041 and 1 A^{-1} is -3.7. The 0.1 wt% f-CNT_A- HSSM BMI demonstrates only minor differences in its SAXS scattering profile compared to the 0.1 wt% p-CNT_A- HSSM BMI. The 0.1 wt% f-CNT_A- HSSM BMI also demonstrates peak deflections at q values of 0.02 and 0.029 A^{-1}, and has a peak at q value of 0.153 A^{-1} (d ~ 4.1 nm) (Figure 3.8). The slope of the I(q) decay between the q values of 0.041 and 1 A^{-1} is -3.2. The SAXS results thus demonstrate that the 0.1 wt% CNT_B- PS BMI has a significantly different molecular architecture compared to the 0.1 wt% p or f CNT_A containing nanocomposites of HSSM BMI or compared to the PS BMI. The results also demonstrate that the 0.1 wt% p or f CNT_A containing nanocomposites of HSSM BMI have a different molecular architecture compared to the HSSM BMI [209].

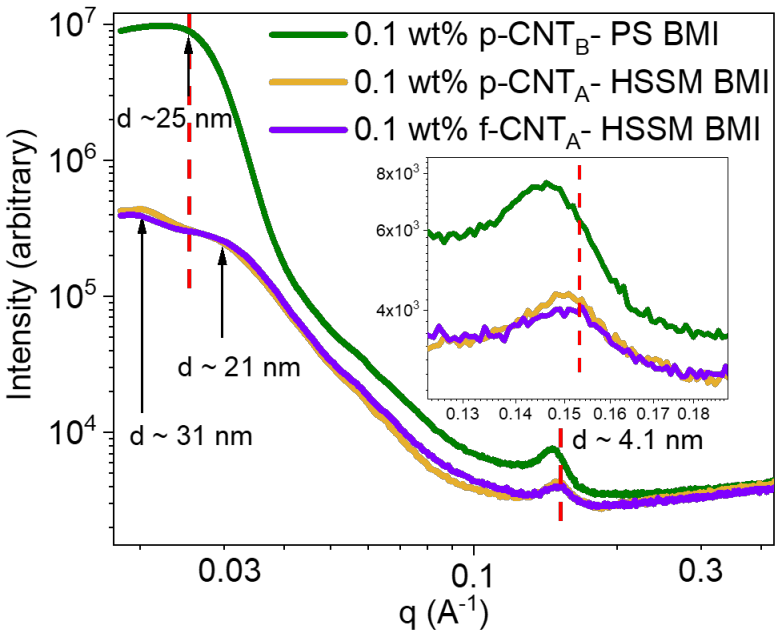

Figure 3.8. SAXS of the 0.1 wt% CNT_B- PS BMI, 0.1 wt% p-CNT_A- HSSM BMI and 0.1 wt% f-CNT_A- HSSM BMI. The scattering profile show that the 0.1 wt% CNT_B- PS BMI has a significantly different molecular architecture compared to the 0.1 wt% p-CNT_A- HSSM BMI or the 0.1 wt% f-CNT_A- HSSM BMI. The SAXS peaks have been analyzed assuming Bragg's diffraction and the d-spacing corresponding to the peaks have been listed in the plot. While the SAXS peaks could also result from scattering, any differences in the SAXS peak positions would still signify a different molecular architecture, irrespective of how they are analyzed.

3.3 Experimental

3.3.1 Materials:

Cycom 5250-4 RTM from Solvay is the multi- component Bismaleimide system used in this study. CNT_A are multiwalled Miralon CNTs obtained from Nanocomp Technologies, Inc. (Merrimack, NH). The manufacturer reported that the length of individual CNTs was 1−10 mm and the diameter id ~8 nm. The Raman I_D/I_G of the as received CNT_A (p-CNT_A) was measured to be 0.39 ± 0.02. CNT_B are multi-walled carbon nanotubes obtained from Nanointegris, Inc. (Canada). The manufacturer reported that the outer diameter of the CNTs is less than 8 nm and the length of individual CNT is between

10-30 µm. The Raman I_D/I_G of the as received CNT_B was measured to be 1.62 ± 0.03. For functionalization and wetting of CNT_A, nitric acid (ACS reagent, 70%) from Sigma-Aldrich and THF (99.9% purchased from Sigma-Aldrich) were used, respectively.

3.3.2 Sample Preparation

3.3.2.1 Functionalization of CNT_A:

p-CNT_A were sonicated in 10 M nitric acid (40 mg/dl) for 30 min (Branson bath sonicator 3510R-MT, 100 W, 42 kHz)) for 30 min. The mixture was refluxed at 120 °C (oil-bath temperature) for 24 h. The mixture was then centrifuged and washed in DI water until the pH value reached that of the DI water. The f-CNT_A were then filtered and washed with THF. f-CNT_A, wet in THF were then used to make nanocomposites with BMI. For characterizing the f-CNT_A, the CNT_A wet in THF were dried overnight at room temperature followed by drying at 120 °C under vacuum (20 mbar) for 30 min. The Raman I_D/I_G of the functionalized CNT_A (f-CNT_A) was 1.44 ± 0.03.

3.3.2.2 Melt, HSSM and PS process:

The as-received BMI system was melted and degassed at 110 °C. This sample is termed as Melt BMI. For HSSM processed BMI nanocomposites, p-CNT_A or f-CNT_A were added to the melted and degassed BMI system at 110 °C and then subjected to dual asymmetric centrifugal high-speed shear mixing using a DAC 150.1 from Flacktec Inc. for 10 min followed by degassing. Control HSSM BMI specimens were processed without the addition of CNT_A. For PS processed BMI nanocomposites, CNT_B were added to the melted and degassed BMI system at 110 °C and then subjected to a probe-sonication treatment. A

probe sonicator (Q700 from QSonica) with a frequency of 20 kHz at 100% amplitude was used to probe sonicate the CNT_B-BMI mixture for a pulse duration of 30 second-1 minute (on and off pulse), while temperature was maintained at 110°C. The total effective sonication time (excluding off time) was 12 minutes.

3.3.2.3 Casting Specimen and Cure:

A silicone mold with impact bar and tensile "dog-bone" specimen cavities was used for casting specimens. A mold release agent, Ease release 205 from Mann Formulated Products, was applied to the mold and left to dry for 30 min at room temperature. The mold was then preheated to 191 °C and held under vacuum for 10 min along with the Melt, HSSM or PS processed BMI or HSSM/ PS processed CNT-BMI mixtures (as applicable). The processed BMI or CNT-BMI mixture was then poured in the mold and cured at 191 °C for 4 h with no external pressure applied. The oven was then cooled to room temperature, and the specimens were drawn out of the mold followed by postcured at 227 °C for 2 h in a free-standing form (no mold) and with no externally applied pressure. The post-cured samples were then polished on a Buehler MetaServ polisher using a silicon carbide paper, first with abrasive grade P280, followed by P600, and then by P1200.

3.3.3 Characterization

FT-IR, Raman, impact test, tensile test, DMA, DSC and SEM were conducted as described in a prior work.[209] SAXS was conducted on Panalytical Empyrean (Cu Kα λ= 0.1542 nm, operating voltage and current 40 kV and 0.40 mA, respectively).

3.4 Conclusion

Well dispersed CNTs in the polymer nanocomposites typically improve the impact strength of the polymers through several energy absorbing mechanisms including CNT breakage, elongation and pullouts during the bridging of the propagating crack. Herein, 0.1 wt% f-CNT_A- HSSM BMI contained well dispersed CNTs (f-CNT_A) which non-covalently interacted with the BMI and had an interfacial layer with a T_g ~40 °C higher, yet it demonstrated a significantly lower impact strength. The CNTs (p-CNT_A and f-CNT_A) in the 0.1 wt% p-CNT_A- HSSM BMI and 0.1 wt% f-CNT_A- HSSM BMI compressed upon the cure of BMI. The Raman G' band upshifted by 11 cm^{-1} in the 0.1 wt% p-CNT_A- HSSM BMI compared to the p-CNTs, corresponding to a compressive stress of 2.9 GPa.[99] DMA results demonstrated that the CNTs (p-CNT_A and f-CNT_A) in the 0.1 wt% p-CNT_A- HSSM BMI and 0.1 wt% f-CNT_A- HSSM BMI also disrupted the HSSM BMI cross-linked network. The SAXS results also show that the HSSM BMI nanocomposites containing 0.1 wt% p or f CNTs have a different molecular architecture compared to the HSSM BMI. These factors combined lead to a 52% reduction of the impact strength in the composites with as little as 0.1 wt% p or f- CNT_A. On the contrary, nanocomposites containing 0.1wt% CNT_B and processed through the PS method demonstrated a 60% improvement in the impact strength. DMA results show that the CNT_B in the 0.1 wt% CNT_B- PS BMI did not disrupt the PS BMI cross-linked network. The SAXS result showed that the 0.1 wt% CNT_B- PS BMI has a significantly different molecular architecture compared to the (a) PS BMI and (b) 0.1 wt% p or f CNT_A containing nanocomposites of HSSM BMI. The CNT type and the processing method are thus critical parameters for making nanocomposites with improved fracture toughness. The impact strength of the 0.1 wt% CNT_B- PS BMI (54

± 8 kJ/m^2) is also the highest reported impact strength for any CNT-BMI nanocomposite to date. The highest impact strength reported in the literature for the BMI-CNT system is 30 kJ/m^2. The uncured 0.1 wt% CNT_B- PS BMI has thus been identified as a system of interest for being employed as the CNT-reinforced-matrix, for the manufacturing of toughened CNT-reinforced- hybrid carbon fiber BMI composites or the CNT-reinforced-hybrid CNT Yarn-BMI composites.

CHAPTER 4. CNT- BMI NANOCOMPOSITES WITH HIGH CNT CONTENT: CURE BEHAVIOR CHANGES AND COMPRESSION OF CARBON NANOTUBES IN NANOCOMPOSITES CONTAINING CARBON NANOTUBE SHEETS

4.1 Introduction

Here, we ask, would CNTs alter the cure reaction and/or the cure temperature of the BMI? BMI are a multiple component system that undergo complex cure reactions. These reactions have been summarized in our prior work.[20] CNTs can interact with the BMI system through the NH$-\pi$[20], [21], $\pi-\pi$,[22] CH$-\pi$,[16], [22] and OH$-\pi$,[23] non-covalent interactions. The individual components of the BMI however can have exclusive non-covalent interactions with the CNTs. For e.g., in a BMI system containing 4,4'- bismaleimidodiphenylmethane (BDM) and diallylbisphenol A (DABA) components,[24] only the BDM component contains the maleimide functional group which can potentially interact with the CNTs through the NH$-\pi$ bonding, while only the DABA component, containing the OH functional group can potentially interact with the CNTs through the OH$-\pi$ interactions. The potential for the preferential stacking of the different BMI components around the CNTs, can have important implications on the cure behavior of the BMI in the nanocomposite and consequently on the overall mechanical properties of the nanocomposite.

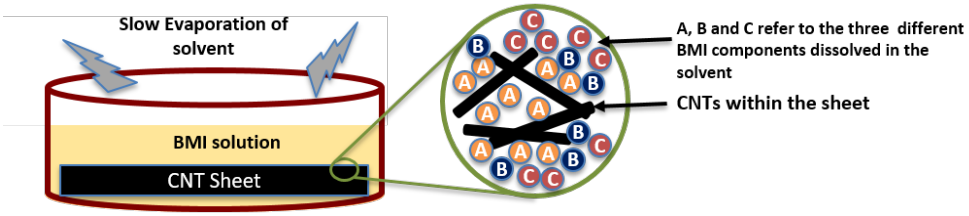

Figure 4.1. Schematic of the process of solvent (THF) assisted infiltration of BMI within the CNT sheets. The slow evaporation of the THF can promote preferential stacking of the different components of the BMI around the CNTs within the CNT sheet.

Herein, we use a multi-component,[162] aerospace grade BMI to study the effect of the CNTs on the cure reactions of the BMI, as well as the effect of the cure of the BMI on the CNTs in the nanocomposites containing up to 40 wt% CNT. We used a BMI-THF solution to infiltrate the CNT sheets. Post infiltration, instead of rapidly evaporating the THF, we opted for a slow evaporation of THF under ambient temperature and pressure to promote any potential preferential stacking of the different BMI components around the CNTs (Figure 4.1). Prior studies in the literature on the CNT-BMI nanocomposites which have used the solution assisted infiltration process, have relied on rapid evaporation of the solvent post infiltration through heating and/or using vacuum.[79], [84], [114], [115], [118] To understand the effect that the varying CNT content in different nanocomposites have on the inter-CNT spacing and how that could be critical for understanding the effects on the cure reactions and on the thermomechanical properties in BMI nanocomposites, an ideal CNT-polymer model[229] has been employed. Two different kinds of CNT sheets have been used to prepare the nanocomposites, one containing amorphous carbon (termed as UB CNT), and another where the UB CNT are thermally treated to eliminate the amorphous carbon (termed as B CNT).[219] More details on the UB and B CNT sheets can be found in our prior work.[219]

4.2 Results and Discussion

4.2.1 Effect of CNTs on the BMI Cure Reaction and Cure Kinetics

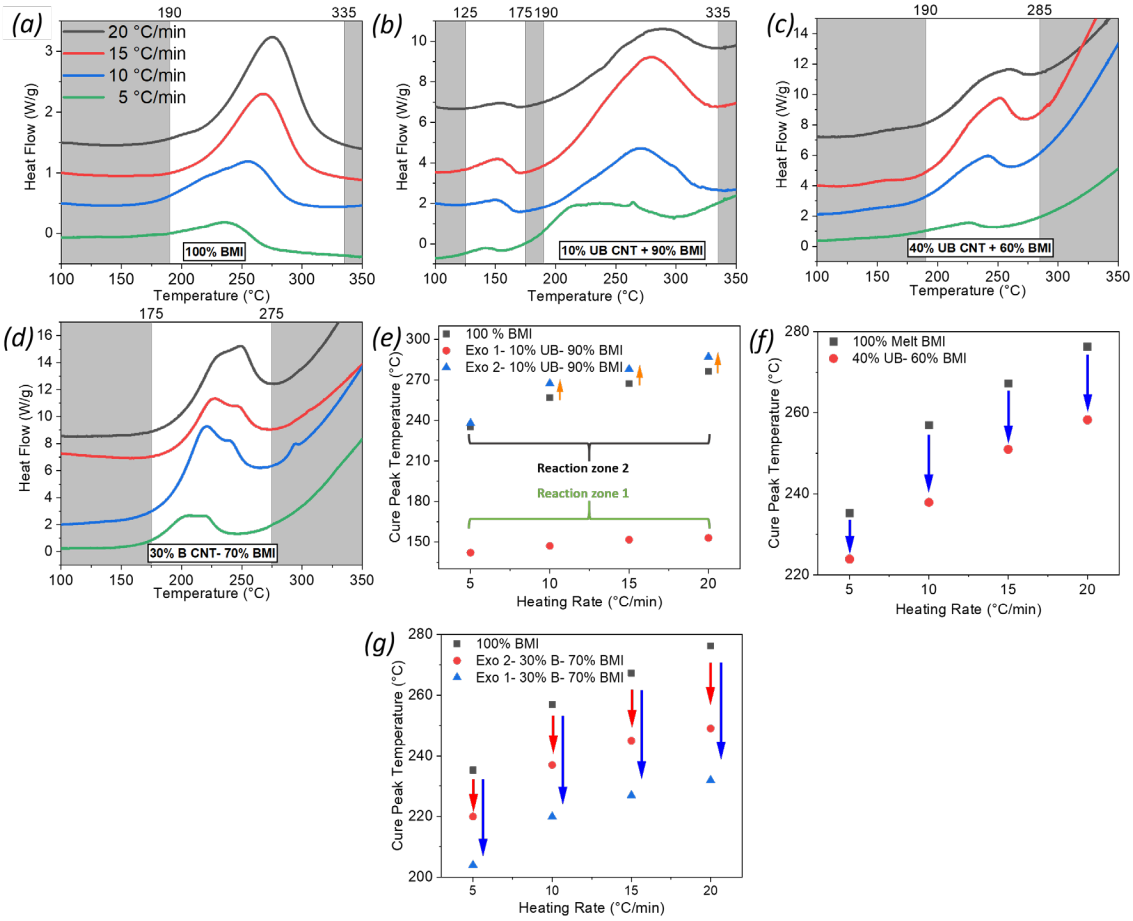

Figure 4.2 (a-d) DSC cure profile at heating rates of 5, 10, 15 and 20 °C/min for (a) 100 wt% BMI (no CNTs), (b) 10 wt% UB CNT- 90 wt% BMI, (c) 40 wt% UB CNT- 60 wt% BMI, (d) 30 wt% B CNT- 70 wt% BMI. (e-f) Exothermic peak temperatures of 100% BMI and (e) 10 wt% UB CNT- 90 wt% BMI, (f) 40 wt% UB CNT- 60 wt% BMI and (f) 30 wt% B CNT- 70 wt% BMI. The plots have been shifted along the y-axis for clarity.

Differential scanning calorimetry (DSC) scans on the BMI with no CNTs (termed as 100% BMI) and the CNT-BMI nanocomposites were done to study the effect of the CNTs on the BMI cure reaction. Scans were done at heating rates of 5, 10, 15 and 20 °C/min

under air. Cure activation energies (E_a) were determined through the Kissinger[177] ($E_{a\text{-}K}$) and Ozawa[178] ($E_{a\text{-}O}$) methods. The cure reaction temperatures and the activation energies are listed in Table C 1. The BMI containing 10 wt% UB CNT (10 wt% UB – 90 wt% BMI) demonstrated an exothermic cure peak at up to 123 °C lower temperature than the exothermic peak temperature for the 100% BMI with no CNTs (temperatures being 153 and 276 °C, respectively, when the DSC heating rate used, was 20 °C/min) (Figure 4.2 a,b,e). The 10 wt% UB – 90 wt% BMI demonstrated two distinct exothermic peaks (Figure 4.2 b) whereas the 100% BMI demonstrated a single peak (Figure 4.2 a), signifying that the 10 wt% UB CNT alters the BMI cure reactions. The two exothermic peaks of the 10 wt% UB – 90 wt% BMI were in the range of 142-153 °C (termed as reaction zone 1) and 238- 287 °C (termed as reaction zone 2) while the single exothermic peak for the 100% BMI was in the range of 235- 276 °C. A range of the peak cure temperature is obtained from the DSC scans performed at different heating rates. The $E_{a\text{-}K}$ of the reaction zone 2, for the 10 wt% UB – 90 wt% BMI was 22% lower than that for the 100% BMI, being 73 and 57 kJ/mol, respectively. The $E_{a\text{-}K}$ of the reaction zone 1 for the 10 wt% UB – 90 wt% BMI was 168 kJ/mol. Nanocomposites of BMI containing 40 wt% UB CNT demonstrated up to 18 °C lower cure temperature, compared to the 100 wt% BMI (Figure 4.2 f) and had a single distinct exothermic peak (Figure 4.2 c). The 30 wt% B CNT – 70 wt% BMI demonstrated up to 27 °C lower cure temperature (Figure 4.2 g) and had two distinct exothermic peaks (Figure 4.2 d). The $E_{a\text{-}K}$ of the 40 wt% UB – 60 wt% BMI was 78 kJ/mol while the $E_{a\text{-}K}$ for both the reactions of the 30 wt% B – 70 wt% BMI was ~90 kJ/mol. The $E_{a\text{-}O}$ values of these reactions were similar to the $E_{a\text{-}K}$ values at are listed in Table C 1.

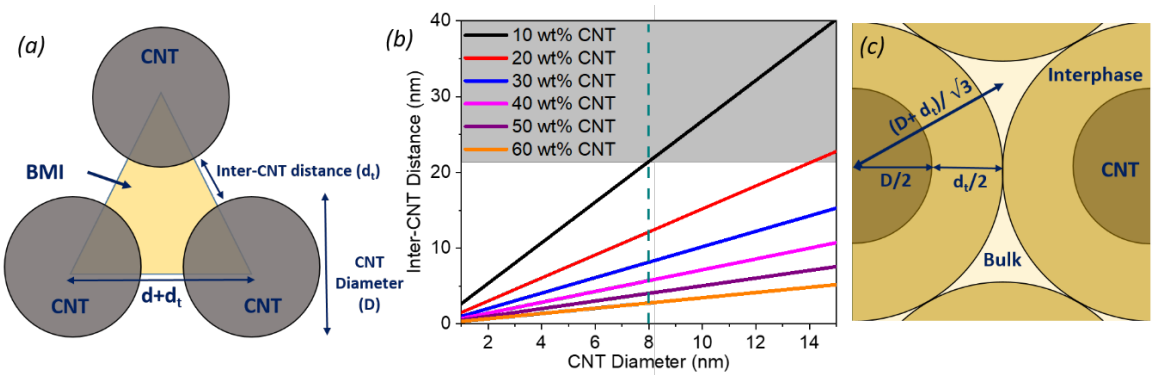

Figure 4.3. (a) Schematic of the unit cell for an ideal BMI-CNT arrangement. The inter-CNT distance in this arrangement depends upon the CNT diameter and the CNT content in the nanocomposite. (b) Plot demonstrating the relation between the inter-CNT distance and the CNT diameter for nanocomposites containing different CNT loading. For a given CNT content, the inter-CNT distance increases as the CNT diameter increases and for a given CNT diameter, the inter-CNT distance decreases with increasing CNT content within the nanocomposite. (c) Schematic of a CNT-BMI nanocomposite where the BMI is present in two different phases: an interphase and the bulk, the interphase thickness (IT) being 0.5 dT. For all the BMI in the nanocomposite to be part of the interphase, the IT should be at least $((D + d_T)/\sqrt{3}) - D/2)$.

The differences in the cure activation energy and the cure reaction temperatures of the 100 wt% BMI and the 10, 30 and 40 wt% CNT containing nanocomposites, could result from: (a) Non-covalent preferential stacking of the components of the BMI around the CNTs (Figure 4.1). (b) Difference in the amount of BMI between the CNTs. Assuming an ideal CNT-polymer model,[229] as the CNT content in the nanocomposite increases, the thickness of the BMI layer between the CNTs decreases (Figure 4.3 a, b). The ratio of the amount of BMI in the nanocomposite that interacts with the CNT (interphase), to the amount of BMI that does not interact with the CNT (bulk BMI), should increase with decreasing BMI thickness between the CNTs and should eventually plateau, once all the BMI is transformed to the interphase. The difference in the molecular interactions within the different phases, and the varying phase ratios of BMI within different nanocomposites could alter their cure reactions. We also considered the effect of the differences in thermal

conductivity of the nanocomposites on the cure behavior. Nguyen *et. al.*[230] reported the thermal conductivity of CNT buckypaper with randomly oriented CNTs to be 20 W/ mK, and Wan *et. al.*[231] reported the thermal conductivity of a BMI system to be 0.32 W/ mK. The thermal conductivity of a CNT-BMI nanocomposite would thus be higher in the nanocomposite with a higher CNT content which consequently should lead to a similar or lower cure temperature of the nanocomposite. containing while the 10 wt% UB – 90 wt% BMI has up to 123 ℃ lower cure temperature compared to 100 wt% BMI, the 40 wt% UB – 60 wt% BMI has only up to 18 ℃ lower cure temperature compared to 100 wt% BMI. This signifies that the thermal conductivity of the nanocomposite is not the major factor that alters the cure behavior of the nanocomposites. Instead, preferential molecular stacking of the different components of the BMI around the CNTs and the difference in BMI thickness between the CNTs in nanocomposites with varying CNT content are the major reasons for the change in cure behavior of the nanocomposites.

4.2.2 Ideal CNT-Polymer Interaction Model: Inter-CNT spacing and Minimum Interphase Thickness Required for all the Polymer to be in the Interphase Form as a Function of CNT Content and CNT Diameter within the Nanocomposite

To further have a quantitative understanding of the thickness of the BMI between the CNTs in the nanocomposites with different CNT loading or CNT diameter, we employ an ideal CNT-polymer interaction model.[229] The model assumes a nanocomposite with: individual CNTs, the CNTs have a degree of orientation equal to one, the CNTs are equally spaced from each other and the space between the CNTs is filled by the BMI (Figure 4.3a). The distance between the surface of the adjacent CNTs through a line connecting their

centers, is termed as the inter-CNT distance (d_T) (Figure 4.3). The CNT content, the CNT diameter (D) and d_T in the ideal CNT-BMI system are related through equation 5.

$$\frac{M_{CNT} \times \rho_{BMI}}{(M_{CNT} \times (\rho_{BMI} - \rho_{CNT})) + \rho_{CNT}} = \frac{\pi D^2}{2\sqrt{3}(d_T + D)^2} \quad (5)$$

$$I_T \geq ((D + d_T)/\sqrt{3}) - D/2) \quad (6)$$

$$\frac{V_I}{V_T} = \frac{\pi ({I_T}^2 + I_T D)}{\sqrt{3}/2 (D + d_t)^2} \quad (7)$$

Here, M_{CNT}, ρ_{BMI}, ρ_{CNT} and I_T refer to the weight fraction of the CNTs in the nanocomposites, the density of BMI, the density of CNTs and the interphase thickness, respectively. Using equation 5 and solving for D and d_T, we obtain $d_T = kD$ where k is the scaling and is inversely proportional to the CNT weight fraction. Using the d_T obtained from equation 5 and for a given CNT diameter, equation 2 provides the condition necessary for all the BMI to be present in the form of an interphase, i.e., the ratio of the volume of interphase (V_I) to total volume of BMI (V_T) in the nanocomposite =1. If equation 6 is not satisfied, the ratio of the volume of interphase to total BMI in the nanocomposite is less than 1 and can be calculated using equation 7. For a CNT with a diameter of 8 nm, the nanocomposites containing 10, 20, 30, 40, 50 and 60 wt% will have: (a) inter-CNT distance of ~ 21, 12, 8, 6, 4 and 3 nm, respectively. (b) The minimum interphase thickness necessary for V_I / V_T = 1 in these nanocomposites would be ~12.7, 7.5, 5.3, 4, 3 and 2.4 nm. To be better understand in the context of the nanocomposite prepared in this study, if the interphase thickness was 5.3 nm for all nanocomposites (irrespective of the CNT type or CNT weight fraction), the nanocomposites containing 30 wt% and more CNTs will have

all the BMI in the form of the interphase, however the 10 wt% CNT containing nanocomposite will have only 30 vol% BMI in the form of the interphase. The difference in the V_I / V_T in different nanocomposites could contribute to differences in the cure behavior of BMI. Furthermore, given that the components of the BMI can stack preferentially around the CNTs, there could infact be a preferential structural and molecular interaction variation within the interphase as well.

The ideal CNT-polymer interaction model could also be used for calculating the inter-CNT distance and the minimum interphase thickness necessary for V_I / V_T = 1, as a function of CNT diameter (Figure 4.3b). For a given CNT content, the inter-CNT distance d_T increases linearly ($d_T = kD$) with increasing CNT diameter (D) (Figure 4.3b). The scaling factor k can be calculated using equation 5. Since the CNTs could also exist in bundles instead of individual tubes, the effective CNT diameter of the CNTs in that scenario would be higher than the individual CNT diameter, which consequently would increase both, the inter-CNT distance and the minimum interphase thickness necessary for V_I / V_T = 1, for a nanocomposite, at a given CNT loading.

4.2.3 CNT Content Dependent Thermal Relaxations

The dynamic mechanical tan δ plots can provide direct evidence of the presence of an interphase/ multiple phases within a nanocomposite,[5], [232] provided the different phases have different thermal relaxations. In another work,[232] the nanocomposites of BMI containing only 0.1 wt% functionalized CNTs demonstrated two thermal relaxations of the BMI, one associated with the bulk BMI, at 288 °C, and another with the interphase, at 328 °C. Herein, for the 10 wt% UB – 90 wt% BMI, we

observe two thermal relaxations as well, one at 294 and another at 385 °C (Figure 4.4 a), signifying the presence of at least two different phases. The relaxation at 294 °C can be attributed to the bulk BMI while the peak at 385 °C can be attributed to the interphase relaxation. The interphase in the 10 wt% UB – 90 wt% BMI is different than the interphase in the 0.1 wt% functionalized CNT nanocomposite of BMI,[232] given a 57 °C difference in the interphase relaxation temperature of the two nanocomposites. The 40 wt% UB – 60 wt% BMI demonstrates a single tan δ peak at 379 °C (Figure 4.4 a), signifying an absence of the bulk BMI phase. Since all of the BMI in the 40 wt% UB – 60 wt% BMI is in the interphase form, and the BMI thickness between the CNTs, predicted from the ideal CNT-polymer model in the 40 wt% CNT containing nanocomposite is 5.3 nm (equation 6), the interphase thickness in the nanocomposite is at least 5.3 nm. The onset temperature for the first tan δ peak in the 40 wt% UB – 60 wt% BMI is at 291 °C, 66 °C higher than the 10 wt% UB- 90 wt% BMI. The 30 wt% B – 70 wt% BMI demonstrates a broad glass transition where the tan δ value starts to increase at ~240 °C and continues to rise till the end of the test, thus resulting in an absence of the tan δ peak (Figure 4.4 a). Absence of a distinct peak associated with the bulk BMI relaxation signifies that the 30 wt% B – 70 wt% BMI has a $V_I / V_T = 1$ and thus has an interphase thickness of at least 7.5 nm (equation 6). The 30 wt% B – 70 wt% BMI also demonstrates a thermal stiffening behavior, i.e., the storage modulus increases in the rubbery region (Figure 4.4 b). Neither of the 10 wt% or 40 wt% UB CNT containing nanocomposites of BMI demonstrated thermal stiffening, and their storage modulus decreased with increasing temperature in the rubbery region. The storage modulus demonstrates an increasing trend with an increase in the CNT content in the nanocomposites. The nanocomposites containing 10, 30 and 40 wt% CNTs have a storage

modulus of 4.5, 10.1 and 14.5 GPa, respectively, at 50 °C (Figure 4.4 b). The specific tensile strength and modulus also improved with increasing CNT content (Figure 4.4 c and Table C 2). The nanocomposites containing 10, 30 and 40 wt% CNTs had a specific tensile strength of 43 ± 7, 104 ± 5 and 230 ± 8 MPa/g/cc and a specific tensile modulus of 1.4 ± 0.1, 4.1 ± 0.5 and 7.7 ± 0.5 GPa/g/cc (Figure 4.4 c and Table C 2).

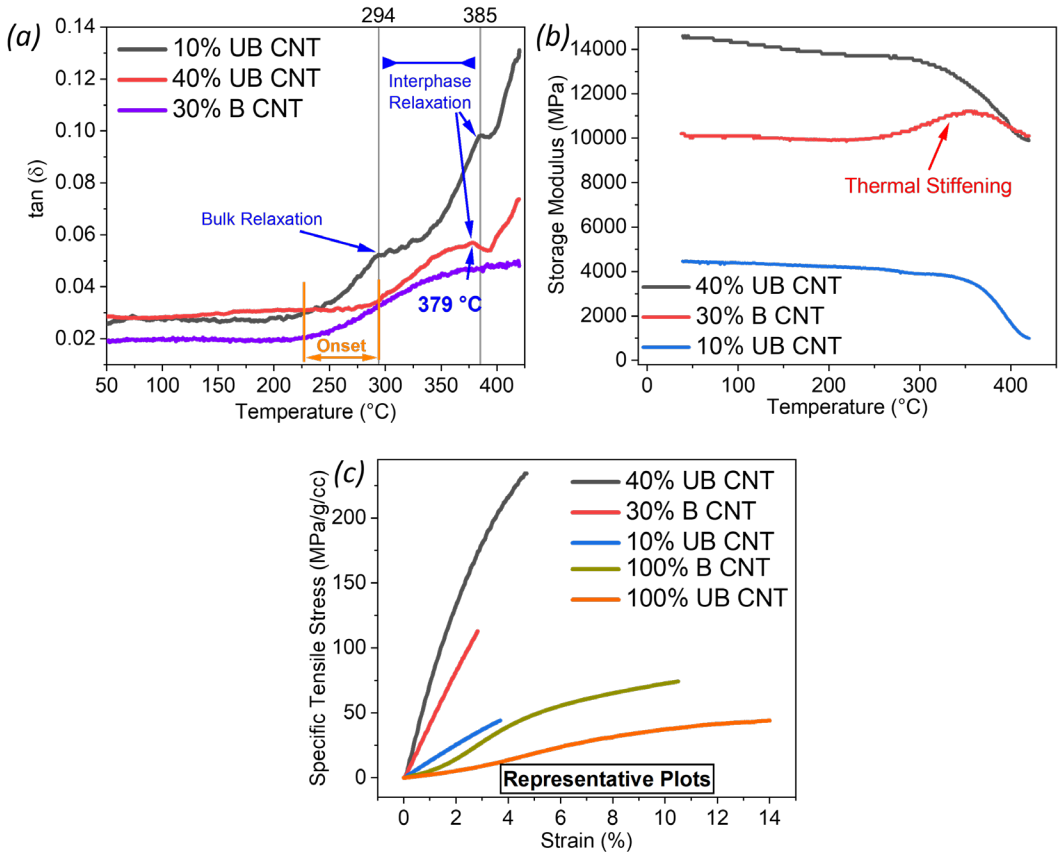

Figure 4.4. (a) tan δ and (b) storage modulus plots of nanocomposites of BMI containing 10,30 and 40 wt% CNT UB, CNT B and CNT UB, respectively. (a) The 10 wt% UB – 90 wt% BMI demonstrates, two unique tan δ peaks at 294 and 385 °C signifying the presence of at least two different BMI phases (bulk and interphase). The 40 wt% UB – 60 wt% BMI demonstrates a single distinct tan δ peak at 379 °C, signifying the absence of the bulk BMI phase. The 30 wt% UB – 70 wt% BMI, does not demonstrate a tan δ peak associated with bulk BMI relaxation. (b) The 30 wt% UB – 70 wt% BMI demonstrates thermal stiffening in the rubbery region whereas the 10 and 40 wt% UB CNT containing nanocomposites of BMI, do not show a stiffening behavior. (c) Representative specific tensile stress- strain curves of the 100% UB and B CNTs, and their nanocomposites with BMI.

4.2.4 *BMI Curing Induced CNT Compression in the Nanocomposites*

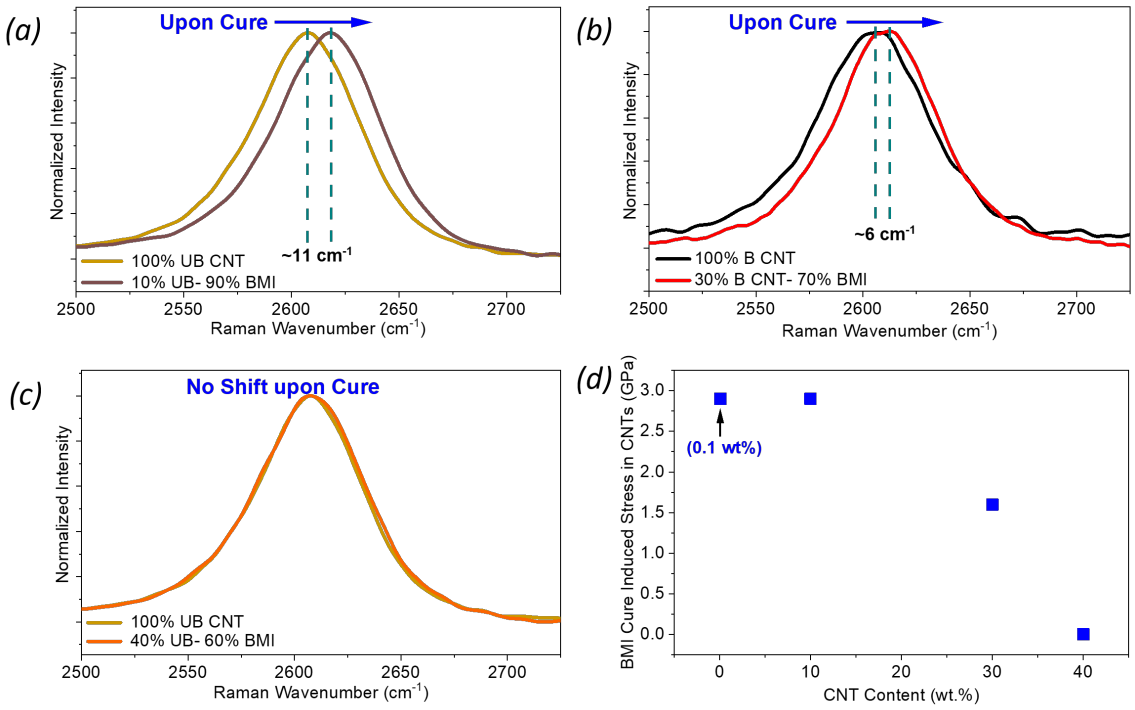

Figure 4.5. Raman G' band of (a) 100% UB CNT and 10 wt% UB – 90 wt% BMI, (b) 100% B CNT and 30 wt% B – 70 wt% BMI and (c) 100% UB CNT and 40 wt% UB – 60 wt% BMI. Raman G' band upshifts by (a) 11 cm^{-1} upon the cure of BMI in 10 wt% UB – 90 wt% BMI, signifying a compressive stress of 2.9 GPa. (b) 6 cm^{-1} upon the cure of BMI in 30 wt% B – 70 wt% BMI, signifying a compressive stress of 1.6 GPa. (c) The 40 wt% UB – 60 wt% BMI doesn't demonstrate a Raman shift upon cure of the BMI in the nanocomposite. (d) Compressive stress in the CNTs within CNT-BMI nanocomposites containing 0.1,[232] 10, 30 and 40 wt% CNTs.

Next we explored the effect of the cure of BMI on the CNTs within the nanocomposite. Raman spectroscopy has been used in prior studies for evaluating the tensile[219], [220] or compressive stress[221], [232] on the CNTs in the nanocomposites. In our prior[232] work, CNTs were radially and axially compressed upon the cure of BMI in the nanocomposites containing 0.1 wt% pristine or functionalized CNTs. The Raman G' band of the pristine CNTs upshifted by 11 cm^{-1}, upon the cure of BMI, and this Raman upshift is estimated to be a result of a compressive stress of 2.9 GPa.[99] The CNTs in the

nanocomposite could be compressed either physically[221] upon the cure of BMI or through electron charge transfer between the CNTs and the BMI, during cure.[21], [222], [223] Here, we use Raman spectroscopy to investigate if the BMI cure induced stresses in the CNTs change as the CNT content in the nanocomposites is varied. The Raman G' band upshifted by 11 cm^{-1} in the 10 wt% UB – 90 wt% BMI, compared to the UB CNT ((Figure 4.5 a) and 6 cm^{-1} in the 30 wt% B – 70 wt% BMI, compared to the B CNT ((Figure 4.5 b). The Raman G' upshifts of 11 and 6 cm^{-1} correspond to a compressive stress of 2.9 and 1.6 GPa in the CNTs, respectively ((Figure 4.5 d). The 40 wt% UB – 60 wt% BMI however, did not demonstrate any shift in the Raman G' peak position compared to the UB CNT (Figure 4.5c), signifying an absence of the BMI cure induced stresses in the 40 wt% UB – 60 wt% BMI ((Figure 4.5d).

The compression of CNTs could result from: (a) physical compression of BMI upon cure or (b) electron donor-acceptor complex formation between the BMI and the CNTs. In either scenarios, the compression of CNTs would be both, in the axial and radial directions. From the perspective of physical compression of the CNTs upon the cure of BMI: the reduction in the compressive stress of the CNTs within the nanocomposite, with increasing CNT content signifies that the ability of the BMI to physically compress the CNTs reduces as the thickness of the BMI layer between the CNTs. BMI thickness between two CNTs is ~21, 8 and 6 nm for the 10, 30 and 40 wt% CNT nanocomposites, respectively. From the perspective of the CNT compression through the electron donor-acceptor complex formation, upon the cure of BMI: as the CNT loading in the nanocomposite increases, the total amount of electrons available to be withdrawn from the CNTs increases, but since the BMI loading decreases, the overall demand for the electron withdrawal by the BMI

decreases. Thus, there is an overall higher availability and lesser demand for electron withdrawal, limiting the electron acceptor-donor complex formation. The cure of the 40 wt% UB – 60 wt% BMI thus, does not involve enough electron exchange for the UB CNTs to get compressed.

4.2.5 Comparing Molecular Architectures using SAXS

SAXS has been used in other studies to calculate the domain size associated with the molecular heterogeneity of the BMI[20] or CNT-BMI composites,[227], [232] inter-CNT distance[228] and CNT bundle size.[228] In our other work,[227] assuming Bragg's diffraction, SAXS peak corresponding to Bragg's d-spacing of 10.6, 5.4 and 4 nm was observed in Melt BMI (BMI that did not undergo any mixing prior to curing). BMI that was processed through a probe sonication method (termed PS BMI) demonstrated SAXS peak corresponding to Bragg's d-spacing of 24 and 4 nm.[8] CNT-BMI nanocomposites containing 0.1 wt% pristine or functionalized CNTs (CNT_A) and processed through a shear mixing route (termed HSSM) demonstrated SAXS peaks corresponding to Bragg's d-spacing of ~31.3, 21.3 and 4.1 nm.[8] CNT-BMI nanocomposites containing 0.1 wt% pristine CNT (CNT_B) and processed through a probe sonication route demonstrated SAXS peaks corresponding to Bragg's d-spacing of ~25 and 4.3 nm.[8] While a SAXS peak corresponding to a d-spacing of ~4 nm has been observed in Melt BMI, PS BMI and PS or HSSM processed, CNT-BMI nanocomposites containing 0.1 wt% pristine or functionalized CNTs, this peak was absent in HSSM- BMI,[20] which demonstrated ~4x enhancement in the impact strength compared to Melt BMI, owing to the molecular rearrangement of the BMI components.[20]

Herein, we have analyzed the SAXS peaks assuming Bragg's diffraction. While the SAXS peaks could also result from scattering, irrespective of how the SAXS profile are analyzed, any differences in the SAXS peak positions still signify a different molecular architecture. The 10 wt% UB – 90 wt% BMI demonstrates SAXS peaks at q values of 0.019, 0.03 and 0.15 A^{-1} which correspond to the Bragg's d-spacing of 32.8, 20.7 and 4.2 nm (Figure 4.6). The 30 wt% B – 70 wt% BMI demonstrates SAXS peaks at q values of 0.02 (d~ 31.3 nm), 0.038 (d~ 16.2 nm), 0.064 (d~ 9.7 nm) and 0.128 A^{-1} (d~ 4.9 nm), while the 40 wt% UB – 60 wt% BMI demonstrates SAXS peaks at q values of 0.026 (d~ 32.8 nm) and 0.052 A^{-1} (d~ 12 nm) (Figure 4.6). The differences in the SAXS profiles, including the peak positions, of the 10, 30 and 40 wt% CNT containing composites of BMI signify a that each of these nanocomposites have a different molecular architecture compared to each other.

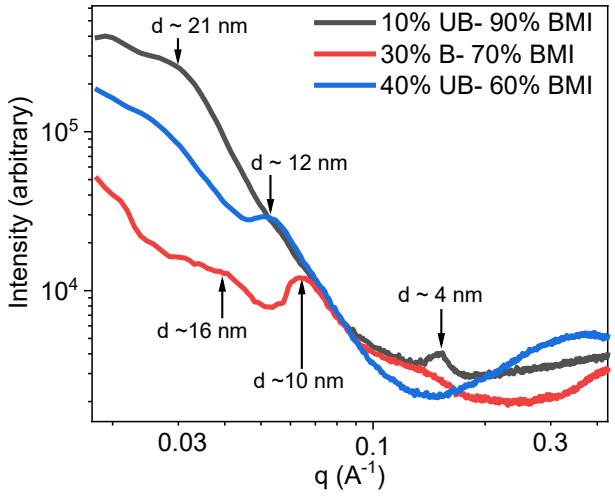

Figure 4.6. SAXS of the 10 wt% UB – 90 wt% BMI, 30 wt% B – 70 wt% BMI and 40 wt% UB – 60 wt% BMI. The scattering profile show that the molecular architecture of each nanocomposite is different from the other. The SAXS peaks have been analyzed assuming Bragg's diffraction and the d-spacing corresponding to the peaks have been listed in the plot. While the SAXS peaks could also result from scattering, any differences in the SAXS peak positions would still signify a different molecular architecture, irrespective of how they are analyzed.

4.2.6 XRD Analysis

In the work discussed in Chapter 6 using UB and B CNTs [219], the B CNT and its nanocomposite with polyurea demonstrated two additional x-ray diffraction (XRD) peaks at ~30 and 35.5 °2θ which were not observed in the UB CNT and its nanocomposite with polyurea. The x-ray photoelectron spectroscopy (XPS) results signified an absence of any 'foreign particle', i.e., a catalyst or an impurity in the B CNTs, to which the additional XRD peaks could be assigned to.[219] The Raman I_D/ I_G of the B CNT was ~2x that of the UB CNT, signifying that the baking treatment created defects in the CNTs.[219] Herein, we observe that the XRD peaks ~30 and 35.5 °2θ are significantly stronger in intensity for the 30 wt% B CNT- 70 wt% BMI, compared to the 100 wt% B CNT (Figure 4.7). The crystal size corresponding to the ~30 °2θ increased by ~77% compared to the 100 wt% B CNT (from 11.1 to 19.6 nm) and by ~100% for the peak corresponding to the 35.5 °2θ (from 9.1 to 18.1 nm), respectively in the 30 wt% B CNT- 70 wt% BMI, compared to the 100 wt% B CNT. The increased crystal size in the B CNTs upon the cure of BMI signifies that the defects created upon the baking treatment are chemically active[219] and participate in the cure reaction with the BMI. The unique characteristics of the 'active defects' in the B CNTs are potentially another major factor that could alter the cure reactions of the BMI and consequently the mechanical properties of the composites. The BMI containing nanocomposite of UB and B sheets also demonstrated XRD peaks at ~17, 25.6, 43 and 44 °2θ, associated with the amorphous BMI, CNT (002), CNT (100) and CNT (101), respectively.

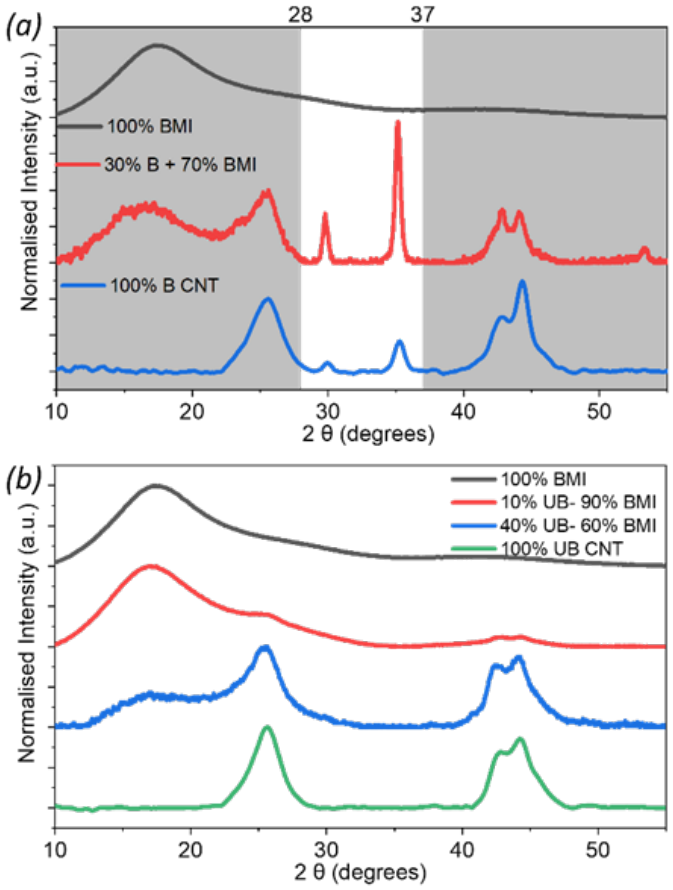

Figure 4.7. XRD spectra of (a) 100 wt% BMI, 100 wt% B CNT and 30 wt% B – 70 wt% BMI. (b) 100 wt% BMI, 100 wt% UB CNT, 10 wt% UB – 90 wt% BMI and 40 wt% UB- 40 wt% BMI. (a) The B CNT and its nanocomposite with BMI demonstrate two additional x-ray diffraction (XRD) peaks at ~30 and 35.5 °2θ which are not observed in the UB sheet and its nanocomposites with BMI.

4.3 Experimental

4.3.1 Materials

The UB and B CNT sheets were provided by Nanocomp Technologies, Inc. (Merrimack, NH). The manufacturer reported that the length of individual CNTs is 1−10 mm.[54] More details on the UB and B CNT sheets are reported in our prior work.[219]

Cycom 5250-4 RTM from Solvay is the multi- component Bismaleimide system used in this study. THF (99.9%) was purchased from Sigma-Aldrich.

4.3.2 Nanocomposite preparation:

BMI was mixed with THF at ambient temperature through a dual asymmetric centrifugal high-speed shear mixing using a DAC 150.1 from Flacktec Inc. for 5 min, to prepare a 45 mg/dl solution of BMI. CNT sheets were soaked in appropriate amount of BMI-THF solution and then dried under ambient temperature and pressure for 48 h. The dried CNT-BMI sheets were then cured at 191 °C for 4 h and post- cured at 227 °C for 2 h with no external pressure applied.

DSC was conducted on a TA Q100. The activation energies have been calculated using Kissinger and Ozawa methods, as described in a prior work.[24] DMA was conducted on a TA Instruments DMA Q800 at a frequency of 1 Hz and 0.01% strain over the 35–350 °C. The gauge length and the width of the specimen used for DMA was 10 and 2 mm, respectively. Tensile tests were conducted on a TA Instruments DMA Q800 where the gauge length and the width of the specimen was 10 and 2 mm, respectively. Raman spectra were collected using a HORIBA XploRA ONE (λ = 785 nm) as described in a prior work.[219] XRD was conducted on Rigaku MicroMax-002 beam generator (Cu Kα λ= 0.1542 nm, operating voltage and current 50 kV and 0.60 mA, respectively) equipped with R-axis IV++ detector. SAXS was conducted on Panalytical Empyrean (Cu Kα λ= 0.1542 nm, operating voltage and current 40 kV and 0.40 mA, respectively). SEM was conducted on a Hitachi SU8230, at an accelerating voltage of 0.5 kV.

4.4 Conclusion

The CNTs alter the cure of the BMI and the cure of BMI can compress the CNTs. 10 wt% UB – 90 wt% BMI demonstrated up to 123 °C lower cure temperature while the 40 wt% UB – 60 wt% BMI and the 30 wt% B CNT – 70 wt% BMI demonstrated up to 18 and 27 °C lower cure temperature, compared to the 100% BMI. The CNTs in the 10 wt% UB – 90 wt% BMI and 30 wt% B CNT – 70 wt% BMI compressed upon the cure of BMI, while the CNTs in the 40 wt% UB – 60 wt% BMI did not compress. Raman G' band upshift of 11 and 6 cm^{-1} was observed in the 10 and 30 wt% CNT UB and B containing nanocomposites, compared to the UB CNT and B CNT, respectively, signifying a cure induced compressive stress of 2.9 and 1.6 GPa, respectively. We think that the stored compressive stress of the CNTs in the nanocomposites could be harnessed for additional gains in the overall tensile strength of the composite. For example, if a CNT- polymer nanocomposite containing CNTs with no compression and has a tensile strength of 't' GPa, then a similar CNT-polymer nanocomposite, but containing CNTs with a compressive stress of 'c' GPa, should have a tensile strength of 'c+t' GPa (assuming that the CNT strength is the limiting factor of the overall nanocomposite strength). Such a strategy could be considered for systems that need to be designed for tensile loading.

The CNT content and CNT type significantly altered their thermomechanical properties of the nanocomposites. The 10 wt% UB – 90 wt% BMI demonstrated, two unique tan δ peaks at 294 and 385 °C signifying the presence of at least two different BMI phases (bulk and interphase) while the 40 wt% UB – 60 wt% BMI demonstrated a single distinct tan δ peak at 379 °C, signifying an absence of the bulk BMI phase. An ideal CNT-BMI model has been used to quantitatively understand The effect of the varying CNT

content on the inter-CNT spacing and consequently the cure reactions of the BMI, compression of CNTs and the thermomechanical properties of the nanocomposites. Based on the thermomechanical properties and the ideal CNT-BMI model, the interphase thickness in the 30 wt% B CNT – 70 wt% BMI and the 40 wt% UB – 60 wt% BMI is estimated to be at least 5.3 and 4 nm, respectively. The SAXS results further corroborate that the 10 wt% UB – 90 wt% BMI, 30 wt% B – 70 wt% BMI and the 40 wt% UB – 60 wt% BMI CNT, all have different molecular architectures compared to each other. This study provides an understanding of the effects of the CNTs on the cure of BMI as well as the effects of the cure of BMI on the CNTs. Since the cure temperature of the CNT-BMI nanocomposite can affect its mechanical properties, going forward, optimizing the cure temperature for a CNT-BMI nanocomposite should result in further improvement in the mechanical properties of the CNT-BMI nanocomposites.

CHAPTER 5. SIZING AND CNT-BMI NANOCOMPOSITES WITH SIZING COATED CNTS

5.1 Introduction

The next generation of composite materials, for example those required for human travel to Mars and beyond, call for a factor of 2 to 3 improvement in the mechanical properties of the composites compared to the current SOA CFRPs [3]. Carbon nanotube (CNT) based polymer nanocomposites have the potential to be the next generation, SOA composite materials [4], [84], [100], [219]. The mechanical property potential of the CNT-polymer nanocomposites has been realized to some extent in selected CNT-polymer systems. For example, the tensile strength and modulus of up to 6.5 [100] and 350 GPa [84] has been achieved in CNT- Bismaleimide (BMI) nanocomposites while interfacial stress between the CNTs and polyurea of up to 10 GPa [219] has been inferred. However, the CNTs in the nanocomposites are yet to reach their full potential [4], [5], [10], [113]. One of the key factors limiting the mechanical performance of the CNT-polymer nanocomposites is the load transfer at the CNT-polymer interface [5], [10], [113]. Several approaches have been undertaken to tailor the CNT-polymer interface-interphase including CNT modification through: (a) acid [11], [12], [100], [232], ozone [233], plasma [234]. and thermal [219], [226] treatment. (b) Coating the CNTs with a polymer [235], [236] including, ordered wrapping of polymer around the CNTs [237], [238].

With the recent advancement in the large scale production and availability of CNT macro-assemblies [54], [239] such as CNT yarns [239], [240], tapes and sheets [54], CNT-polymer composites could now be prepared through conventional CFRP manufacturing

techniques including filament winding, pultrusion and continuous lamination. Kim *et. al.* [241] used CNT yarns to prepare composite overwrapped pressure vessel using a filament winder originally designed for winding conventional carbon, glass and Kevlar fibers. Up to 209% increase in the hoop tensile properties was reported in the CNT/yarn-polymer composite overwrapped aluminium rings compared to the bare aluminum rings, owing to the interfacial adhesion between the CNT yarn and the polymer matrix [241]. We ask, could we add another critical step of the conventional CFRP manufacturing, 'sizing', to the CNT-polymer composite preparation to tailor the CNT-polymer interface-interphase? To be able to answer that question, we need to understand the sizing-CNT interactions and reactions.

Herein, we first study the effects that (a) CNTs, (b) the degree of functionalization and defects (DOFD) in the CNTs and (c) the sizing content, have on the sizing cure reaction and cure kinetics. To this end we use three different types of CNTs: p-CNT_A, f-CNT_A and f-CNT_B, with different DOFD (Table 5.1) to prepare sizing coated CNT films. The DOFD of the CNTs has been characterized using XPS (Figure D 1 a-c), Raman Spectroscopy (Figure S1 d) and TGA (Figure D 1 e and f). The p-CNT_A has the lowest DOFD while the f-CNT_A has the highest DOFD (Table 5.1, Figure D 1). We then use sizing coated f-CNT_A to prepare composites with a high performance aerospace grade BMI. Three different CNT-BMI interface-interphase have been created using: p-CNT_A, f-CNT_A and sized f-CNT_A. The effect of the different interface- interphase on the BMI cure reaction in the composites containing 60 wt% CNTs has been studied. Furthermore, the effect of the different CNT-BMI interface-interphase on the thermomechanical properties and the structural heterogeneity of the nanocomposites has been discussed.

Table 5.1. The three different CNTs used in this study and their degree of functionalization and defects (DOFD) based on the Raman I_D/I_G, weight loss associated with the functional groups attached on the CNTs and the carbon, oxygen atomic percentage.

CNT Type	Raman I_D/I_G Ratio	Weight loss at 500 °C (TGA)	Atomic % (XPS)	Degree of functionalization and defects (Relative, among the 3 CNTs)
p-CNT_A	0.67 ± 0.03	~2.5%	C 1s- 98% O 1s- 2%	Low
f-CNT_A	2.2 ± 0.02	~16%	C 1s- 93.25% O 1s- 6.75%	High
f-CNT_B	1.44 ± 0.03	~9%	C 1s- 94.25% O 1s- 5.75%	Medium

5.2 Results and Discussion

5.2.1 The Effects of CNT and CNT Degree of Functionalization and Defects on the Sizing Reactions

5.2.1.1 Cure reactions and Cure Kinetics using DSC

We first use DSC to understand the effect that the CNTs and the CNT DOFD have on the sizing reactions. 100 wt% sizing film (with no CNTs) demonstrated an endothermic peak at 159 °C and another broad endothermic peak in the range of 185- 255 °C (Figure 5.1). The broad endothermic peak also has significant vibration/noise in the DSC signal, signifying (a) a very fast reaction and/or (b) evolution of volatiles. The DSC scan was repeated twice and a similar thermal profile was observed each time. We also cured the

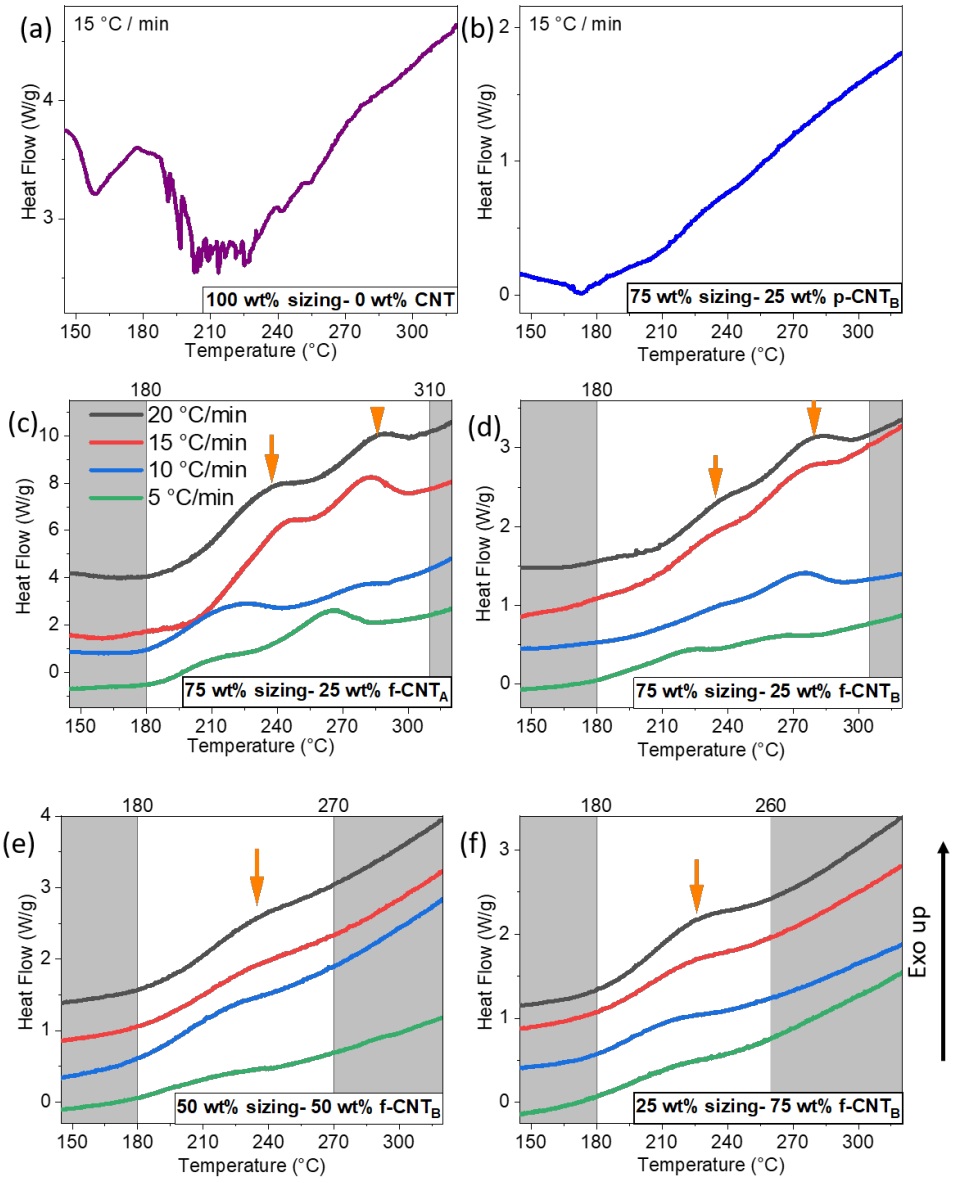

Figure 5.1. DSC of (a) 100 wt% sizing, (b) 75 wt% sizing– 25 wt% p-CNTA, (c) 75 wt% sizing– 25 wt% f-CNTA, (d) 75 wt% sizing– 25 wt% f-CNTB, (e) 50 wt% sizing– 50 wt% f-CNTB, (f) 25 wt% sizing– 75 wt% f-CNTB. (a) The 100 wt% sizing demonstrates endothermic peaks which are not observed in the (b) 75 wt% sizing– 25 wt% p-CNTA, signifying that the addition of p-CNTA alters the reactions of 100 wt% sizing. (c) The 75 wt% sizing– 25 wt% f-CNTA demonstrates two exotherms while the 75 wt% sizing– 25 wt% p-CNTA demonstrates a minor endotherm, signifying that the functionalization of CNTA alters the sizing reaction. (d) The 75 wt% sizing– 25 wt% f-CNTB also demonstrates two exotherms, however the e) 50 wt% sizing– 50 wt% f-CNTB and (f) 25 wt% sizing– 75 wt% f-CNTB demonstrates one exotherm signifying that the sizing content affects the sizing cure reaction. (c-f) The plots have been shifted along the y axis for clarity.

100 wt% sizing in an oven at 250 C for 2 min which resulted in foaming of the sizing (Figure D 2), corroborating the DSC results. The sized p-CNT_A film containing 75 wt% sizing (75 wt% sizing- 25 wt% p-CNT_A) demonstrated only a minor endothermic peak at 173 °C (Figure 5.1 b), signifying that the presence of p-CNT_A alters the sizing reaction. The sized f-CNT_A, and f-CNT_B films, containing 75 wt% f-CNTs, both demonstrated two exothermic peaks and no endothermic peaks (Figure 5.1c and d), signifying that: (a) the functionalization of CNTs further affects the sizing reaction and (b) sizing reacts with the functional groups present on the f-CNTs. For the 75 wt% sizing – 25 wt% f-CNT_A, the first exothermic peak, referred as reaction 1, is observed in the range of 210- 242 °C (depending on the heating rate of DSC), while the second exothermic peak, referred as reaction 2, is observed in the range of 265- 286 °C (Figure 5.1c). For the 75 wt% sizing– 25 wt% f-CNT_B, the reaction 1 and 2 occur in the range of 222- 236 °C and 258- 276 °C, respectively (Figure 5.1d). The sized f-CNT_B films containing 50 and 25 wt% f-CNT_B, both demonstrated only one exothermic peak (Figure 5.1e and f), signifying that the sizing content in the f-CNT_B containing films, affects the sizing cure reaction as well. For the 50 wt% sizing– 50 wt% f-CNT_B, the reaction occurs between 213-235 °C, while for the 25 wt% sizing– 75 wt% f-CNT_B, the reaction occurs between 204- 225 °C. None of the CNT containing sizing films demonstrated any visible pores/ foam as was the case with 100% sizing film.

The cure activation energy (E_a) of the sized- f-CNT specimens was evaluated through the Kissinger [177] ($E_{a\text{-}K}$) and Ozawa [178] ($E_{a\text{-}O}$) methods and the $E_{a\text{-}K}$ and $E_{a\text{-}O}$ are listed in Table 5.2. The $E_{a\text{-}K}$ of the reaction 1 in 75 wt% sizing– 25 wt% f-CNT_A is only 40% of the $E_{a\text{-}K}$ of the reaction 1 in 75 wt% sizing– 25 wt% f-CNT_B (81 and 204 kJ/mol, respectively).

The $E_{a\text{-}K}$ of the reaction 2 in 75 wt% sizing– 25 wt% f-CNT_A is 87% of the $E_{a\text{-}K}$ of the reaction 2 in the 75 wt% sizing– 25 wt% f-CNT_B (154 and 178 kJ/mol, respectively). The lower E_a and their extent of reduction for the reaction 1 and 2 in the 75 wt% f-CNT_A – 25 wt% BMI compared to the 75 wt% f-CNT_B – 25 wt% BMI, signifies that: (a) Since the f-CNT_A has a higher DOFD compared to the f-CNT_B, there are more functional sites on the f-CNT_A available to react with the sizing which consequently reduces the cure activation energy of the sizing. (b) Reaction 1 is influenced more by the DOFD of the f-CNTs compared to the reaction 2. The $E_{a\text{-}K}$ of the single reaction in 50 wt% sizing– 50 wt% f-CNT_B and 25 wt% sizing–75 wt% f-CNT_B, was 122 and 121 kJ/mol, respectively. The $E_{a\text{-}O}$ values are similar to the $E_{a\text{-}K}$ values and are listed in Table 5.3. The comparable E_a of the 50 and 25 wt% sized- f-CNT_B signify that for both sized specimens, there are more functional sites available on the f-CNT_B than what the sizing can react with. The same does not hold for the 75 wt% sizing– 25 wt% f-CNT_B which has ~82% higher $E_{a\text{-}K}$ compared to the 50 wt% sized f-CNT_B, owing to an overall higher amount of reactants on the sizing and an overall lower reaction sites available at the f-CNT_B due to the higher sizing and lower f-CNT_B content.

Table 5.2. The cure activation energy (E_a) of the sized- f-CNT specimens calculated using Kissinger and Ozawa methods.

Sample	Reaction	Activation Energy : Kissinger Method (E_{a-K}) kJ/mol	Activation Energy : Ozawa Method (E_{a-O}) kJ/mol
75 wt% sizing- 25 wt% f-CNT_A	1	81	85
	2	154	155
75 wt% sizing- 25 wt% f-CNT_B	1	204	202
	2	178	178
50 wt% sizing- 50 wt% f-CNT_B	1	122	123
	2	N/A	N/A
25 wt% sizing- 75 wt% f-CNT_B	1	121	123
	2	N/A	N/A

5.2.1.2 Analysis of the Elemental Composition using XPS

To further understand the differences in the reactions of the 100 wt% sizing, 75 wt% sizing- 25 wt% p-CNT_A and the 75 wt% sizing- 25 wt% f-CNT_A and f-CNT_B films, XPS was employed to evaluate the elemental compositions of these films (Figure D 1 a-c and Figure D 2). The penetration depth of the x-rays in the XPS is 5- 10 nm and the spot size was 400 μm. The atomic percentages of the Si 2s and 2p in these films, are listed in Table 5.3. We first evaluate the effect of curing of the sizing on the Si 2s and 2p atomic content. The atomic percentage of the Si 2s and 2p in the uncured, 100% sizing film was 2.4 and 2.3%, respectively which reduced by ~50%, to 1.2 and 1.2%, respectively upon curing the sizing. This loss of silane groups is likely associated with the boiling of the silane coupling agent in the sizing. 3-aminopropyl triethoxysilane (3APTES), one of the silane based coupling agent, for example has a boiling point of ~215 °C.[242] The DSC results of the 100 wt% sizing, which demonstrated a broad endothermic peak in the range of 185- 255 °C (Figure 5.1 a), with significant noise corroborates the inference of silane being boiled

upon the curing of 100 wt% sizing. The atomic percentage of the uncured Si 2s and 2p in the 75 wt% sizing- 25 wt% f-CNT_A was 1.8 and 1.8%, respectively, in the 75 wt% sizing- 25 wt% f-CNT_B it was 1.7 and 1.65%, respectively and 0.42 and 0.66%, respectively, in the 75 wt% sizing- 25 wt% p-CNT_A. This signifies that the boiling of silane is directly related with the DOFD of the CNTs, where a higher level of silane is retained with higher DOFD of the CNTs. The DSC results of the sized f-CNT films demonstrating exothermic reactions and the XPS showing retention of silane groups, together signify that the silane groups in the sizing reacts with the functional groups of the CNTs.

Table 5.3. The atomic percentage of Si 2s and 2p in the uncured and cured sizing and the sized p-CNT_A, f-CNT_A and f-CNT_B films containing 75 wt% sizing.

Sample	Si Content (Atomic %)	
	Si 2s	Si 2p
100 wt% uncured sizing (no CNTs)	2.4	2.3
100 wt% cured sizing (no CNTs)	1.2	1.2
75 wt% sizing- 25 wt% p-CNT_A	0.4	0.7
75 wt% sizing- 25 wt% f-CNT_A	1.8	1.8
75 wt% sizing- 25 wt% f-CNT_B	1.7	1.7

5.2.2 SEM Analysis of Sized-CNT Films

The effect of the sizing content in the f-CNT_B films, on the tensile failure mode has been evaluated. SEM of the tensile fractured surfaces of the f-CNT_B films containing no sizing demonstrated maximum f-CNT_B pullouts among all the samples, while the extent of f-CNT_B pullout decreased with increasing sizing and decreasing f-CNT_B content (Figure 5.2 a-d). Decreasing f-CNT_B pullout signifies decreasing f-CNT_A slippage and a transition

from ductile to brittle fracture. The 50 wt% sizing– 50 wt% f-CNT_B demonstrates a horizontally stacked, layered structure across the thickness of the film. The SEM of the surface of the 50 wt% sizing– 50 wt% f-CNT_B film demonstrates that sizing coats and interconnects the f-CNT_B, signifying favorable interactions between the sizing and the f-CNT_B (Figure 5.3 a-c). The SEM of the 100 wt% f-CNT_B that do not contain any sizing are illustrated in Figure 5.3 d,e.

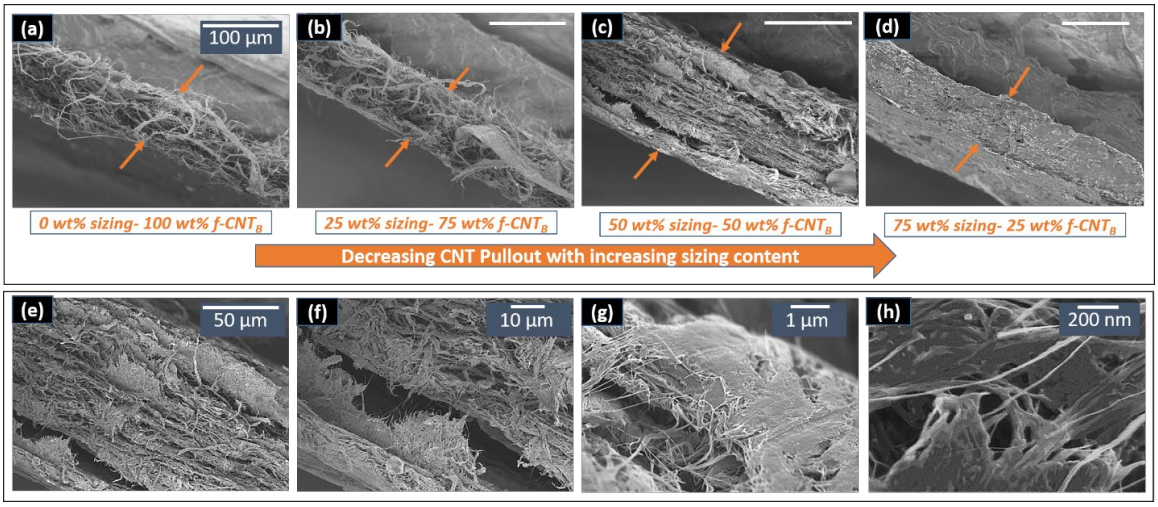

Figure 5.2. SEM images of the tensile fractured surfaces of (a) f-CNT_B, (b) 25 wt% sizing– 75 wt% f-CNT_B, (c) 50 wt% sizing– 50 wt% f-CNT_B, (d) 75 wt% sizing– 25 wt% f-CNT_B, (e-f) higher magnification images of 50 wt% sizing– 50 wt% f-CNT_B. (a) The f-CNT_B demonstrates the maximum CNT pullouts, which decreases with increasing sizing content in the f-CNT_B films. Decreasing f-CNT_B pullout signifies lower f-CNT_A slippage and a transition from ductile to brittle fracture.

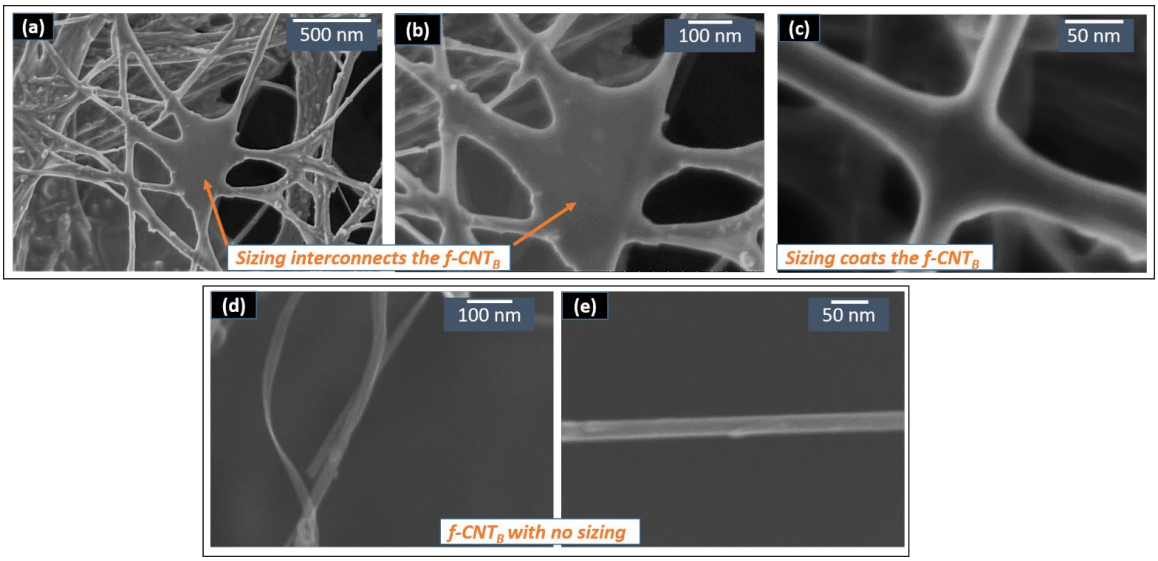

Figure 5.3. (a-e) SEM images of the surface of the (a-c) 50 wt% sizing– 50 wt% f-CNT$_B$. Sizing interconnects and coats the f-CNT$_B$. (d and e) 100 wt% f-CNT$_B$.

5.2.3 Three different CNT-BMI Interface-Interphase

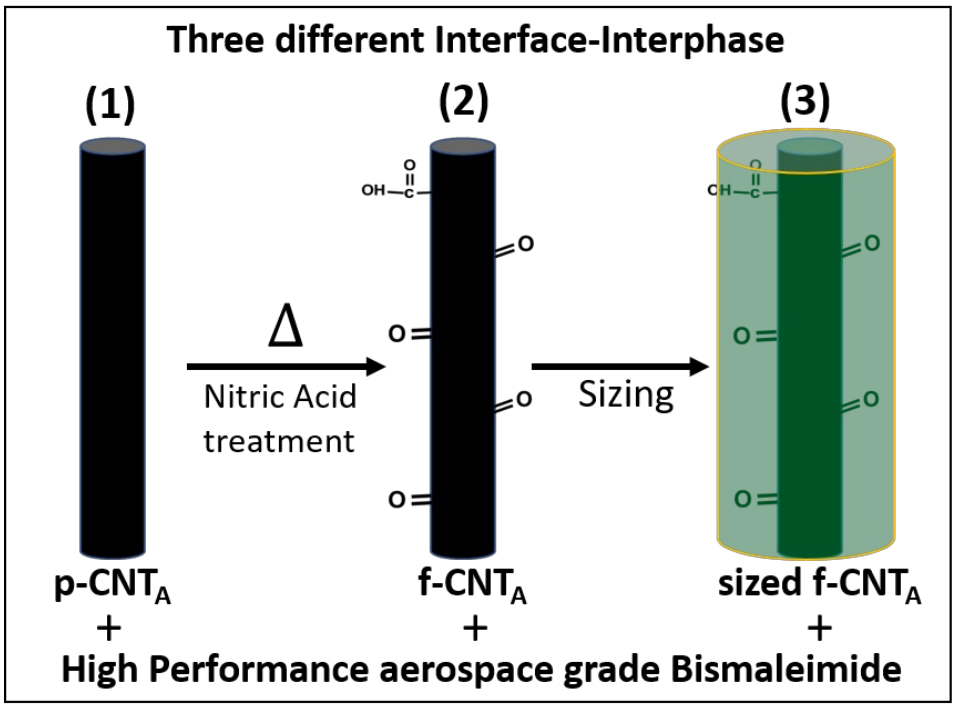

Figure 5.4. Three different BMI-CNT interface-interphase: p-CNT$_A$- BMI, f-CNT$_A$- BMI, and sized f-CNT$_A$- BMI.

Next we evaluate the effect of three different BMI-CNT interface-interphase: p-CNT_A- BMI, f-CNT_A- BMI, and sized f-CNT_A- BMI on the BMI cure reaction in the composites containing 60 wt% CNTs. The 100 wt% BMI, 60 wt% p-CNT_A – 40 wt% BMI and the 60 wt% f-CNT_A – 40 wt% BMI demonstrated one exothermic peak in the range of 235- 276, 216-247 and 206-241 °C, respectively (Figure 5.5 a-c). The 60 wt% f-CNT_A – 7 wt% sizing- 33 wt% BMI demonstrated three exothermic peaks (Figure 5.5 d), signifying that the sizing altered the BMI cure reaction. The first peak (termed reaction 1) is observed in the range of 213- 226 °C, the second peak (termed reaction 2) is in the range of 333-371 °C. The third peak (termed reaction 3) is at 371 and 390 °C, when the heating rate was 5 and 10 °C/min, respectively. The third exothermic peak of the 60 wt% f-CNT_A – 7 wt% sizing- 33 wt% BMI is not observed when the heating rate was 15 and 20 °C/min as the peak is likely at a temperature above 400 °C, which is beyond the equipment's limit. Compared to the 100 wt% BMI (with no CNTs), addition of p-CNT_A reduced the BMI cure temperature by up to 30 °C in the 60 wt% p-CNT_A – 40 wt% BMI (Figure 5.5 e) and the f-CNT_A in the 60 wt% f-CNT_A – 40 wt% BMI reduced the BMI cure temperature by up to 36 °C (Figure 5.5 f). While the reaction 1 in the 60 wt% f-CNT_A – 7 wt% sizing- 33 wt% BMI occurs at up to 50 °C lower temperature compared to the 100 wt% BMI cure reaction, the reaction 2 reactions however, occur at at least 90 °C higher temperature compared to the 100% BMI cure reaction (Figure 5.5 g). Compared to the 60 wt% f-CNT_A – 40 wt%, the reaction 2 in the 60 wt% f-CNT_A – 7 wt% sizing- 33 wt% occur at, at least 126 °C higher cure temperature compared to 100 wt% BMI.

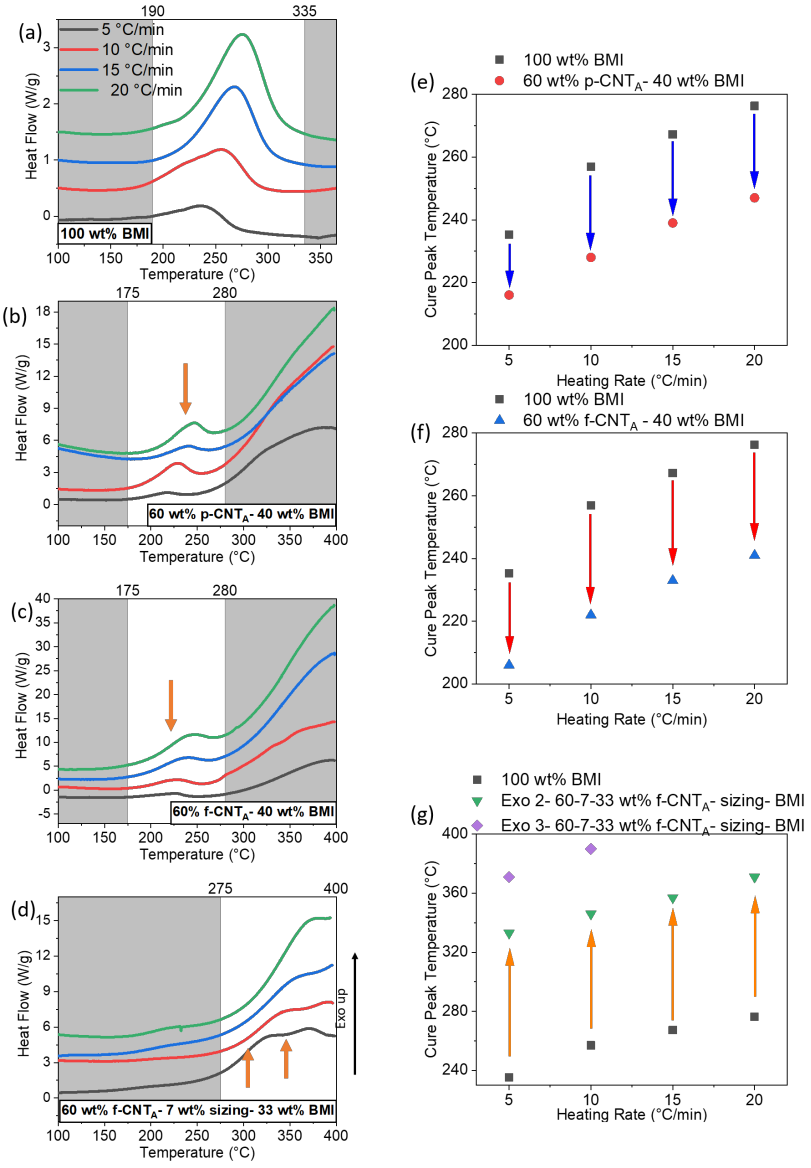

Figure 5.5. (a-d) DSC cure profile for (a) 100 wt% BMI, (b) 60 wt% p-CNT$_A$ – 40 wt% BMI, (c) 60 wt% f-CNT$_A$ – 40 wt% BMI, (d) 60 wt% f-CNT$_A$ – 7 wt% sizing- 33 wt% BMI. (e-g) Peak cure temperature comparison of (e) 60 wt% p-CNT$_A$ – 40 wt% BMI, (f) 60 wt% p-CNT$_A$ – 40 wt% BMI and (g) 60 wt% p-CNT$_A$ – 40 wt% BMI, with the 100 wt% BMI at heating rates of 5- 20 °C. The (a) 100 wt% BMI, (b) 60 wt% p-CNT$_A$ – 40 wt% BMI and (c) 60 wt% f-CNT$_A$ – 40 wt% BMI demonstrate a single exothermic peak while the (d) 60 wt% f-CNT$_A$ – 7 wt% sizing- 33 wt% BMI demonstrate three exothermic peaks. (e) The 60 wt% p-CNT$_A$ – 40 wt% BMI has up to 30 °C lower cure temperature compared to the 100% BMI, while the (f) 60 wt% f-CNT$_A$ – 40 wt% BMI has up to 36 °C lower cure temperature compared to the 100% BMI. (g) The major cure reaction in the 60 wt% f-CNT$_A$ – 7 wt sizing- 33 wt% BMI has at at least 90 °C higher temperature compared to p-BMI. (a-d) The plots have been shifted along the y axis for clarity.

5.2.3.1 Effect of CNT-BMI Interface-Interphase on the BMI cure reactions

In another work [226] on CNT-BMI nanocomposites containing up to 40 wt% CNT sheets, the nanocomposites of BMI containing 40 wt% unbaked CNT sheet demonstrated up to 18 °C lower cure temperature for the BMI, compared to the 100 wt% BMI. The nanocomposites of BMI containing 10 wt% unbaked CNT sheet demonstrated two exothermic peaks and the BMI cure temperature reduced by up to 123 °C, compared to the 100 wt% BMI. The change in the BMI cure reactions and/or their temperature was attributed to the preferential stacking of the different BMI components around the CNTs [226]. Liu et. al. [122] doped the sizing with luminescent nanoparticles (LN) to evaluate the interfacial thickness through fluorescence microscopy. The LN doped sizing was applied to prepare monofilament, sized carbon fiber- epoxy nanocomposite. A 155 nm sizing layer was applied on the carbon fiber, however, the luminescent particles were seen up to 1.2 μm apart from the carbon fiber surface, signifying that the sizing inter-diffused in the epoxy. Herein, the BMI contains multiple components[162] and undergoes complex cure reactions. The arrangement of the BMI components affects the cure reactions.[24] The reduced cure temperature of the BMI in the 60 wt% p-CNT_A – 40 wt% BMI and the 60 wt% f-CNT_A – 40 wt% BMI could thus be attributed to the altered packing of the multiple-components of the BMI around the CNTs that alters the BMI cure reactions.[226] The increased cure temperature of the major reactions in the 60 wt% f-CNT_A – 7 wt% sizing- 33 wt% BMI could be attributed to the inter-diffusion of the sizing into the BMI. The three exotherms in the 60 wt% f-CNT_A – 7 wt% sizing- 33 wt% BMI could result from sizing-sizing, sizing- BMI and BMI-BMI reactions. The different components of the BMI can have a different preference for reaction with the sizing as well.

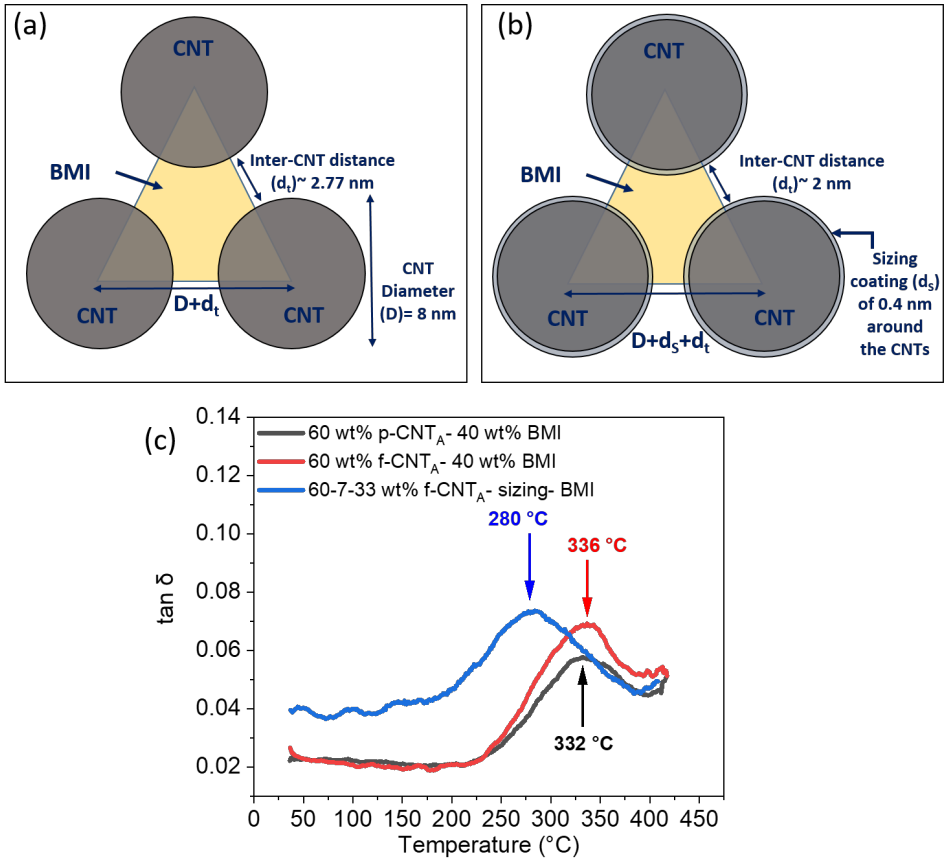

Figure 5.6. (a-b) Schematic of a unit cell for an ideal CNT-polymer arrangement in (a) 60 wt% CNT_A – 40 wt% BMI and (b) 60 wt% f-CNT_A – 7 wt% sizing- 33 wt% BMI. (c) Tan δ plots of the 60 wt% p-CNT_A – 40 wt% BMI, 60 wt% f-CNT_A – 40 wt% BMI and 60 wt% f-CNT_A – 7 wt% sizing- 33 wt% BMI demonstrating T_g of 280, 332 and 334 °C, respectively. (a) For the CNT- BMI nanocomposite containing 60 wt% CNT where the CNT diameter is 8 nm, the inter-CNT distance (d_t) is ~2.8 nm. (b) The theoretical thickness of the sizing in the 60 wt% f-CNT_A – 7 wt% sizing- 33 wt% BMI, around the CNTs is 0.4 nm and the d_t is ~2 nm.

5.2.3.2 Ideal CNT-Polymer Interaction Model

We then use an ideal polymer-CNT model [229] to quantitatively evaluate the thickness of the BMI between the CNTs in the nanocomposites with p-CNT_A, f-CNT_A and sized f-CNT_A. The model assumes that the CNTs are equally spaced from each other and that the space between them is completely filled with the BMI or the sizing and BMI

(Figure 5.6 a and b). The inter-CNT distance (d_t), i.e., the distance between the surface of the adjacent CNTs through a line connecting their centers has been calculated using equation 1, where M_{CNT} is the CNT weight fraction, ρ_{BMI} and ρ_{CNT} are the densities of BMI and CNT, respectively and D is the CNT diameter. For a D= 8 nm, the d_t for the 60 wt% p and f-CNT_A – 40 wt% BMI is 2.8 nm while for the 60 wt% f-CNT_A – 7 wt% sizing- 33 wt% BMI, it is ~2 nm. The theoretical sizing thickness, assuming a homogenous sizing coating around the CNTs in the given system is 0.4 nm (using equation 2, where $r_{CNT+Sizing}$ is the radius of the CNT+ the sizing thickness, r_{CNT} is the CNT radius, M_{Sizing} is the sizing weight fraction, ρ_{Sizing} is the sizing density). The minimum interphase thickness (I_T) for all the BMI to be present in the form of interphase can be calculate using equation 3.[226] Herein, the I_T for the 60 wt% p and f-CNT_A – 40 wt% BMI is 2.2 nm while for the 60 wt% f-CNT_A – 7 wt% sizing- 33 wt% BMI, it is 1.8 nm.

$$\frac{M_{CNT} \times \rho_{BMI}}{(M_{CNT} \times (\rho_{BMI} - \rho_{CNT})) + \rho_{CNT}} = \frac{\pi D^2}{2\sqrt{3}(d_T + D)^2} \tag{8}$$

$$\frac{r_{CNT+Sizing}^2 - r_{CNT}^2}{r_{CNT+Sizing}^2} = \frac{M_{Sizing}\rho_{CNT}}{M_{Sizing}\rho_{CNT} + (1 - M_{Sizing})\rho_{Sizing}} \tag{9}$$

$$I_T \geq ((D + d_T)/\sqrt{3}) - D/2) \tag{10}$$

5.2.3.3 Thermomechanical Properties

The tan δ plots from the dynamic mechanical analysis (DMA) can be used to evaluate the presence of multiple phases within a nanocomposite,[5], [226], [232]

given the different phases have different thermal relaxations. 100 wt% BMI has a glass transition (T_g) of 272 °C,[24] the 0.1 wt% f-CNT_B containing nanocomposites of BMI demonstrated two thermal relaxation peaks, one at 288 °C, associated with bulk BMI relaxation and another at 328 °C, associated with the BMI interphase relaxation.[232] The BMI nanocomposite containing 10 wt% unbaked CNT sheet demonstrated two thermal relaxation peaks at 294 and 385 °C, however the BMI nanocomposite containing 40 wt% unbaked CNT sheet demonstrated one thermal relaxation peak at 379 °C, signifying an absence of the bulk BMI phase.[226] Herein, the 60 wt% p-CNT_A – 40 wt% BMI and the 60 wt% f-CNT_A – 40 wt% BMI, demonstrated a single tan δ relaxation at 332 and 336 °C (Figure 5.6 c), respectively, signifying a single BMI phase. The T_g of the 60 wt% p-CNT_A – 40 wt% BMI and the 60 wt% f-CNT_A – 40 wt% BMI is 60 and 64 °C higher, respectively, compared to the 100% p-BMI.[24] The 60 wt% f-CNT_A – 7 wt% sizing- 33 wt% BMI demonstrated a single tan δ relaxation at ~280 °C, and its peak width (peak termination- peak onset temperature) is broader by ~55 °C compared to either the 60 wt% p-CNT_A – 40 wt% BMI or the 60 wt% f-CNT_A – 40 wt% BMI. The tan δ peak onset for the 60 wt% f-CNT_A – 7 wt% sizing- 33 wt% BMI is at ~171 °C, while for the 60 wt% p-CNT_A – 40 wt% BMI and the 60 wt% f-CNT_A – 40 wt% BMI, it is at ~226 °C. Sizing thus alters the thermomechanical properties of the 60 wt% f-CNT_A containing nanocomposites of BMI.

5.2.3.4 Comparing Molecular Architectures using SAXS

SAXS can be used to obtain information about the domain sizes associated with the inter CNT distance [228], CNT bundle size [228] and the molecular heterogeneity of the BMI.[24] The SAXS peak can result from structural hierarchy [228] and the domain size

associated with the peak can be determined using Bragg's law, $d = 2\pi/q$, where d is the Braggs d-spacing and q is the scattering vector. The SAXS peak can also result from heterogeneity in the electron density of the constituents [181], where for a two-phase heterogeneous system, the scattered intensity $I \propto \Delta\rho \times \varphi_\alpha \times \varphi_\beta$, $\Delta\rho$ is the difference in the density of the two phases and φ_α, φ_β are the volume fractions of the two phases. For a polystyrene- CNT nanocomposite containing 3 wt% CNTs, Fie et. al. [228] reported SAXS peak at a q value 0.0244 A^{-1}, which corresponds to Bragg's d spacing of 26 nm. The peak was assigned to the size of the CNT bundle in the nanocomposite. In our prior work [24] we observed electron density heterogeneity in BMI at the length scale of ~11 nm and the length scale of the heterogeneity increased up to ~16 nm depending on the BMI processing condition [24].

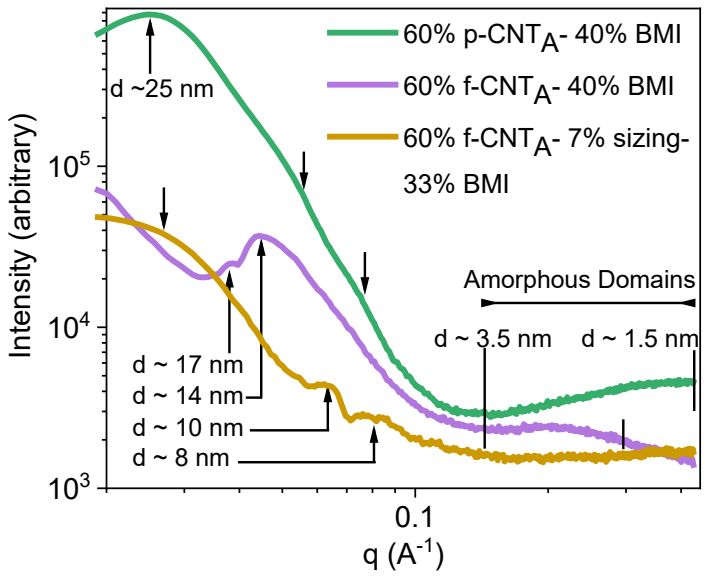

Figure 5.7. SAXS of the 60 wt% p-CNT$_A$ – 40 wt% BMI, 60 wt% f-CNT$_A$ – 40 wt% BMI and 60 wt% f-CNT$_A$ – 7 wt% sizing- 33 wt% BMI. The significant differences in the scattering profiles signify that the CNT-BMI nanocomposites made with different interface- interphase have different molecular heterogeneity and hierarchy.

Herein, we compare the SAXS from the 60 wt% p-CNT_A – 40 wt% BMI, 60 wt% f-CNT_A – 40 wt% BMI and the 60 wt% f-CNT_A – 7 wt% sizing- 33 wt% BMI (Figure 5.7). The scattering profiles show significant differences in the molecular heterogeneity within these samples (Figure 5.7). The p-CNT_A – 40 wt% BMI demonstrated a strong peak at q value of 0.024 A^{-1} (d= 25.4 nm), and lower intensity peaks at q value of 0.049 (d= 12.8 nm) and 0.075 A^{-1} (d= 8.3 nm), and a broad peak between q values of 0.14 (d= 4.4 nm) and 0.42 A^{-1} (d= 1.5 nm). The 60 wt% f-CNT_A – 40 wt% BMI demonstrated strong peaks at q values of 0.037 (d= 16.6 nm) and 0.044 A^{-1} (d= 14.1 nm). The 60 wt% f-CNT_A – 7 wt% sizing- 33 wt% BMI demonstrated peaks at q values of 0.064 (d= 9.6 nm) and 0.081 A^{-1} (d= 7.6 nm). The SAXS results demonstrate that the nanocomposites of BMI with three different interface-interphase have different molecular architectures.

5.3 Experimental

5.3.1 Materials:

Hydrosize HP 1632, a polyimide based sizing from Michelman was the sizing selected for this study. The polyimide base is to facilitate sizing reactions and compatibility with BMI. The sizing has a high thermal resistance with a degradation temperature of 578 °C (Figure S4), as determined from the peak of the TGA derivative curve and thus can be used in high temperature applications where a CNT-BMI nanocomposite may otherwise be used. The as received sizing was a water based solution with 10% solid content and a measured density (ρ_{Sizing}) of 1 g/cc. Cycom 5250-4 RTM from Solvay is the multi-component[162] BMI system used in this study. p-CNT_A and p-CNT_B are multiwalled Miralon CNTs obtained from Nanocomp Technologies, Inc. (Merrimack, NH). The

manufacturer reported that the length of the individual CNTs was 1−10 mm, for both, the p-CNT_A and p-CNT_B. The Raman I_D/I_G of the p-CNT_A and p-CNT_B was measured to be 0.67 ± 0.03 and 0.39 ± 0.02. The ρ_{BMI} and ρ_{CNT} used for calculations in equation 1 and 2 are 1.2 and 1.8 g/cc, respectively. For functionalization and wetting of CNTs, nitric acid (ACS reagent, 70%) and THF (99.9%) from Sigma-Aldrich were used, respectively.

5.3.2 Functionalization of CNTs:

5.3.2.1 f-CNT_A:

p-CNT_A were sonicated in 10 M nitric acid (40 mg/dl) for 30 min (Branson bath sonicator 3510R-MT, 100 W, 42 kHz)) . The mixture was refluxed at 120 °C (oil-bath temperature) for 12 h. The mixture was then centrifuged and washed in DI water until the pH value reached that of the DI water. The f-CNT_A were then filtered and washed with THF. For characterizing the f-CNT_A, the CNT_A wet in THF were dried overnight at room temperature followed by drying at 120 °C under vacuum (20 mbar) for 30 min. The Raman I_D/I_G of the f-CNT_A was 2.2 ± 0.02.

5.3.2.2 f-CNT_B:

p-CNT_B were used for functionalization, following a similar protocol as described above for the f-CNT_A, but the functionalization time was changed to 24 h. The Raman I_D/I_G of the f-CNT_B was 1.44 ± 0.03.

5.3.3 Sizing coated CNT films:

15 mg CNT were added to 10 ml DI water and shear mixed using a dual asymmetric centrifugal high-speed shear mixer (DAC 150.1 from Flacktec Inc.) for 5 min. The p-CNT_B were added in their dry, as-received form, while the f-CNT_A and f-CNT_B were wet in THF. Pre-determined amount of sizing dispersion (or solution) was added to the shear mixed CNT- DI water dispersion and shear mixed for 5 min. The shear mixed sizing-CNT dispersion was then placed overnight in an oven at 90 °C at atmospheric pressure to cast sizing-CNT films. The films obtained after overnight drying were further dried in an oven at 120 °C under 30 mbar vacuum. The films were then cured at 250 °C for 2 min. The 100% sizing sample were prepared by drying the sizing solution overnight in an oven at 90 °C at atmospheric pressure followed by further drying in an oven at 120 °C under 30 mbar vacuum, followed by curing at 250 °C for 2 minutes. All the DSC studies on the sizing and the sizing-CNT systems as well as the XPS of the uncured sizing were performed on uncured specimens while all other characterizations were performed on cured specimens.

5.3.4 CNT-BMI Nanocomposite film preparation:

5.3.4.1 p-CNT_A – BMI and f-CNT_A -BMI nanocomposites

A 2.25 mg/ml solution of BMI in THF was prepared through shear mixing of BMI in THF for 5 min. p-CNT_A or f-CNT_A were added to the BMI-THF solution and shear mixed for 5 min. The CNT-BMI-THF dispersion was dried overnight under ambient temperature and pressure to obtain CNT-BMI films. The films were cured in an oven at 191 °C for 4 h and post-cured at 227 °C for 2 h.

5.3.4.2 Sized f-CNT_A- BMI nanocomposite

Dried uncured sized CNTs were homogenized in a 2.25 mg/ml BMI-THF solution for 2 min at 7000 rpm. The homogenized dispersion was shear mixed for 5 min. The dispersion was then dried and the nanocomposite film cured, as stated above for the p-CNT_A-BMI and f-CNT_A -BMI nanocomposites.

XPS was conducted on a Thermo K-Alpha (Thermo Scientific) system utilizing a monochromatic Al Kα source (1486.6 eV) as described in a prior work.[243] Raman spectra were collected using a HORIBA XploRA ONE (λ = 785 nm) as described in a prior work.[219] TGA was conducted on a TA Instruments Q500 at a heating rate of 10 °C/min in air. DSC was conducted on a TA Q100. The activation energies have been calculated using Kissinger and Ozawa methods, as described in a prior work.[24] SEM was conducted on a Hitachi SU8230, at an accelerating voltage of 1 kV. SAXS was conducted on Panalytical Empyrean (Cu Kα λ= 0.1542 nm, operating voltage and current 40 kV and 0.40 mA, respectively). WAXD was conducted on Rigaku MicroMax-002 beam generator (Cu Kα λ= 0.1542 nm, operating voltage and current 50 kV and 0.60 mA, respectively) equipped with R-axis IV++ detector

5.4 Conclusion

First, the effect of the CNT and the DOFD of the CNTs on the sizing and sizing-CNT reactions have been studied. DSC and XPS analysis combined, demonstrated that the silane groups in the sizing reacts with the functional groups of the f-CNTs and when the CNTs or the functional groups on the CNTs are absent (100% sizing and 75 wt% p-CNT_A- 25 wt% sizing), the silane coupling agent in the sizing boils off upon curing of the sizing. The 75 wt% sizing– 25 wt% f-CNT_A, with a higher DOFD of CNTs, compared to the 75 wt%

sizing– 25 wt% f-CNT_B, had a 60 and 13% lower cure activation energy for the reactions 1 and 2 in these systems, signifying that a higher DOFD facilitates a more favorable reaction between the sizing and the functional groups of the f-CNT_A. SEM images of the surface of the 50 wt% sizing– 50 wt% f-CNT_B film demonstrated sizing coated f-CNT_B signifying favorable interactions between the sizing and the f-CNT_B.

Second, three different types of CNT-BMI interface-interphase: p-CNT_A- BMI, f-CNT_A- BMI and sizing coated f-CNT_A-BMI were prepared and studied in nanocomposites containing 60 wt% CNTs. p-CNT_A, f-CNT_A and the sizing coated f-CNT_A in the 60 wt% CNT containing nanocomposites of BMI, all altered the BMI cure reaction. The BMI cure temperature reduced by up to 30 and 36 °C in the 60 wt% p-CNT_A – 40 wt% BMI and 60 wt% f-CNT_A – 40 wt% BMI, respectively while for the 60 wt% f-CNT_A – 7 wt sizing- 33 wt% BMI, three different exothermic peaks were observed, reaction 1, with up to 50 °C lower cure reaction while the major cure reaction occurred at at least 90 °C higher temperature compared to p-BMI. The 60 wt% p-CNT_A – 40 wt% BMI and the 60 wt% f-CNT_A – 40 wt% BMI demonstrated 60 and 64 °C higher T_g, respectively, compared to the 100% BMI (with no CNTs) (330, 336 and 272 °C, respectively). The T_g of the 60 wt% f-CNT_A – 7 wt% sizing- 33 wt% BMI was 8 °C higher (280 °C) compared to the 100% BMI. Significant differences in the molecular heterogeneity and hierarchy among the 60 wt% p-CNT_A – 40 wt% BMI and 60 wt% f-CNT_A – 40 wt% BMI, and the 60 wt% f-CNT_A – 7 wt sizing- 33 wt% BMI, observed through SAXS, signifies that the three different CNT-BMI interface- interphase have different molecular architecture.

This study demonstrates that coating the CNTs with a sizing can significantly alter the cure reactions of the resin as well as the over structure and thermo-mechanical

properties of the CNT polymer nanocomposites. Further efforts towards optimizing the sizing type, thickness of the sizing coating around the CNTs, and the overall CNT- sizing-polymer ratio for a given CNT- sizing- polymer system is needed for designing nanocomposites with desirable structure and properties.

CHAPTER 6. THE EFFECTS OF AMORPHOUS CARBON AND THE BAKING TREATMENT OF CNTS ON THE THEIR INTERFACE- INTERPHASE WITH POLYUREA

6.1 Introduction

Ultra-high strength and lightweight structures are highly desirable in various applications including the automobile [244] and aerospace sector [1], [4], [6], [245], [246]. Polymer-CNT composites are expected to have significantly better mechanical properties than those for the current state of the art carbon fiber reinforced plastics (CFRP) [1], [4]. However, CNT containing composites have some limitations, including load transfer at the CNT- polymer interface [4]–[7]. The interface plays a critical role in determining the overall macroscale properties of the composite [8]–[12]. While, significant attention has been directed to this end [5], [7], [10], [13]–[19], the CNTs in the composites have not yet reached their full potential.

Several factors contribute to the load transfer efficacy of the CNT- polymer interface and interphase. Some of these are closely inter-related and inter-dependent. First, CNT related variables including its helicity [64], number of walls [15], length [65], and functionalization [66]. Second, polymer related variables including, functional groups [23], [68]–[70], conjugation and aromaticity [22], [23], [69], crystalline/amorphous [71] content, and the polymer molecular weight [72]. Third category of factors include combination of polymer and CNT related variables [73], [74]. The polymer-CNT interaction can be covalent [68], or non-covalent [20], [22],

[23], [69]. Examples of non-covalent interactions include $\pi - \pi$ [22], CH$-\pi$ [16], [22], NH$-\pi$ [20], [21] and OH$-\pi$ [23] interactions. Fourth, composite processing related variables including, solution processing [71], melt processing [16], in-situ polymerization [75], and molecular layer deposition [76]. The processing route is closely tied to the macroscopic form of CNTs used for composite preparation. CNTs can be in various forms including : powder/fluff [5], [16], [77], forest [78], buckypaper/sheet/tape [17], [79]–[81], or yarn [82]. Polyurea interacts with CNT through $\pi - \pi$ [22] CH$-\pi$[16], [22], and NH$-\pi$[20], [21] non-covalent interactions, as it contains nitrogen, aromatic and aliphatic groups (Figure 6.1) [247].

Studies on the interfacial characterization of polymer-CNT composites have been conducted using Raman spectroscopy [19], wetting measurements [87], Fourier transform infrared spectroscopy (FTIR) [16], [87], X-ray scattering [71], electron energy loss spectroscopy (EELS) [88], [89] and CNT pullout tests using atomic force microscopy (AFM) [90]–[93]. Theoretical [94], [95] and computational models [10], [96], [97] have been developed and utilized towards this end as well. Raman spectroscopy has proven to be a powerful tool for characterizing the interfacial load transfer [19], [98]. The tensile strain in CNTs results in Raman band frequency downshift (D ~ 1300 cm^{-1}, G ~ 1580^{-1}, G' ~ 2600^{-1}), which in turn is associated with the weakening of $C - C$ bonds [99]. Here, Raman spectroscopy has been used to investigate the interfacial strain in polyurea-CNT systems with unbaked and baked CNT sheets.

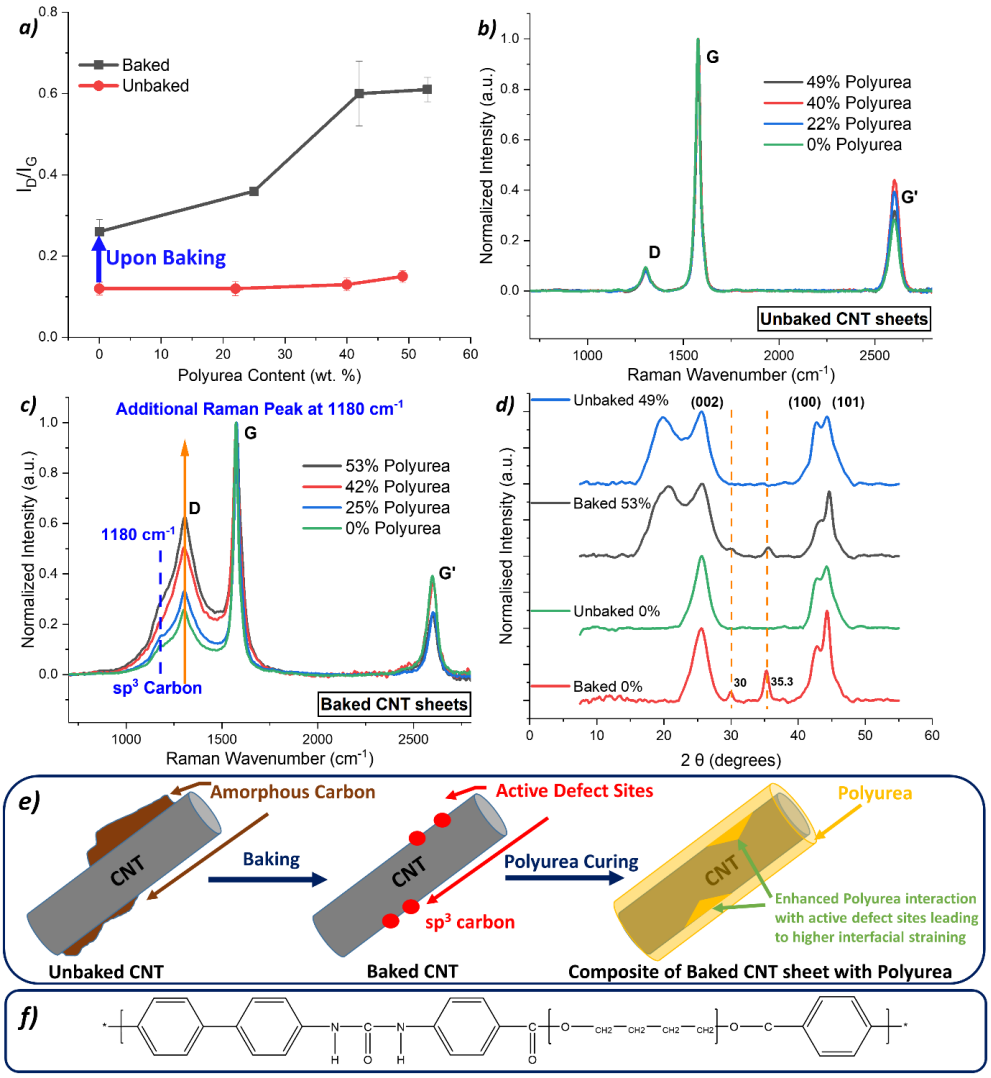

Figure 6.1. (a-d) Characterization of unbaked and baked CNT sheets. (a) I_D/I_G of composites of polyurea with unbaked and baked CNT sheets. The plot shows that baking introduces defects in the CNTs, and that defects in the baked CNTs further increase with the addition of polyurea. From the CNT defect standpoint, unbaked CNTs remain largely unaffected with the addition of polyurea. (b and c) Representative Raman spectra of polyurea composites with (b) unbaked and (c) baked CNT sheet. Intensity of each curve has been normalized to the G band intensity (~1578 cm^{-1}). (c) An increase in the D band intensity with an increasing polyurea content is observed. It is postulated that baking forms chemically active defect sites on CNTs that react with polyurea triggering a further ring opening of the CNT surface. Raman peak at 1180 cm^{-1} associated with sp^3 carbon in either nano-crystalline or hexagonal diamond structures is observed in baked CNTs. (d) X-ray diffraction of unbaked and baked CNTs and their composite at ~50 wt. % polyurea. Peaks at ~ 30° and 35.3° 2θ, not associated with CNTs is observed in the baked CNTs and its composite. (e) Schematic of the proposed mechanism showing the formation of active defects upon removal of amorphous carbon and their reaction with polyurea. (f) Structure of polyurea.[247]

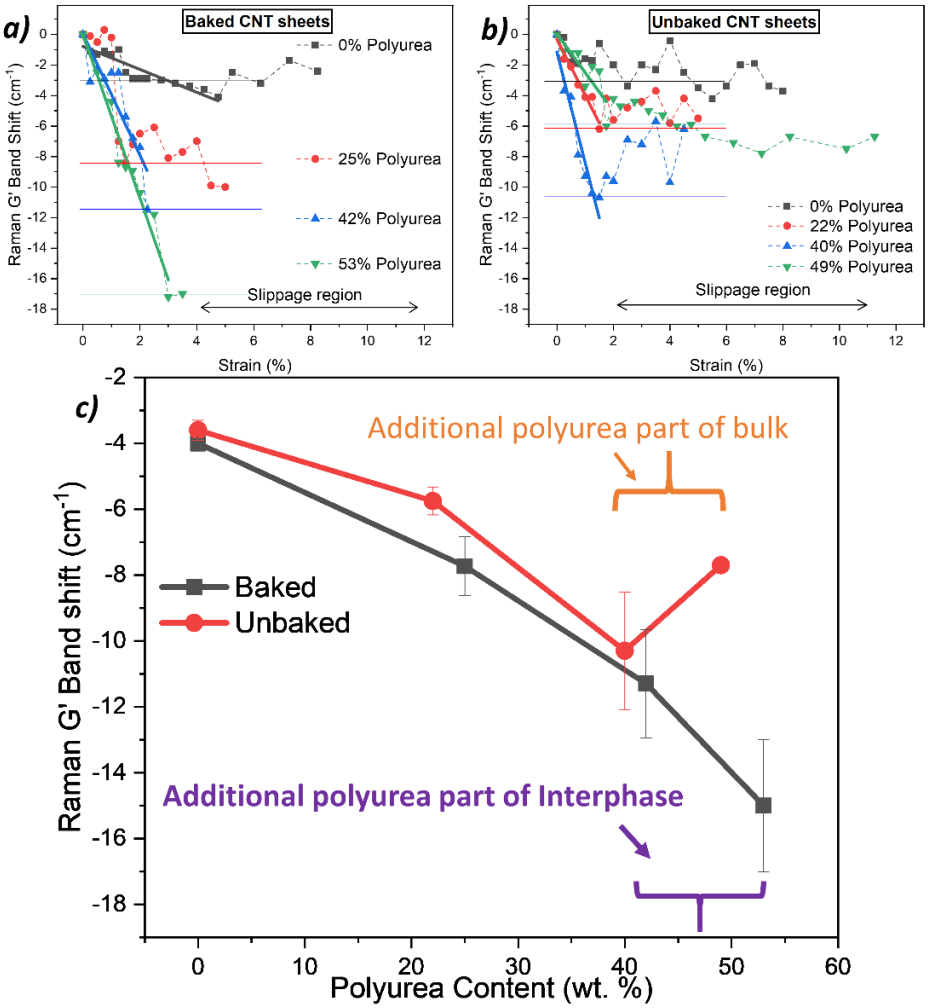

Figure 6.2. (a and b) Representative Raman G' band downshift upon application of strain in polyurea composites at various polyurea loading with (a) baked CNT sheets, (b) unbaked CNT sheets. (c) Maximum Raman G' downshift upon application of strain is plotted against varying polyurea content in the composites of polyurea with unbaked and baked CNT sheets. The drop in the downshift of the G' peak position in composites of unbaked CNT sheets going from 40 wt.% to 49 wt.% polyurea loading signifies that the additional polyurea forms part of the bulk, whereas in composite of baked CNT sheet, going from 42 wt.% to 53 wt.% polyurea loading, an increase in the downshift of G' peak position signifies that the additional polyurea is still part of the interphase.[5]

Prior studies in the literature have reported baking of CNTs between 600 °C to 1000 °C to selectively eliminate impurities, and amorphous carbon [25], [248]. To enhance interfacial interactions between the CNTs and the polymer, surface modification of the CNTs through their functionalization [23], [68]–[70], wrapping

[17] or coating [16] with polymers has been reported in the literature. These surface modifications involve use of either individually or in combination of strong acids [16], organic solvents [16], plasma and ozone [233], [234]. In this study, in addition to the removal of amorphous carbon, it is observed that baking also creates chemically active defects in the CNTs, sp^3 carbon, and these lead to record interfacial strain in the system. The enhanced interfacial interaction is achieved without any further modification of CNTs.

6.2 Results and Discussion

The effect of baking on the thermal stability of the CNT sheet and their composites was evaluated using TGA (Figure E 1) and is discussed in the supplementary information. The CNT orientation in the sheets was determined from the second $<P_2(\cos\theta)>$ and fourth $<P_4(\cos\theta)>$ order orientation parameters as described elsewhere [249]. The value of these parameters remained between 0 to 0.08, signifying random or little orientation of the CNTs in these sheets (Figure E 2 and Table E 1).

6.2.1 Raman Analysis

The intensity ratio of the Raman D band (I_D) at ~ 1300 cm^{-1} which is associated with the CNT disorder [250], to the G band (I_G) at ~ 1580 cm^{-1} which is associated with the tangential vibration of the graphitic carbon, is used to estimate the graphitic perfection in CNTs [251]. Higher I_D/ I_G represents a less perfect graphitic structure. Here, we observed an I_D/I_G of 0.12 ± 0.02 in the unbaked CNT sheet without polyurea, which increased to 0.26 ± 0.03 in the baked CNT sheet (Figure 6.1a). This suggests that the baking treatment, intended for removing amorphous carbon, is also damaging the graphitic structure of the

CNTs. Furthermore, I_D/I_G increased with an increase in the polyurea content only in composites of baked CNT sheet (Figure 6.1 a and c), but not significantly for the unbaked CNT-polyurea sheet (Figure 1 a and b). I_D/I_G was 0.61 ± 0.03 for baked CNT composite with 53 wt. % polyurea, an increase of factor of five from the unbaked CNT sheet without polyurea. While, an increase in the I_D/I_G is typical for CNTs undergoing covalent functionalization [252], such a behavior is not expected by simply adding the polymer to CNTs, as has also been observed for unbaked CNTs, where no significant change in I_D/I_G is observed with the addition of polyurea Figure 6.1 a and b). We thus postulate that baking leads to formation of chemically active defects which react with polyurea triggering ring opening of the CNT surface (Figure 6.1e), that results in further increase in the Raman I_D/I_G.

Raman peak at 1180 cm^{-1}, not associated with CNTs and not observed in unbaked CNTs (Figure 6.1b), was observed in baked CNT sheets and their composites (Figure 6.1c). This peak has been reported to be associated with sp^3 carbon in nano-crystalline and in hexagonal diamond structures [253]. X-ray diffraction peaks at ~ 30° and 35.3° 2θ, again, not associated with CNTs, was observed in baked CNT sheet and its composite (Figure 1 d), and not in unbaked CNT sheet and its composite. Polyurea amorphous peak is observed at ~ 20° 2θ. X-ray diffraction peaks associated with CNT (002), (100), (101) are observed at ~ 25.6°, 43° and 44° 2θ, respectively. The CNT sheets and their composites were also characterized by x-ray photoelectron spectroscopy (XPS) (Figure E 3).

6.2.2 Interfacial Strain Measurements using in-situ Raman

Representative Raman G' shifts with strain in composites of polyurea with baked and unbaked CNT sheets are plotted in Figure 6.2 a and b, respectively. After initial downshift upon strain, G' position ultimately reaches a plateau and the downshift no longer increases with strain. This plateau signifies the failure through slippage at the polyurea-CNT interface/interphase or within polyurea leading to no further increase in strain within the CNTs upon application of external strain on the sheets. The unbaked CNT sheet without polyurea demonstrated a Raman G' band downshift of 3.6 ± 0.3 cm^{-1} which increased with increasing polyurea loading up to 40 wt. % (Figure 2c), where a downshift of 10.3 ± 1.8 cm^{-1} was observed. Upon further increase in the polyurea content to 49 wt. %, the downshift dropped to 7.7 ± 0.15 cm^{-1} (Figure 6.2c). On the other hand, composites of polyurea with baked CNT sheets demonstrated a steady increase in the Raman G' band downshift with increasing polyurea loading up to 53 wt. % (Figure 6.2c). Downshift of 4 ± 0.15 cm^{-1} and 15 ± 2 cm^{-1} were observed for baked CNT sheets without polyurea and with 53 wt. % polyurea loading, respectively.

The reduction in the Raman G' band downshift in the composite of unbaked sheet with 49 wt. % polyurea compared to the composite with 40 wt.% polyurea signifies that the additional polyurea constitutes to the limiting factor in straining of CNTs within the composite sheet. This suggests that the further addition of 9% polyurea (increasing from 40 to 49%) constitute the bulk phase, and not something that is part of the interphase region [5]. This leads to slippage/failure within the bulk domain, before the polyurea-CNT interfacial shear strain limit is reached. Given, the composite of baked CNT sheet with 53 wt. % polyurea demonstrated a higher Raman G' band downshift compared to composite

of baked CNT sheets with 42 wt. % polyurea, where a downshift of 11.3 ± 1.7 cm^{-1} was observed, it is concluded that the additional 11 wt. % polyurea (from 42 to 53%) is still part of the interphase and thus the polyurea in the bulk phase must be absent. If this was not the case, then the increase in the Raman G' band downshift would not be there, and the failure within polyurea bulk region, would be the limiting case, as observed for the composite of unbaked CNT with 49 wt. % polyurea.

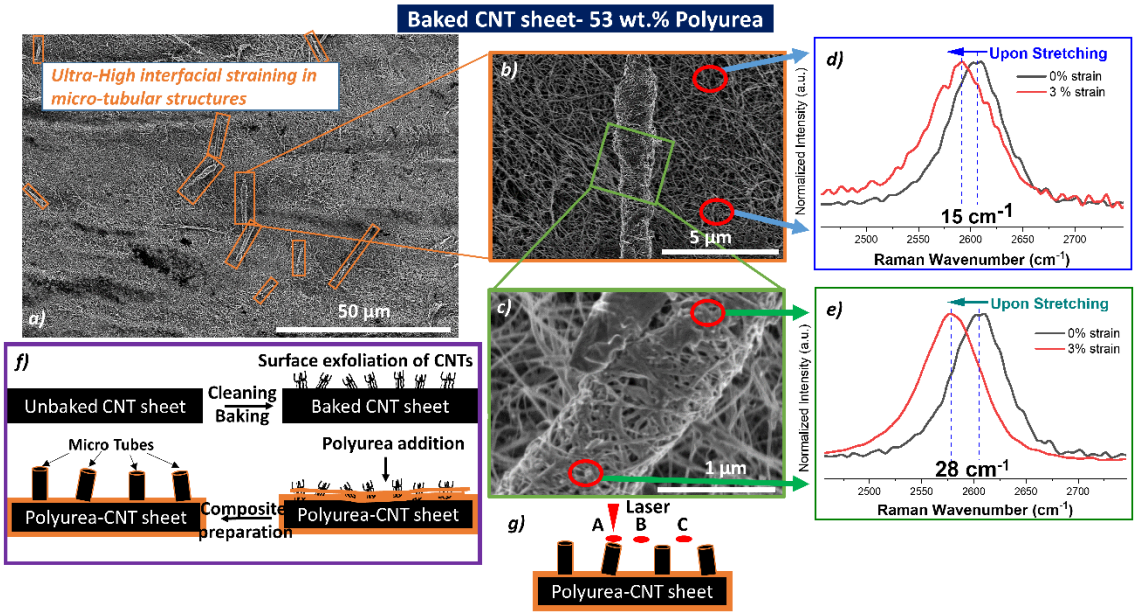

Figure 6.3. For composite of baked CNT sheet with 53 wt. % polyurea (a) low magnification SEM image of the surface of sheet. The orange insets show micro-tubular structures distributed randomly on the surface of the sheet. (b and c) Higher magnification image of micro-tubules. (d) Raman G' band downshift of 15 cm^{-1} associated with regions other than microtubules. (e) Raman G' band downshift of 28 cm^{-1} associated with micro-tubules with higher interfacial straining. (f) Schematic of the proposed mechanism for the formation of micro-tubules. (g) When Raman laser focuses at spot A (micro-tubules) Raman G' downshift of 28 cm^{-1} is observed while when at spot B/C (rest of the sheets surface), Raman G' downshift of 15 cm^{-1} is observed.

Overall, the baked CNT sheets with 53 wt. % polyurea, demonstrated the maximum Raman G' downshift of 15 ± 2 cm^{-1} , which is amongst the highest Raman downshift reported in the literature to-date for various CNT-polymer systems (Table 6.1). This

downshift corresponds to a local CNT strain of 0.4% or a stress of 4 GPa (based on a CNT modulus of 1 TPa). Most interestingly, the same sheet also demonstrated extraordinary Raman G' downshift of ~28 cm^{-1} (Figure 6.3e), in some regions, which corresponds to a local CNT strain of 0.75%, and it was measured reproducibly. This high value was not used for calculating the average downshift value of 15 ± 2 cm^{-1}. This extraordinarily high shift suggest heterogeneous strain within the sheet. To investigate the origin of the strain variation, CNT sheet surfaces were first examined in the SEM to check for any visible signs of heterogeneity, followed by Raman mapping of the sheet.

Table 6.1. Comparison of maximum Raman G' or D band shifts in polymer-CNT composites observed upon stretching reported in the literature and in this work.

Matrix	CNT	Maximum Raman Shift (cm^{-1}) - band followed	External Strain (%)
Polyurea (this Work)	**baked MWNT**	**33-39 - G'**	**3**
Polyvinyl alcohol[75]	collagen treated SWNT	15 - G'	6.5
Polyacrylonitrile[19]	FWNT	13 - G'	0.4
Polyacrylonitrile[76]	poly (methyl methacrylate) wrapped SWNT	13 - G'	6
Polyvinyl alcohol[98]	f-SWNT	9 - G'	1.5
Polypropylene[217]	f-MWNT	9 - D	3

6.2.3 SEM Analysis

SEM images of the baked CNT sheet with 53 wt. % polyurea revealed randomly distributed micro-tubules present in small regions of the sheet (Figure 6.3 a, b, c). It is further noted that these microtubular features were not observed in unbaked CNT sheet, with 49 wt. % polyurea (Figure E 5), or without polyurea (Figure 6.4 a, b, c). Microtubules

were also not observed in the baked CNT sheets without polyurea (Figure 6.4 d, e, f). When the laser beam (spot size ~0.6 μm) is focused on the microtubules, extraordinary Raman G' downshift of ~28 cm^{-1} is observed (Figure 6.3e). On the other hand, when the laser is focused on the other parts of the sheet (with no micro-tubular structures) a downshift of 15 ± 2 cm^{-1} is observed (Figure 6.3d). A schematic of the proposed mechanism for the formation of such micro tubular structures is illustrated in Figure 6.3f and will be discussed in a later section.

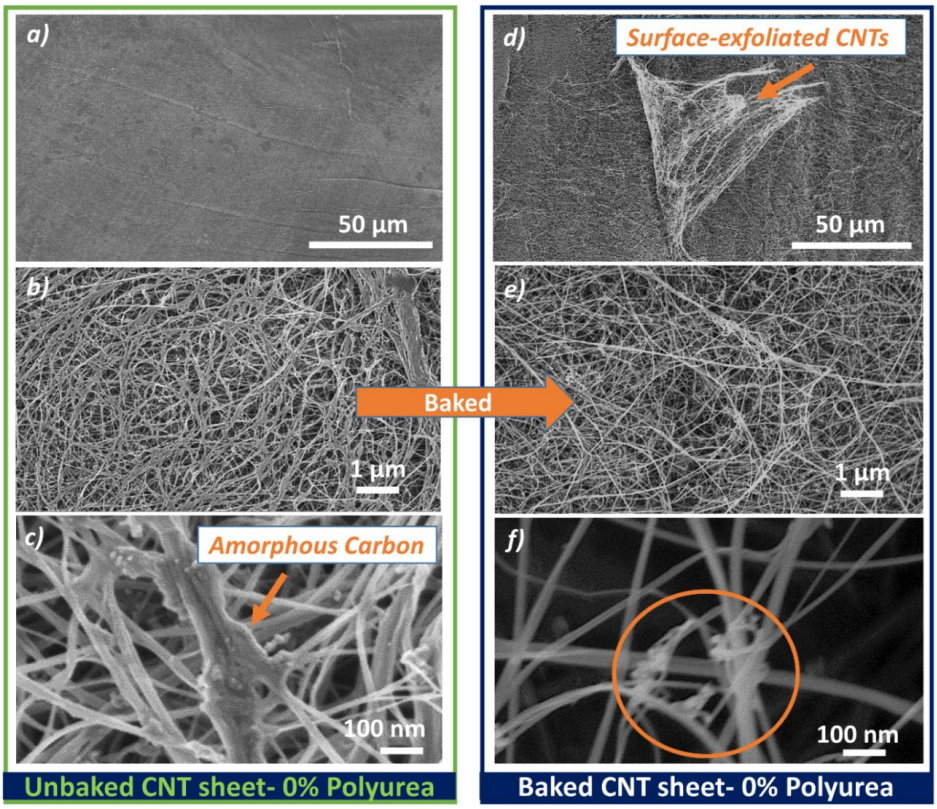

Figure 6.4. SEM images of (a-c) unbaked CNT sheet without polyurea, (d-f) baked CNT sheet without polyurea. (a) Low magnification image showing a rather smooth surface compared to baked CNT sheet. (b-c) Coating of amorphous carbon and other impurities on top of the CNT sheet can be seen. This coating seems to be holding the CNTs together. (d) Surface exfoliated CNTs could be observed in baked CNT sheets as the amorphous carbon coating that held the CNTs together is eliminated. (e) Much cleaner baked CNTs (no coating on top of CNTs) upon baking. (f) Some impurities can be spotted at higher magnification. The measured average CNT and CNT bundle diameter is 15 ± 5 nm.

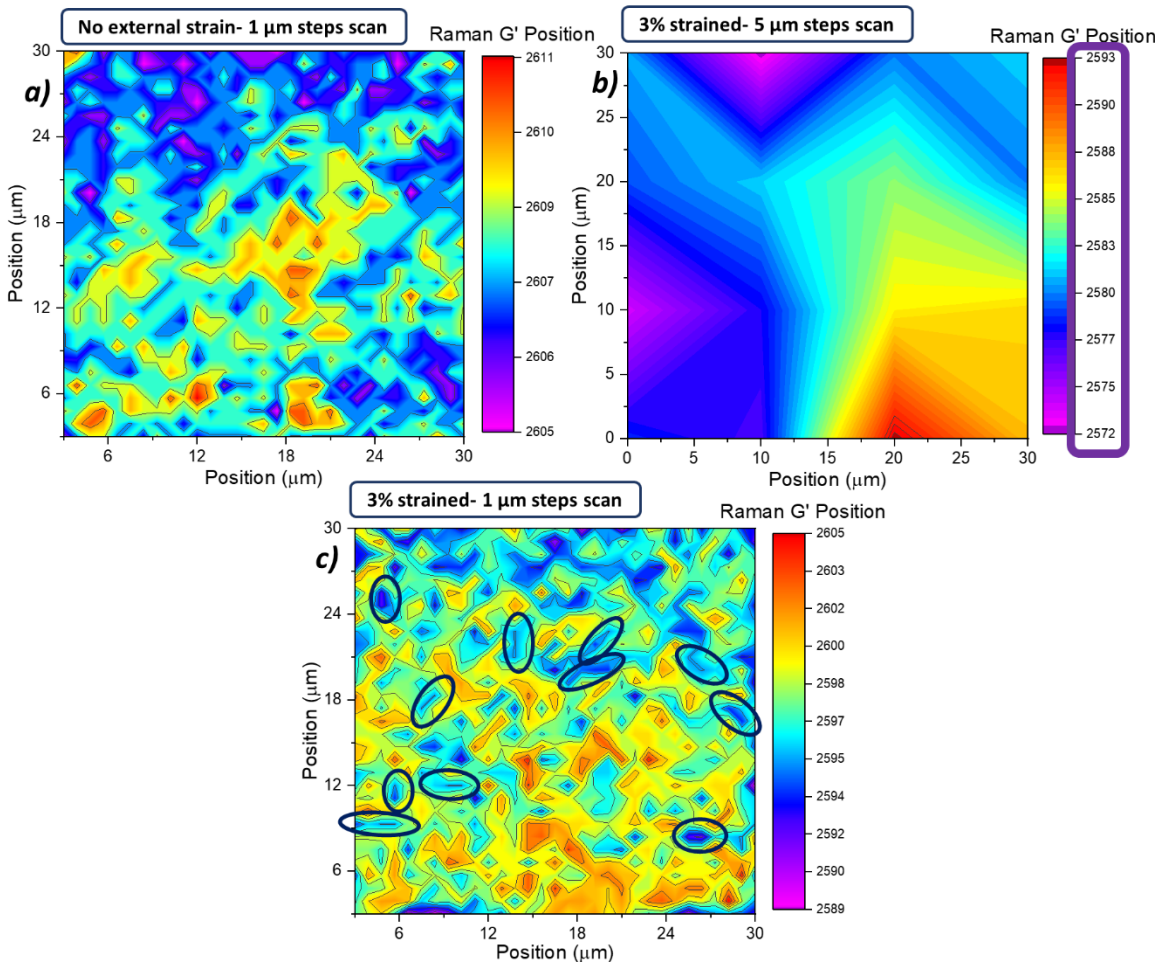

Figure 6.5. (a – c) Raman maps of the G' peak position in baked CNT sheet with 53 wt. % polyurea. (a) Unstrained sheet with G' peak position between 2605 to 2611 cm^{-1}. (b) Mapping at 5 µm step to minimize scan time while 3% strain is applied in an attempt to capture maximum strain values. G' peak from 2572 to 2593 cm^{-1} are observed. This corresponds to a maximum downshift of 33 to 39 cm^{-1}, and is equivalent to 0.9 – 1 % strain or 9-10 GPa stress locally in the CNT. (c) Mapping at 1 µm step with 3% strain on the same area as in (b) for a better resolution and to identify features leading to heterogeneous strain. A clear strain relaxation is evident as can be seen from different G' range in (b) than in (c). G' peak position in (c) ranges from 2589 to 2605 cm^{-1}. Microtubular structure can be identified (black insets) and show that strain is higher in these regions compared to the surrounding regions.

6.2.4 Raman Mapping

To further understand the heterogeneous G' shift behavior, Raman mapping was conducted on baked CNT sheet with 53 wt. % polyurea under three different conditions.

Sheet with no external strain demonstrated a distribution in the Raman G' peak position from 2611 to 2605 cm^{-1} (Figure 6.5 a). This signifies inherent strain heterogeneity in the sheet which could result from factors including, (a) mechanical tension/compression in the CNTs induced during their synthesis and/or composite preparation. (b) Variation in polyurea distribution within the CNT sheet. Formation of electron donor-acceptor complexes between CNT and polymer involves electron charge transfer that results in a shift in the Raman peak associated with CNTs [21], [254]. Thus, variation in polyurea distribution in the sheet could lead to variation in the extent of electron charge transfer and consequently the variation in the Raman peak position. Next, we conducted Raman mapping on sheet uniaxially stretched by 3% (Figure 5 b and c). Raman mapping of polymer-CNT composites in strained form is challenging as longer data acquisition time leads to stress relaxation. Thus, the acquired data would be an underrepresentation of the maximum interfacial strain limits. To minimize stress relaxation, and thus to minimize mapping time, we first scanned in 5 μm steps across the 30 μm × 30 μm section. For this map, G' peak position is in the range of 2572 cm^{-1} to 2593 cm^{-1} (Figure 6.5 b), and corresponds to a maximum downshift of the G' peak position in the range of 33 to 39 cm^{-1} (comparing lower limit of strained sheet to the limits of the unstrained sheet, 2572-2605 and 2572-2611 cm^{-1}). This shift corresponds to a local CNT strain in the range of ~ 0.9-1% or a stress of 9- 10 GPa (assuming a CNT modulus of 1 TPa). When the same area (with no external change in strain and position of the section mapped in Figure 6.5 b) is further mapped in 1 μm step size, the observed Raman G' peak position distribution is in the range of 2589 to 2605 cm^{-1} (Figure 6.5 c). The decrease in the downshift is due to stress relaxation during the two mapping periods. Mapping time was 25 minutes in 5 μm steps

and 12 hours in 1 μm step mapping. However, features corresponding to the micro-tubular structures observed in the SEM images (Figure 6.3 a, b, and c) are also observed in the Raman map (features within black insets in Figure 6.5 c). These black insets in Figure 6.5 c clearly are micro-tubular regions of greater downshift in the G' peak position compared to their surrounding regions in the sheet. These micro-tubular regions signify regions of high interfacial strain. Microtubular features observed in Raman map (Figure 6.5 c) are ~3-7 μm long and ~1 μm wide and are comparable to their dimensions observed in SEM (Figure 6.3a).

6.2.5 Proposed Mechanism for Microtubule Formation

Mechanism for the formation of microtubules (Figure 6.3f) is proposed based on the following observations: (a) surface exfoliated CNTs in baked sheets. The unbaked CNT sheet is held together through (1) mechanical interlocking of CNTs, (2) van der Waals interactions between CNTs, (3) amorphous carbon. Presence of amorphous carbon also renders a smooth surface to the sheet by holding the CNTs on the surface of the sheets together (Figure 6.4a). Upon baking, the amorphous carbon is eliminated and the CNTs at the surface of the baked sheet are exposed and more prone to exfoliation (referred to as surface exfoliated CNTs) (Figure 6.4d). (b) Infiltration of CNT network with polymer in the solution [84]–[86] or melt form [79] is a commonly used technique for composite manufacturing when using CNTs in the sheet form. The solution approach, however is preferred over melt to facilitate better polymer diffusion into the CNT network. In either case, the solvent evaporation post infiltration and/or curing of pre-polymer (in case of thermosets), both lead to densification of the CNT network. The exfoliated CNTs have a higher degree of freedom from a densification standpoint compared to CNTs in the bulk of

the sheet. These exfoliated CNTs, upon densification assemble as microtubules (Figure 6.3).

6.3 Experimental

6.3.1 Materials

Unbaked and baked CNT sheets, and their composites were provided by Nanocomp Technologies, Inc, Merrimack NH. The manufacturer reported length for individual CNT is 1-10 mm.[73] The sheets contain multi-wall carbon nanotubes (figure S5). Average number of CNT walls is ~9 for both unbaked and baked CNTs, as determined from the full width at half maxima of integrated 2θ~ 26° peak from x-ray diffraction using Scherrer equation (Table S2).

6.3.2 Methods

Raman spectra were collected using a HORIBA XploRA ONE (λ=785 nm) spectrometer with 50x objective, 1200 grating, 5 mW laser power and spectral resolution of 0.4 cm^{-1}. In situ Raman deformation study of the sheets was conducted, using a tensile deformation frame, as described in a previous work.[217] Three samples were tested for each case. The downshift in the Raman G' band is used for calculating the strain in CNTs through the expression $\varepsilon = (\Delta G')/37.3\ cm^{-1}/\%$,c where ε is the strain in the CNTs and $(\Delta G')$ is the shift in Raman G' band. Raman mapping was conducted using a XY stage. The orientation of the CNTs in the sheets was determined from the Raman G' peak as described in a previous work.[249]

XPS was conducted on a Thermo K-Alpha (Thermo Scientific) system utilizing a monochromatic Al Kα source (1486.6 eV) as described in a previous work. [74] FTIR spectra were recorded on Shimadzu Prestige 21 FT-IR spectrometer in attenuated total reflectance (ATR) mode with a spectral resolution of 0.5 cm^{-1}. WAXD was conducted on Rigaku MicroMax-002 beam generator (Cu Kα λ= 0.1542 nm, operating voltage and current 50 kV and 0.60 mA, respectively) equipped with R-axis IV++ detector. SEM images were collected on a Hitachi SU8230 SEM with an accelerating voltage of either 1 or 2 kV. TGA study was carried out at a heating rate of 10 °C/min under nitrogen atmosphere using TA Instrument Q500. ImageJ software was used for measuring CNT diameter from SEM image using 20 different points. Tensile tests were conducted on TA instruments RSA III using a sample with 1 cm width, gauge length of 5 cm and at a strain rate of 5 mm/min. 5 samples were tested. Results of tensile test are included in the supplementary information (Table S3).

6.4 Conclusion

This study provides an understanding of, (a) the effects of baking CNTs, (b) polyurea loading variation and (c) the structural variations within the same composite sheet that leads to differences in interfacial straining capability in polyurea-CNT composite. Maximum Raman G' downshift in the range of 33 cm^{-1} – 39 cm^{-1} has been observed which corresponds to a local CNT strain in the range of ~ 0.9- 1% or a stress of 9- 10 GPa. The shift is also more than two times higher than that reported in the literature for any polymer-CNT system. Raman peak at ~1180 cm^{-1} associated with sp^3 carbon in all samples of baked CNTs and their composites has been observed. Micro-tubular structures with higher interfacial strain compared to their vicinity have been observed.

CHAPTER 7. CONCLUSION AND RECOMMENDATIONS FOR FUTURE WORK

7.1 Conclusion

This thesis elucidates, (a) the effects of processing on the molecular arrangement of the multi-component BMI and consequently their effect on the impact strength. (b) the effects of CNTs with and without surface treatment and sizing on the structure, process and properties of the CNT-BMI nanocomposites containing up to 60 wt% CNTs. (c) the effect of amorphous carbon on the interface- interphase of a CNT-polymer system.

The high speed shear mixing process led to a dramatic increase of 393% in the impact strength of BMI compared to the cured Melt BMI (an increase from 14 ± 6 to 69 ± 13 kJ/m^2), without high shear mixing. The impact strength of 69 kJ/m^2 achieved in this dissertation is the highest reported impact strength for any BMI system. Typically, an increase in the impact strength is achieved at the expense of glass transition temperature through addition of an elastomer to the brittle resin, but herein the cured HSSM BMI exhibited an increase in the glass transition temperature by 16 °C compared to cured Melt BMI. This further signifies the importance of the geometry and arrangement of the different components of the BMI, where an improved T_g can be achieved with an improvement in the impact strength.

Well-dispersed CNTs in the polymer nanocomposites typically improve the impact strength of the polymers. This dissertation however elucidates that good CNT dispersion alone is not a sufficient condition to improve the impact strength of the nanocomposites.

The impact strength of the nanocomposite also depends on the CNT type and the processing conditions. CNTs can disrupt the crosslinking network of BMI, and CNTs can be axially and radially compressed by up to 2.9 GPa upon the cure of BMI, and these factors play a critical role in the impact strength. The CNT-BMI nanocomposite containing 0.1 wt% CNTs and processed through a probe sonication method demonstrated an impact strength of 54 ± 8 kJ/m^2 which is the highest reported impact strength for any CNT-BMI nanocomposite. The highest impact strength reported in the literature prioir for the BMI-CNT system is 30 kJ/m^2. The uncured 0.1 wt% CNT_B- PS BMI has thus been identified as a potential system of interest for being employed in the CNT or CNT- carbon-fiber based hybrid composites.

Further, CNTs altered the cure reactions as well as the cure temperature of the BMI owing to the preferential stacking of the components of the BMI around the CNTs. The change in the cure reactions as well as the cure temperature of the BMI depends on the CNT content in the nanocomposite. The carbon fiber sizing used in this dissertation further altered the cure reactions of the resin as well as the overall structure and thermo-mechanical properties of the CNT polymer nanocomposites. These results signify that the cure cycle for a CNT-BMI system needs to be optimized based on the changes that the CNTs cause to the specific CNT-BMI system. We think that the stored compressive stress of the CNTs in the nanocomposites could be harnessed for additional gains in the overall tensile strength of the composite. For example, if a CNT- polymer nanocomposite containing CNTs with no compression and has a tensile strength of ‘t’ GPa, then a similar CNT-polymer nanocomposite, but containing CNTs with a compressive stress of ‘c’ GPa, should have a tensile strength of ‘c+t’ GPa (assuming that the CNT strength is the limiting factor of the

overall nanocomposite strength). Such a strategy could be considered for systems that need to be designed for tensile loading.

The baking of CNTs has important implications. In addition to removing amorphous carbon, baked CNTs had a higher Raman I_D/I_G ratio signifying that baking also created defects' in the CNTs. These lead to enhanced interfacial interaction with the matrix, resulting in record interfacial stress transfer in a polymer-CNT system. Based on the learnings from this study, baked CNTs could be employed to prepare nanocomposites with a variety of different polymer resins and there is potential to achieve CNT stress of greater than 10 GPa in the nanocomposites.

It is expected that these studies will provide guidance for the manufacturing of CNT, or CNT and carbon fiber hybrid based laminates that will ultimately meet NASA mechanical property goals.

7.2 Recommendations for Future Work

7.2.1 In-situ FTIR, Raman Spectroscopy and SAXS Analysis of the BMI system Processed through Melt, HSSM and PS Techniques

As discussed in Chapter 2: (a) the FTIR, Raman and NMR analysis of the cured Melt and cured HSSM BMI demonstrated significant differences in the molecular environment of the cured Melt and cured HSSM BMI. (b) A direct relationship between the molecular domain size calculated from the SAXS peak position, its intensity, and the impact strength was observed.

The cure and post-cure time and temperature in the current study were kept constant. Going forward, it would be of interest to examine the molecular domain size evolution using in-situ SAXS for the Melt and HSSM BMI system, as they are cured over time. The in-situ SAXS can be performed under different temperature conditions. This would provide further insight into the relationship between the cure and post- cure time and temperature, and the molecular domain size of the BMI processed through Melt and HSSM techniques. BMI with even higher impact strength than the one obtained in the current dissertation may be achieved by potentially achieving a molecular domain size of greater than 16 nm. Combined with in-situ FTIR and Raman spectroscopies, the BMI molecular domain size evolution through in-situ SAXS, could further be correlated with the reaction pathway and the products being formed as the BMI system cures.

7.2.2 Fabricating Carbon Fibre, CNT Yarn or CNT Sheet based Composite Panels using HSSM BMI as the Resin Matrix

The resin dominated properties limit the inter and intra laminar fracture toughness in the CFRPs. The resin rich inter and intra laminar regions of the CNT yarn or sheet based-composite panels should thus also be limited by the resin dominated fracture toughness. Fenner and Daniel [210] demonstrated that improving the impact strength of the epoxy resin through CNT modification by 30%, translated to improved Mode I fracture toughness of the CFRP composite prepared with the CNT modified epoxy by 180%.

The HSSM processed BMI could thus be used for preparing prepregs with carbon fibers, CNT yarns or CNT sheets to eventually obtain composite panels with improved inter and intra-laminar fracture toughness in the composite panel.

7.2.3 Fabricating Carbon Fibre, CNT Yarn or CNT Sheet based Hybrid Composite Panels using 0.1 wt% CNT_B- PS BMI as the CNT Modified Resin Matrix

As discussed in Chapter 3 and in section 7.2.2, improving the impact strength of the epoxy resin through CNT modification, translated to improved Mode I fracture toughness of the CFRP composite prepared with the CNT modified epoxy [210]. In this dissertation, the highest impact strength for a CNT-BMI system has been achieved in the 0.1 wt% CNT_B- PS BMI (54 ± 8 kJ/m^2). The 0.1 wt% CNT_B- PS BMI should thus be used for preparing prepregs with carbon fibers, CNT yarns or CNT sheets to eventually obtain composite panels with improved inter and intra-laminar fracture toughness in the composite panel.

7.2.4 Computational Modelling to Compute Interaction Parameters between the Different Components of the BMI System and the CNTs with Different Functionalization aswell as Different Levels of Functionalization: Before Cure and Evolution of Interactions During Cure.

As discussed in Chapter 4, CNTs alter the cure reaction as well as the cure temperature of the BMI, owing to the preferential stacking of the components of the BMI around the CNTs. CNTs can interact with the BMI system through the NH$-\pi$[20], [21], $\pi-\pi$,[22] CH$-\pi$,[16], [22] and OH$-\pi$,[23] non-covalent interactions. The individual components of the BMI however can have exclusive non-covalent interactions with the CNTs. For example, in a BMI system containing 4,4'-bismaleimidodiphenylmethane (BDM) and diallylbisphenol A (DABA) components,[24] only the BDM component contains the maleimide functional group which can potentially

interact with the CNTs through the NH$-\pi$ bonding, while only the DABA component, containing the OH functional group, can potentially interact with the CNTs through the OH$-\pi$ interactions.

To control the interfacial interactions and reactions within the CNT-BMI system, it is critical to understand the stacking preference of the different BMI components around the CNTs. Computational models should thus be used to evaluate the interaction parameters of the different components of the BMI: (a) before curing starts and (b) any rearrangement of the BMI components and the reacted products, during cure. CNTs with varying functionalization levels could be studied. Effect of the cure conditions on the rearrangement of the BMI components and the reacted products, during cure should be evaluated as well.

7.2.5 Optimizing the CNT-BMI cure cycle

As discussed in Chapter 4, CNTs alter the BMI cure temperature. The change in cure temperature was dependent on the CNT content within the nanocomposite. Prior study in the literature [119] has reported reported that the strength of the CNT-BMI and CNT-polyimide nanocomposites depend on the temperature that the nanocomposites were cured at. Thus, going forward, optimizing the cure conditions for each CNT-BMI system is critical in realizing the best mechanical properties from that system.

7.2.6 Using Machine Learning to Predict Bismaleimide Formulations for Best Interactions with CNTs of different Functionalization Levels

As discussed in Chapter 4 and in section 7.2.4, the individual components of the BMI can have exclusive non-covalent interactions with the CNTs. Now, from a molecular interactions standpoint, it is conceivable that the composition of the BMI system may need to optimised. Machine learning can be used on the computation models proposed in section 7.2.4, to predict what the ideal composition of the BMI system should be, to maximise CNT-BMI interactions based on the CNT content in the nanocomposite and the level of CNT functionalization.

7.2.7 Computational Modelling and Machine Learning Driven Search for Optimal Sizing for a given Bismaleimide- CNT System

As discussed in Chapter 5, sizing can significantly alter the cure reactions of the resin as well as the molecular structure and thermo-mechanical properties of the CNT-BMI nanocomposites. Computational modelling and machine learning can be used for predicting the sizing type, thickness of the sizing coating around the CNTs, and the overall CNT- sizing- polymer ratio needed for a given CNT- sizing- polymer system for designing nanocomposites with specific structure and properties.

7.2.8 Uniform Deposition of Amorphous Carbon on the CNTs followed by their Baking, to Tune the Surface Functionalization of Baked CNTs and Consequently their Interfacial Interactions with a range of Polymers

As discussed in Chapter 6, baking of CNTs lead to record interfacial shear strain with polyurea owing to the removal of amorphous carbon as well as the defects and sp^3 carbon created upon baking. The amorphous carbon in the unbaked CNT sheets however was non-uniformly distributed. Uniform coating of amorphous carbon on the CNTs can be

obtained using some kind of deposition technique (atomic layer deposition, chemical vapor deposition, etc.). Baking of these CNTs with uniformly coated amorphous carbon should results in more uniform defects and sp^3 carbon, which in turn could result in further enhancement of the interfacial interactions with the polymer, than what has been reported in this dissertation.

APPENDIX A. SUPPLEMENTARY INFORMATION FOR CHAPTER 2

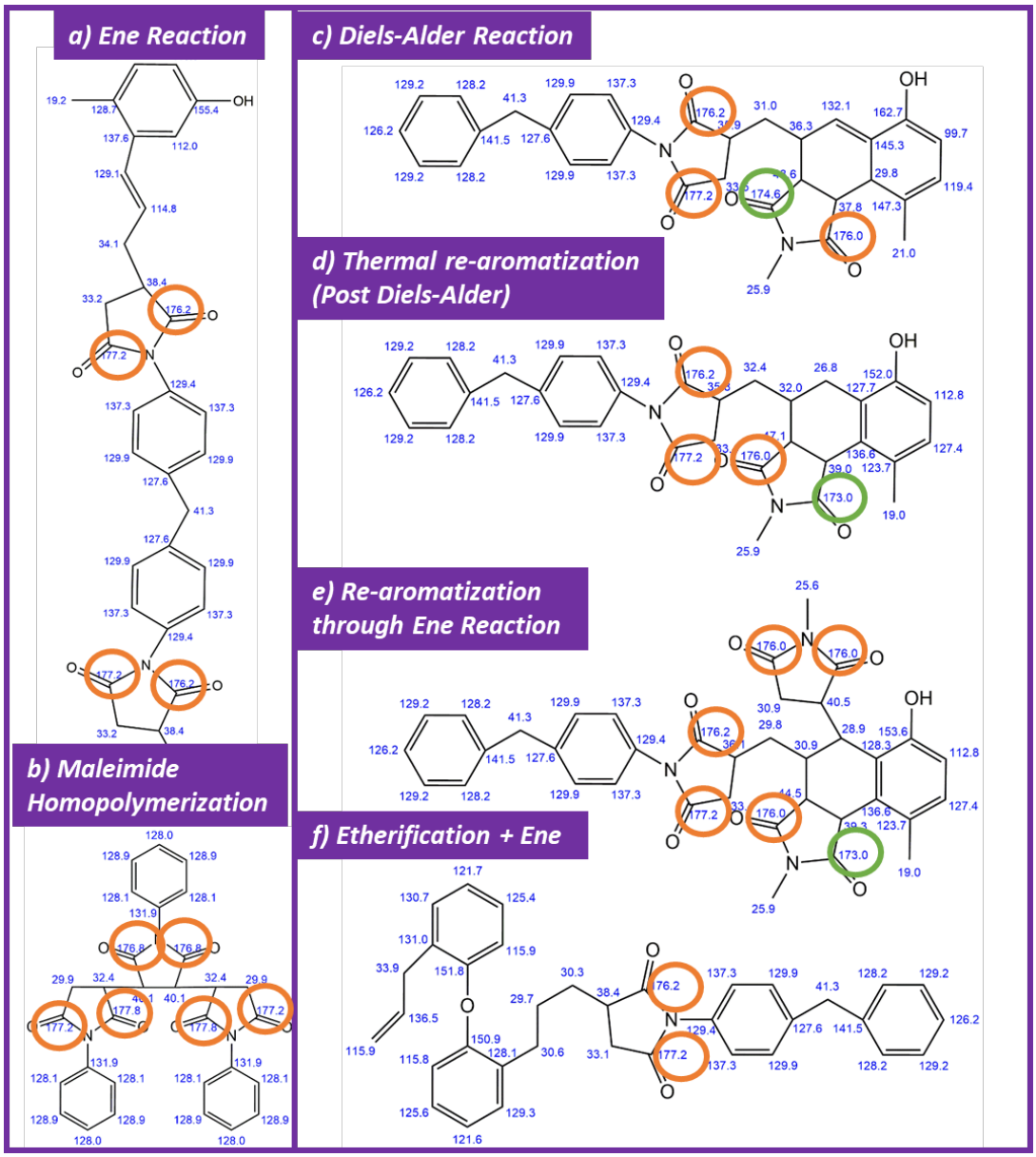

Figure A 1. Predictions of ^{13}C NMR shift for the various possible structures expected to be formed upon curing[43], [45]–[48] of BMI, using ChemDraw Professional software. The orange circles highlight the carbonyl groups contributing to ^{13}C NMR shifts between 177.8-176 ppm whereas the green circles highlight the carbonyl groups contributing to ^{13}C NMR shifts between 174.6-173 ppm.

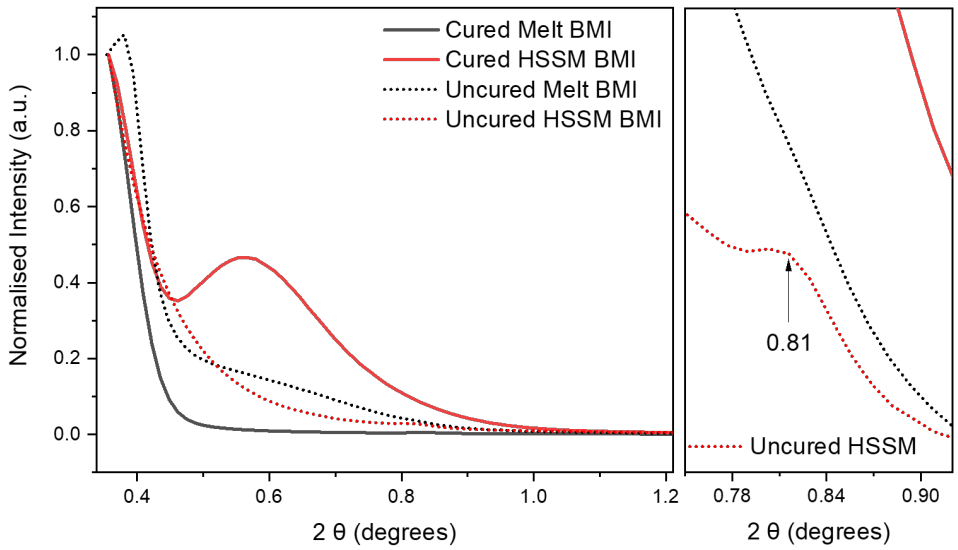

Figure A 2. SAXS plots of both, the uncured and cured BMI processed through Melt and HSSM. While the uncured Melt BMI demonstrated a peak at 0.38 °2θ suggesting heterogeneity, potentially from clustering of individual components, the uncured HSSM demonstrated a rather homogenous system with a minor peak at 0.81 °2θ.

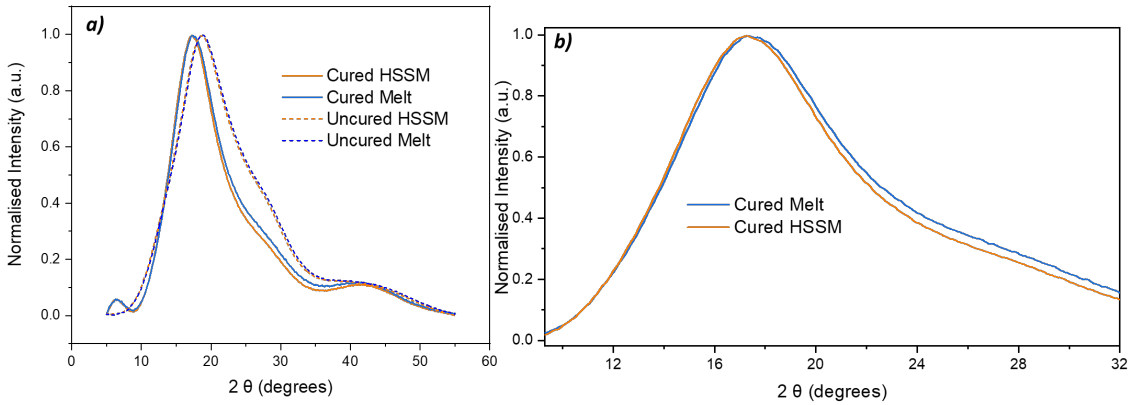

Figure A 3. (a and b) WAXD of the cured and uncured, Melt and HSSM BMI. (a) Differences between the uncured and cured specimens could be observed. No significant differences between the cured Melt and cured HSSM or the uncured Melt and the uncured HSSM were observed. (b) Magnified diffractogram of the cured Melt and HSSM BMI.

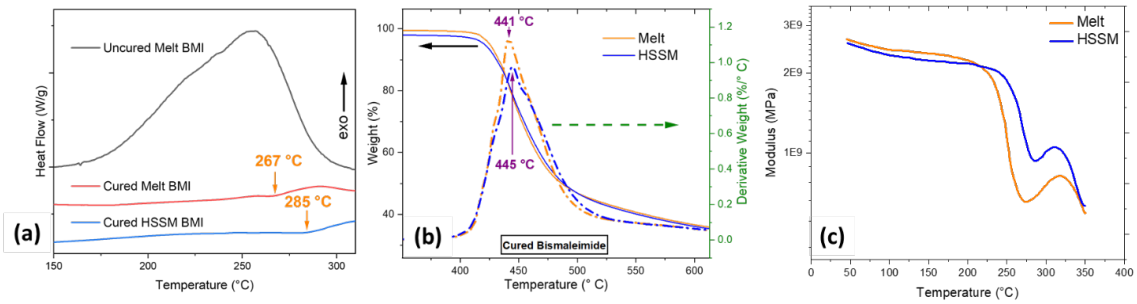

Figure A 4. (a) DSC plots of the uncured Melt BMI, cured, Melt and HSSM BMI at 10 °C/min heating rate in air atmosphere. The plots have been shifted along the y axis for ease of comparison. The cured Melt and HSSM BMI exhibited no exothermic peak related to the heat of cure as could be seen for the uncured melt BMI, thus suggesting that both samples undergwent complete curing. A change in the heat capacity is observed in cured melt BMI starting at about 267 °C and in cured HSSM melt BMI starting at about 285 °C. These temperatures are in close agreement with T_g values observed through DMA. (b) Thermal degradation of cured Melt and HSSM is determined using TGA under N_2 atmosphere at 10 °C/min heating rate. The peak position of the derivative curve of weight with temperature is taken as the degradation temperature. (c) Storage modulus of cured HSSM and Melt BMI with temperature. The discrepancy in the storage modulus at room temperature obtained through DMA and the Young's modulus obtained through universal tensile machine (Table S7) could result from the difference in the test conditions and instrument compliance.[6]

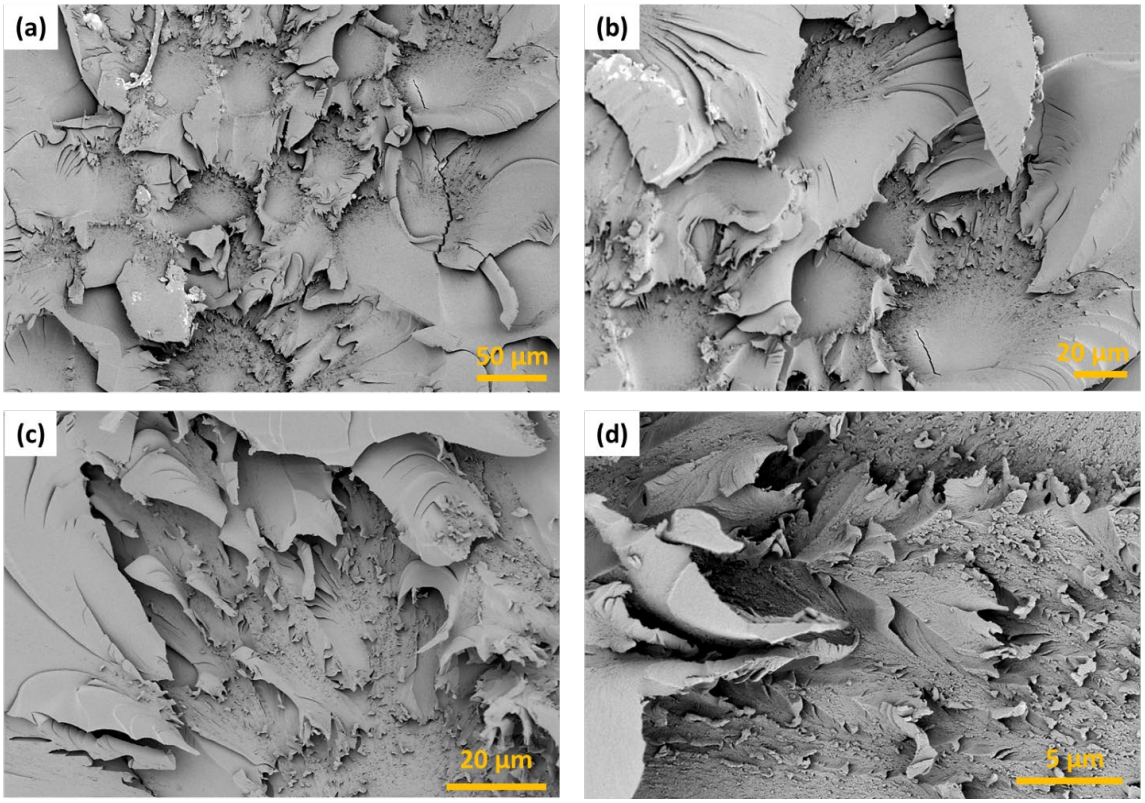

Figure A 5. (a-d) SEM images of cured HSSM BMI fracture surface in the crack initiation and propagation region at different magnifications demonstrating intense plastic deformation.

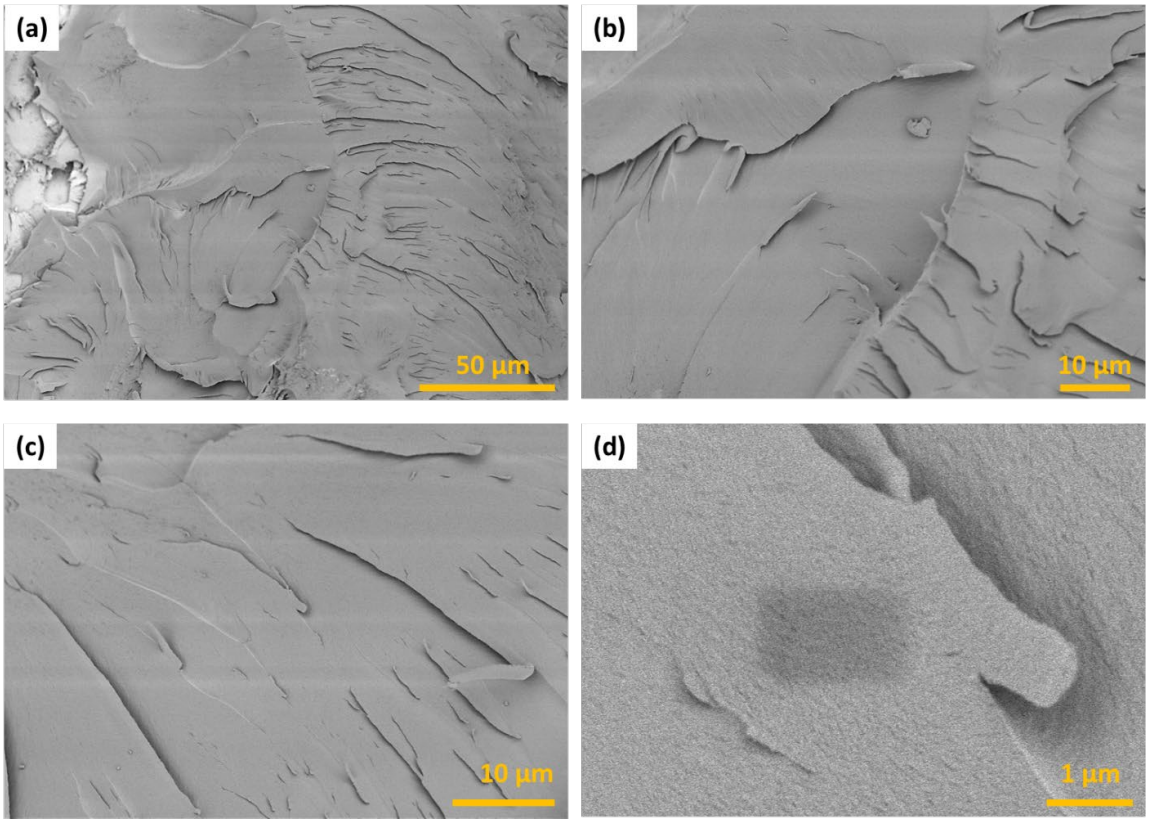

Figure A 6. (a-d) SEM images of cured Melt BMI fracture surface in the crack initiation and propagation region at different magnifications. Much smoother fracture surface is observed compared to the HSSM BMI (Figure S5).

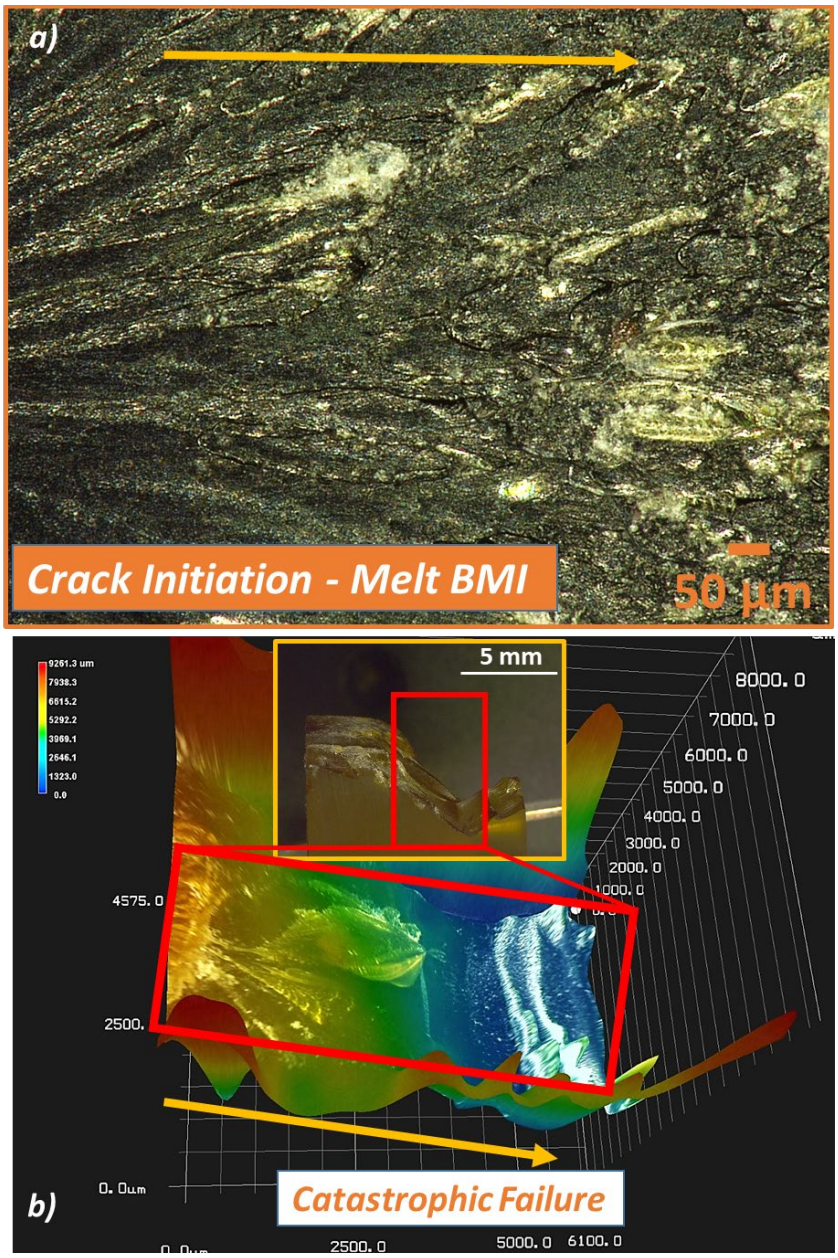

Figure A 7. (a) OM of the Melt BMI fracture surface in the crack initiation zone demonstrating streaks signifying crack propagation. No nodules are observed as were, for HSSM BMI. Yellow arrow points to the crack propagation direction. Yellow arrow points to the crack propagation direction. (b) 3D OM image of the Melt BMI demonstrating catastrophic failure.

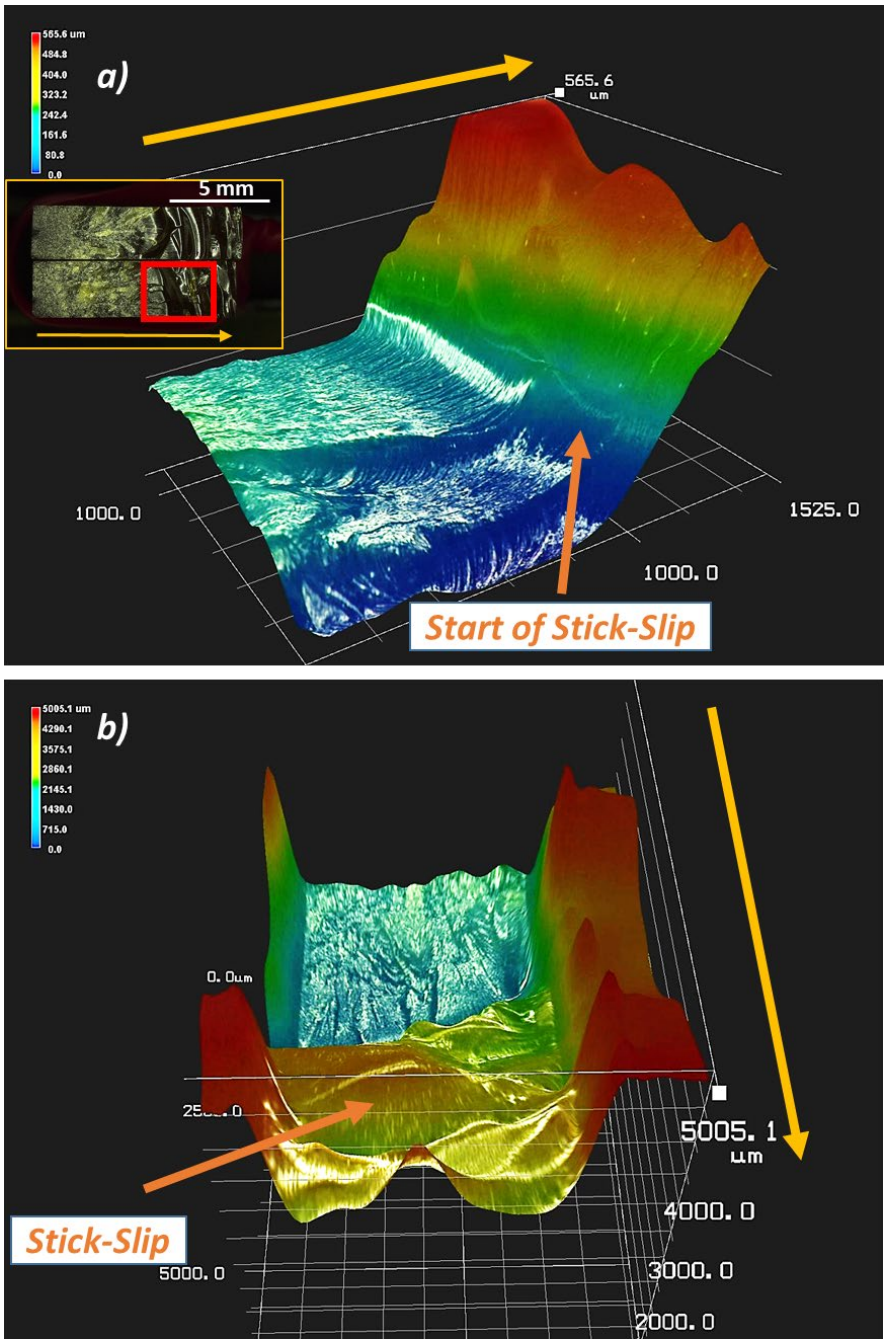

Figure A 8. (a and b) OM of HSSM BMI fracture surface at the transition zone from fast crack propagation to the stick-slip zone. Yellow arrow points to the crack propagation direction.

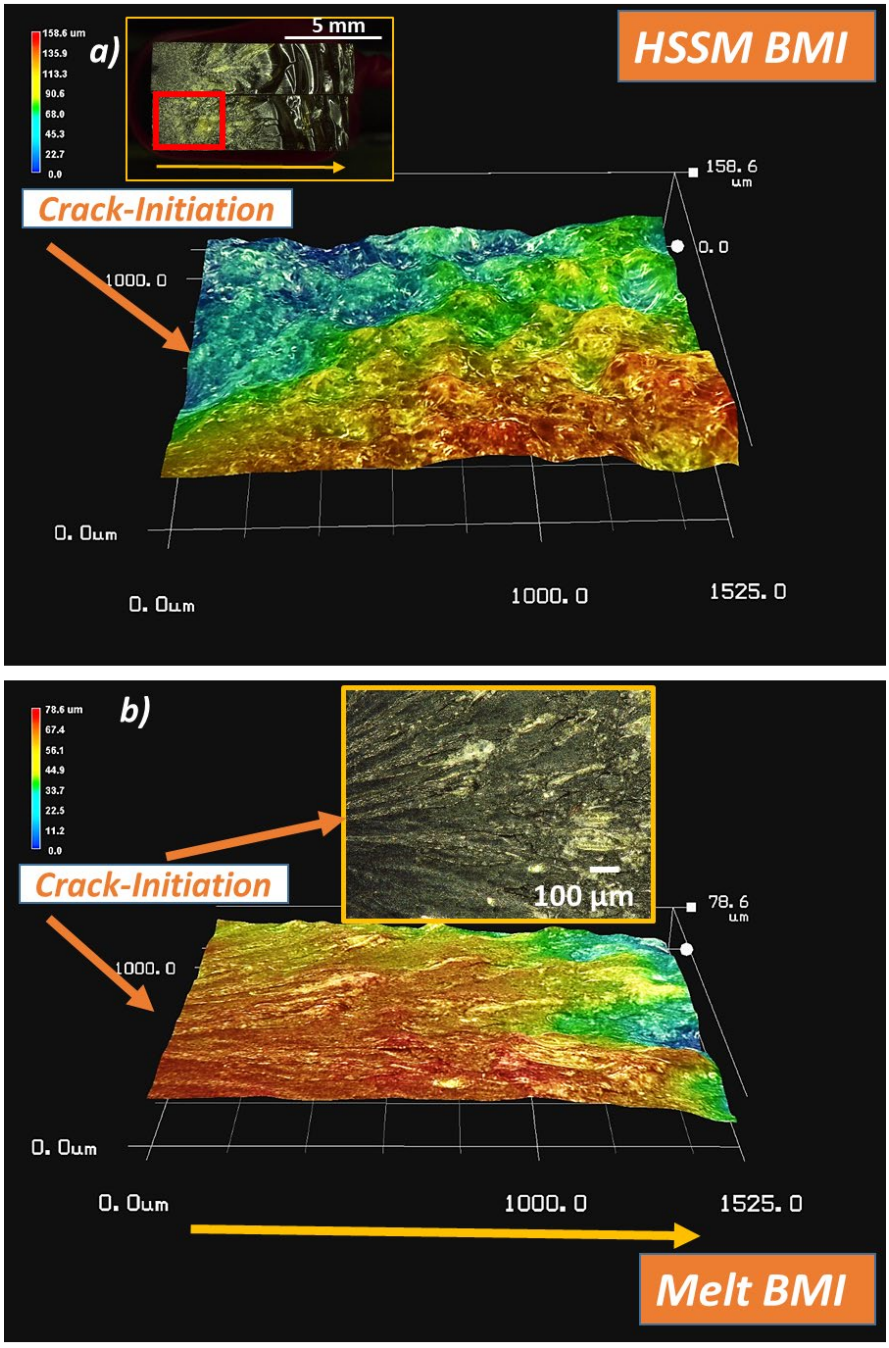

Figure A 9. OM of (a) HSSM BMI and (b) Melt BMI. HSSM BMI demonstrated about 2 times higher roughness in the crack initiation zone. Yellow arrow points to the crack propagation direction.

Table A 1. Impact Strength of p-BMI cast under different processing and casting conditions. Levels connected by same letter are statistically similar.

Condition	Number of samples tested	Impact Strength (kJ/m^2)	Std. Dev	Statistical Connection letter
Melt BMI				
A	10	20	7	a
B1	5	14	2	a
B2	5	14	6	a
HSSM BMI				
A	10	37	12	b
B1	15	56	15	c
B2	**10**	**69**	**13**	**d**

The cure and post cure temperature and their duration were identical for all conditions, 4-hours at 191°C and 2-hours at 227°C, respectively. 3 variations in specimen casting conditions were explored:

a) Condition 'A'- Specimens are in the mold (cure + post cure) for complete duration.

b) Condition 'B1'- Specimens are in the mold while curing but free standing for post cure, that is, specimens are demolded while in the oven at curing temperature upon completion of cure cycle of 4 hours for further free-standing post-cure.

c) Condition 'B2'- Specimens are in the mold while curing but free standing for post cure, oven is cooled down to room temperature after completion of cure cycle, specimens are demolded, and oven is heated to post cure temperatures for free-standing post-cure.

Table A 2. P-values illustrating the statistical significance of impact strength data listed in Table A 1. P-value smaller than 0.05 is considered statistically significant.

Processing type and cure condition	Melt "B1"	Melt "B2"	HSSM "A"	HSSM "B1"	HSSM "B2"
Melt "A"	0.3	0.3	0.003	<0.0001	<0.0001
Melt "B1"	X	0.9	0.001	<0.0001	<0.0001
Melt "B2"		X	0.002	<0.0001	<0.0001
HSSM "A"			X	0.0009	<0.0001
HSSM "B1"				X	0.014
HSSM "B2"					X

Table A 3. List of major FTIR and Raman peaks and their assignments [45], [173]–[175]. The check mark represents a distinct observation of the corresponding peaks in this study in specimens including uncured and cured- Melt and HSSM BMI.

Wavenumber (cm^{-1})	Functional Group	FTIR	Raman
687	C=C−H (out-of-plane bending)	✓	
823	C=C (deformation mode)	✓	
787	C=O (Out of plane)		
947	C−C (maleimide)		
≈1110	C−O (Phenol/Ether)	✓	✓
1145	C−N−C (succinimide)	✓	
≈1169	C−N−C (maleimide)	✓	✓
≈1260	C−O (Phenol/Ester)	✓	✓
≈1395-1373	O=C−N (Ring)	✓	✓
1509	C=C (Aromatic)	✓	✓
1583	C=C Maleimide		✓
≈1605	C=C (Aromatic)		✓
1645	**Unassigned**		✓
1703	C=O (Carbonyl- asymmetric)	✓	
≈1776	C=O (Carbonyl- symmetric)		✓
≈2848	CH_2 (symmetric stretch)	✓	
≈2870	CH_3 (symmetric stretch)	✓	
≈2920	CH_2 (asymmetric stretch)	✓	
≈2960-2980	CH_3 (asymmetric stretch)	✓	

Table A 4. Activation energy and reaction kinetics parameters at various temperatures following Kissinger and Ozawa methods for Melt BMI and HSSM BMI

Kissinger method							
	E_a (kJ/mol)	A (s^{-1})	$k_{150\,°C}$	$k_{175\,°C}$	$k_{200\,°C}$	$k_{225\,°C}$	$k_{250\,°C}$
Melt	73	5×10^6	0.005	0.017	0.05	0.12	0.28
HSSM	83	57×10^6	0.003	0.012	0.04	0.11	0.28
Ozawa method							
	E_a (kJ/mol)	A (s^{-1})	$k_{150\,°C}$	$k_{175\,°C}$	$k_{200\,°C}$	$k_{225\,°C}$	$k_{250\,°C}$
Melt	75	8×10^6	0.005	0.016	0.05	0.12	0.28
HSSM	85	80×10^6	0.003	0.011	0.04	0.11	0.29

E_a- Cure activation energy
A - Pre-exponential factor
k – reaction rate constant at various temperatures

Table A 5. Melt BMI and HSSM BMI exhibit statistically similar tensile properties. However, the properties are lower compared to the manufacturer reported values.[164]

	Tensile Strength (MPa)	**Tensile Modulus (GPa)**	**Strain at break (%)**
Melt	47 ± 7	3.6 ± 0.1	1.2 ± 0.2
HSSM	46 ± 15	3.6 ± 0.2	1.3 ± 0.5
Manufacturer reported	103	4.6	4.8

Table A 6. Tensile strength of p-BMI cast under different processing and casting conditions. Levels connected by same letter are statistically similar

Condition	Number of samples tested	Tensile Strength (MPa)	Std. Dev	Statistical Connection letter
Melt BMI				
A	10	51	16	a
B1	5	57	13	a
B2	5	47	7	a
HSSM BMI				
A	10	53	14	a
B1	15	50	12	a
B2	10	46	15	a

Table A 7. p-values showing the statistical significance of tensile strength data in Table A 6. P-value smaller than 0.05 is considered statistically significant.

Processing type and cure condition	Melt "B1"	Melt "B2"	HSSM "A"	HSSM "B1"	HSSM "B2"
Melt "A"	0.55	0.62	0.78	0.89	0.46
Melt "B1"	X	0.34	0.7	0.46	0.23
Melt "B2"		X	0.47	0.67	0.9
HSSM "A"			X	0.65	0.3
HSSM "B1"				X	0.49
HSSM "B2"					X

Table A 8. Tensile Modulus of p-BMI cast under different processing and casting conditions. Levels connected by same letter are statistically similar.

Condition	Number of samples tested	Tensile Modulus (GPa)	Std. Dev	Statistical Connection letter
Melt BMI				
A	10	4	0.3	a, b
B1	5	3	0.3	e
B2	5	3.6	0.1	b, c, d
HSSM BMI				
A	10	3.6	0.4	b, c
B1	15	4.1	0.4	a
B2	10	3.6	0.2	c

Table A 9. p-values showing the statistical significance of tensile modulus data in Table A 8. P-value smaller than 0.05 is considered statistically significant.

Processing type and cure condition	Melt "B1"	Melt "B2"	HSSM "A"	HSSM "B1"	HSSM "B2"
Melt "A"	<0.0001	0.11	0.058	0.42	0.039
Melt "B1"	X	0.01	0.0022	<0.0001	0.0044
Melt "B2"		X	0.93	0.022	0.91
HSSM "A"			X	0.0046	0.8
HSSM "B1"				X	0.003
HSSM "B2"					X

Table A 10. Strain at break of p-BMI cast under different processing and casting conditions. Levels connected by same letter are statistically similar.

Condition	Number of samples tested	Strain at break (%)	Std. Dev	Statistical Connection letter
Melt BMI				
A	10	1.3	0.5	a
B1	5	2.2	0.5	b
B2	5	1.2	0.2	a
HSSM BMI				
A	10	1.6	0.3	a
B1	15	1.1	0.3	a
B2	10	1.3	0.5	a

Table A 11. p-values showing the statistical significance of strain to break data in Table A 10. P-value smaller than 0.05 is considered statistically significant.

Processing type and cure condition	Melt "B1"	Melt "B2"	HSSM "A"	HSSM "B1"	HSSM "B2"
Melt "A"	0.0015	0.84	0.24	0.48	0.86
Melt "B1"	X	0.0032	0.02	0.0003	0.001
Melt "B2"		X	0.25	0.7	0.95
HSSM "A"			X	0.07	0.19
HSSM "B1"				X	0.59
HSSM "B2"					X

APPENDIX B. SUPPLEMENTARY INFORMATION FOR CHAPTER 3

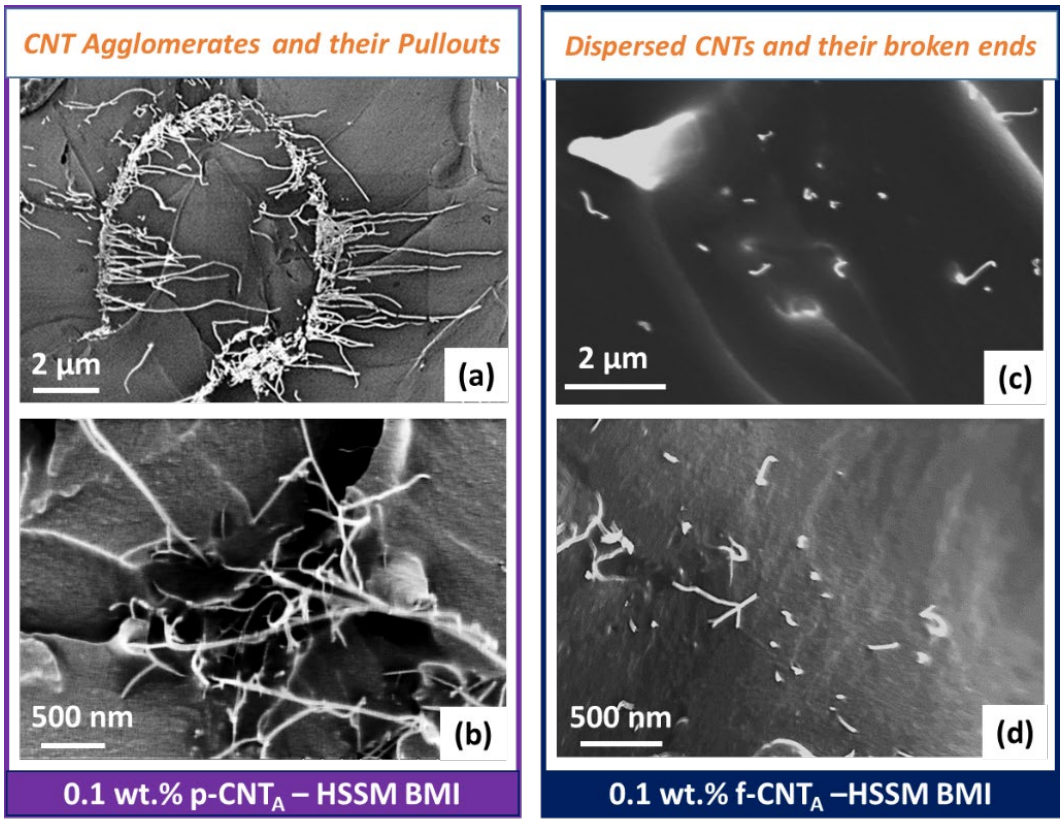

Figure B 1. SEM image of the impact fracture surface of (a, b) 0.1 wt% p-CNT_A- HSSM BMI showing CNT agglomerates and pullout. (c, d) 0.1 wt% f-CNT_A- HSSM BMI showing well dispersed CNTs with broken CNT ends. The broken CNT ends signify strong interfacial bonding between the f-CNT_A and BMI.

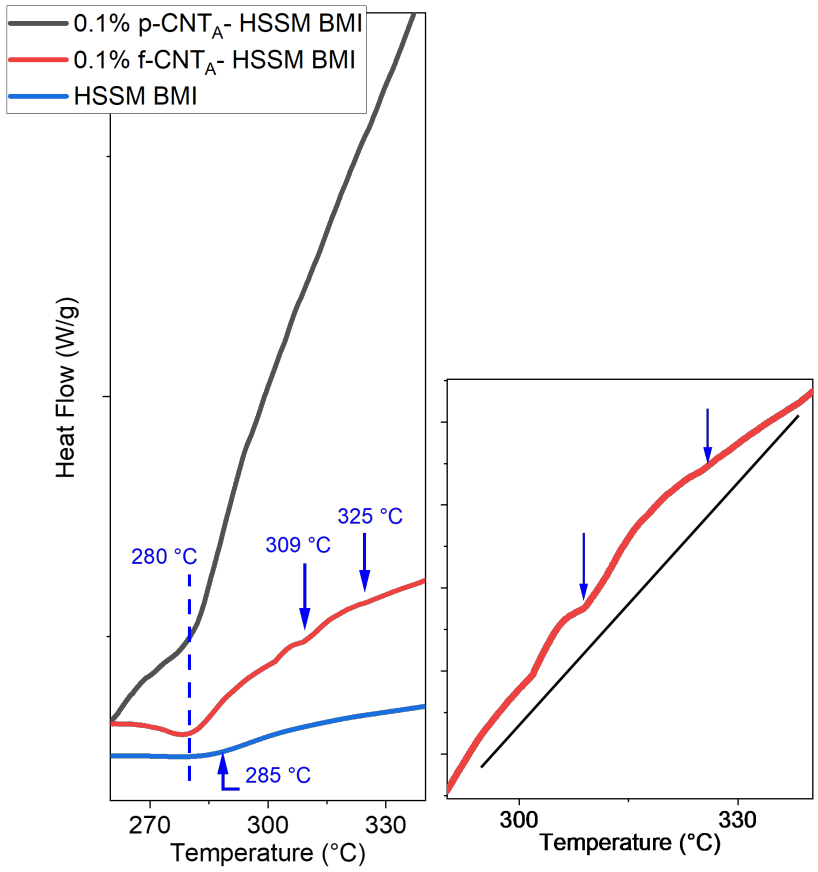

Figure B 2. DSC curve of HSSM BMI, 0.1 wt% p-CNT$_A$- HSSM BMI and 0.1 wt% f-CNT$_A$- HSSM BMI. HSSM BMI demonstrates a single glass transition whereas the 0.1 wt% f-CNT$_A$- HSSM BMI demonstrates multiple glass transitions. DSC was performed at a heating rate of 10 °C/min under air atmosphere. The inset shows a close-up view of the secondary transitions in the 0.1 wt% f-CNT$_A$- HSSM BMI.

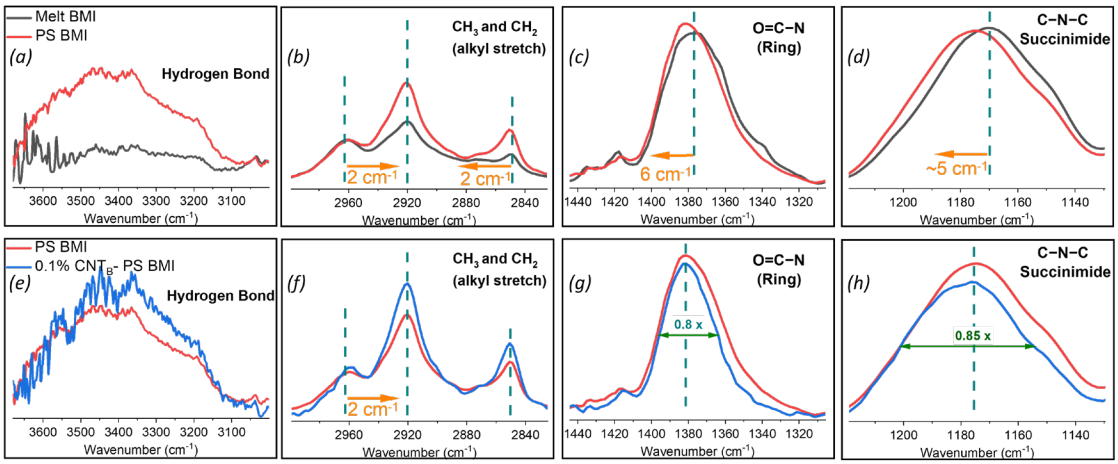

Figure B 3. FTIR spectra of (a-d) Melt BMI and PS BMI and (e-h) PS BMI and 0.1 wt% CNTB-PS BMI. Peak shifts and the change in the FWHM signify a difference in the inter and intra molecular interactions in the system.[255] These plots thus suggest that the inter/intra-molecular interactions in the HSSM p-BMI, 0.1 wt% p and f CNTA- HSSM BMI systems are different from each other. All curves were normalized to the intensity of the C=C peak at 1509 cm−1.

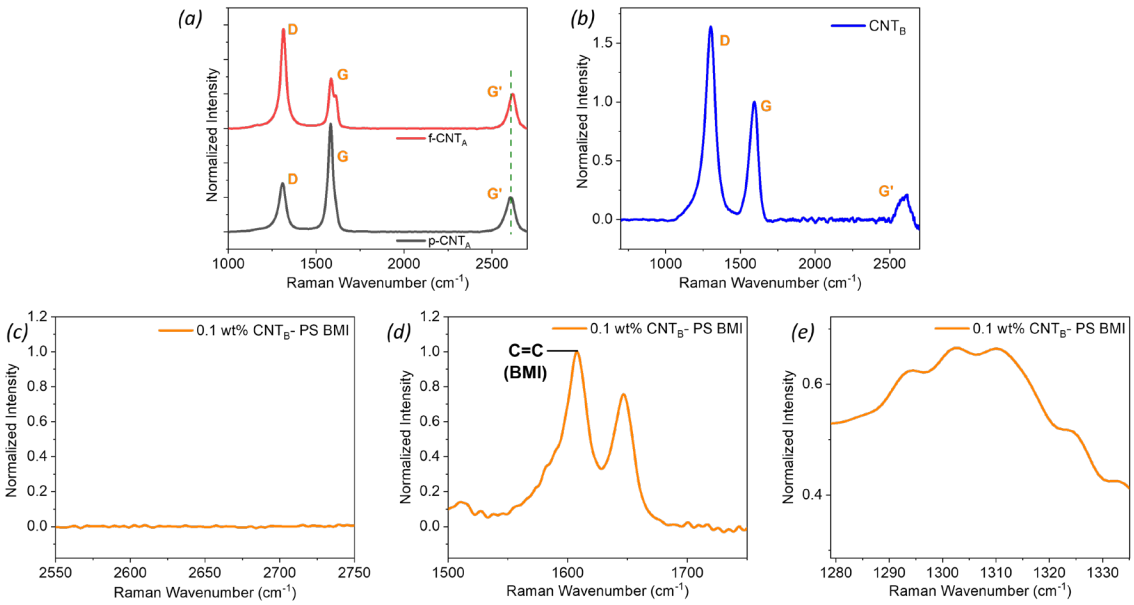

Figure B 4. Raman spectra of (a) p-CNT$_A$ and f-CNT$_A$, (b) CNT$_B$ and (c-e) 0.1 wt% CNT$_B$- PS BMI. The 0.1 wt% CNT$_B$- PS BMI does not show a Raman G' peak from the CNT$_B$. A distinct Raman G or D band from the CNT$_B$ is missing aswell and hence Raman could not be used to confirm if the CNT$_B$ compress upon cure of BMI or not. The Raman G band at ~1593 cm^{-1} also overlaps with the C=C (aromatic) peak at 1608 cm^{-1} from the BMI. Plots in a and b are normalized to the Raman G bands peak intensity. Plots in c and d are normalized to the C=C (aromatic) peak at 1608 cm^{-1} from the BMI, since a distinct G band associated with CNT$_B$ could not be observed

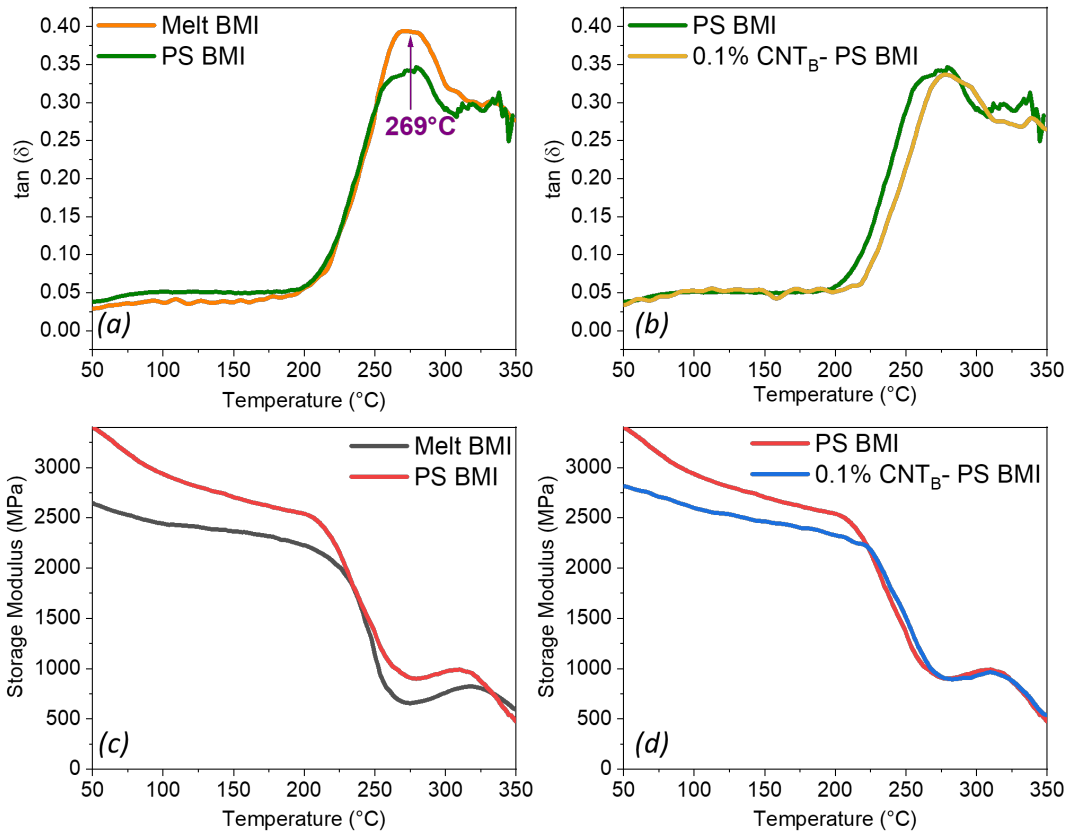

Figure B 5. The PS BMI has 15% lower tan δ peak and ~18-20% higher storage modulus compared to the Melt BMI, in the rubbery region. This signifies that the PS BMI's cross-linked network has higher rubber elasticity. The HSSM BMI had a 33% lower tan δ peak and ~40-45% higher storage modulus compared to Melt BMI as well.[256] The results of PS and HSSM processed BMI suggests that processing the multi-component BMI system before cure leads to a better formed cross-linked network with higher rubber elasticity. The 0.1 wt% CNT_B- PS BMI has a delayed onset of glass transition by 15° C, compared to the PS BMI.

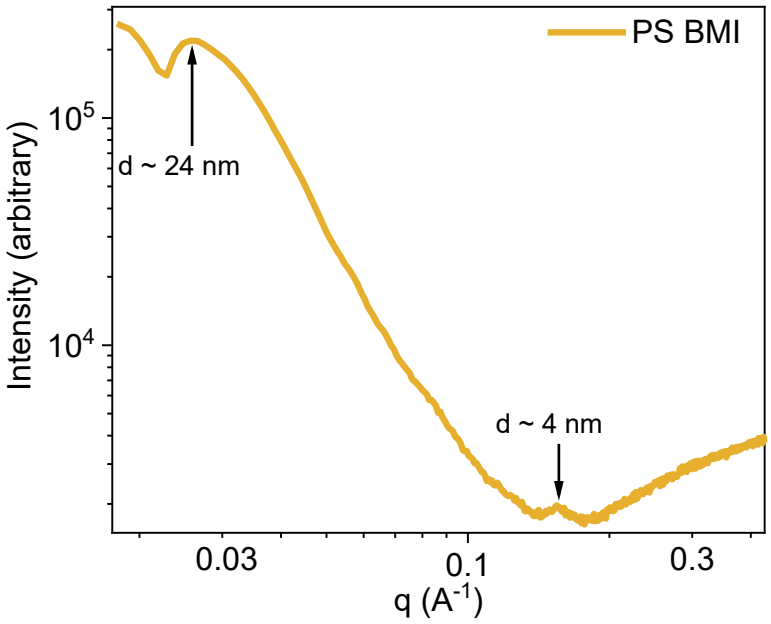

Figure B 6. SAXS of the PS BMI. Peaks at q values of 0.026 and 0.155 A^{-1} are observed which correspond to the Bragg's d-spacing of 23.6 and 4 nm (assuming Bragg's diffraction).

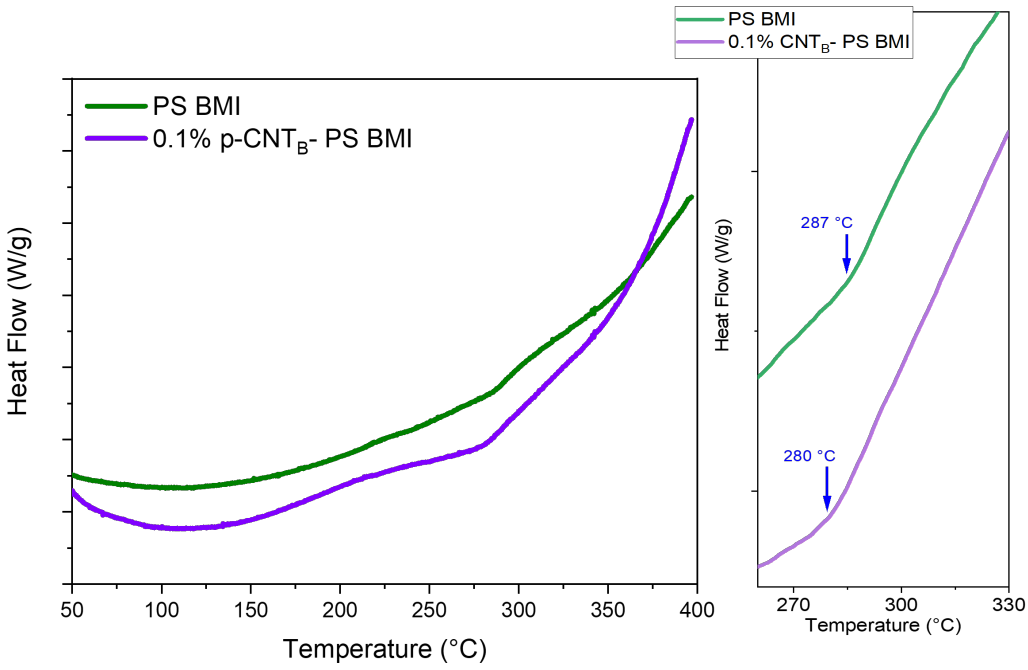

Figure B 7. DSC curve of cured PS BMI and 0.1 wt% CNT_B- PS BMI demonstrating T_g at 287 and 280 °C, respectively.

Table B 1. Improvements and limitation reported in the literature for CFRPs, toughened through 'nano-filler reinforced matrix'.

System	Toughening Strategy	Improvements Reported	Limitations reported	Refere-nce
CF-Epoxy-AS4/ Huntsman GY 6010 + DY070	Matrix reinforcement with CNT	G_{1C} values: Neat epoxy: 106 J/m^2 0.5% CNT-epoxy: 182 J/m^2 CF-Neat Epoxy: 176 J/m^2 CF-CNT-Epoxy Hybrid: 498 J/m^2.	-	Fenner and Daniel[210]
CF-Epoxy-HinFab HCP 301/ Epofine LY5052+ HY5052	Matrix reinforcement with graphene, CNT and nano diamond (total nano-filler content of 0.8 wt.%)	Up to 0.55x increase in Mode I inter-laminar fracture toughness (from 0.18 to 0.28 MPa/m^2).	-	Bisht *et. al*.[211]
CF-Epoxy-Wela/ Huntsman LY564+ HY2954	Matrix reinforcement with CNTs (0.5 wt.%)	0.35x in specific delamination energy, when impact energy was 20 J	No difference in the delamination area and the absorbed energy per unit delamination area at impact energy was 16 J or less	Kostopoulos *et. al*.[212]
CF-Epoxy-Hexcel/ LY564+ HY2954	Matrix reinforcement with up to 0.1, 0.5 and 1 wt.% CNT	Up to 0.65x and 0.75x in G_{IC} and $G_{IIC,}$ respectively (from 0.3 to 0.52 kJ/m^2 and 1 to 1.75 kJ/m^2, respectively)	25% reduction in G_{IIC} upon addition of 0.1 wt. % CNT	Karapappas *et. al*.[257]
CF-Epoxy-Newport graphite unitape G150 NASS/ BA-epichlorohydrin	Matrix reinforcement with 0.1 wt.% CNT	13% in G_{IC} propagation, 12% in G_{IIC} non-precracked, 27% in G_{IIC} precracked.	-	Ashrafi *et. al*.[213]
CF-Epoxy-R&G/ LY556+ Aradur1571+ Accelerator 1573+ XB3403	Matrix reinforcement with up to 1 wt. % nano-filler (graphene, CNT)	Up to 0.45x and 0.25x in G_{1C} and G_{IIC}, respectively (from 0.55 to 0.8 kJ/m^2 and 1.57 to 1.97 kJ/m^2.	-	Kostagiannakopoulou *et. al*.[215]

Table B 1 continued

CF-Epoxy-Tenax G30-700 12K HTA-7C/ D.E.R. 331+ D.E.N 431+ XD5200	Matrix modification with: (a) organo-modified layered silicate, (b) vapor grown carbon fiber (VCGF) and (c) polystyrene butadiene methyl methacrylate (SBM)	1x increase in G_{IIC} for composites containing VCFG reinforced matrix.	G_{IC} initiation decreased for all types of composites made with nano-modified resin (from 0.2 kJ/m^2 up to 0.05 kJ/m^2). 50% reduction in G_{IIC} for composites containing SBM modified matrix.	Quaresimin and Varley[207]

Table B 2. Improvements and limitation reported in the literature for CFRPs, toughened through 'interlayer toughening'.

System	Interlayer Toughening Strategy	Improvements Reported (compared to laminate without interlayer toughening)	Limitations reported	Refere-nce
CF-Epoxy-Toray T800H/3900-2	Adding polyamide particles in the interlayer	2.5x in in Mode I inter-laminar fracture toughness (from 0.2 to 0.71 kJ/m^2).	The crack path transitioned from interlayer to the interlayer- base lamina interface	Hojo *et. al.*[188]
	Adding a thermoplastic-ionomer interlayer	3x in Mode I inter-laminar fracture toughness (from 0.2 to 0.6 kJ/m^2).	The crack propagated through the interlayer- base lamina interface	
CF-Epoxy-AS4/977-3	Adding interlayers of electrospun polycarbonate nanofiber mats	8.1% in first ply failure (FPF) (from 167.2 MPa to 181.2 MPa).	-	Sihn *et. al.*[190]
CF-Epoxy (C12K,450,-45/+45)/ (MY0510)	Adding interlayers of electrospun polyetherketone cardo (PEK-C)	~1x in the strain energy release rate (G_{1C}) for crack initiation (from 151 J/m^2 to up to 249 J/m^2).	Flexure strength decreased by up to 12% to ~ 460 J/m^2 upon increasing polycarbonate fiber diameter up to 950 nm.	Zhang *et. al.*[191]
CF-Epoxy Toray P3052S-22	Adding carbon-nanofiber interlayer	~0.5x and up to 3x in Mode I and Mode II inter-laminar fracture toughness, respectively.	12% decrease in Young's modulus	Arai *et. al.*[193]
CF-Epoxy-IM7/977-3; AS4/8552	Adding a CNT forest interlayer	IM7/977-3: 2.5x in Mode I inter-laminar fracture toughness (from 0.21 to 0.53 kJ/m^2). AS4/8552: 1.5x and 3x in Mode I and Mode II inter-laminar fracture toughness, respectively (from 0.21 to 0.34 kJ/m^2 and 0.35 to 1.1 kJ/m^2, respectively)	Interlayer thickness of ~60 μm was reported owing to the CNT forest height. Future work on using shorter CNTs and thus thinner interlayers was recommended.	Garcia *et. al.*[81]

Table B 2 continued

CF-Epoxy-AS4- 8552	Adding a CNT forest interlayer	7% in short beam shear strength. At least 10% improvement in interlaminar toughness predicted via finite element modeling, based on crack transition to intralaminar region.	The crack transitioned into the intralaminar region. Future work on reinforcing the intralaminar region was recommended.	Ni *et. al.*[194]
CF-Epoxy-USN125/ SKR 2514 from SK-chemicals	Adding nonwoven carbon tissue interlayer (with and without CNTs)	Up to 3.5x and 2.5x in G_{IC} and G_{IIC}.	5% reduction in G_{IC} when using nonwoven carbon tissue without CNTs.	Lee *et. al.*[206]

Table B 3. Improvements and limitation reported in the literature for CFRPs, toughened through 'stitching, z-pins, 'thin ply', interlocking' techniques.

System	Toughening Strategy	Improvements Reported	Limitations reported	Referen-ce
CF-Epoxy-T8000SC-24K/ XNR-H6813	Through thickness stitching using Vectran fiber.	Up to 30% in final failure load (from 13 kN to 17 kN)	Up to 20% reduction in damage initiation load in stitched composites compared to unstitched (from 2.8 kN to 2.2 kN)	Tan *et. al*.[199]
CF-Epoxy-Hexply M21	Using rectangular and circular carbon-fiber/bismaleimide rods as z-pins	When using rectangular z-pins, 42x and 13x increase in G_{1C} of unidirectional and quasi-isotropic laminates, respectively (from 0.4 to 17 kJ/m^2 and 0.5 to 6.5 kJ/m^2, respectively.)	No change in inter-laminar fatigue resistance.	Hoffman and Scharr[196]
CF-Epoxy-T700 prepreg tape (VTM264)	Using carbon-fiber/bismaleimide rods as z-pins	Up to 15x in G_{1C} (from 1 to 15 kJ/m^2)	0.33x lower G_{1C} (10 vs 15 kJ/m^2) when z pin thickness was 510 µm as against 280 µm.(for the same length (4mm) and volume content (2%) of z-pins)	Pingkarawat and Mouritz[197]
CF-Epoxy-T8000SC-24K/ BT250E-1	Using 'thin ply' with thickness of 40 µm compared to base system with ply thickness of 200 µm. (Conventional ply thickness is ~125 µm).	While the thick samples demonstrated microctracks near the edge of the hole edge after static open hole tension loading at 448 MPa, the thin samples didn't demonstrate any microcracks.	Thick samples demonstrated pull-out failure mode whereas the thin samples demonstrated a brittle failure mode.	Sihn *et. al*.[200]
CF-Epoxy-Tenax HTS40/Q-1112	Synergistic effect of (a) 'thin ply' (54 µm thickness as against 162 µm) and (b) interlayer toughening with CNTs.	For samples examined post short beam shear stress (SBS) through Synchrotron Radiation Computed Tomography : Thick samples demonstrated intralaminar cracks extending in consecutive plies, while	CNT interlayer toughening yielded only a 5% increase in the SBS ILSS for the thin specimens.	Kalfon-Cohen *et. al*.[201]

		in the thin plies the cracks were arrested and remained within the interlayer. 10% improvement in interlaminar shear strength (ILSS) of 'thin ply' laminate		
CF-Epoxy-SK Chemicals Skyflex USN 020 A thin-ply prepreg	Using an 'interlocking' tab and slit interlaminar geometry	Up to 049x, 1.1x, 0.08x and 0.24x in G_{IC} initiation, G_{IC} propagation, G_{IIC} initiation, G_{IIC} propagation, respectively (from 0.39, 0.41, 0.88 and 1.01 kJ/m^2 to 0.59, 0.85, 0.95 and 1.25 kJ/m^2, respectively.	-	Pascoe *et. al.*[202]

Table B 4. Tensile properties of the HSSM and PS processed BMI and CNT-BMI nanocomposites.

Processing Method	CNT-BMI ratio (% represents weight %)	Tensile Strength (MPa)	Tensile Modulus (GPa)	Strain at Break (%)
HSSM	**100% BMI**	46 ± 15	3.6 ± 0.2	1.3 ± 0.5
	0.1% p-CNT_A -BMI	58 ± 9	3.5 ± 0.6	1.8 ± 0.1
	0.1% f-CNT_A–BMI	67 ± 3	3.3 ± 0.2	2 ± 0.2
	0.2% p-CNT_A–BMI	54 ± 6	3.4 ± 0.2	1.7 ± 0.2
	0.2% f-CNT_A–BMI	59 ± 8	3.3 ± 0.2	1.7 ± 0.1
PS	**100% BMI**	58 ± 18	3.1 ± 0.3	1.1 ± 0.4
	0.1% CNT_B–BMI	48 ± 15	3.5 ± 0.04	1.3 ± 0.5

APPENDIX C. SUPPLEMENTARY INFORMATION FOR CHAPTER 4

Table C 1. The cure activation energy (E_a) of the 100 wt% BMI, 10 wt% UB- 90 wt% BMI, 40 wt% UB- 60 wt% BMI and 30wt% B- 70 wt% BMI, calculated using Kissinger and Ozawa methods.

Sample	Reaction	Reaction Temperature Range (°C)	Activation Energy : Kissinger Method (E_{a-K}) kJ/mol	Activation Energy : Ozawa Method (E_{a-O}) kJ/mol
100 wt% BMI	1	N/A	N/A	N/A
	2	235-276	73	75
10 wt% UB – 90 wt% BMI	1	142- 153	187	167
	2	238- 287	57	62
40 wt% UB – 60 wt% BMI	1	N/A	N/A	N/A
	2	224-258	78	82
30 wt% B – 70 wt% BMI	1	204-232	90	93
	2	220-249	91	94

Table C 2. Tensile Properties of 100% BMI, 100% UB and B CNTs and their nanocomposites in the current study.

CNT-BMI ratio (% represents weight %)	Tensile Strength (MPa)	Tensile Modulus (GPa)	Strain at Break (%)	Density (g/cc)	Specific Tensile Strength (MPa/g/cc)	Specific Tensile Modulus (GPa/g/cc)
0% CNT- 100 % BMI	46 ± 15	3.6 ± 0.2	1.3 ± 0.5	1.17 ± 0.03	39 ± 13	3 ± 0.2
10% UB CNT sheet – 90% BMI	61 ± 10	2.1 ± 0.1	3.4 ± 0.6	1.42 ± 0.07	43 ± 7	1.4 ± 0.1
40% UB CNT sheet – 60% BMI	**222 ± 7**	**7.4 ± 0.5**	**5.1 ± 0.6**	**0.97 ± 0.09**	**230 ± 8**	**7.7 ± 0.5**
30% B CNT sheet – 70% BMI	123 ± 8	4.8 ± 0.4	3.1 ± 0.4	1.17 ± 0.1	104 ± 0.5	4.1 ± 0.5
100% UB CNT sheet- 0% BMI	3.5 ± 0.5	0.045 ± 0.007	14 ± 2	0.077 ± 0.005	46 ± 6	0.6 ± 0.1
100% B CNT sheet- 0% BMI	2.5 ± 0.2	0.046 ± 0.007	10 ± 1.6	0.036 ± 0.002	69 ± 6	1.3 ± 0.2

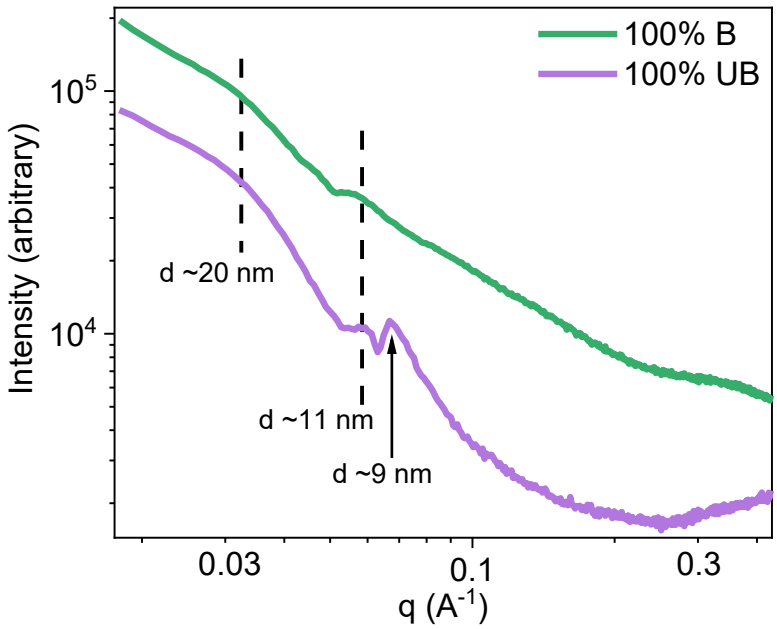

Figure C 1. SAXS of the 100 wt% B and 100 wt% UB CNT sheets. The 100 wt% B CNT sheet demonstrates peaks at q values of 0.032 (d~ 19.5 nm) and 0.054 A^{-1} (d~ 11.4 nm). The 100% UB CNT sheet demonstrates peaks at q values of 0.032 (d~ 19.5 nm), 0.058 (d~ 10.7 nm) and 0.067 A^{-1} (d~ 9.2 nm).

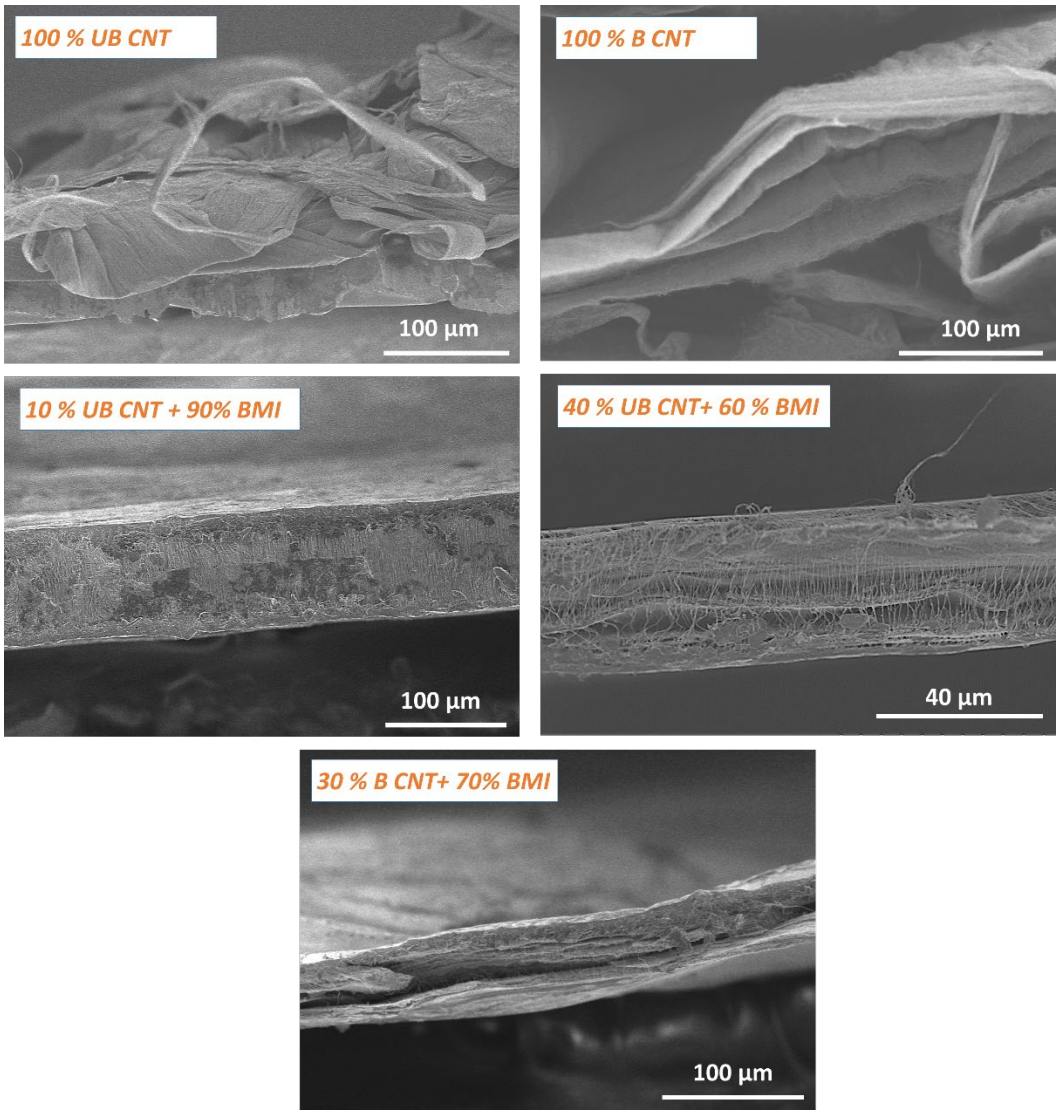

Figure C 2. SEM images of the tensile fractured cross-sections of the 100 wt% UB and B CNTs and their nanocomposites.

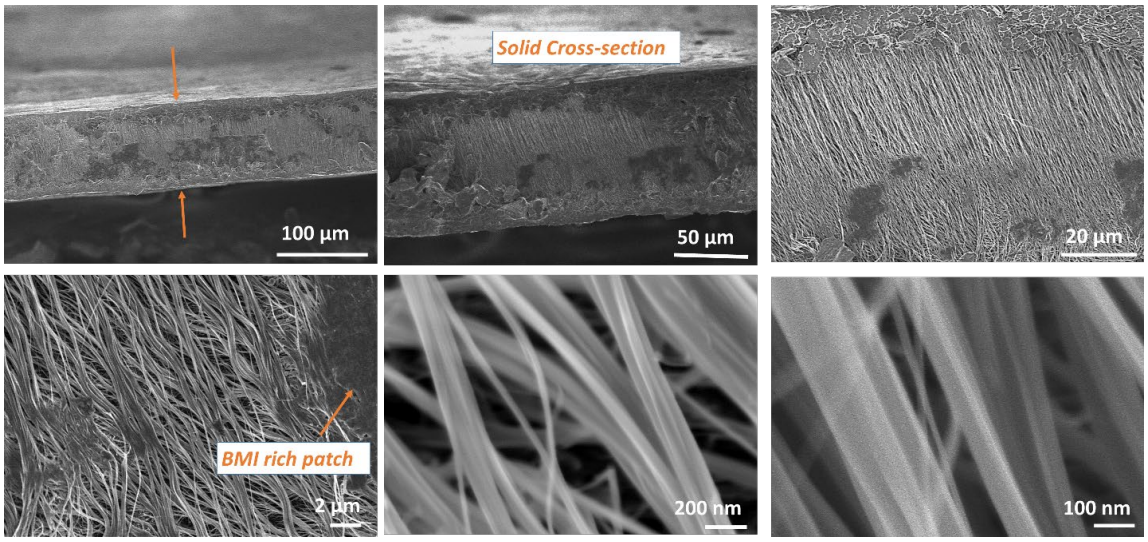

Figure C 3. SEM images of the tensile fractured cross-section of the 10 wt.% UB CNT- 90 wt% BMI nanocomposite.

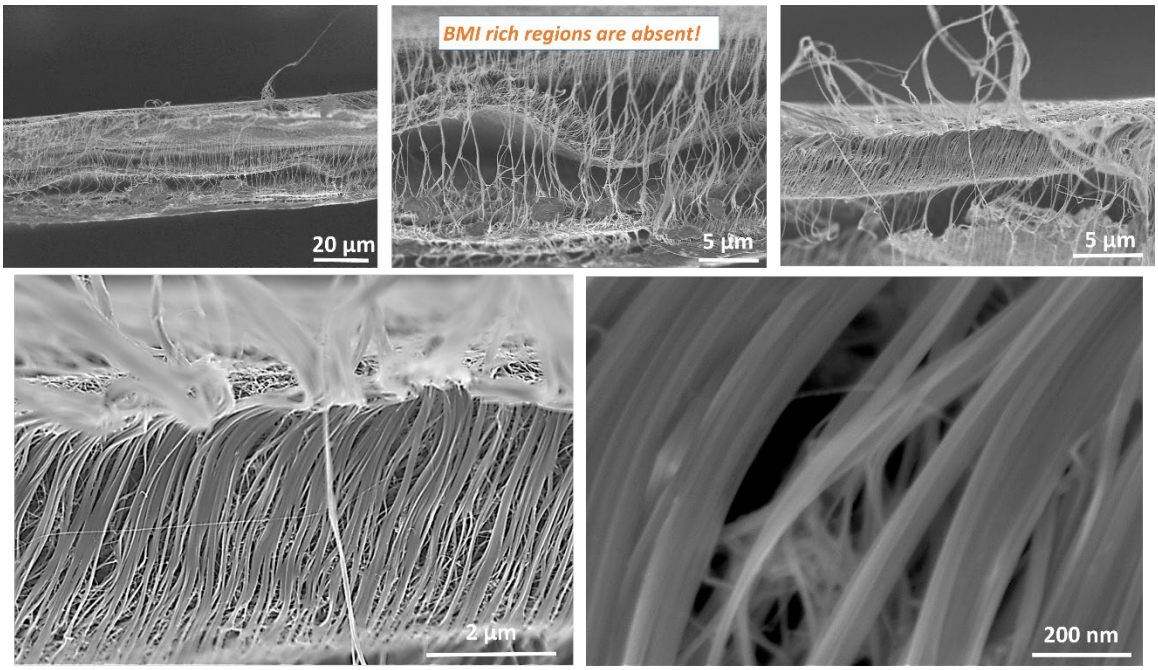

Figure C 4. SEM images of the tensile fractured cross-section of the 40 wt.% UB CNT- 60 wt% BMI nanocomposite.

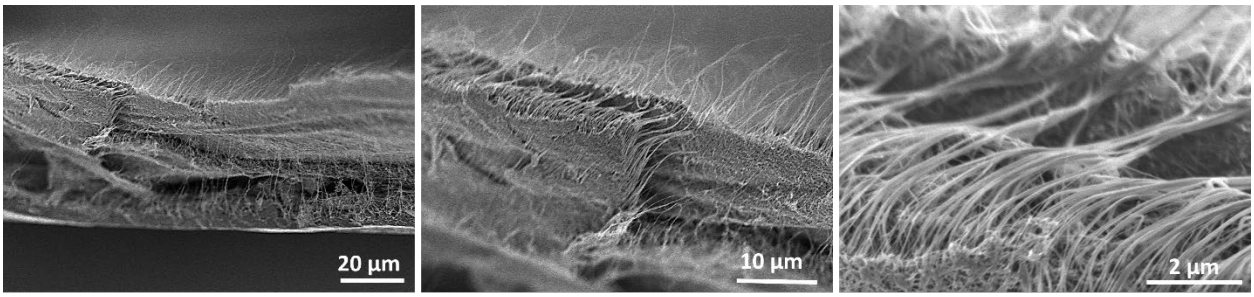

Figure C 5. SEM images of the tensile fractured cross-section of the 30 wt.% B CNT- 70 wt% BMI nanocomposite.

APPENDIX D. SUPPLEMENTARY INFORMATION FOR CHAPTER 5

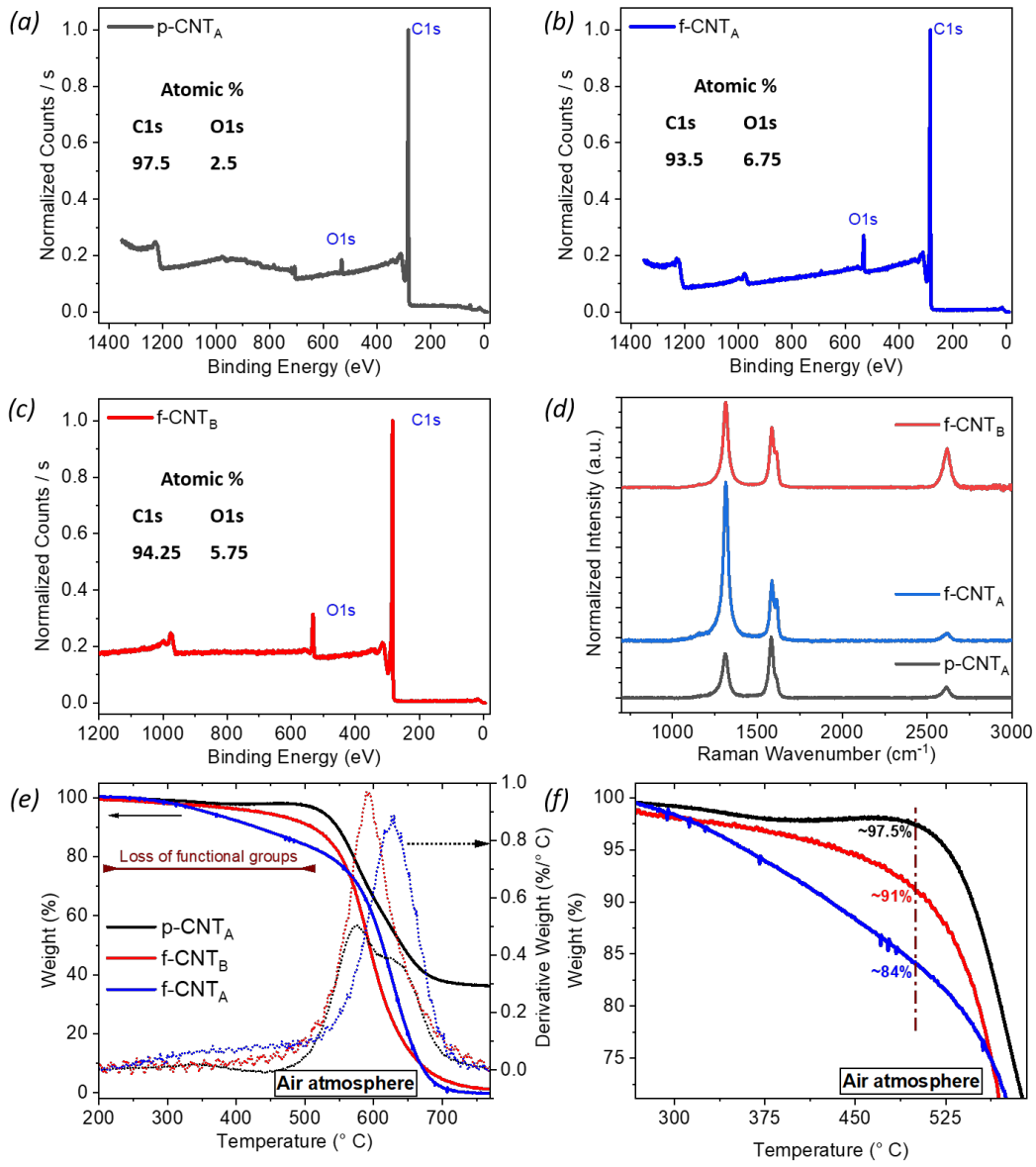

Figure D 1. (a-c) XPS survey scans of (a) p-CNT$_A$, (b) f-CNT$_A$, (c) f-CNT$_B$. (d) Representative Raman spectra of p-CNT$_A$, f-CNT$_A$, f-CNT$_B$. All curves are normalized to the Raman G band at ~1580 cm^{-1}. (e,f) TGA plots of p-CNT$_A$, f-CNT$_A$, f-CNT$_B$. TGA was conducted in air at a heating rate of 10 °C/min.

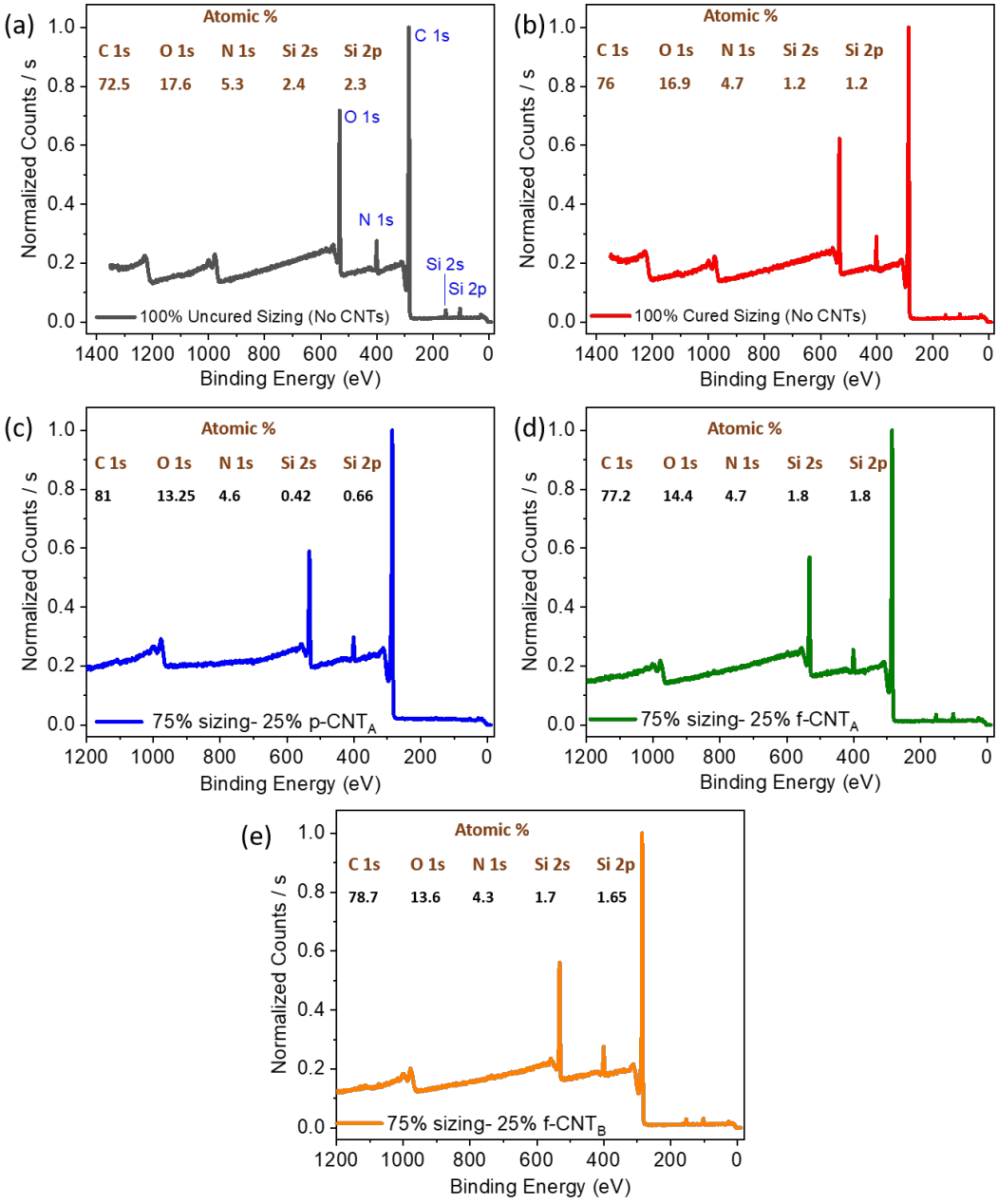

Figure D 2. XPS survey scans of (a) uncured 100 wt% sizing, (b) cured 100 wt% sizing, (c) 75 wt% sizing– 25 wt% p-CNT_A, (d) 75 wt% sizing– 25 wt% f-CNT_A, (e) 75 wt% sizing– 25 wt% f-CNT_B.

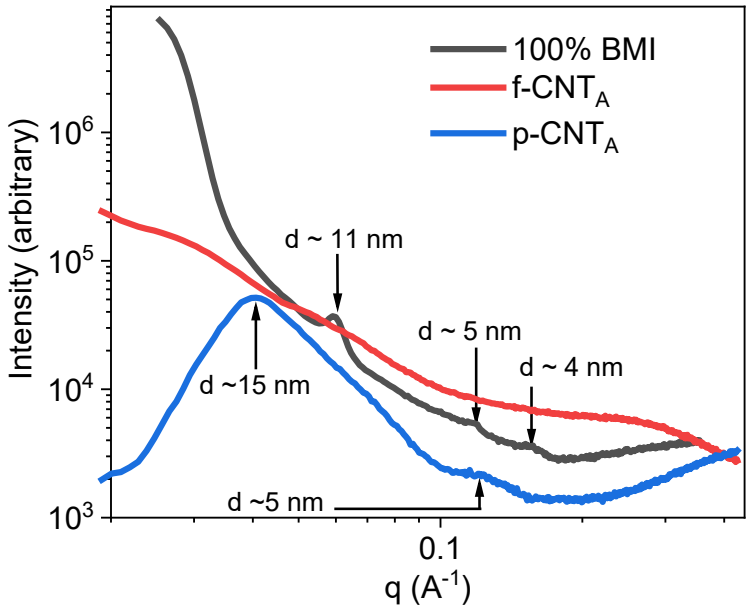

Figure D 3. SAXS plots of 100 wt% BMI, f-CNT$_A$ and p-CNT$_A$. The p-CNT$_A$ has peaks at q value of 0.0406 (d~ 15 nm) and 0.12 (d~ 5nm). The peak associated with the domain size of 15 nm could correspond to the CNT bundle size, and at the peak associated with the domain size of 5 nm could correspond to the inter-CNT spacing. The f-CNT$_A$ does not demonstrate the peaks observed in the p-CNT$_A$, likely because the CNTs are separated out of their bundles in the f-CNT$_A$ owing to the functionalization treatment.

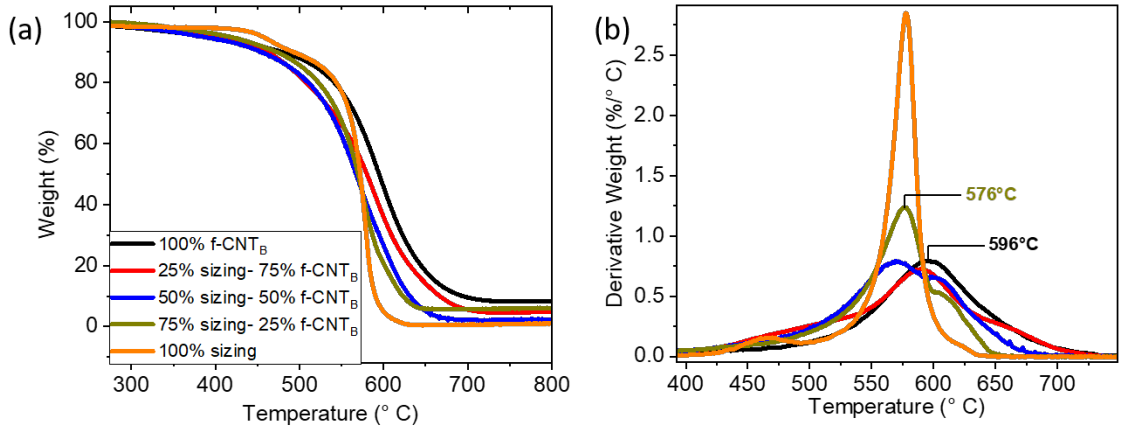

Figure D 4. (a-b) The TGA plots of f-CNT$_B$, 25 wt% sizing– 75 wt% f-CNT$_B$, 50 wt% sizing– 50 wt% f-CNT$_B$, 75 wt% sizing– 25 wt% f-CNT$_B$ and 100 wt% sizing. (a) weight loss and (b) The peak of the weight derivative with temperature is taken as the degradation temperature. All the specimens here have a degradation temperature in excess of 550 °C.

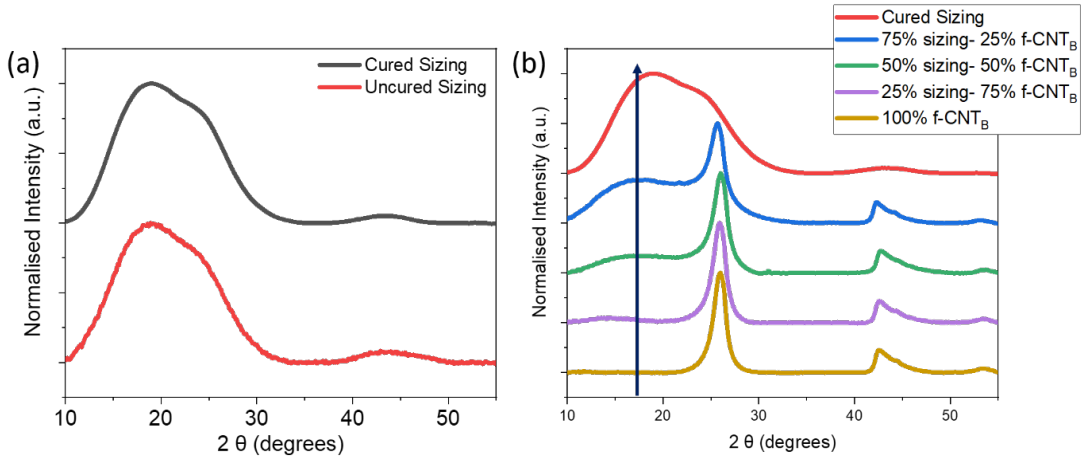

Figure D 5. X-ray diffraction of (a) cured and uncured 100 wt% sizing, (b) f-CNT_B, 25 wt% sizing– 75 wt% f-CNT_B, 50 wt% sizing– 50 wt% f-CNT_B, 75 wt% sizing– 25 wt% f-CNT_B and 100 wt% cured sizing.

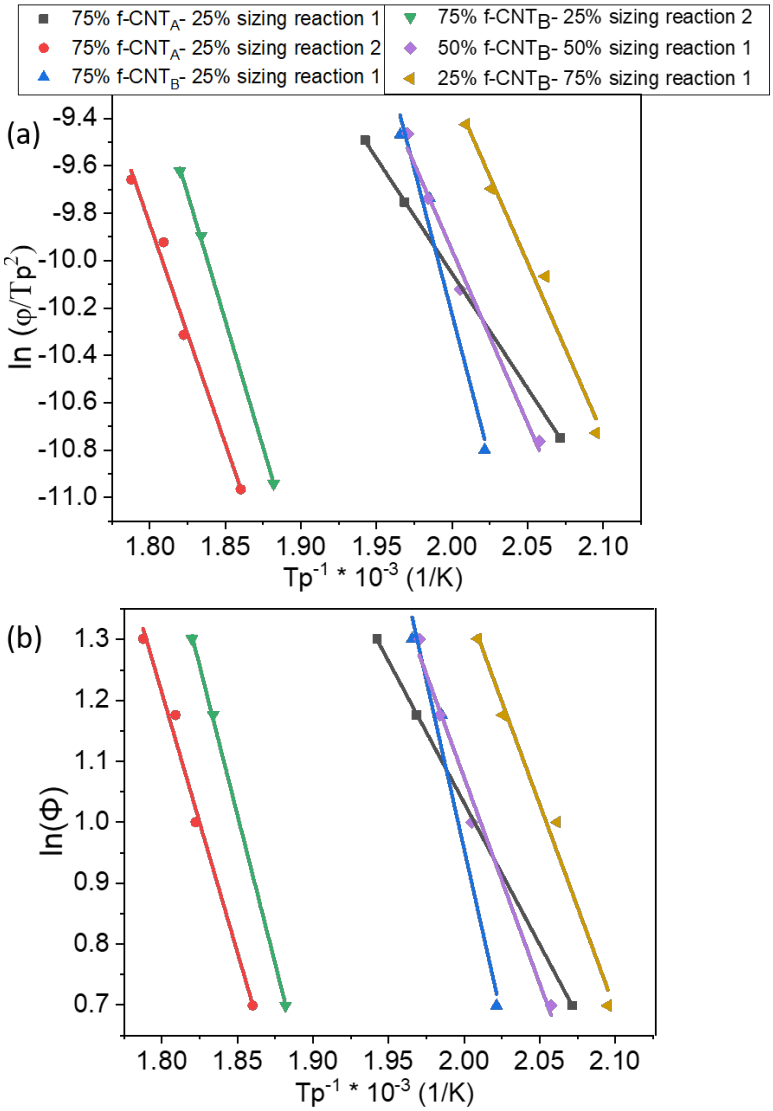

Figure D 6. Plots for determining the activation energy of the 25 wt% sizing– 75 wt% f-CNTB, 50 wt% sizing– 50 wt% f-CNT$_B$, 75 wt% sizing– 25 wt% f-CNT$_B$ and the 75 wt% sizing– 25 wt% f-CNT$_A$ using (a) the Kissinger method and (b) the Ozawa method. The slope of the linear plots was used for calculating the activation energy.

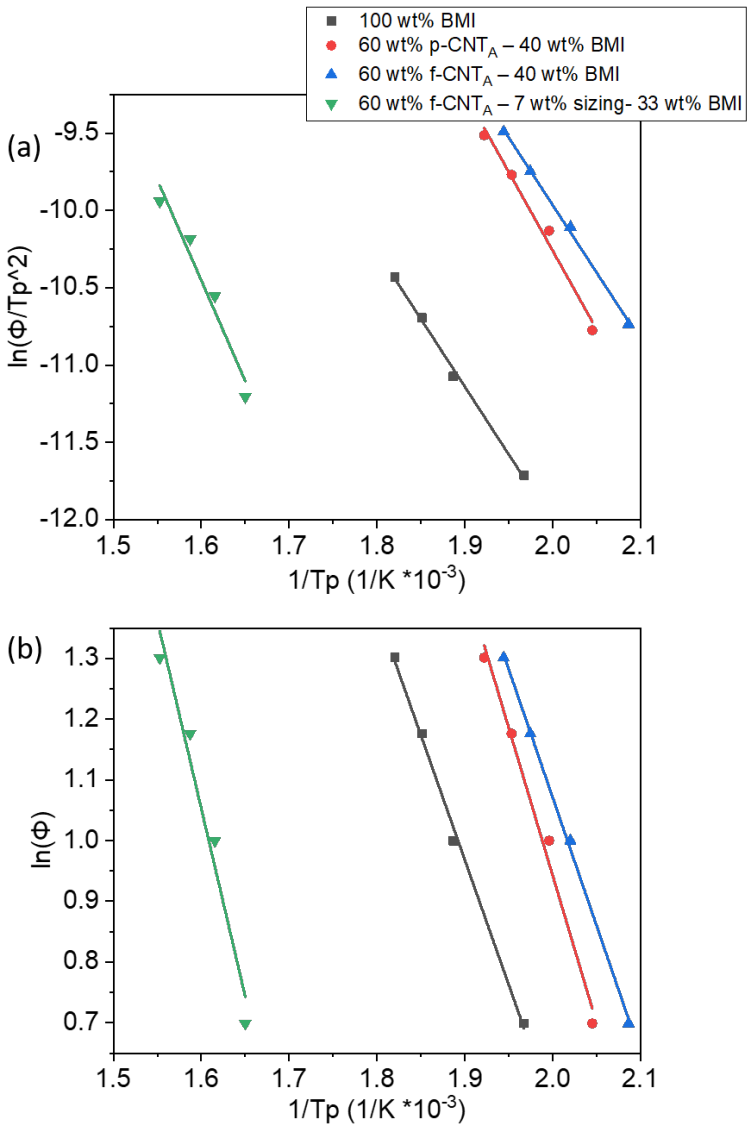

Figure D 7. Plots for determining the activation energy of the 100 wt% BMI, 60 wt% p-CNT_A – 40 wt% BMI, 60 wt% f-CNT_A – 40 wt% BMI and the 60 wt% f-CNT_A – 7 wt sizing- 33 wt% BMI using (a) the Kissinger method and (b) the Ozawa method. The slope of the linear plots was used for calculating the activation energy.

Table D 1. The cure activation energy (E_a) of the 100 wt% BMI, 60 wt% p-CNT_A – 40 wt% BMI, 60 wt% f-CNT_A – 40 wt% BMI and the 60 wt% f-CNT_A – 7 wt sizing- 33 wt% BMI, calculated using Kissinger and Ozawa methods.

Sample	Reaction	Activation Energy : Kissinger Method (E_{a-K}) kJ/mol	Activation Energy : Ozawa Method (E_{a-O}) kJ/mol
0% CNT- 100% BMI	1	73	75
60 wt% p-CNT_A – 40 wt% BMI	1	87	90
60 wt% f-CNT_A – 40 wt% BMI	1	73	77
60 wt% f-CNT_A – 7 wt% sizing- 33 wt% BMI	2	108	113
	3	N/A	N/A

Table D 2. Tensile properties of the different CNT and sizing coated CNT films prepared in this study.

Specimen	Tensile Strength (MPa)	Tensile Modulus (GPa)	Strain at Break (%)	Density (g/cc)	Specific Tensile Strength (MPa/g/cc)	Specific Tensile Modulus (GPa/g/cc)
p-CNT_A	0.6 ± 0.2	0.09 ± 0.02	1.1 ± 0.5	0.35 ± 0.04	1.3 ± 0.5	0.26 ± 0.05
f-CNT_A	6.5 ± 0.2	0.5 ± 0.01	1.4 ± 0.1	0.24 ± 0.01	28 ± 0.6	2.2 ± 0.1
f-CNT_B	7.6 ± 0.4	0.8 ± 0.03	1.4 ± 0.05	0.4 ± 0.05	19 ± 0.9	2 ± 0.09
75 wt% sizing– 25 wt% p-CNT_A	24.1 ± 5	1.5 ± 0.1	1.9 ± 0.34	0.64 ± 0.09	38 ± 6	2.4 ± 0.5
75 wt% sizing– 25 wt% f-CNT_A	28 ± 3	2.2 ± 0.25	1.4 ± 0.14	0.63 ± 0.07	43.4 ± 5	3.5 ± 0.2
75 wt% sizing– 25 wt% f-CNT_B	29 ± 3	2 ± 0.6	1.9 ± 0.3	0.6 ± 0.05	48 ± 4	3.4 ± 1
50 wt% sizing– 50 wt% f-CNT_B	12 ± 4.5	1.7 ± 0.1	0.9 ± 0.2	0.44 ± 0.04	28 ± 11	3.9 ± 0.4
25 wt% sizing– 75 wt% f-CNT_B	5.6 ± 0.8	0.7 ± 0.05	1.1 ± 0.1	0.3 ± 0.02	19 ± 3	2.4 ± 0.2

APPENDIX E. SUPPLEMENTARY INFORMATION FOR CHAPTER 6

Thermogravimetric analysis (TGA)

TGA in N_2 atmosphere at 10 °C/min heating rate was carried out to investigate the effect of baking of CNT sheets on their thermal stability and that of their composites with ~ 50 wt. % polyurea (Figure E 1). The weight content for both, the unbaked and baked CNTs remained at ~ 94- 95% at 400 °C, with degradation peaks (derivative peak of weight with temperature) at 206 °C and 346 °C for the unbaked CNT sheet and 354 °C for the baked CNT sheet. Beyond 400 °C, the unbaked CNTs demonstrated a higher weight loss and only ~ 65% of the initial weight remained at 800 °C with peak degradation temperatures at 493 °C and 690 °C, while the baked CNTs had ~ 90% of the initial weight remaining at 800 °C (Figure E 1a). This confirms that CNT sheet of higher purity are obtained upon baking as has also been demonstrated in prior works.[25], [248], [258]

Polyurea undergoes a two-step degradation where the first step is associated with the loss of harder segment containing the lesser thermally stable urea group while the second step is associated with loss of softer aliphatic segment.[247] The two step peak degradation of unbaked CNT sheet with 49 wt. % polyurea is at 298 °C and 393 °C whereas the degradation temperature increases to 301 °C and 401 °C for baked CNT sheet with 53 wt. % polyurea (Figure E 1 c, d). The increase in thermal stability in CNT-polymer composites could be attributed to factors including, (a) stronger barrier effect of CNT network that hinders the diffusion of polymer to the gas phase,[259] (b) thermal

conductivity of CNT network which facilitates in heat dissipation in the composite and thereby delays polymer degradation.[259] (c) stronger interfacial interaction between the CNTs and polymer.[16], [259] The composite of unbaked CNT sheet has a higher bulk density of 0.65 ± 0.05 g/cc compared to composite of baked CNT sheet with 0.3 ± 0.05 g/cc (Table E 3) and thus the barrier effect from the composite network would be higher in the composite with unbaked CNT sheet. The thermal conductivity of CNTs reduce upon damage to the CNT walls.[6], [260] Here, the thermal conductivity should thus be higher in unbaked CNTs with fewer defects and consequently a higher thermal stability. Two of the three factors listed above, i.e., the barrier effect and thermal conductivity would predict a higher thermal degradation temperature for the composite of unbaked CNT sheet yet, however the strong interfacial interaction factor outweighs both of them as the observed degradation temperature is higher for composite of baked CNT sheet. This signifies that the polyurea-CNT interfacial interaction in the composite with baked CNT sheet leads to a more thermally stable polyurea interphase as well.

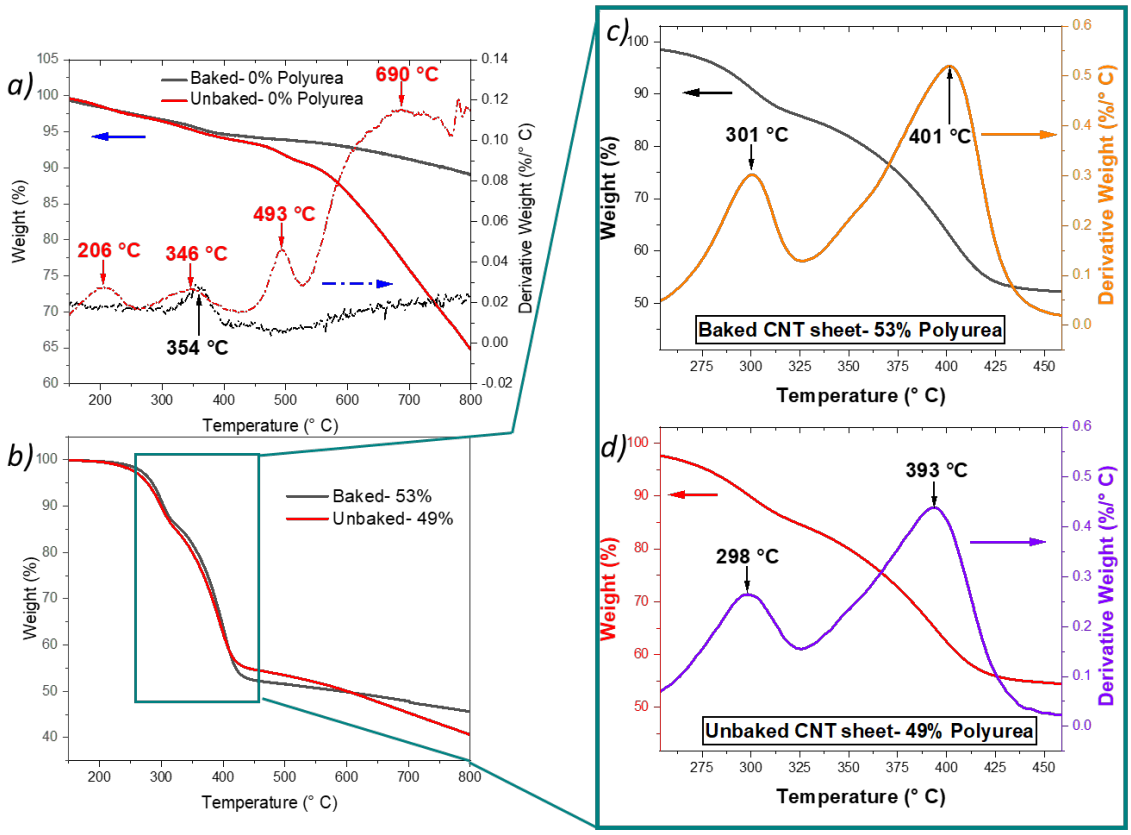

Figure E 1. TGA plot of unbaked and baked CNT sheets, (a) without polyurea, (b) with ~ 50 wt. % polyurea. (a) The dotted curves correspond to the derivative of the weight with temperature. The baked sheet demonstrates a higher thermal stability. (c-d) two-step degradation of polyurea could be observed at ~ 300 °C and ~400 °C. The peak of the derivative curve of the weight with temperature is taken as the degradation temperature. (c) Baked CNT sheet with 53 wt. % polyurea demonstrates a higher degradation temperature by 3 °C and 8 °C for the two steps respectively compared to (d) unbaked CNT sheet with 49 wt. % polyurea.

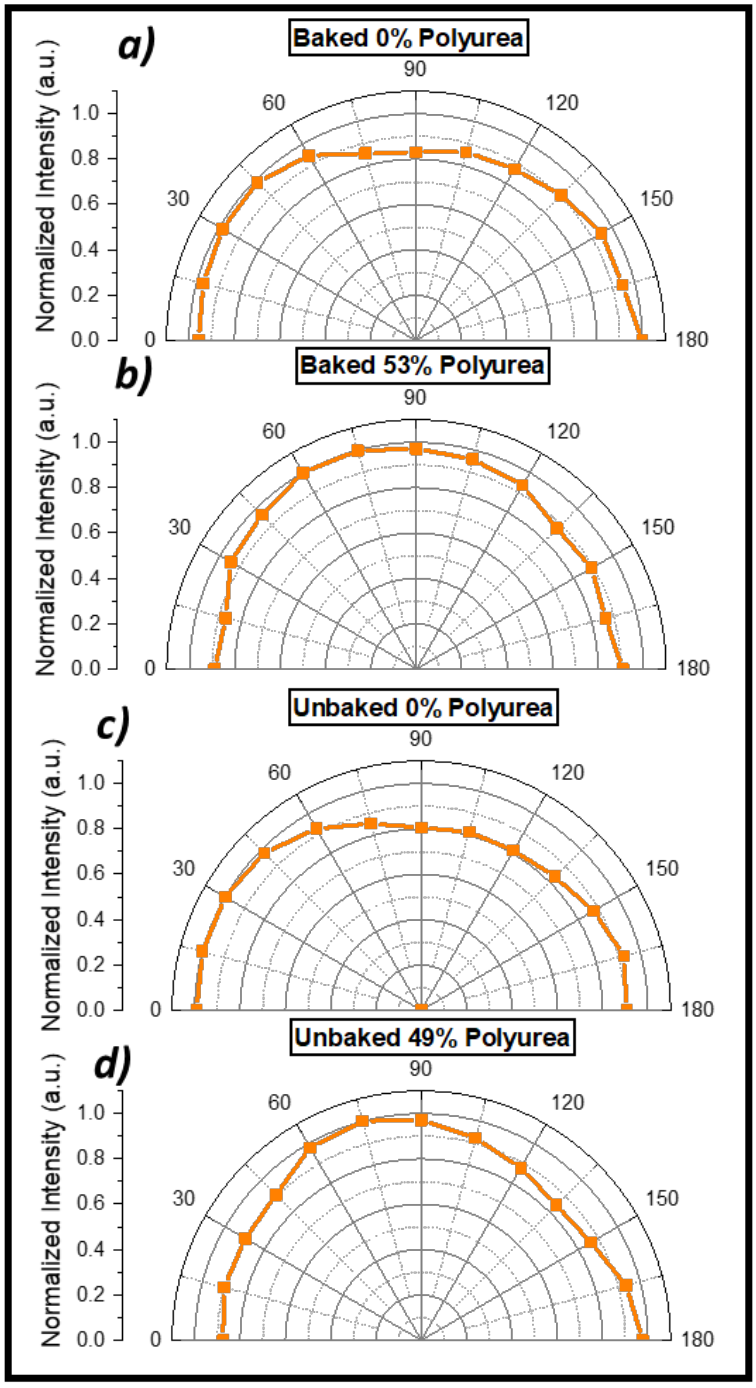

Figure E 2. Polar plots showing the intensity of the Raman G' band as a function of rotation angle under VV configuration of (a) baked CNT sheet without polyurea, (b) baked CNT sheet with 53 wt. % polyurea, (c) unbaked CNT sheet without polyurea, (d) unbaked CNT sheet with 49 wt. % polyurea.

Table E 1. CNT orientation parameter for unbaked and baked CNT sheets and their composites with polyurea at ~50 wt. % loading. P_2 represents second order orientation factor or the Herman's orientation factor. P_4 represents the fourth order orientation factor. The $<P_2(\cos\theta)>$ and $<P_4(\cos\theta)>$ values are between 0 to 0.08, signifying random or little orientation of CNTs in these sheets.

Sheet Type	$<P_2(\cos\theta)>$	$<P_4(\cos\theta)>$
Baked 0% Polyurea	0.03	0.02
Baked 53% Polyurea	0	0.04
Unbaked 0% Polyurea	0.07	0.02
Unbaked 49% Polyurea	0	0.08

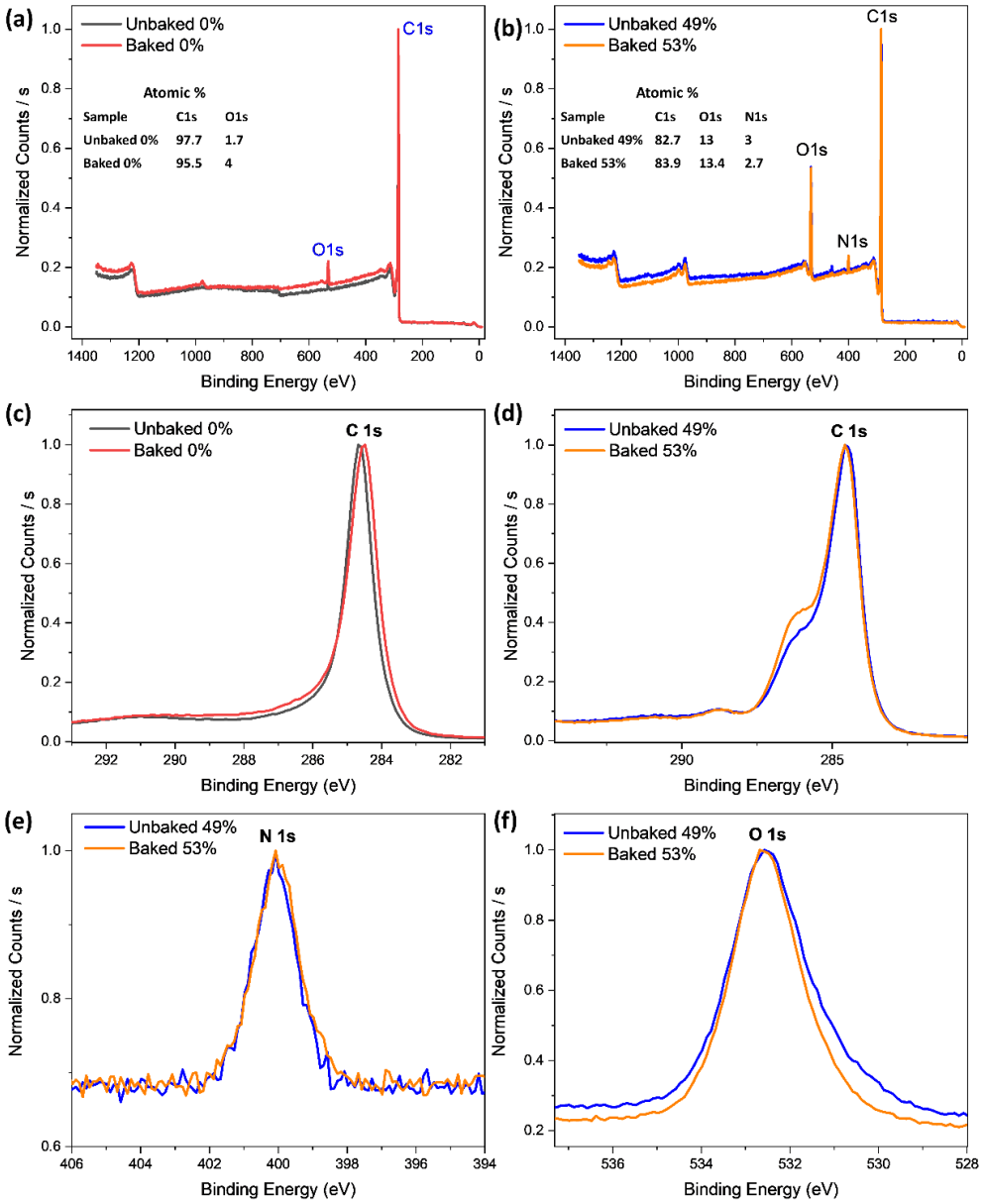

Figure E 3. (a and b) XPS survey scan of (a) unbaked and baked CNT sheets with no polyurea. (b) unbaked and baked CNT sheet with 49 wt.% and 53 wt.% polyurea, respectively. (c) XPS spectra of C 1s for unbaked and baked CNT sheet with no polyurea. Difference in the peaks signifies difference in sp^2 and sp^3 carbon content resulting from the removal of amorphous carbon and the formation of sp^3 carbon in nano-crystalline or hexagonal diamond structures upon baking (as observed through Raman spectroscopy).[253] (d-f) XPS spectra of unbaked and baked CNT sheet with 49 wt.% and 53 wt.% polyurea in different regions. (d) C 1s region. The difference in the spectra signifies an overall difference in distribution of $C=C$, $C-C$, $C-N-C$ and $C=O$ content.[261] (e) N1s region, (f) O 1s region.

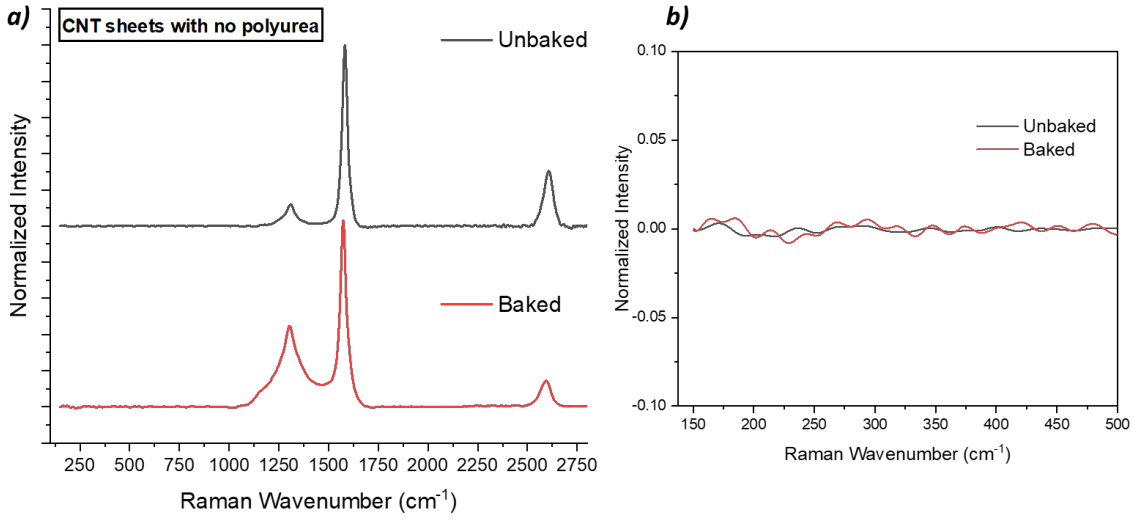

Figure E 4. Raman spectra of unbaked and baked CNT sheets with no polyurea: (a) in the 150-2800 wavenumber range, (b) magnified spectra in the 150-500 wavenumber range. The plots have been normalized to the intensity of the G band at ~1580 cm^{-1}. No radial breathing modes (RBM) are observed, signifying that the CNTs are multiwall.

Table E 2. CNT (002) crystal size derived from FWHM of 2θ ~26° integrated x-ray diffraction peak. The number of walls of CNT is calculated based on 0.347 nm interlayer spacing corresponding to the 002 peak position.

CNT (No Polyurea)	(002) Crystal Size (nm)	No. of walls
Unbaked	3.1	8.9
Baked	3	8.7

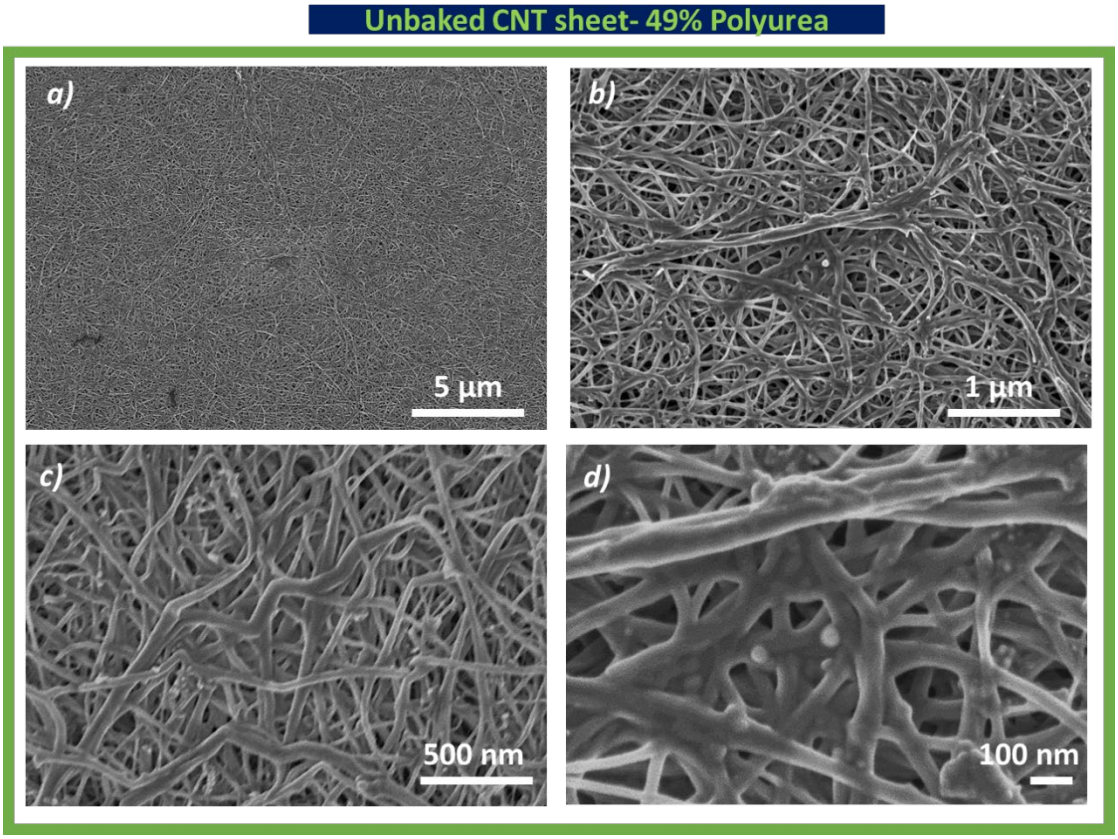

Figure E 5. (a-d) SEM images of the surface of unbaked CNT sheets containing 49 wt. % polyurea in increasing order of magnification.

Table E 3. Tensile properties: tensile strength, tensile modulus, strain at break, specific tensile strength and specific tensile modulus of unbaked and baked CNT sheets and their composites with polyurea. The mechanical properties do not correlate with Raman G′ shifts, the reasons for which remain to be understood.

Sheet Type	Tensile Strength (MPa)	Tensile Modulus (GPa)	Strain at Break (%)	Specific Tensile Strength (MPa/g/cc)	Specific Tensile Modulus (GPa/g/cc)
Baked 0% Polyurea	2.5 ± 0.2	0.046 ± 0.007	10 ± 2	53 ± 7	1.3 ± 0.2
Baked 25% Polyurea	18 ± 4	1 ± 0.1	2.8 ± 0.7	104 ± 25	5.6 ± 0.2
Baked 42% Polyurea	15 ± 4	0.6 ± 0.1	3 ± 0.7	79 ± 17	2.9 ± 0.3
Baked 53% Polyurea	30 ± 3	1.2 ± 0.2	3.7 ± 1	104 ± 26	4 ± 0.8
Unbaked 0% Polyurea	3.5 ± 0.5	0.045 ± 0.007	14 ± 2	25 ± 1	0.6 ± 0.1
Unbaked 22% Polyurea	52 ± 7	1.3 ± 0.2	12 ± 1	131 ± 16	4.4 ± 0.2
Unbaked 40% Polyurea	90 ± 13	2.4 ± 0.2	12 ± 5	101 ± 26	4.6 ± 0.1
Unbaked 49% Polyurea	93 ± 14	3.5 ± 0.4	12 ± 3	79 ± 18	5.1 ± 0.4

Table E 4. Bulk density of composites of unbaked and baked CNT sheets. The increase in density of composites with increasing Polyurea content suggests a decreasing porosity level and higher densification. Thickness of the samples were measured using a micrometer at 25 different points on each sheet. Density is calculated from weight to volume ratio from 5 different measurements.

Sheet Type	Thickness (μm)	Density (g/cc)
Baked 0% Polyurea	277 ± 41	0.036 ± 0.003
Baked 25% Polyurea	81 ± 10	0.17 ± 0.02
Baked 42% Polyurea	108 ± 14	0.19 ± 0.02
Baked 53% Polyurea	80 ± 10	0.3 ± 0.05
Unbaked 0% Polyurea	208 ± 28	0.07 ± 0.01
Unbaked 22% Polyurea	67 ± 14	0.3 ± 0.04
Unbaked 40% Polyurea	39 ± 4	0.53 ± 0.05
Unbaked 49% Polyurea	29 ± 4	0.65 ± 0.05

REFERENCES

[1] J. A. Samareh and E. J. Siochi, "Systems analysis of carbon nanotubes: opportunities and challenges for space applications," *Nanotechnology*, vol. 28, no. 37, p. 372001, Sep. 2017.

[2] "Human Exploration - NASA Mars." [Online]. Available: https://mars.nasa.gov/programmissions/science/goal4/. [Accessed: 02-Nov-2019].

[3] "The Institute for Ultra-Strong Composites by Computational Design (US- | NASA." [Online]. Available: https://www.nasa.gov/directorates/spacetech/strg/stri/us_comp/. [Accessed: 02-Nov-2019].

[4] I. A. Kinloch, J. Suhr, J. Lou, R. J. Young, and P. M. Ajayan, "Composites with carbon nanotubes and graphene: An outlook.," *Science*, vol. 362, no. 6414, pp. 547–553, Nov. 2018.

[5] Y. Liu and S. Kumar, "Polymer/Carbon Nanotube Nano Composite Fibers–A Review," *ACS Appl. Mater. Interfaces*, vol. 6, no. 9, pp. 6069–6087, May 2014.

[6] P. M. Ajayan and J. M. Tour, "Materials Science: Nanotube composites," *Nature*, vol. 447, no. 7148, pp. 1066–1068, Jun. 2007.

[7] J. Chen, L. Yan, W. Song, and D. Xu, "Interfacial characteristics of carbon nanotube-polymer composites: A review," *Compos. Part A Appl. Sci. Manuf.*, vol. 114, pp. 149–169, Nov. 2018.

[8] A. V. Desai and M. A. Haque, "Mechanics of the interface for carbon nanotube–polymer composites," *Thin-Walled Struct.*, vol. 43, no. 11, pp. 1787–1803, Nov. 2005.

[9] M. Rahmat and P. Hubert, "Carbon nanotube–polymer interactions in nanocomposites: A review," *Compos. Sci. Technol.*, vol. 72, no. 1, pp. 72–84, Dec. 2011.

[10] C. Pramanik *et al.*, "Molecular engineering of interphases in polymer/carbon nanotube composites to reach the limits of mechanical performance," *Compos. Sci.*

Technol., vol. 166, pp. 86–94, Sep. 2018.

[11] M. Shtein, R. Nadiv, N. Lachman, H. Daniel Wagner, and O. Regev, "Fracture behavior of nanotube-polymer composites: Insights on surface roughness and failure mechanism," *Compos. Sci. Technol.*, 2013.

[12] N. Lachman and H. Daniel Wagner, "Correlation between interfacial molecular structure and mechanics in CNT/epoxy nano-composites," in *Composites Part A: Applied Science and Manufacturing*, 2010, vol. 41, no. 9, pp. 1093–1098.

[13] J. N. Coleman, U. Khan, W. J. Blau, Y. K. Gun 'ko, and Y. K. Gun'ko, "Small but strong: A review of the mechanical properties of carbon nanotube–polymer composites," *Carbon N. Y.*, vol. 44, no. 9, pp. 1624–1652, Aug. 2006.

[14] J. N. Coleman *et al.*, "High Performance Nanotube-Reinforced Plastics: Understanding the Mechanism of Strength Increase," *Adv. Funct. Mater.*, vol. 14, no. 8, pp. 791–798, Aug. 2004.

[15] L. S. Schadler, S. C. Giannaris, and P. M. Ajayan, "Load transfer in carbon nanotube epoxy composites," *Appl. Phys. Lett.*, vol. 73, no. 26, pp. 3842–3844, Dec. 1998.

[16] P. H. Wang, S. Ghoshal, P. Gulgunje, N. Verghese, and S. Kumar, "Polypropylene nanocomposites with polymer coated multiwall carbon nanotubes," *Polym. (United Kingdom)*, vol. 100, pp. 244–258, 2016.

[17] A. A. Bakhtiary Davijani, H. Chang, H. C. Liu, J. Luo, and S. Kumar, "Stress transfer in nanocomposites enabled by poly(methyl methacrylate) wrapping of carbon nanotubes," *Polymer (Guildf).*, vol. 130, pp. 191–198, Nov. 2017.

[18] P. M. Ajayan, L. S. Schadler, C. Giannaris, and A. Rubio, "Single-Walled Carbon Nanotube-Polymer Composites: Strength and Weakness," *Adv. Mater.*, vol. 12, no. 10, pp. 750–753, May 2000.

[19] B. A. Newcomb *et al.*, "Stress transfer in polyacrylonitrile/carbon nanotube composite fibers," *Polymer (Guildf).*, vol. 55, no. 11, pp. 2734–2743, May 2014.

[20] S. Tsuzuki, K. Honda, T. Uchimaru, M. Mikami, and K. Tanabe, "Origin of the Attraction and Directionality of the NH/π Interaction: Comparison with OH/π and CH/π Interactions," *J. Am. Chem. Soc.*, vol. 122, no. 46, pp. 11450–11458, 2000.

[21] K. E. Wise, C. Park, E. J. Siochi, and J. S. Harrison, “Stable dispersion of single wall carbon nanotubes in polyimide: the role of noncovalent interactions,” *Chem. Phys. Lett.*, vol. 391, no. 4–6, pp. 207–211, Jun. 2004.

[22] T. Kar, H. F. Bettinger, S. Scheiner, and A. K. Roy, “Noncovalent π−π Stacking and CH---π Interactions of Aromatics on the Surface of Single-Wall Carbon Nanotubes: An MP2 Study,” *J. Phys. Chem. C*, vol. 112, no. 50, pp. 20070–20075, Dec. 2008.

[23] D. A. Britz and A. N. Khlobystov, “Noncovalent interactions of molecules with single walled carbon nanotubes,” *Chem. Soc. Rev.*, vol. 35, no. 7, p. 637, Jun. 2006.

[24] M. H. Kirmani, P. Gulgunje, J. Ramachandran, P. J. Arias-Monje, P.-H. Wang, and S. Kumar, “Learning from Nature: Molecular Rearrangement in the Bismaleimide System Leading to Dramatic Increase in Impact Strength,” *ACS Appl. Polym. Mater.*, vol. 2, no. 2, pp. 758–767, Feb. 2020.

[25] T. W. Ebbesen, P. M. Ajayan, H. Hiura, and K. Tanigaki, “Purification of nanotubes,” *Nature*, vol. 367, no. 6463, pp. 519–519, Feb. 1994.

[26] “COMPIMIDE® - Composites from Evonik.” [Online]. Available: http://composites.evonik.com/product/composites/en/markets/pages/compimide.aspx. [Accessed: 24-Jun-2018].

[27] “Lockheed Martin extends Cytec contract for F-35 prepreg : CompositesWorld.” [Online]. Available: https://www.compositesworld.com/news/lockheed-martin-extends-cytec-contract-for-f-35-prepreg. [Accessed: 24-Jun-2018].

[28] D. Wilson, “Polyimides as resin matrices for advanced composites.,” in *Wilson D., Stenzenberger H.D., Hergenrother P.M. (eds) Polyimides.*, Dordrecht: Springer Netherlands, 1990, pp. 187–226.

[29] J. K. Fink, “Bismaleimide Resins,” in *Reactive Polymers Fundamentals and Applications*, Elsevier, 2013, pp. 269–301.

[30] H. Stezenberegr and J. Boyd, *Bismaleimide Resins, In: ASM handbook. Volume 21, Composites p. 97-104*. 2001.

[31] H. D. Stenzenberger, “Bismaleimide Resins for Flame Resistant Honeycomb Sandwich Panels.”

[32] D. A. Kourtides, “FLAME-RETARDANT COMPOSITE MATERIALS.”

[33] D. Paul, ¤ L Kelly, V. Venkayya, and T. Hess, “Evolution of U.S. Military Aircraft Structures Technology,” *J. Aircr.*, vol. 39, no. 1.

[34] S. Iijima, “Helical microtubules of graphitic carbon,” *Nature*, vol. 354, no. 6348, pp. 56–58, Nov. 1991.

[35] Y. Bai, R. Zhang, and X. Ye, “Carbon nanotube bundles with tensile strength over 80 GPa,” *Nat. Nanotechnol.*

[36] B. Peng *et al.*, “Measurements of near-ultimate strength for multiwalled carbon nanotubes and irradiation-induced crosslinking improvements,” *Nat. Nanotechnol.*, vol. 3, no. 10, pp. 626–631, Oct. 2008.

[37] M. F. Yu, O. Lourie, M. J. Dyer, K. Moloni, T. F. Kelly, and R. S. Ruoff, “Strength and breaking mechanism of multiwalled carbon nanotubes under tensile load,” *Science (80-.).*, vol. 287, no. 5453, pp. 637–640, Jan. 2000.

[38] M. K. K. Samani, N. Khosravian, G. C. K. C. K. Chen, M. Shakerzadeh, D. Baillargeat, and B. K. K. Tay, “Thermal conductivity of individual multiwalled carbon nanotubes,” *Int. J. Therm. Sci.*, vol. 62, pp. 40–43, Dec. 2012.

[39] S. Berber, Y.-K. Kwon, and D. Tománek, “Unusually High Thermal Conductivity of Carbon Nanotubes,” *Phys. Rev. Lett.*, vol. 84, no. 20, pp. 4613–4616, May 2000.

[40] T. W. Ebbesen, H. J. Lezec, H. Hiura, J. W. Bennett, H. F. Ghaemi, and T. Thio, “Electrical conductivity of individual carbon nanotubes,” *Nature*, vol. 382, no. 6586, pp. 54–56, 1996.

[41] H. Stenzenberger, “Chemistry and properties of addition polyimides,” in *Wilson D., Stenzenberger H.D., Hergenrother P.M. (eds) Polyimides.*, Dordrecht: Springer Netherlands, 1990, pp. 79–128.

[42] F. Grundschober and J. Sambeth, “Reticulated polyimides consisting of repeating units of producing same from N,N’-BES-IMIDES,” U.S. Patent 3,380,964, 1968.

[43] R. J. Iredale, C. Ward, and I. Hamerton, “Modern advances in bismaleimide resin

technology: A 21st century perspective on the chemistry of addition polyimides," *Prog. Polym. Sci.*, vol. 69, pp. 1–21, 2017.

[44] A.-C. Zahir and A. Renner, "Process for the Manufacture of Crosslinked Polymers which Contain Imide Groups. US 4,100,140," 1976.

[45] J. C. Phelan and C. S. P. Sung, "Cure Characterization in Bis(maleimide)/Diallylbisphenol A Resin by Fluorescence, FT-IR, and UV-Reflection Spectroscopy," *Macromolecules*, vol. 30, no. 22, pp. 6845–6851, Nov. 1997.

[46] D. B. Curliss, B. A. Cowans, and J. M. Caruthers, "Cure Reaction Pathways of Bismaleimide Polymers: A Solid-State 15N NMR Investigation," *Macromolecules*, vol. 31, no. 20, pp. 6776–6782, 1998.

[47] J. Mijović and S. Andjelić, "Study of the Mechanism and Rate of Bismaleimide Cure by Remote in-Situ Real Time Fiber Optic Near-Infrared Spectroscopy," *Macromolecules*, vol. 29, no. 1, pp. 239–246, Jan. 1996.

[48] G. Pritchard and M. Swan, *THE CROSSLINKING OF EUTECTIC MIXTURES OF BISMALEIMIDES*, vol. 29. 1993, pp. 357–363.

[49] C. P. R. Nair, "Advances in addition-cure phenolic resins," *Progress in Polymer Science (Oxford)*, vol. 29, no. 5. Pergamon, pp. 401–498, 01-May-2004.

[50] M. Ouyang, J. L. Huang, and C. M. Lieber, "Fundamental electronic properties and applications of single-walled carbon nanotubes," *Acc. Chem. Res.*, vol. 35, no. 12, pp. 1018–1025, Dec. 2002.

[51] J. Zhao *et al.*, "A comparison of the twisted and untwisted structures for one-dimensional carbon nanotube assemblies," *Mater. Des.*, vol. 146, pp. 20–27, 2018.

[52] L. M. Ericson *et al.*, "Macroscopic, neat, single-walled carbon nanotube fibers," *Science (80-.).*, vol. 305, no. 5689, pp. 1447–1450, Sep. 2004.

[53] "Nanocomp Technologies makes bulk carbon nanotubes 100 times longer at 1-10 millimeters instead of 5 to 20 microns – NextBigFuture.com." [Online]. Available: https://www.nextbigfuture.com/2017/01/nanocomp-technologies-makes-builk.html. [Accessed: 30-Oct-2019].

[54] “Nanocomp Technologies’ Products | Sheet/Tape.” [Online]. Available: http://www.miralon.com/sheet/tape. [Accessed: 28-Sep-2019].

[55] J. Zhang and D. Jiang, “Influence of geometries of multi-walled carbon nanotubes on the pore structures of Buckypaper,” *Compos. Part A Appl. Sci. Manuf.*, vol. 43, no. 3, pp. 469–474, Mar. 2012.

[56] P. C. Krzysztof Koziol, Juan Vilatela, Anna Moisala, Marcelo Motta and A. W. Michael Sennett, “High-Performance Carbon Nanotube Fiber,” *Science (80-.).*, vol. 318, no. 5858, pp. 1889–1892, 2007.

[57] W. Z. Li *et al.*, “Large-Scale Synthesis of Aligned Carbon Nanotubes,” *Science (80-.).*, vol. 274, no. 5293, pp. 1701–1703, 1996.

[58] J. Lee, M. Abdulhafez, and M. Bedewy, “Multizone Rapid Thermal Processing to Overcome Challenges in Carbon Nanotube Manufacturing by Chemical Vapor Deposition,” *J. Manuf. Sci. Eng.*, vol. 141, no. 9, Sep. 2019.

[59] A. L. Kaiser, I. Y. Stein, K. Cui, and B. L. Wardle, “Process-morphology scaling relations quantify self-organization in capillary densified nanofiber arrays,” *Phys. Chem. Chem. Phys.*, vol. 20, no. 6, pp. 3876–3881, 2018.

[60] B. L. Wardle, D. S. Saito, E. J. García, A. J. Hart, R. Guzmán De Villoria, and E. A. Verploegen, “Fabrication and characterization of ultrahigh-volume-fraction aligned carbon nanotube-polymer composites,” *Adv. Mater.*, vol. 20, no. 14, pp. 2707–2714, Jul. 2008.

[61] T. V. Sreekumar, T. Liu, S. Kumar, L. M. Ericson, R. H. Hauge, and R. E. Smalley, “Single-wall carbon nanotube films,” *Chem. Mater.*, vol. 15, no. 1, pp. 175–178, Jan. 2003.

[62] B. D. Jensen *et al.*, “Toward ultralight high strength structural materials via collapsed carbon nanotube bonding,” *Carbon N. Y.*, vol. 156, pp. 538–548, 2020.

[63] L. Zhu, J. Wang, and F. Ding, “The Great Reduction of a Carbon Nanotube’s Mechanical Performance by a Few Topological Defects,” *ACS Nano*, vol. 10, no. 6, pp. 6410–6415, Jun. 2016.

[64] R. Rao *et al.*, “Carbon Nanotubes and Related Nanomaterials: Critical Advances and

Challenges for Synthesis toward Mainstream Commercial Applications," *ACS Nano*, vol. 12, no. 12, pp. 11756–11784, Dec. 2018.

[65] B. D. Jensen, G. M. Odegard, J.-W. Kim, G. Sauti, E. J. Siochi, and K. E. Wise, "Simulating the effects of carbon nanotube continuity and interfacial bonding on composite strength and stiffness," *Compos. Sci. Technol.*, vol. 166, pp. 10–19, Sep. 2018.

[66] P.-C. Ma, N. A. Siddiqui, G. Marom, and J.-K. Kim, "Dispersion and functionalization of carbon nanotubes for polymer-based nanocomposites: A review," *Compos. Part A Appl. Sci. Manuf.*, vol. 41, no. 10, pp. 1345–1367, Oct. 2010.

[67] S. L. Mielke, S. Zhang, R. Khare, R. S. Ruoff, T. Belytschko, and G. C. Schatz, "The effects of extensive pitting on the mechanical properties of carbon nanotubes," *Chem. Phys. Lett.*, vol. 446, no. 1–3, pp. 128–132, Sep. 2007.

[68] S.-O. Lee, S.-H. Choi, S. H. Kwon, K.-Y. Rhee, and S.-J. Park, "Modification of surface functionality of multi-walled carbon nanotubes on fracture toughness of basalt fiber-reinforced composites," *Compos. Part B Eng.*, vol. 79, pp. 47–52, Sep. 2015.

[69] D. Baskaran, J. W. Mays, and M. S. Bratcher, "Noncovalent and Nonspecific Molecular Interactions of Polymers with Multiwalled Carbon Nanotubes," *Chem. Mater.*, vol. 17, no. 13, pp. 3389–3397, Jun. 2005.

[70] L.-C. Tang, H. Zhang, S. Sprenger, L. Ye, and Z. Zhang, "Fracture mechanisms of epoxy-based ternary composites filled with rigid-soft particles," *Compos. Sci. Technol.*, vol. 72, no. 5, pp. 558–565, Mar. 2012.

[71] P.-H. Wang, S. Sarkar, P. Gulgunje, N. Verghese, and S. Kumar, "Structure and rheological behavior of polypropylene interphase at high carbon nanotube concentration," *Polymer (Guildf).*, vol. 150, pp. 10–25, Aug. 2018.

[72] M. Namasivayam, M. Andersson, J. Shapter, M. Namasivayam, M. R. Andersson, and J. Shapter, "Role of Molecular Weight in Polymer Wrapping and Dispersion of MWNT in a PVDF Matrix," *Polymers (Basel).*, vol. 11, no. 1, p. 162, Jan. 2019.

[73] J. Meng, Y. Zhang, S. W. Cranford, and M. L. Minus, "Nanotube Dispersion and Polymer Conformational Confinement in a Nanocomposite Fiber: A Joint

Computational Experimental Study," *J. Phys. Chem. B*, vol. 118, no. 31, pp. 9476–9485, Aug. 2014.

[74] J. R. Gissinger, C. Pramanik, B. Newcomb, S. Kumar, and H. Heinz, "Nanoscale Structure–Property Relationships of Polyacrylonitrile/CNT Composites as a Function of Polymer Crystallinity and CNT Diameter," *ACS Appl. Mater. Interfaces*, vol. 10, no. 1, pp. 1017–1027, Jan. 2018.

[75] H. Zeng *et al.*, "In situ polymerization approach to multiwalled carbon nanotubes-reinforced nylon 1010 composites: Mechanical properties and crystallization behavior," *Polymer (Guildf).*, vol. 47, no. 1, pp. 113–122, Jan. 2006.

[76] Y. Chen, B. Zhang, Z. Gao, C. Chen, S. Zhao, and Y. Qin, "Functionalization of multiwalled carbon nanotubes with uniform polyurea coatings by molecular layer deposition," *Carbon N. Y.*, vol. 82, pp. 470–478, Feb. 2015.

[77] A. Wilson, "The formation of dry, wet, spunlaid and other types of nonwovens," *Appl. Nonwovens Tech. Text.*, pp. 3–17, Jan. 2010.

[78] E. J. García, A. J. Hart, B. L. Wardle, and A. H. Slocum, "Fabrication of composite microstructures by capillarity-driven wetting of aligned carbon nanotubes with polymers," *Nanotechnology*, vol. 18, no. 16, p. 165602, Apr. 2007.

[79] J. W. Kim *et al.*, "Toward high performance thermoset/carbon nanotube sheet nanocomposites via resistive heating assisted infiltration and cure," *ACS Appl. Mater. Interfaces*, vol. 6, no. 21, pp. 18832–18843, 2014.

[80] R. D. Downes *et al.*, "Geometrically constrained self-assembly and crystal packing of flattened and aligned carbon nanotubes," *Carbon N. Y.*, vol. 93, pp. 953–966, 2015.

[81] E. J. Garcia, B. L. Wardle, and A. John Hart, "Joining prepreg composite interfaces with aligned carbon nanotubes," *Compos. Part A Appl. Sci. Manuf.*, vol. 39, no. 6, pp. 1065–1070, Jun. 2008.

[82] R. J. Mora, J. J. Vilatela, and A. H. Windle, "Properties of composites of carbon nanotube fibres," *Compos. Sci. Technol.*, vol. 69, no. 10, pp. 1558–1563, Aug. 2009.

[83] J. P. Salvetat *et al.*, "Mechanical properties of carbon nanotubes," *Appl. Phys. A*

Mater. Sci. Process., vol. 69, no. 3, pp. 255–260, Sep. 1999.

[84] Q. Cheng, B. Wang, C. Zhang, and Z. Liang, "Functionalized carbon-nanotube sheet/bismaleimide nanocomposites: Mechanical and electrical performance beyond carbon-fiber composites," *Small*, vol. 6, no. 6, pp. 763–767, 2010.

[85] W. Liu *et al.*, "Producing superior composites by winding carbon nanotubes onto a mandrel under a poly(vinyl alcohol) spray," *Carbon N. Y.*, vol. 49, no. 14, pp. 4786–4791, Nov. 2011.

[86] Y. Han *et al.*, "Bio-Inspired Aggregation Control of Carbon Nanotubes for Ultra-Strong Composites," *Sci. Rep.*, vol. 5, p. 11533, 2015.

[87] M. Q. Tran, J. T. Cabral, M. S. P. Shaffer, and A. Bismarck, "Direct measurement of the wetting behavior of individual carbon nanotubes by polymer melts: the key to carbon nanotube− polymer composites," *Nano Lett.*, vol. 8, no. 9, pp. 2744–2750, 2008.

[88] Y. Liu *et al.*, "Quantitative Study of Interface/Interphase in Epoxy/Graphene-Based Nanocomposites by Combining STEM and EELS," *ACS Appl. Mater. Interfaces*, vol. 8, no. 49, pp. 34151–34158, Dec. 2016.

[89] Y.-F. Su *et al.*, "Characterization at Atomic Resolution of Carbon Nanotube/Resin Interface in Nanocomposites by Mapping sp 2-Bonding States Using Electron Energy-Loss Spectroscopy," *Microsc. Microanal.*, vol. 22, no. 3, pp. 666–672, 2016.

[90] A. H. Barber, S. R. Cohen, S. Kenig, and H. D. Wagner, "Interfacial fracture energy measurements for multi-walled carbon nanotubes pulled from a polymer matrix," *Compos. Sci. Technol.*, vol. 64, no. 15, pp. 2283–2289, Nov. 2004.

[91] D. Qian, G. J. Wagner, W. K. Liu, M.-F. Yu, and R. S. Ruoff, "Mechanics of carbon nanotubes," *Appl. Mech. Rev.*, vol. 55, no. 6, p. 495, Nov. 2002.

[92] C. D. Wood, L. Chen, C. Burkhart, K. W. Putz, J. M. Torkelson, and L. C. Brinson, "Measuring interphase stiffening effects in styrene-based polymeric thin films," *Polymer (Guildf).*, vol. 75, pp. 161–167, Sep. 2015.

[93] A. H. Barber, S. R. Cohen, and H. D. Wagner, "Measurement of carbon nanotube–

polymer interfacial strength," *Appl. Phys. Lett.*, vol. 82, no. 23, pp. 4140–4142, Jun. 2003.

[94] Y. Zare, "Effects of interphase on tensile strength of polymer/CNT nanocomposites by Kelly–Tyson theory," *Mech. Mater.*, vol. 85, pp. 1–6, Jun. 2015.

[95] F. T. Fisher and L. C. Brinson, "Viscoelastic interphases in polymer–matrix composites: theoretical models and finite-element analysis," *Compos. Sci. Technol.*, vol. 61, no. 5, pp. 731–748, Apr. 2001.

[96] K. Liao and S. Li, "Interfacial characteristics of a carbon nanotube–polystyrene composite system," *Appl. Phys. Lett.*, vol. 79, no. 25, pp. 4225–4227, Dec. 2001.

[97] M. Simeoni, C. De Luca, S. Picozzi, S. Santucci, and B. Delley, "Interaction between zigzag single-wall carbon nanotubes and polymers: A density-functional study," *J. Chem. Phys.*, vol. 122, no. 21, p. 214710, Jun. 2005.

[98] N. Lachman *et al.*, "Raman Response of Carbon Nanotube/PVA Fibers under Strain," *J. Phys. Chem. C*, vol. 113, no. 12, pp. 4751–4754, Mar. 2009.

[99] S. B. Cronin, A. K. Swan, M. S. Ünlü, B. B. Goldberg, M. S. Dresselhaus, and M. Tinkham, "Resonant Raman spectroscopy of individual metallic and semiconducting single-wall carbon nanotubes under uniaxial strain," *Phys. Rev. B*, vol. 72, no. 3, p. 035425, Jul. 2005.

[100] Y. Han *et al.*, "Bio-Inspired Aggregation Control of Carbon Nanotubes for Ultra-Strong Composites," *Sci. Rep.*, vol. 5, p. 11533, 2015.

[101] Y. Han, H. Zhou, K. Ge, Y. Guo, F. Liu, and T. Zhao, "Toughness reinforcement of bismaleimide resin using functionalized carbon nanotubes," *High Perform. Polym.*, vol. 26, no. 8, pp. 874–883, 2014.

[102] J. Qiu, qianqian Wu, and lei Jin, "Effect of hyperbranched polyethyleneimine grafting functionalization of carbon nanotubes on mechanical, thermal stability and electrical properties of carbon nanotubes/bismaleimide composites," *RSC Adv.*, vol. 6, pp. 96245–96249, 2016.

[103] A. Gu, G. Liang, D. Liang, and M. Ni, "Bismaleimide/carbon nanotube hybrids for potential aerospace application: I. Static and dynamic mechanical properties,"

Polym. Adv. Technol., vol. 18, no. 10, pp. 835–840, Oct. 2007.

[104] C. Wang and L. Liu, "N-phenyl maleimide grafted MWNT/bismaleimide-allyl bisphenol A nanocomposites: Improved MWNT dispersion, resin reactivity and composite mechanical strength," *Mater. Lett.*, vol. 194, pp. 38–41, 2017.

[105] L. Xiong, X. Qin, H. Liang, S. Huang, and Z. Lian, "Preparation and Properties of Nanocomposites Based on Hyperbranched Aliphatic Polyamide Functionalized Multiwalled Carbon Nanotubes and Bismaleimide Resin," *Polym. - Plast. Technol. Eng.*, vol. 53, no. 15, pp. 1607–1614, 2014.

[106] S. Li, X. Y. Zhao, and X. Wang, "Preparation and Properties of CNTs Reinforced BMI/DBA Nanocomposites," *Adv. Mater. Res.*, vol. 1120–1121, pp. 357–360, 2015.

[107] Z. Wang, W. Wu, X. Zhang, J. Wang, and B. Liu, "Effects of silane-modified multiwalled carbon nanotubes and 9,10-dihydro-9-oxa-10 phosphaphenanthrene-10-oxide on the flame retardancy and mechanical properties of bismaleimide resin," *High Perform. Polym.*, vol. 28, no. 7, pp. 831–841, 2016.

[108] W. A.-L. Li Wei A4 - Zhou, Baoquan A4 - Wang, Mingyu A4 - Li, Zhonghui A4 - Ren, Rong, "Silane functionalization of graphene oxide and its use as a reinforcement in bismaleimide composites," *J. Mater. Sci.*, vol. v. 50, no. 16, pp. 5402-5410–2015 v.50 no.16, 2015.

[109] W. Li, F. Xue, and Q. Li, "Modification of bismaleimide resin by using γ-aminopropyl triethoxysilane functionalised graphene oxide," *Plast. Rubber Compos.*, vol. 47, no. 5, pp. 187–191, May 2018.

[110] W. Li, M. Wang, Y. Yue, W. Ji, and R. Ren, "Enhanced mechanical and thermal properties of bismaleimide composites with covalent functionalized graphene oxide," *RSC Adv.*, vol. 6, no. 59, pp. 54410–54417, 2016.

[111] C. Liu, H. Yan, Z. Chen, L. Yuan, and Q. Lv, "Effect of surface-functionalized reduced graphene oxide on mechanical and tribological properties of bismaleimide composites," *RSC Adv.*, vol. 5, no. 58, pp. 46632–46639, 2015.

[112] M. Liu, Y. Duan, Y. Wang, and Y. Zhao, "Diazonium functionalization of graphene nanosheets and impact response of aniline modified graphene/bismaleimide nanocomposites," *Mater. Des.*, vol. 53, pp. 466–474, 2014.

[113] C. A. C. Chazot and A. J. Hart, “Understanding and control of interactions between carbon nanotubes and polymers for manufacturing of high-performance composite materials,” *Compos. Sci. Technol.*, vol. 183, p. 107795, Oct. 2019.

[114] M. Zhang *et al.*, “The loading-rate dependent tensile behavior of CNT film and its bismaleimide composite film,” *Mater. Des.*, vol. 117, pp. 37–46, 2017.

[115] Q. Cheng, J. Bao, J. Park, Z. Liang, C. Zhang, and B. Wang, “High mechanical performance composite conductor: Multi-walled carbon nanotube sheet/bismaleimide nanocomposites,” *Adv. Funct. Mater.*, vol. 19, no. 20, pp. 3219–3225, 2009.

[116] C. Jolowsky, R. Sweat, J. G. Park, A. Hao, and R. Liang, “Microstructure evolution and self-assembling of CNT networks during mechanical stretching and mechanical properties of highly aligned CNT composites,” *Compos. Sci. Technol.*, Apr. 2018.

[117] X. Wang *et al.*, “Ultrastrong, Stiff and Multifunctional Carbon Nanotube Composites,” *Mater. Res. Lett.*, vol. 1, no. 1, pp. 19–25, 2013.

[118] Y. N. Liu, M. Li, Y. Gu, Y. Zhang, Q. Li, and Z. Zhang, “Ultrastrong carbon nanotube/ bismaleimide composite film with super-aligned and tightly packing structure,” *Compos. Sci. Technol.*, vol. 117, pp. 176–182, 2015.

[119] S. Li *et al.*, “Enhancement of carbon nanotube fibres using different solvents and polymers,” *Compos. Sci. Technol.*, vol. 72, no. 12, pp. 1402–1407, Jul. 2012.

[120] L. T. Drzal, M. J. Rich, M. F. Koenig, and P. F. Lloyd, “Adhesion of Graphite Fibers to Epoxy Matrices: II. The Effect of Fiber Finish,” *J. Adhes.*, vol. 16, no. 2, pp. 133–152, 1983.

[121] M. A. Downey and L. T. Drzal, “Toughening of carbon fiber-reinforced epoxy polymer composites utilizing fiber surface treatment and sizing,” *Compos. Part A Appl. Sci. Manuf.*, vol. 90, pp. 687–698, Nov. 2016.

[122] D. Liu, B. Li, G. Li, L. Wang, and X. Yang, “Tagged and enhanced interface of carbon fiber/epoxy by doping sizing agent with upconversion luminescent nanoparticles,” *Mater. Lett.*, vol. 196, pp. 37–41, Jun. 2017.

[123] R. Aoki *et al.*, “Preparation of carbon fibers coated with epoxy sizing agents

containing degradable acetal linkages and synthesis of carbon fiber-reinforced plastics (CFRPs) for chemical recycling," *Polym. J.*, vol. 51, no. 9, pp. 909–920, Sep. 2019.

[124] W. Liu *et al.*, "Fabrication of carbon nanotubes/carbon fiber hybrid fiber in industrial scale by sizing process," *Appl. Surf. Sci.*, vol. 284, pp. 914–920, Nov. 2013.

[125] X. Yuan, B. Zhu, X. Cai, J. Liu, K. Qiao, and J. Yu, "Optimization of interfacial properties of carbon fiber/epoxy composites via a modified polyacrylate emulsion sizing," *Appl. Surf. Sci.*, vol. 401, pp. 414–423, Apr. 2017.

[126] J. Liu, H. Ge, J. Chen, D. Wang, and H. Liu, "The preparation of emulsion type sizing agent for carbon fiber and the properties of carbon fiber/vinyl ester resin composites," *J. Appl. Polym. Sci.*, vol. 124, no. 1, pp. 864–872, Apr. 2012.

[127] Y. Yang, C. X. Lu, X. L. Su, G. P. Wu, and X. K. Wang, "Effect of nano-SiO2 modified emulsion sizing on the interfacial adhesion of carbon fibers reinforced composites," *Mater. Lett.*, vol. 61, no. 17, pp. 3601–3604, Jul. 2007.

[128] D. Cho, Y. Choi, J. H. Chang, and L. T. Drzal, "Interphase sizing temperature effect of LaRC PETI-5 on the dynamic mechanical thermal properties of carbon fiber/BMI composites," *Compos. Interfaces*, vol. 13, no. 2–3, pp. 215–229, 2006.

[129] M. Dey, J. M. Deitzel, J. W. Gillespie, and S. Schweiger, "Influence of sizing formulations on glass/epoxy interphase properties," *Compos. Part A Appl. Sci. Manuf.*, vol. 63, pp. 59–67, 2014.

[130] "Fiber Sizing for Glass, Carbon and Natural Fibers - Michelman." [Online]. Available: https://www.michelman.com/Industrial-Manufacturing/Reinforced-Plastic-Composites/Fiber-Sizing/. [Accessed: 03-Nov-2019].

[131] M. Sharma, S. Gao, E. Mäder, H. Sharma, L. Y. Wei, and J. Bijwe, "Carbon fiber surfaces and composite interphases," *Composites Science and Technology*, vol. 102. Elsevier Ltd, pp. 35–50, 06-Oct-2014.

[132] W. E. Bascorr; and L. T. Drza, "NASA Technical Reports Server (NTRS) - The surface properties of carbon fibers and their adhesion to organic polymers," 1987. [Online]. Available: https://ntrs.nasa.gov/search.jsp?R=19870016001. [Accessed: 10-Nov-2019].

[133] K. H. Atsushi Sumida; Toyokazu Minakuchi; Motoi ItohItsuki Taniguchi, K. M. S. Hasegawa, and Kyoto, “United States Pat. US5298576,” 1994.

[134] I. Naoki Sugiura and T. Norihito Maki, “United States Pat. US 7135516B2,” 2006.

[135] E. Mäder, S. lin Gao, and R. Plonka, “Static and dynamic properties of single and multi-fiber/epoxy composites modified by sizings,” *Compos. Sci. Technol.*, vol. 67, no. 6, pp. 1105–1115, May 2007.

[136] S. Zhang, W. B. Liu, L. F. Hao, W. C. Jiao, F. Yang, and R. G. Wang, “Preparation of carbon nanotube/carbon fiber hybrid fiber by combining electrophoretic deposition and sizing process for enhancing interfacial strength in carbon fiber composites,” *Compos. Sci. Technol.*, vol. 88, pp. 120–125, Nov. 2013.

[137] D. J. P. Ii, “Polyurea Elastomer Technology: History, Chemistry & Basic Formulating Techniques.”

[138] C. Gao *et al.*, “Polyurea-Functionalized Multiwalled Carbon Nanotubes: Synthesis, Morphology, and Raman Spectroscopy,” *J. Phys. Chem. B*, vol. 109, no. 24, pp. 11925–11932, Jun. 2005.

[139] J.-C. Zhao *et al.*, “Thermal conductive and electrical properties of polyurethane/hyperbranched poly(urea-urethane)-grafted multi-walled carbon nanotube composites,” *Compos. Part B Eng.*, vol. 42, no. 8, pp. 2111–2116, Dec. 2011.

[140] H.-L. Wu, C.-C. M. Ma, Y.-T. Yang, H.-C. Kuan, C.-C. Yang, and C.-L. Chiang, “Morphology, electrical resistance, electromagnetic interference shielding and mechanical properties of functionalized MWNT and poly(urea urethane) nanocomposites,” *J. Polym. Sci. Part B Polym. Phys.*, vol. 44, no. 7, pp. 1096–1105, Apr. 2006.

[141] C.-C. M. Ma, Y.-L. Huang, H.-C. Kuan, and Y.-S. Chiu, “Preparation and electromagnetic interference shielding characteristics of novel carbon-nanotube/siloxane/poly-(urea urethane) nanocomposites,” *J. Polym. Sci. Part B Polym. Phys.*, vol. 43, no. 4, pp. 345–358, Feb. 2005.

[142] D. Sen and M. J. Buehler, “Structural hierarchies define toughness and defect-tolerance despite simple and mechanically inferior brittle building blocks,” *Sci. Rep.*, vol. 1, no. 1, p. 35, Dec. 2011.

[143] F. J. Martin-Martinez, K. Jin, D. López Barreiro, and M. J. Buehler, "The Rise of Hierarchical Nanostructured Materials from Renewable Sources: Learning from Nature," *ACS Nano*, vol. 12, no. 8, pp. 7425–7433, Aug. 2018.

[144] S. Kamat, X. Su, R. Ballarini, and A. H. Heuer, "Structural basis for the fracture toughness of the shell of the conch Strombus gigas," *Nature*, vol. 405, no. 6790, pp. 1036–1040, Jun. 2000.

[145] H. Gao, B. Ji, I. L. Jäger, E. Arzt, and P. Fratzl, "Materials become insensitive to flaws at nanoscale: Lessons from nature," *Proc. Natl. Acad. Sci.*, vol. 100, no. 10, pp. 5597–5600, 2003.

[146] M. E. Launey, M. J. Buehler, and R. O. Ritchie, "On the Mechanistic Origins of Toughness in Bone," *Annu. Rev. Mater. Res.*, vol. 40, no. 1, pp. 25–53, 2010.

[147] F. Barthelat, Z. Yin, and M. J. Buehler, "Structure and mechanics of interfaces in biological materials," *Nat. Rev. Mater.*, vol. 1, no. 4, p. 16007, Apr. 2016.

[148] S. Keten, Z. Xu, B. Ihle, and M. J. Buehler, "Nanoconfinement controls stiffness, strength and mechanical toughness of β-sheet crystals in silk," *Nat. Mater.*, vol. 9, no. 4, pp. 359–367, Apr. 2010.

[149] H. Tao, D. L. Kaplan, and F. G. Omenetto, "Silk Materials - A Road to Sustainable High Technology," *Adv. Mater.*, vol. 24, no. 21, pp. 2824–2837, Jun. 2012.

[150] R. Menig, M. H. Meyers, M. A. Meyers, and K. S. Vecchio, "Quasi-static and dynamic mechanical response of Haliotis rufescens (abalone) shells," *Acta Mater.*, vol. 48, no. 9, pp. 2383–2398, May 2000.

[151] J. C. Phelan, C. S. P. Sung, C. Sook, and P. Sung, "Cure Characterization in Bis(maleimide)/Diallylbisphenol A Resin by Fluorescence, FT-IR, and UV-Reflection Spectroscopy," *Macromolecules*, vol. 30, no. 22, pp. 6845–6851, Nov. 1997.

[152] D. B. Curliss*, B. A. C. and, J. M. Caruthers, D. B. Curliss, B. A. Cowans, and J. M. Caruthers, "Cure Reaction Pathways of Bismaleimide Polymers: A Solid-State 15N NMR Investigation," *Macromolecules*, vol. 31, no. 20, pp. 6776–6782, 1998.

[153] J. Mijović, S. Andjelić, J. Mijovi, and S. Andjeli, "Study of the Mechanism and Rate

of Bismaleimide Cure by Remote in-Situ Real Time Fiber Optic Near-Infrared Spectroscopy," *Macromolecules*, vol. 29, no. 1, pp. 239–246, Jan. 1996.

[154] R. J. Iredale, C. Ward, and I. Hamerton, "Modern advances in bismaleimide resin technology: A 21st century perspective on the chemistry of addition polyimides," *Prog. Polym. Sci.*, vol. 69, pp. 1–21, Jun. 2017.

[155] M. S. Radue, V. Varshney, J. W. Baur, A. K. Roy, and G. M. Odegard, "Molecular Modeling of Cross-Linked Polymers with Complex Cure Pathways: A Case Study of Bismaleimide Resins," *Macromolecules*, vol. 51, no. 5, pp. 1830–1840, Mar. 2018.

[156] L. Geng *et al.*, "Superior Impact Toughness and Excellent Storage Modulus of Poly(lactic acid) Foams Reinforced by Shish-Kebab Nanoporous Structure," *ACS Appl. Mater. Interfaces*, vol. 9, no. 25, pp. 21071–21076, Jun. 2017.

[157] A. C. Steenbrink and E. van der Giessen, "On cavitation, post-cavitation and yield in amorphous polymer–rubber blends," *J. Mech. Phys. Solids*, vol. 47, no. 4, pp. 843–876, Feb. 1999.

[158] R. j. m. Smit, W. a. m. Brekelmans, and H. e. h. Meijer, "Prediction of the large-strain mechanical response of heterogeneous polymer systems: local and global deformation behaviour of a representative volume element of voided polycarbonate," *J. Mech. Phys. Solids*, vol. 47, no. 2, pp. 201–221, Feb. 1999.

[159] J. Dai, J. Singh, and N. Yamamoto, "Nonbrittle nanopore deformation of anodic aluminum oxide membranes," *J. Am. Ceram. Soc.*, vol. 101, no. 5, pp. 2170–2180, May 2018.

[160] S. Ruan, J. J. Lannutti, S. Prybyla, and R. R. Seghi, "Increased fracture toughness in nanoporous silica–polyimide matrix composites," *J. Mater. Res.*, vol. 16, no. 07, pp. 1975–1981, Jul. 2001.

[161] C. Barlow, V. Kumar, B. Flinn, R. K. Bordia, and J. Weller, "Impact Strength of High Density Solid-State Microcellular Polycarbonate Foams," *J. Eng. Mater. Technol.*, vol. 123, no. 2, pp. 229–233, Sep. 2000.

[162] G. Wei and H.-J. Sue, "Fracture Mechanisms in Preformed Polyphenylene Oxide Particle-Modified Bismaleimide Resins," *J Appl Polym Sci*, vol. 74, no. 10, pp. 2539–2545, Dec. 1999.

[163] Y. Li, R. J. Morgan, F. Tschen, H.-J. Sue, and V. Lopata, "Electron-beam curing of bismaleimide-reactive diluent resins," *J. Appl. Polym. Sci.*, vol. 94, no. 6, pp. 2407–2416, 2004.

[164] "CYCOM 5250-4 RTM | Solvay." [Online]. Available: https://www.solvay.com/en/product/cycom-5250-4-rtm. [Accessed: 12-Jul-2019].

[165] Y. Wang, K. Kou, L. Zhuo, H. Chen, Y. Zhang, and G. Wu, "Thermal, mechanical and dielectric properties of BMI modified by the Bis allyl benzoxazine," *J. Polym. Res.*, vol. 22, no. 4, p. 51, Mar. 2015.

[166] Y. Wang, K. Kou, G. Wu, A. Feng, and L. Zhuo, "The effect of bis allyl benzoxazine on the thermal, mechanical and dielectric properties of bismaleimide–cyanate blend polymers," *RSC Adv.*, vol. 5, no. 72, pp. 58821–58831, 2015.

[167] G. Wu, K. Kou, M. Chao, L. Zhuo, J. Zhang, and N. Li, "Preparation and characterization of bismaleimide-triazine/epoxy interpenetrating polymer networks," *Thermochim. Acta*, vol. 537, pp. 44–50, 2012.

[168] P. Li, T. Li, and H. Yan, "Mechanical, tribological and heat resistant properties of fluorinated multi-walled carbon nanotube/bismaleimide/cyanate resin nanocomposites," *J. Mater. Sci. Technol.*, vol. 33, no. 10, pp. 1182–1186, 2017.

[169] G. Wu, Y. Cheng, K. Wang, Y. Wang, and A. Feng, "Fabrication and characterization of OMMt/BMI/CE composites with low dielectric properties and high thermal stability for electronic packaging," *J. Mater. Sci. Mater. Electron.*, vol. 27, no. 6, pp. 5592–5599, Jun. 2016.

[170] Z. BAOYAN, L. I. PING, and C. XIANGBAO, "Studies of modified bismaleimide resins Part I The influence of resin composition on thermal and impact properties," *J. Mater. Sci.*, vol. 33, no. 23, pp. 5683–5687, Dec. 1998.

[171] D. Wang, X. Wang, L. Liu, C. Qu, C. Liu, and H. Yang, "Vinyl-terminated butadiene acrylonitrile improves the toughness, processing window, and thermal stability of bismaleimide resin," *High Perform. Polym.*, vol. 29, no. 10, pp. 1199–1208, Dec. 2017.

[172] J. Wu, Y.-W. Mai, and A. F. Yee, "Fracture toughness and fracture mechanisms of polybutylene-terephthalate/polycarbonate/ impact-modifier blends," *J. Mater. Sci.*, vol. 29, no. 17, pp. 4510–4522, 1994.

[173] S. F. Parker, S. M. Mason, and K. P. J. Williams, “Fourier Transform Raman and infrared spectroscopy of N-phenylmaleimide and methylene dianiline bismaleimide,” 1990.

[174] X. Xu, X. Wang, W. Liu, X. Zhang, Z. Li, and S. Du, “Microwave curing of carbon fiber/bismaleimide composite laminates: Material characterization and hot pressing pretreatment,” *Mater. Des.*, vol. 97, pp. 316–323, May 2016.

[175] M. Sava, C. Gaina, V. Gaina, and D. Timpu, “Synthesis and Characterization of Some Bismaleimides Containing Ether Groups in the Backbone,” *Macromol. Chem. Phys*, vol. 202, pp. 2601–2605, 2001.

[176] N. J. Heaton, P. Bello, B. Herradón, A. del Campo, and J. Jiménez-Barbero, “NMR Study of Intramolecular Interactions between Aromatic Groups: Van der Waals, Charge-Transfer, or Quadrupolar Interactions?,” *J. Am. Chem. Soc.*, vol. 120, no. 37, pp. 9632–9645, 1998.

[177] H. E. Kissinger, “Reaction Kinetics in Differential Thermal Analysis,” *Anal. Chem.*, vol. 29, no. 11, pp. 1702–1706, 1957.

[178] T. Ozawa, “A New Method of Analyzing Thermogravimetric Data,” *Bull. Chem. Soc. Jpn.*, vol. 38, no. 11, pp. 1881–1886, 1965.

[179] S. Förster *et al.*, “Order causes secondary Bragg peaks in soft materials,” *Nat. Mater.*, vol. 6, no. 11, pp. 888–893, Nov. 2007.

[180] E. Girard-Reydet *et al.*, “Reaction-induced phase separation mechanisms in modified thermosets,” 1998.

[181] S. Kumar and M. Pineri, “Interpretation of small-angle x-ray and neutron scattering data for perfluorosulfonated ionomer membranes,” *J. Polym. Sci. Part B Polym. Phys.*, vol. 24, no. 8, pp. 1767–1782, 1986.

[182] S. Kumar and W. W. Adams, “Structural studies of epoxy resins, acetylene terminated resins and polycarbonate,” *Polymer (Guildf).*, vol. 28, no. 9, pp. 1497–1504, Aug. 1987.

[183] A. J. Kinloch, S. J. Shaw, D. A. Tod, and D. L. Hunston, “Deformation and fracture behaviour of a rubber-toughened epoxy: 1. Microstructure and fracture studies,”

Polymer (Guildf)., vol. 24, no. 10, pp. 1341–1354, Oct. 1983.

[184] H. Zhang, L.-C. Tang, Z. Zhang, K. Friedrich, and S. Sprenger, "Fracture behaviours of in situ silica nanoparticle-filled epoxy at different temperatures," *Polymer (Guildf).*, vol. 49, no. 17, pp. 3816–3825, Aug. 2008.

[185] J. Spanoudakis and R. J. Young, "Crack propagation in a glass particle-filled epoxy resin," *J. Mater. Sci.*, vol. 19, no. 2, pp. 473–486, Feb. 1984.

[186] C. Soutis, "Fibre reinforced composites in aircraft construction," *Progress in Aerospace Sciences*, vol. 41, no. 2. Elsevier Ltd, pp. 143–151, 01-Feb-2005.

[187] R. A. Sullivan, "Automotive carbon fiber: Opportunities and challenges," *JOM*, vol. 58, no. 11. Springer, pp. 77–79, Nov-2006.

[188] M. Hojo, S. Matsuda, M. Tanaka, S. Ochiai, and A. Murakami, "Mode I delamination fatigue properties of interlayer-toughened CF/epoxy laminates," *Compos. Sci. Technol.*, vol. 66, no. 5, pp. 665–675, May 2006.

[189] N. H. Nash, T. M. Young, P. T. McGrail, and W. F. Stanley, "Inclusion of a thermoplastic phase to improve impact and post-impact performances of carbon fibre reinforced thermosetting composites - A review," *Mater. Des.*, vol. 85, pp. 582–597, Nov. 2015.

[190] S. Sihn, R. Y. Kim, W. Huh, K. H. Lee, and A. K. Roy, "Improvement of damage resistance in laminated composites with electrospun nano-interlayers," *Compos. Sci. Technol.*, vol. 68, no. 3–4, pp. 673–683, Mar. 2008.

[191] J. Zhang, T. Lin, and X. Wang, "Electrospun nanofibre toughened carbon/epoxy composites: Effects of polyetherketone cardo (PEK-C) nanofibre diameter and interlayer thickness," *Compos. Sci. Technol.*, vol. 70, no. 11, pp. 1660–1666, Oct. 2010.

[192] Y. A. Dzenis and D. H. Reneker, "Delamination resistant composites prepared by small diameter fiber reinforcement at ply interfaces." US Patent 6265333B1., 24-Jul-2001.

[193] M. Arai, Y. Noro, K. ichi Sugimoto, and M. Endo, "Mode I and mode II interlaminar fracture toughness of CFRP laminates toughened by carbon nanofiber interlayer,"

Compos. Sci. Technol., vol. 68, no. 2, pp. 516–525, Feb. 2008.

[194] X. Ni, C. Furtado, N. K. Fritz, R. Kopp, P. P. Camanho, and B. L. Wardle, "Interlaminar to intralaminar mode I and II crack bifurcation due to aligned carbon nanotube reinforcement of aerospace-grade advanced composites," *Compos. Sci. Technol.*, vol. 190, p. 108014, Apr. 2020.

[195] R. J. Cano, J. H. Kang, B. W. Grimsley, J. G. Ratcliffe, and E. J. Siochi, *Properties of Multifunctional Hybrid Carbon Nanotube/Carbon Fiber Polymer Matrix Composites*. 2016.

[196] J. Hoffmann and G. Scharr, "Mode I delamination fatigue resistance of unidirectional and quasi-isotropic composite laminates reinforced with rectangular z-pins," *Compos. Part A Appl. Sci. Manuf.*, vol. 115, pp. 228–235, Dec. 2018.

[197] K. Pingkarawat and A. P. Mouritz, "Improving the mode I delamination fatigue resistance of composites using z-pins," *Compos. Sci. Technol.*, vol. 92, pp. 70–76, Feb. 2014.

[198] K. Dransfield, C. Baillie, and Y. W. Mai, "Improving the delamination resistance of CFRP by stitching-a review," *Compos. Sci. Technol.*, vol. 50, no. 3, pp. 305–317, Jan. 1994.

[199] K. T. Tan, A. Yoshimura, N. Watanabe, Y. Iwahori, and T. Ishikawa, "Effect of stitch density and stitch thread thickness on damage progression and failure characteristics of stitched composites under out-of-plane loading," *Compos. Sci. Technol.*, vol. 74, pp. 194–204, Jan. 2013.

[200] S. Sihn, R. Y. Kim, K. Kawabe, and S. W. Tsai, "Experimental studies of thin-ply laminated composites," *Compos. Sci. Technol.*, vol. 67, no. 6, pp. 996–1008, May 2007.

[201] E. Kalfon-Cohen *et al.*, "Synergetic effects of thin plies and aligned carbon nanotube interlaminar reinforcement in composite laminates," *Compos. Sci. Technol.*, vol. 166, pp. 160–168, Sep. 2018.

[202] R. Amacher, J. Cugnoni, J. Botsis, L. Sorensen, W. Smith, and C. Dransfeld, "Thin ply composites: Experimental characterization and modeling of size-effects," *Compos. Sci. Technol.*, vol. 101, pp. 121–132, Sep. 2014.

[203] J. A. Pascoe, S. Pimenta, and S. T. Pinho, “The effect of tab orientation on the toughening mechanisms produced by interlocked interlaminar thin-ply CFRP reinforcements,” *Compos. Struct.*, vol. 238, p. 111932, Apr. 2020.

[204] J. A. Pascoe, S. Pimenta, and S. T. Pinho, “Interlocking thin-ply reinforcement concept for improved fracture toughness and damage tolerance,” *Compos. Sci. Technol.*, vol. 181, p. 107681, Sep. 2019.

[205] A. Karakassides, A. Ganguly, K. Tsirka, A. S. Paipetis, and P. Papakonstantinou, “Radially Grown Graphene Nanoflakes on Carbon Fibers as Reinforcing Interface for Polymer Composites,” *ACS Appl. Nano Mater.*, 2020.

[206] S. H. Lee, H. Kim, S. Hang, and S. K. Cheong, “Interlaminar fracture toughness of composite laminates with CNT-enhanced nonwoven carbon tissue interleave,” *Compos. Sci. Technol.*, vol. 73, no. 1, pp. 1–8, Nov. 2012.

[207] M. Quaresimin and R. J. Varley, “Understanding the effect of nano-modifier addition upon the properties of fibre reinforced laminates,” *Compos. Sci. Technol.*, vol. 68, no. 3–4, pp. 718–726, Mar. 2008.

[208] J. Misumi and T. Oyama, “Low viscosity and high toughness epoxy resin modified by in situ radical polymerization method for improving mechanical properties of carbon fiber reinforced plastics,” *Polymer (Guildf).*, vol. 156, pp. 1–9, Nov. 2018.

[209] M. H. Kirmani, P. Gulgunje, J. Ramachandran, P. J. Arias-Monje, P.-H. Wang, and S. Kumar, “Learning from Nature: Molecular Rearrangement in the Bismaleimide System Leading to Dramatic Increase in Impact Strength,” *ACS Appl. Polym. Mater.*, vol. 2, no. 2, pp. 758–767, Feb. 2020.

[210] J. S. Fenner and I. M. Daniel, “Hybrid nanoreinforced carbon/epoxy composites for enhanced damage tolerance and fatigue life,” *Compos. Part A Appl. Sci. Manuf.*, vol. 65, pp. 47–56, Oct. 2014.

[211] A. Bisht, K. Dasgupta, and D. Lahiri, “Investigating the role of 3D network of carbon nanofillers in improving the mechanical properties of carbon fiber epoxy laminated composite,” *Compos. Part A Appl. Sci. Manuf.*, vol. 126, p. 105601, Nov. 2019.

[212] V. Kostopoulos, A. Baltopoulos, P. Karapappas, A. Vavouliotis, and A. Paipetis, “Impact and after-impact properties of carbon fibre reinforced composites enhanced

with multi-wall carbon nanotubes," *Compos. Sci. Technol.*, vol. 70, no. 4, pp. 553–563, Apr. 2010.

[213] B. Ashrafi *et al.*, "Enhancement of mechanical performance of epoxy/carbon fiber laminate composites using single-walled carbon nanotubes," *Compos. Sci. Technol.*, vol. 71, no. 13, pp. 1569–1578, Sep. 2011.

[214] M. Siegfried, C. Tola, M. Claes, S. V. Lomov, I. Verpoest, and L. Gorbatikh, "Impact and residual after impact properties of carbon fiber/epoxy composites modified with carbon nanotubes," *Compos. Struct.*, vol. 111, no. 1, pp. 488–496, May 2014.

[215] C. Kostagiannakopoulou, X. Tsilimigkra, G. Sotiriadis, and V. Kostopoulos, "Synergy effect of carbon nano-fillers on the fracture toughness of structural composites," *Compos. Part B Eng.*, vol. 129, pp. 18–25, Nov. 2017.

[216] M. H. G. Wichmann, K. Schulte, and H. D. Wagner, "On nanocomposite toughness," *Compos. Sci. Technol.*, vol. 68, no. 1, pp. 329–331, Jan. 2008.

[217] P.-H. Wang, S. Sarkar, P. Gulgunje, N. Verghese, and S. Kumar, "Fracture mechanism of high impact strength polypropylene containing carbon nanotubes," *Polymer (Guildf).*, vol. 151, pp. 287–298, Aug. 2018.

[218] S. Ghoshal, P.-H. Wang, P. Gulgunje, N. Verghese, and S. Kumar, "High impact strength polypropylene containing carbon nanotubes," *Polymer (Guildf).*, vol. 100, pp. 259–274, 2016.

[219] M. H. Kirmani, P. J. Arias-Monje, and S. Kumar, "High Interfacial Shear Strain in Polyurea–Carbon Nanotube Composite Sheets," *ACS Appl. Nano Mater.*, vol. 2, no. 11, pp. 6849–6857, Oct. 2019.

[220] P. J. Arias-Monje, A. A. Bakhtiary Davijani, M. Lu, J. Ramachandran, M. H. Kirmani, and S. Kumar, "Engineering the Interphase of Single Wall Carbon Nanotubes/Polyacrylonitrile Nanocomposite Fibers with Poly(methyl methacrylate) and Its Effect on Filler Dispersion, Filler–Matrix Interactions, and Tensile Properties," *ACS Appl. Nano Mater.*, p. acsanm.0c00364, Apr. 2020.

[221] Y. Gao *et al.*, "Axial Compression of Hierarchically Structured Carbon Nanotube Fiber Embedded in Epoxy," *Adv. Funct. Mater.*, vol. 20, no. 21, pp. 3797–3803, Nov. 2010.

[222] L. G. Bulusheva *et al.*, "Effect of nitrogen doping on Raman spectra of multi-walled carbon nanotubes," *Phys. status solidi*, vol. 245, no. 10, pp. 1971–1974, Oct. 2008.

[223] Q. H. Yang, P. X. Hou, M. Unno, S. Yamauchi, R. Saito, and T. Kyotani, "Dual Raman features of double coaxial carbon nanotubes with N-doped and B-doped multiwalls," *Nano Lett.*, vol. 5, no. 12, pp. 2465–2469, Dec. 2005.

[224] Y. J. Lee, "The second order Raman spectroscopy in carbon crystallinity," *J. Nucl. Mater.*, vol. 325, no. 2–3, pp. 174–179, Feb. 2004.

[225] Y. Liu and S. Kumar, "Polymer/Carbon Nanotube Nano Composite Fibers−A Review," 2014.

[226] M. H. Kirmani, R. Liang, and S. Kumar, "Cure Behavior Changes and Compression of Carbon Nanotubes in Aerospace grade Bismaleimide-Carbon Nanotube Sheet Nanocomposites," *Unpubl. Manuscr.*, 2020.

[227] M. H. Kirmani, K. K. Gupta, N. Kondekar, J. Ramachandran, P. J. Arias-Monje, and S. Kumar, "Using a Carbon Fiber Sizing to Tailor the Interface-Interphase of a Carbon Nanotube- Polymer System," *Unpubl. Manuscr.*, 2020.

[228] G. Fei, Q. Gong, D. Li, M. Lavorgna, and H. Xia, "Relationship between electrical conductivity and spatial arrangements of carbon nanotubes in polystyrene nanocomposites: The effect of thermal annealing and plasticization on electrical conductivity," *Compos. Sci. Technol.*, vol. 146, pp. 99–109, Jul. 2017.

[229] R. Jain, "CARBON NANOTUBE REINFORCED POLYACRYLONITRILE AND POLY(ETHERKETONE) FIBERS A Dissertation Presented to The Academic Faculty," Georgia Institute of Technology, Mar. 2009.

[230] N. Nguyen, A. Hao, J. G. Park, and R. Liang, "In Situ Curing and Out-of-Autoclave of Interply Carbon Fiber/Carbon Nanotube Buckypaper Hybrid Composites Using Electrical Current ," *Adv. Eng. Mater.*, vol. 18, no. 11, pp. 1906–1912, Nov. 2016.

[231] L. Wan, X. Zhang, G. Wu, and A. Feng, "Thermal conductivity and dielectric properties of bismaleimide/cyanate ester copolymer," *High Volt.*, vol. 2, no. 3, pp. 167–171, Sep. 2017.

[232] M. H. Kirmani, J. Ramachandran, P. J. Arias-Monje, P. Gulgunje, and S. Kumar,

"The Effects of Processing and CNT type on the Impact strength of Aerospace grade Bismaleimide based Nanocomposites," *Unpubl. Manuscr.*, 2020.

[233] L. cheng Tang, H. Zhang, J. hua Han, X. ping Wu, and Z. Zhang, "Fracture mechanisms of epoxy filled with ozone functionalized multi-wall carbon nanotubes," *Compos. Sci. Technol.*, 2011.

[234] X. Liu, F. Xu, K. Zhang, B. Wei, Z. Gao, and Y. Qiu, "Characterization of enhanced interfacial bonding between epoxy and plasma functionalized carbon nanotube films," *Compos. Sci. Technol.*, vol. 145, pp. 114–121, Jun. 2017.

[235] S. Ghoshal, P. H. Wang, P. Gulgunje, N. Verghese, and S. Kumar, "High impact strength polypropylene containing carbon nanotubes," *Polymer (Guildf).*, vol. 100, pp. 259–274, Sep. 2016.

[236] P. H. Wang, S. Sarkar, P. Gulgunje, N. Verghese, and S. Kumar, "Fracture mechanism of high impact strength polypropylene containing carbon nanotubes," *Polym. (United Kingdom)*, vol. 151, pp. 287–298, Aug. 2018.

[237] H. Chang, J. Luo, H. C. Liu, A. A. Bakhtiary Davijani, P.-H. Wang, and S. Kumar, "Orientation and interfacial stress transfer of cellulose nanocrystal nanocomposite fibers," *Polymer (Guildf).*, vol. 110, pp. 228–234, Feb. 2017.

[238] P. J. Arias-Monje *et al.*, "Engineering the Interphase of Single Wall Carbon Nanotubes/Polyacrylonitrile Nanocomposite Fibers with Poly(methyl methacrylate) and Its Effect on Filler Dispersion, Filler–Matrix Interactions, and Tensile Properties," *ACS Appl. Nano Mater.*, vol. 0, no. 0, p. acsanm.0c00364, Apr. 2020.

[239] "Nanocomp Technologies' Products | Yarn." [Online]. Available: https://www.miralon.com/yarn?hsCtaTracking=8b116b66-d50d-4fb6-b7b2-e6b4ab13f62f%7Cf6c9da00-6bb4-4d34-88fd-d5140289e507. [Accessed: 19-Jul-2020].

[240] M. Miao, Ed., *Carbon Nanotube Fibers and Yarns*. Elsevier, 2020.

[241] J. W. Kim *et al.*, "Assessment of carbon nanotube yarns as reinforcement for composite overwrapped pressure vessels," *Compos. Part A Appl. Sci. Manuf.*, vol. 84, pp. 256–265, May 2016.

[242] D. I. Tee, M. Mariatti, A. Azizan, C. H. See, and K. F. Chong, “Effect of silane-based coupling agent on the properties of silver nanoparticles filled epoxy composites,” *Compos. Sci. Technol.*, vol. 67, no. 11–12, pp. 2584–2591, Sep. 2007.

[243] N. Kondekar *et al.*, “The Effect of Nickel on MoS2 Growth Revealed with in Situ Transmission Electron Microscopy,” *ACS Nano*, vol. 13, no. 6, pp. 7117–7126, May 2019.

[244] P. K. Mallick, *Materials, design and manufacturing for lightweight vehicles*. CRC Press, 2010.

[245] E. J. Siochi and J. S. Harrison, “Structural nanocomposites for aerospace applications,” *MRS Bull.*, vol. 40, no. 10, pp. 829–835, Oct. 2015.

[246] M. F. L. De Volder, S. H. Tawfick, R. H. Baughman, and A. J. Hart, “Carbon Nanotubes: Present and Future Commercial Applications,” *Science (80-.).*, vol. 339, no. 6119, pp. 535 LP – 539, Feb. 2013.

[247] W. H. Awad and C. A. Wilkie, “Investigation of the thermal degradation of polyurea: The effect of ammonium polyphosphate and expandable graphite,” *Polymer (Guildf).*, vol. 51, no. 11, pp. 2277–2285, May 2010.

[248] T. Ebbesen, P. Ajayan M., and H. Hiura, “Method of purifying carbon nanotubes,” *United States Pat.*, vol. US5641466A, Jun. 1997.

[249] T. Liu and S. Kumar, “Quantitative characterization of SWNT orientation by polarized Raman spectroscopy,” *Chem. Phys. Lett.*, vol. 378, no. 3–4, pp. 257–262, Sep. 2003.

[250] M. J. Matthews, M. A. Pimenta, G. Dresselhaus, M. S. Dresselhaus, and M. Endo, *Origin of dispersive effects of the Raman D band in carbon materials*, vol. 59, no. 10. American Physical Society, 1999, pp. R6585–R6588.

[251] M. S. Dresselhaus, G. Dresselhaus, R. Saito, and A. Jorio, “Raman spectroscopy of carbon nanotubes,” *Phys. Rep.*, vol. 409, no. 2, pp. 47–99, Mar. 2005.

[252] M. S. Strano *et al.*, “Electronic Structure Control of Single-Walled Carbon Nanotube Functionalization,” *Science (80-.).*, vol. 301, no. 5639, pp. 1519–1522, 2003.

[253] J. Schwan, S. Ulrich, V. Batori, H. Ehrhardt, and S. R. P. Silva, "Raman spectroscopy on amorphous carbon films," *J. Appl. Phys.*, vol. 80, p. 440, 1996.

[254] G. R. Dieckmann *et al.*, "Controlled Assembly of Carbon Nanotubes by Designed Amphiphilic Peptide Helices," *J. Am. Chem. Soc.*, vol. 125, no. 7, pp. 1770–1777, Feb. 2003.

[255] M. Kirmani, P. Gulgunje, J. Ramachandran, P. J. Arias-Monje, P.-H. Wang, and S. Kumar, "Learning from Nature: Molecular Rearrangement in the Bismaleimide System Leading to Dramatic Increase in Impact Strength," *ACS Appl. Polym. Mater.*, vol. 2, no. 2, pp. 758–767, 2020.

[256] M. H. Kirmani, P. Gulgunje, J. Ramachandran, P. J. Arias-Monje, P.-H. Wang, and S. Kumar, "Learning from Nature: Molecular Rearrangement in the Bismaleimide System Leading to Dramatic Increase in Impact Strength," *ACS Appl. Polym. Mater.*, p. acsapm.9b01065, Jan. 2020.

[257] P. Karapappas, A. Vavouliotis, P. Tsotra, V. Kostopoulos, and A. Paipetis, "Enhanced fracture properties of carbon reinforced composites by the addition of multi-wall carbon nanotubes," in *Journal of Composite Materials*, 2009, vol. 43, no. 9, pp. 977–985.

[258] P. Nikolaev, O. Gorelik, R. kumar Allada, E. Sosa, S. Arepalli, and L. Yowell, "Soft-Bake Purification of Single-Walled Carbon Nanotubes Produced by Pulsed Laser Vaporization," *J. Phys. Chem. C*, vol. 111, no. 48, pp. 17678–17683, Dec. 2007.

[259] K. Chrissafis and D. Bikiaris, "Can nanoparticles really enhance thermal stability of polymers? Part I: An overview on thermal decomposition of addition polymers," *Thermochim. Acta*, vol. 523, no. 1–2, pp. 1–24, Aug. 2011.

[260] J. G. Park *et al.*, "Thermal conductivity of MWCNT/epoxy composites: The effects of length, alignment and functionalization," *Carbon N. Y.*, vol. 50, no. 6, pp. 2083–2090, May 2012.

[261] A. Sharma, V. Panwar, V. Chopra, J. Thomas, S. Kaushik, and D. Ghosh, "Interaction of Carbon Dots with Endothelial Cells: Implications for Biomedical Applications," *ACS Appl. Nano Mater.*, Aug. 2019.